Modelling Lytic Polysaccharide Monooxygenases: From Small Molecules to Artificial Enzymes

Martin Steward

PhD

University of York
Chemistry

June 2021

Abstract

Lytic polysaccharide monooxygenases (LPMOs) are Cu containing enzymes which break down lignocellulostic biomass *via* an oxidative mechanism. These enzymes are well studied, however the active species which performs this oxidation is unknown. The active site of LPMOs is known as the "histidine brace", which coordinates a Cu ion *via* two histidine side chains and the primary amine of the N terminus of the protein. Small molecule models of enzyme active sites have been widely used within the literature to gain insight into enzymatic processes.

We have investigated a new ligand system which aims to faithfully model the histidine brace by the incorporation of a primary amine into the coordination sphere of a Cu ion, which has been unexplored in the literature so far. To this end, (2S)-1-(1H-imidazol-4-yl)-3-[(pyridin-2-yl)methoxy]propan-2-amine, **2.3**, was synthesised and characterised along with its corresponding copper complexes. The electronic environment was probed using electron paramagnetic resonance spectroscopy which found that the electronics of this complex were similar to that of LPMOs (*LsAA9*) after substrate binding.

In order to evaluate the effect of hydrogen bonding on complex reactivity, an artificial enzyme methodology was used. A biotin-streptavidin system was devised in which **2.3** was modified *via* a Sonogashira cross coupling and subsequently biotinylated to form (1-*H* -imidazol-4-yl)propoxy]methyl)pyridin-4-yl)pro-2-yn-1-yl)-2-(2-oxohexahydro-1H-thieno[3,4-d]imidazole-4-yl) pentamide , **3.12** and its corresponding Cu complex. Incorporation into streptavidin significantly changes the electronic environment as observed by EPR and UV/Visible spectroscopy. Furthermore, at high pH the system was able to stabilise a new species, similar to one which has been observed in LPMOs.

Incorporation of **Cu(3.12)** into streptavidin resulted in a decrease in H_2O_2 production compared to the free complex. However, point mutations within the streptavidin vestibule restored activity to the level of the free complex, indicating that the hydrogen bonding network provided by the protein affects the reactivity of the complexes.

Table of Contents

List of Figures

List of Tables

Accompanying material

The CIF files of the from the single crystal X-ray diffractions of both the protein and small molecule crystals are submitted with this thesis.

Table A. CIF files provided with the thesis

Compound	File Name
$[Cu(Histamine)_2](NO3)_2$	Steward_108021168_Cu(Histamine)2(NO3)2
$[Cu(Histamine)_2](PF6)_2$	Steward_108021168_Cu(Histamine)2]PF6)2
$[Cu(Histamine)_2](PF6)_2$	Steward_108021168_Cu(Histamine)2(PF6)2 B
$[Cu(Histamine)]Cl_2$	Steward_108021168_Cu(Histamine)(Cl)2
$[Cu(2.3)_2](SO_4)$	Steward_108021168_Cu(2.3)2(SO4)
(3.12) ⊂ Sav	Steward_108021168_Sav2XM-Optimal

Acknowledgements

The completion of this thesis is the finish line of what has definitely been a marathon, during which I have been thoroughly challenged both scientifically and physically. During my time at York, I have met incredible people and done things that I could not have imagined. I will always remember this time of my life.

First I would like to thank my supervisors Paul Walton and Gideon Davies who have given me this fantastic opportunity. They have provided so much insight during the course of the work but also given me the space to allow for my own ideas to flourish. You have taught me so much and given me an enthusiasm for learning and science that I hope to always carry with me. A special thank you to Paul who always encouraged me especially when I was struggling, and put up with the results of my crazy ideas, rapid cooling in N_2 was never going to end well… Thank you for all the effort you have put in with me its truly appreciated!

A big thanks goes to my 'second' group across the pond, the Boroviks. Thank you for having me, Andy, it was amazing! I have never felt more welcomed than by you all. It was a real privilege to spend time in your lab and working with you was a pleasure that relighted my passion for chemistry. Thank you to you all as without you this project would not have been possible.

Thank you to all of the technical staff at York, you are a fantastic team and without your hard work this thesis would not have been possible. A special thanks to Naser for always going the extra mile with us Waltons, we all really appreciate it, you really are a glove box magician.

What a journey it has been and I would not have been able to do it without all of the amazing people I have met along the way. Thanks to all of the members of E002 past and present, the sense of comradery that started before me and lasted across my entire PhD is a testament to you all. Hopefully at some point the coffee club will return to the office, as both the support, discussion and more importantly caffeine was invaluable. Thanks to the Lunch group, Derwent lunch times were great and I'm going to miss them. Lewis, you were a great friend and flatmate, I miss living with you buddy!

Thanks to all the Waltons past and present, you have all taught me so much and your help and insight provided in "group meetings" have been fantastic. Thank you Daniel and Saioa for all of your expertise I would not be here without your contributions.

Thanks to the staff at Leeds hospital for putting me back together, my PhD didn't make me jump off the cliff, I promise. Thanks to Jon who taught me how to walk and sit at a desk again as without you I would never have been able to get to this point.

Now for a few extra special thank yous! Luisa, I would never have got here without all the love and support you have given me, you truly are my chemistry "mum" and you mean the world to me. You have been a fantastic "extra supervisor" and I know you will be amazing with your own group. It has been a pleasure being your friend. The MENZ, Ale, Peter and George: your insight, support and friendship mean the world to me, you are all incredible scientists and I wish you the best for the future. I owe all of you too many drinks to count, hopefully I can start paying you back soon.

A gigantic thank you to my parents and grandparents: without your love, support and help you have all given me I would not have finished. Thank you for looking after me after the accident and giving me the opportunity to put myself back together. The patience and kindness you have shown me is truly amazing, I can't thank you all enough. Sorry for worrying you all so much!

Finally, thank you Lucy for all of your love and support through everything. Thank you for making me so happy, I don't know what I would have done without you.

Author's Declaration

The work presented in this thesis has been carried out by the author, unless otherwise stated in the text. I declare that this thesis is a presentation of original work and I am the sole author. This work has not previously been presented for an award at this, or any other, University. All sources are acknowledged in the Bibliography section.

Some work which features in **Chapter 1** is published in the following paper,

Walton, P. H.; Steward, M.; Lindley, P.; Paradisi, A.; Davies, G. J., Copper oxygenases. In Comprehensive Coordination Chemistry III, Que, L.; Lu, Y., Eds. ELSEVIER ACADEMIC PRESS INC: 2020; 1-24.

Work carried out by other persons:

ESI-MS experiments were carried out by Mr Karl Heaton.

X-ray crystallography was performed by, or with the assistance of, Dr Adrian Whitwood and Mr Theo Tanner.

Elemental analyses were carried out by Dr Graeme McAllister.

MALDI TOF experiments were collected under the guidance of Dr Saioa Urresti.

Streptavidin and its corresponding mutants were produced and purified by Dr Kelsey Miller and Miss Ankita Biswas under the supervision of Prof. Andrew Borovik, at the University of California, Irvine.

Amplex Red assays were carried out under the guidance of Dr. Nicholas McGregor.

Stopped Flow experiments were carried out by Dr. Daniel Diaz.

Protein crystallography work was carried out under the guidance of Dr Saioa Urresti.

Chapter 1. Introduction

1.1 Copper in Nature

Copper is a transition metal crucial for biological life. It is used as a metallocofactor in enzymes with a wide range of functions and across the tree of life. However, due to the relatively high abundance of copper in the earth's crust and its moderate solubility, organisms must be able to transport, store, and control copper levels in order to function. These processes are tightly regulated in order to avoid the toxic effects of excess copper.[1] Copper-containing enzymes are broadly characterised into several types based on function and active site geometry: Type 1, Type 2 and Type 3 copper centres.

1.1.1 Type 1 Copper Proteins

The coordination geometry of proteins containing a Type 1 copper site (Cupreodoxins) consist of a mononuclear copper centre which is coordinated by a combination of histidine (his), methionine (met), cysteine (cys) and glycine (gly) amino acid residues. Variation of the coordination geometry and coordinative residues in the active site result in the further splitting of type 1 copper proteins into four subclasses. Type 1 copper proteins are primarily involved in electron transport as opposed to catalysis. They are used for electron transport as the self-exchange of electrons between Type 1 copper sites is rapid, with a rate constant of 10^4 – 10^6 M^{-1} s^{-1}.[2] This rapid rate constant is facilitated by both a small energetic gap between the Cu(I)/Cu(II) redox couple and a low reorganisation energy between Cu(I)/Cu(II) due to the rigidity of the site, as postulated by Marcus theory.

Type 1 copper sites are characterised spectroscopically by an intense ligand to metal charge transfer (LMCT) band in the UV/Visible spectrum. This occurs due to a charge transfer from the cysteinate sulphur to the copper ($\varepsilon_M \sim 5000$ M^{-1} cm^{-1}) in the 600 nm region, shown in Figure 1 left. The electron paramagnetic resonance (EPR) spectra of these proteins consist of a magnetically isolated spin = ½ Cu centre with a $d_{x^2-y^2}$ ground state. A characteristic feature of these proteins is a low A_z (< 176 cm^{-1}) , shown in Figure 1 right, due to the highly covalent Cu –S Bond which results in a reduction of spin density on the copper ion compared to a less covalent system. [3]

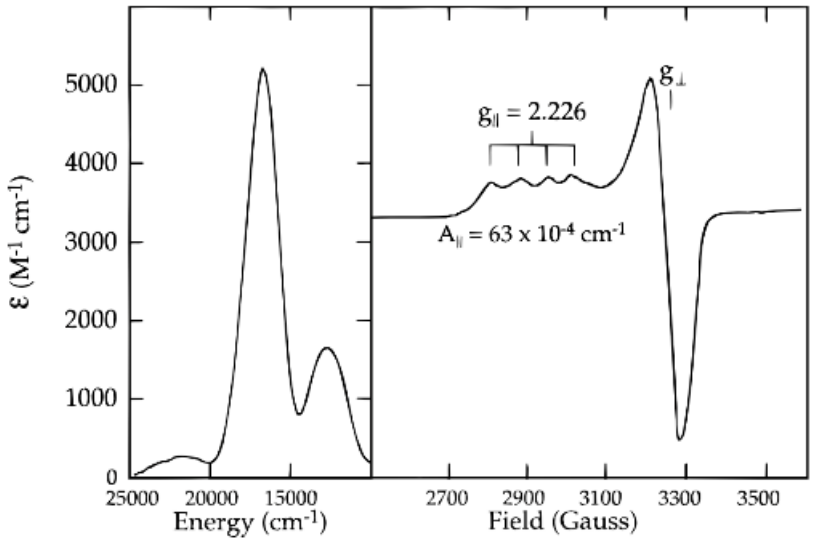

Figure 1. Left, the electronic absorption spectra of poplar plastocyanin. Right, the EPR spectrum of poplar plastocyanins. Figure adapted from Richard H. Holm et al.[3]

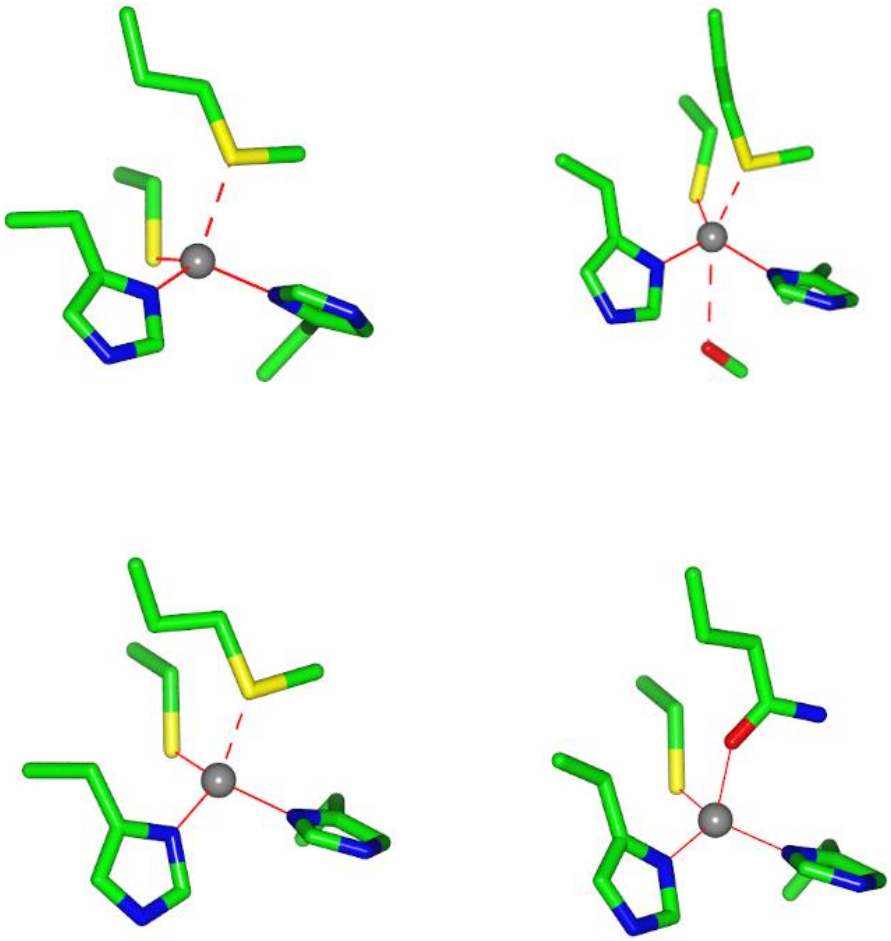

Figure 2. The active site geometry of different subclass Copper Type 1 site. Top Left, Active site of Plastocyanin from Ulva pertusa (PDB 1IUZ).[4] *Top Right, Active site of Azurin from Achromobacter denitrificans (PDB 2AZA).*[5] *Bottom Left, Active site of Pseudoazurin from Methylorubrum extorquens (PDB 1PMY).*[6] *Bottom Right, Active site of Stellacyanin from Cucumis sativus* (PDB 1JER).[7]

The active site geometry of the four subclasses of Type 1 copper sites is shown in Figure 2. The first of these subclasses is found in plastocyanins, and the copper coordination sphere consists of a cysteinate, methionine, and two histidine residues in a distorted tetrahedron configuration, Figure 2 top left.[8] The second subclass is comprised of the azurins. The coordination environment of the Cu site in azurins is similar to that of plastocyanins, the only difference being a carbonyl from a nearby glutamine residue *trans* to the methionine which forms a weak ionic interaction with the Cu centre, Figure 2 top right.[9] The third subclass consists of nitrite reductases and pseudoazurins, which have the same coordinating residues as those found in plastocyanins. The coordination environment differs as the angles between the coordinating ligands have significantly changed, with the overall geometry of the Cu centre becoming more planar, and a significant shortening of the Cu methionine bond has occurred, Figure 2 bottom left. The fourth class lacks the methionine residue seen in all other subclasses, with the methionine residue replaced by a glutamine residue which coordinates the copper ion *via* the oxygen atom, Figure 2 bottom right.[3, 10-11]

1.1.2 Type 2 Copper Sites

The coordination geometry of a type 2 copper site consists of a mononuclear copper centre which is coordinated by up to six nitrogen or oxygen ligands in a tetragonal geometry, an example is shown in Figure 3.[12] The diverse ligand set available to copper proteins of this type includes amino acid side chains, the protein backbone and exogenous ligands such as water or hydroxide. The large number of potential ligands results in a structurally diverse class of proteins. As such, all possible variations in coordination geometries will not be discussed in detail here, but instead will be categorised according to function in the following sections.

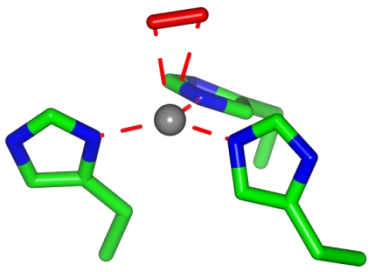

Figure 3. The active site of hydroperoxo-bound copper amine oxidase an example of a type II copper site. (PDB 1D6Z)[13]

As structure and function are inherently linked, the chemistry performed by type 2 copper proteins is also broad. The Cu centre in type 2 copper proteins is able to perform a wide range of oxidative chemistry. The dissociation of exogenous ligands allows for the coordination of substrate by the Cu centre, followed by direct electron transfer from the metal during oxidation.

Spectroscopically the type 2 Cu centre is defined as a magnetically isolated s = ½ Cu with a $d_{x^2-y^2}$ ground state with an A_{II} > 340 MHz.[12] The UV/Visible spectrum of type 2 copper proteins only features weak *d-d* transitions ($\varepsilon_M \sim 100\ M^{-1}\ cm^{-1}$) at higher wavelengths due to the absence of a covalent bond from cysteine compared to type 1 copper site.

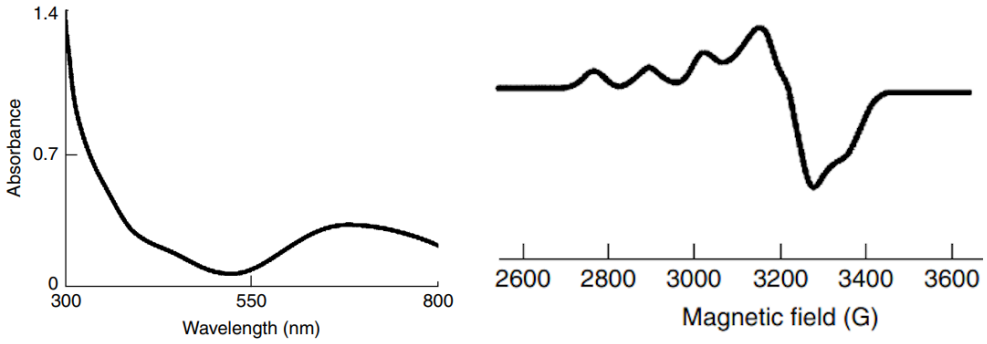

Figure 4. The electronic absorption spectra (Left) and EPR spectrum (Right) of Cu, Zn SOD. Figure adapted from McGuirl et al.[12]

1.1.3 Type 3 Copper Sites

The coordination geometry of proteins containing a type 3 copper site consists of an antiferromagnetically coupled dicopper centre. Both copper centres are coordinated by three histidine side chains and are bridged by an exogenous ligand in the Cu(II) state, which is lost on reduction to Cu(I).[14] Functionally these proteins can behave as both oxidases, as in tyrosinases, and oxygen transport proteins, as in haemocyanin. However, oxidase activity can be induced in haemocyanins *via* the addition of hydrogen peroxide, indicating that these proteins share some functional overlap.[15-16]

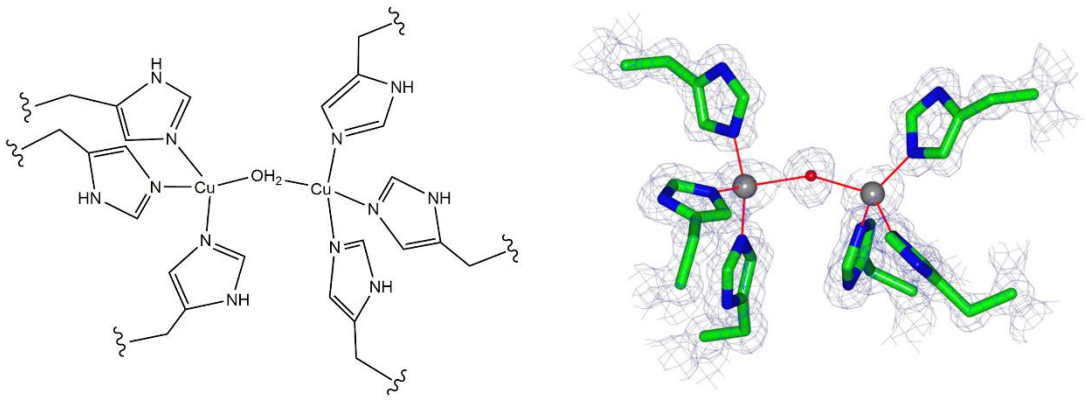

*Figure 5. An example of the coordination geometry seen in a type 3 copper sites. Image from a tyrosinase from Streptomyces castaneoglobisporus (PDB 5Z0D).**

Spectroscopically the type 3 copper centre differs significantly from both type 1 and 2 copper centres. This is due to the antiferromagnetic coupling between the two copper centres which results in the overall spin state of the type 3 site being zero and thus it cannot be studied by EPR spectroscopy. The oxy form of the enzyme , where O_2 is bridging both coppers in the μ-η^2:η^2-Peroxo form, has a characteristic UV/Visible spectrum, with absorption bands at ~330 nm (ε_M = ~ 3000 M^{-1} cm^{-1}) and ~600 nm (ε_M = ~ 5000 M^{-1} cm^{-1}) (Figure 6).[17]

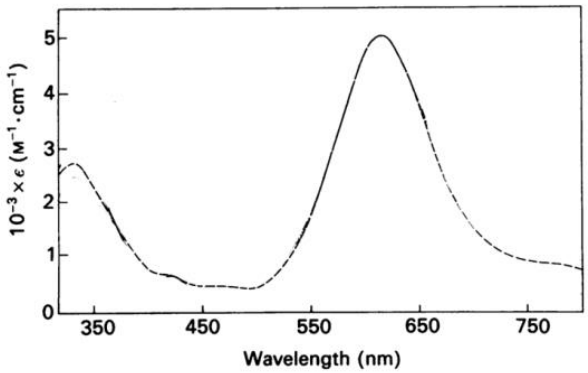

Figure 6. The electronic absorption spectra of oxy form of native laccase. Figure adapted from Tamilarsan et al.[17]

1.2 Copper oxygenases

Copper oxygenases are a diverse group of copper-containing enzymes that use dioxygen (O_2) as the terminal oxidant. This is a broad class of enzymes which features a diverse set of Cu active sites. The nature of this oxidation can be used to further categorise these enzymes: if one of the O atoms in O_2 is incorporated into the product the enzyme is known as a monooxygenase, and if both O atoms are incorporated, it is known as a dioxygenase.

1.2.2 The Chemistry of Oxygenases

In order to incorporate O_2 into an organic product, a change in spin state must occur. This is because O_2 is in a triplet ground state ($S = 1$), while the organic reactant is assumed to be in a singlet ground state, and the process will result in a singlet product, hence this process is spin forbidden. Therefore, in order to catalyse a reaction in which O_2 is incorporated into a product, the enzyme must be capable of changing the spin state of O_2 by intersystem crossing, which will allow for a spin allowed process and hence reactivity. This intersystem crossing is facilitated by the use of enzymatic co-factors which are commonly transition metals such as, in the case of copper oxygenases, copper. Transition metal cofactors are commonly utilised by enzymes for this purpose, as spin-orbit coupling at the metal ion enhances intersystem crossing between the spin state surfaces. Furthermore, transition metals can provide electrons for redox reactions where the redox partner is either substrate or O_2. Hence, copper oxygenases can form a range of Cu derived species such as superoxide, peroxide, hydroxide and oxyl, along with their protonated congeners, shown in Figure 7.

Copper oxygenases oxidise a wide range of substrates, which include polysaccharides in the case of lytic polysaccharide monooxygenases and Cu itself in the case of Cuprous oxidase (CueO). In many of these oxidations a C-H bond must be broken, which must occur in a hydrogen-atom abstraction (HAA) step, hence the strength of the C-H bond must be considered. This is due to the fact that the hydrogen atom transfer step contains a large contribution from the strength of this bond as such the strength of the newly formed O-H bond must be as equally large or otherwise the energetic barrier would be too high preventing reactivity.

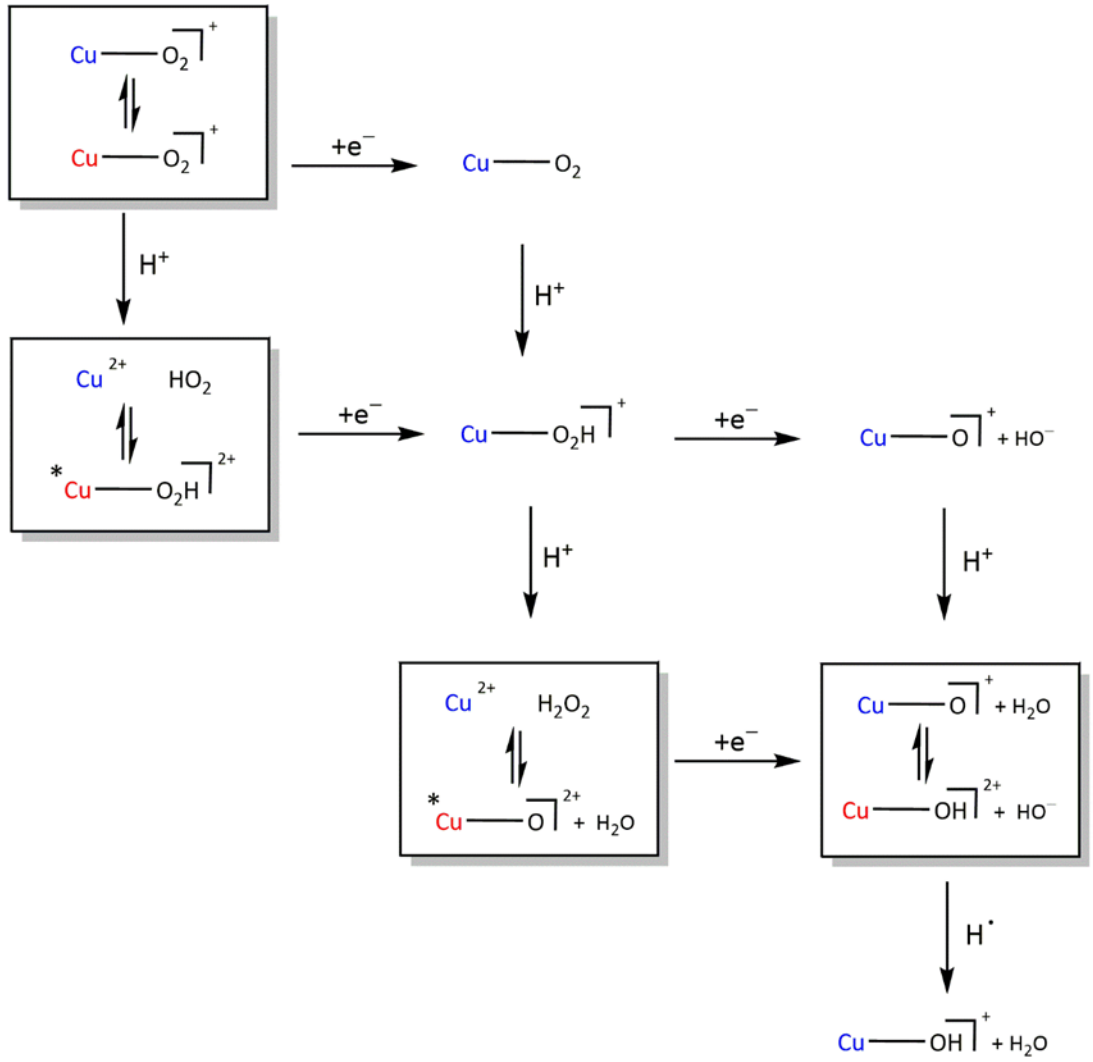

Figure 7 Copper-oxygen species that have been observed or proposed, with indications of copper oxidation state, blue = +2, red = +3. Reproduced from Walton et al.*[18]

1.2.3 The Four Electron Reduction of O_2 to H_2O

1.2.3.1 Multicopper Oxidases

Multicopper Oxidases (MCOs) catalyse the reduction of O_2 to H_2O with the oxidation of an organic or inorganic substrate. The active site of MCO is conserved across all enzymes and consists of a total of four copper ions divided in to a mononuclear type 1 copper centre (T1) and a trinuclear copper centre (TNC), 12-13 Å apart.[19-20] The trinuclear site comprises of a binuclear type 3 copper site and a type 2 copper site. The coordinating residues and overall geometry of the TNC are conserved across the entire MCO family as shown by enzyme sequence alignments and known crystal structures. An example structure from *Bacillius subtilis* (PDB 2BHF) is shown in Figure 8.

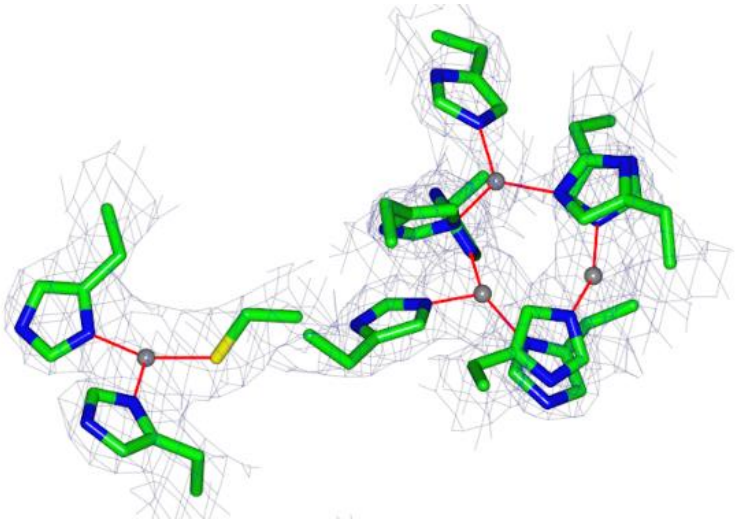

Figure 8. An example structure of a multicopper oxygenase with the TNC site in reduced form from Bacillius subtilis (PDB 2BHF) with electron density map at 0.3 e/Å^3. Adapted from Walton et al.[18]

These enzymes oxidise a diverse range of substrates,[21-25] but despite this the general reaction scheme (Figure 9) does not change. Oxidation of substrates occurs at the T1 site and reduction of O_2 to water occurs at the TNC. The T1 site is responsible for the substrate specificity of this class of enzymes where the Cu coordination sphere modulates the reactivity of the Cu centre. Following the oxidation of the substrate, the resultant electrons are transferred to the TNC *via* a highly conserved electron pathway, which are then used for the reduction of O_2.[26]

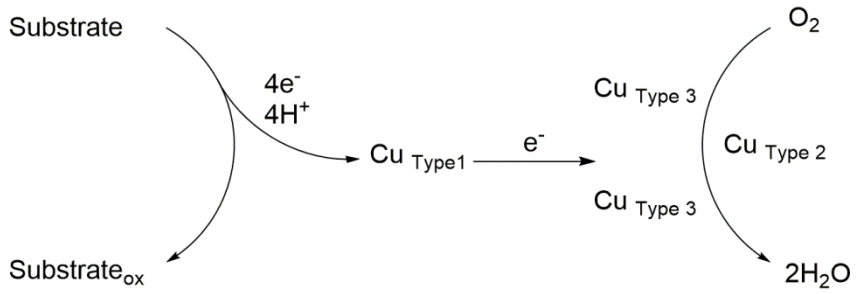

Figure 9. General reaction scheme of the oxidation carried out by multicopper oxidases. Reproduced from Walton et al.[18]

1.2.3.2 Heme-Copper oxidases

Heme-copper oxidases catalyse the final step of the respiratory process where dioxygen is reduced to water, coupled with the translocation of four protons across the mitochondrial or cytoplasmic membrane.[27] This reaction mechanism occurs *via* the binding of dioxygen to Fe(II) and Cu(I) to form a Fe(III)-peroxide Cu(II) complex, which is then followed by the reductive cleavage of the dioxygen to form a Cu(II) hydroxide and Fe(IV)-oxo. Subsequently, the reduction of the oxygen species to two equivalents of water occurs, Figure 10. [27] It should be noted that this process requires four electrons to complete; however, the metal centres can only provide three. Hence, an additional electron is provided by a tyrosine which is cross-linked to one histidine coordinating the Cu ion, which can transiently form a tyrosyl radical thus providing the additional electron.

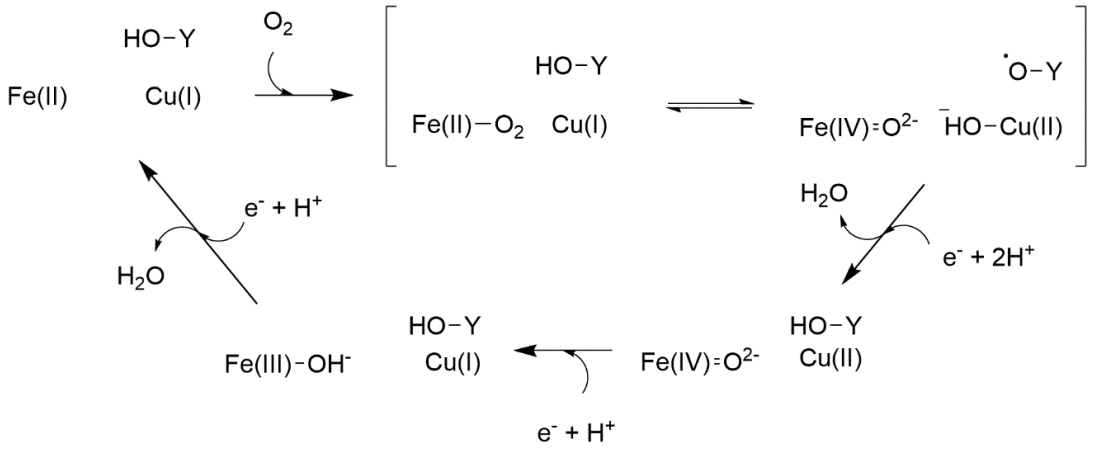

Figure 10. The general reaction scheme of the oxidation carried out by heme-copper oxidases Reproduced from Walton et al.[18]

The site of O_2 reduction in heme-copper oxidases is highly conserved and consists of a bimetallic site (Figure 11) where the Cu and Fe are separated by ~ 4.3 – 5.4 Å. The copper is coordinated by three histidine side chains, one of which has been post translationally modified with a covalent link to a nearby tyrosine.[28] The Fe site is a high-spin heme coordinated by an axial histidine side chain.[29-31]

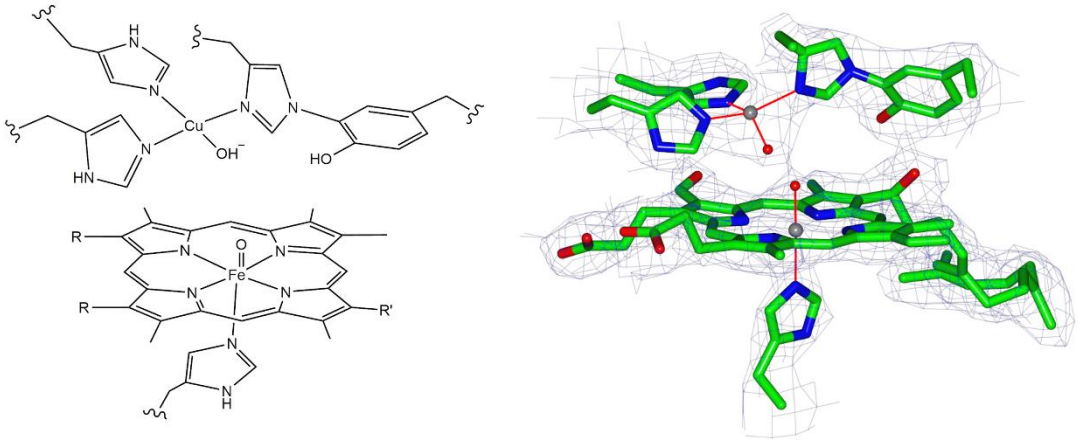

Figure 11. The structure of the O_2 activation site of heme-copper oxidases galactose oxidase from Bos Taurus (PDB 6NKN). left, schematic diagram, right, electron density map at 0.6 e/Å^3 Reproduced from Walton et al.[18]

1.2.4 The Two Electron Reduction of O_2 to H_2O_2

1.2.4.1 Galactose oxidase

Galactose oxidases (GO) are a class of enzymes which catalyse the oxidation of primary alcohols, including the C6 carbon of the monosaccharide galactose, to the corresponding aldehyde in an overall 2-electron reaction (Figure 12) and the oxidation of aldehydes to corresponding carbocyclic acids at a reduced rate.[32] More recently a wider substrate scope for these enzymes has been identified and hence this class may be better named aliphatic alcohol oxidases.[33]

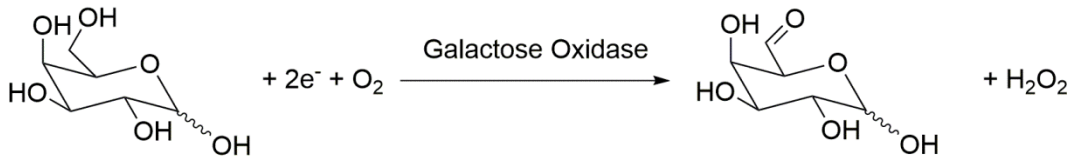

Figure 12. The general reaction scheme of the oxidation carried out by galactose oxidase Reproduced from Walton et al.[18]

The active site of galactose oxidase consists of a mononuclear copper centre which is coordinated to two histidine side chains and two tyrosines, and the coordination sphere is then completed by a water molecule in an overall square pyramidal geometry (Figure 13). Interestingly, one of the tyrosines has been post translationally modified via a cysteine crosslink in the *ortho* position and has formed a tyrosyl radical which has been shown spectroscopically to be redox active.[34-35] This tyrosine is key for this enzyme's reactivity as it performs a deprotonation on the substrate which lowers the strength of the C−H bond on the α-carbon by ~10 kcal/mol, which facilitates reactivity.[35] Following substrate oxidation the tyrosyl radical is regenerated *via* the binding of O_2 and the subsequent formation of a hydroperoxo, which is converted to H_2O_2 on the binding of substrate to the Cu centre. This ping-pong mechanism highlights the importance of both the Cu(I)/Cu(II) and tyrosine/tyrosyl redox couples. [36-38]

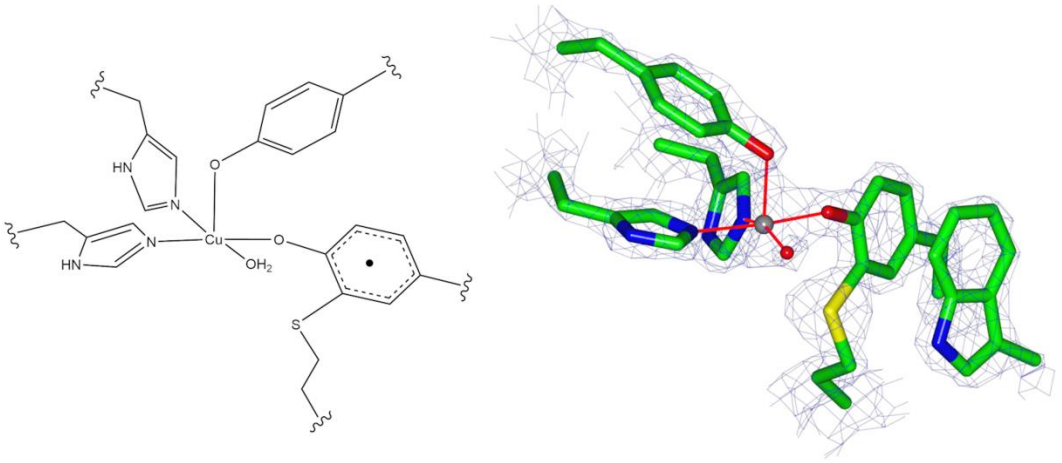

Figure 13 Structure of the active site of galactose oxidase from Streptomyces lividans TK24 (PDB 4UNM). Left, schematic diagram, Right, electron density map at 0.6 e/Å^3. Reproduced from Walton et al.[18]

1.2.4.2 Copper Amine Oxidase

Copper amino oxidises are a class of the mononuclear copper enzymes which catalyse the oxidative deamination of primary amines and cyclic imines.[39-40] This reaction occurs *via* two half-reactions. The first is the reductive half reaction in which 2,4,5-trihydroxyphenylalanine quinone (TPQ), a protein bound cofactor, is reduced and the amine is oxidised to the corresponding aldehyde. The oxidative half reaction follows this, as TPQ is reoxidised by the Cu site which is coupled with the generation of H_2O_2 and ammonia (Figure 14). [41-42]

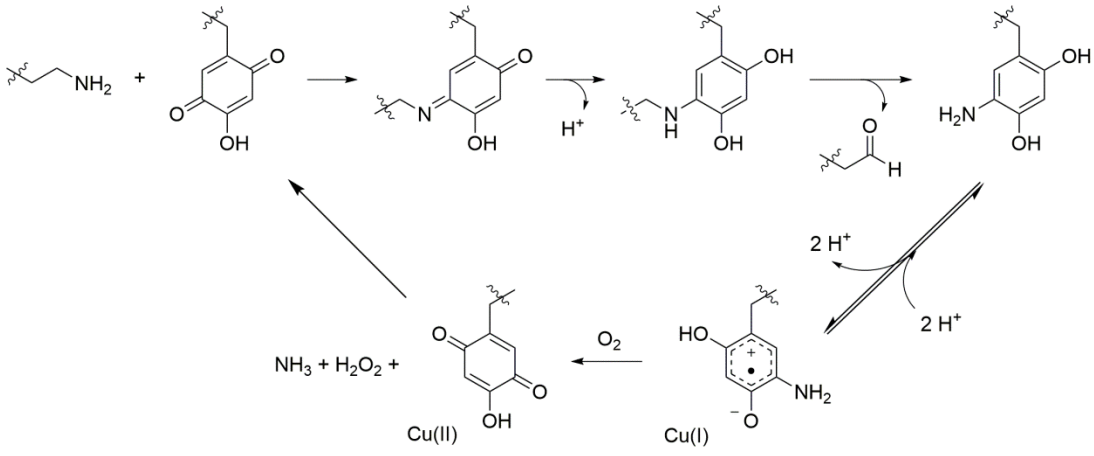

Figure 14. The general reaction scheme of the oxidation of an amine by a copper amine oxidase: Top reductive half reaction, Bottom oxidative half reaction. Reproduced from Walton et al.[18]

The active site of copper amine oxidase is well conserved and consist of a Cu ion coordinated by three histidine side chains (Type 2 Cu site) and by two water molecules in an overall square pyramidal geometry (Figure 15).[43] The nearby TPQ cofactor is generated by the reaction of an unmodified tyrosine with molecular oxygen at the copper active site.[42]

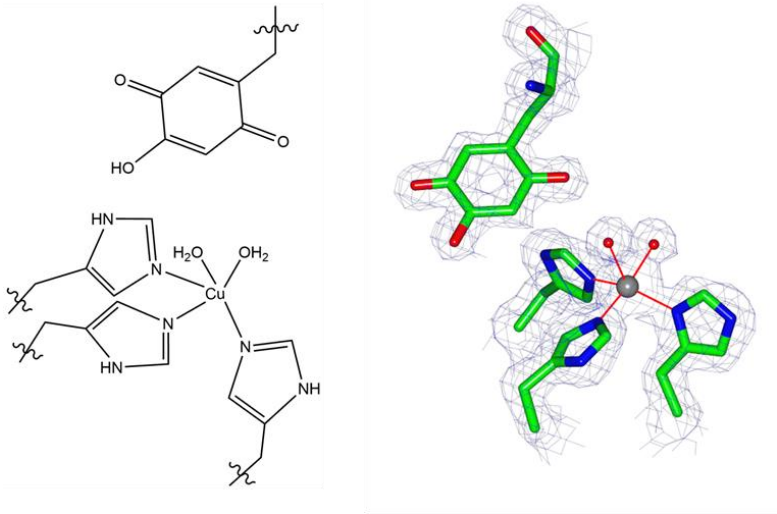

Figure 15. Left The schematic representation of the active site of Cu amine oxidase. Right the active site of Copper amine oxidase in the Active from Arthrobacter globiformis (PDB 3WA3) electron density maps at 0.6 e/Å^3. Adapted from Walton et al.[18]

1.2.5 Copper Monooxygenases

1.2.5.1 Lytic Polysaccharide Monooxygenases

Lytic polysaccharide monooxygenases (LPMOs) are enzymes that cleave the glycosidic bonds of polysaccharides in either the C1 or C4 position *via* an oxidative mode of action. They carry out this chemistry using either H_2O_2 or O_2 and an external electron donor, to provide the necessary electrons, Figure 16.[44-47] LPMOs are widespread in Nature and are found in many different organisms including fungi, bacteria, molluscs, insects and some animals. The substrate specificity of LPMOs is broad as they have been demonstrated to degrade polysaccharides such as cellulose, chitin, xylan, xyloglucan and starch. These enzymes are classified in the carbohydrate active enzyme (CAZy) Database as Auxiliary Activity (AA) families based on similarities in their amino-acidic sequences. Within the literature there are currently seven distinct phylogenetic groups called: AA9[48], AA10,[46] AA11, AA13,[49-50] AA14,[51] AA15 [52] and AA16. [53]

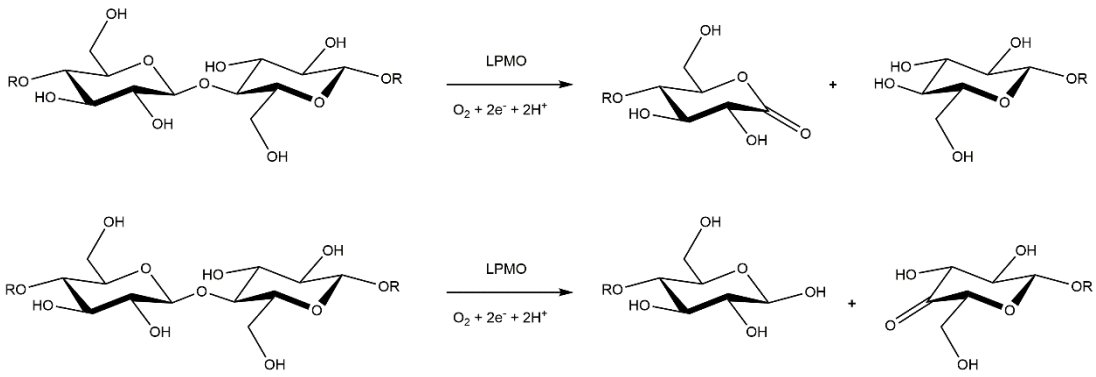

Figure 16. The general reaction schemes of the oxidations carried out by LPMOs. Reproduced from Walton et al.[18]

The primary copper coordination sphere is conserved in all families and consists of a mononuclear Cu site, in which the Cu ion is coordinated by two histidine residues. The N-terminal histidine which chelates the Cu ion through the NH_2 group and the δ-N of the imidazole side chain, together with the ε-N of the imidazole ring of the second histidine residue, form an overall T-shaped geometry known as the 'histidine brace' (or *His brace*). The coordination sphere is then completed by two exogenous water molecules resulting in either a square pyramidal or Jahn-Teller distorted octahedral geometry, shown in Figure 17.[45] These enzymes will be discussed in more detail in section **1.3**.

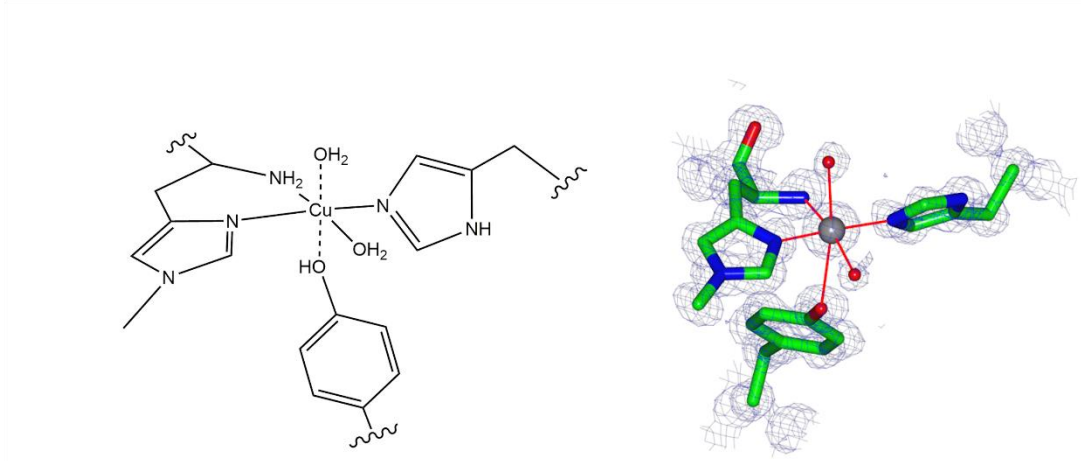

Figure 17. The structure of the active site a Lytic Polysaccharide Monooxygenase from Hypocrea jecorina (PDB 5O2X): left, schematic diagram, right, electron density map at 0.7 e/Å^3 Reproduced from Walton et al.[18]

1.2.5.2 Particulate Methane Monooxygenase

Methane monooxygenases (MMOs) are a class of enzymes which oxidize methane to methanol and form one molecule of H_2O in the presence of a reducing agent and proton source (Figure 19). These enzymes oxidize the strong methane C−H bond (bond dissociation energy ~104 kcal/mol) *via* a currently unknown mechanism. These enzymes can be subdivided into two forms: a soluble form (sMMO) where the active site consists of a non-heme di-nuclear Fe site, and a particulate membrane-bound form (pMMO), in which the active site is believed to be a mononuclear Cu centre.[54] Of the two forms, pMMO is the most common whereas sMMO is produced by methanotrophs at low copper concentrations.[55]

$$CH_4 \xrightarrow[O_2 + 2H^+ + 2e^-]{\text{pMMO}} CH_3OH + H_2O$$

Figure 18. The general reaction scheme of the oxidation carried out by pMMO

pMMO is a large protein (~390 kDa)[44-] which consists of a trimeric assembly of protomers each of which comprises of two transmembrane domains (PmoA and PmoC) and a transmembrane subunit with a large periplasmic domain (PmoB). [56-57] Within this structure, three Cu binding sites have been identified: the Cu_B site, found in the PmoB domain, the Cu_C, found in the PmoC domain and a third site found in PmoB known as the bis-His site. The bis-His site is not conserved across the pMMO family and is therefore believed to be a crystallographic artefact that will not be discussed further.[58]

The nature of the active site of pMMO has been controversial within the literature. Initially it was believed to be the Cu_B site located within the PmoB domain of the protein, which was assigned as a di-nuclear Cu site; [59-60] however, recent work resulted in the reassignment of this site as mononuclear following quantum refinement of the crystal structure[61] and additional electron paramagnetic resonance data. [62] Following the quantum reassignment of the Cu_B site as mononuclear, the Cu ion was found to be coordinated by four nitrogen atoms in an overall square planar geometry. Three of the nitrogen atoms are from hystidyl imidazole side chains, while the fourth is the NH_2 group from the amino terminus histidine of the PmoB domain, Figure 19. Furthermore, electron nuclear double resonance (ENDOR) spectroscopy provides evidence supporting the presence of an axial water molecule bound to the Cu ion in the resting state of the enzyme which could not be resolved crystallographically. Therefore, the copper coordination geometry may instead be best described as square pyramidal.[62]

The Cu_c site consists of a mononuclear copper ion which is coordinated by two histidine residues *via* the imidazole side chains and an aspartate ligand which is coordinating as a monodentate ligand (Figure 19). ENDOR spectroscopy suggests that the coordination sphere is completed with a water molecule, hence the overall coordination geometry of this site is best described as square planar.[63]

It was previously thought that the Cu_B site was the active site for methane oxidation. However, the relevant catalytic site of the enzyme has been re-assigned to Cu_C which was previously thought to play a structural role. This reassignment has occurred as the Cu_c site, rather than the Cu_B site, was found to interact with NO_2^- *via* EPR studies. This indicates that the Cu_c site is able to interact with exogenous ligands, which is required for activity with dioxygen.[62]

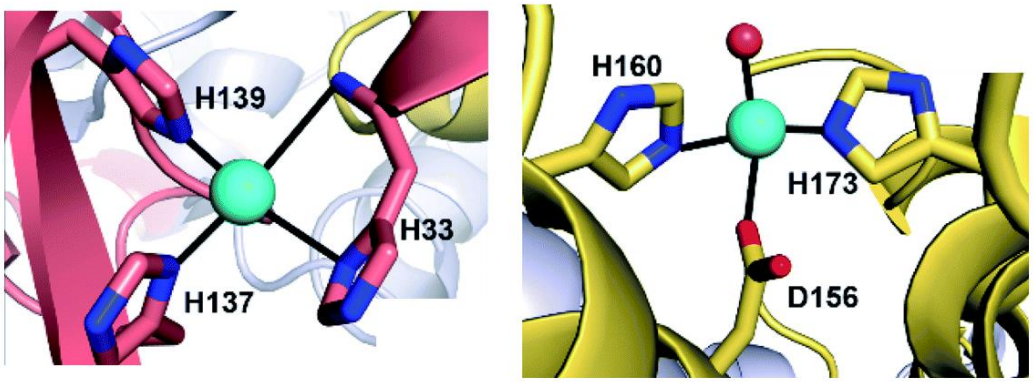

Figure 19. Schematic representations of the two characterised Cu binding sites in pMMO. Left, Cu_B site. Right, the Cu_C site. Reproduced from Cutsail et al.[63]

1.2.5.3 Non-coupled Binuclear Copper Monoxygenases

The non-coupled binuclear copper monoxygenases (NCBMs) make up a diverse class of enzymes which perform C–H bond hydroxylation during the synthesis of physiologically important neurotransmitters and hormones. This hydroxylation occurs via a two electron oxidation which is coupled to the reduction of O_2 to water and the incorporation of the second oxygen into the substrate (Figure 20), which is both regio- and stereospecific for the target C–H bond. This class contains peptidylglycine α-hydroxylating monooxygenase (PHM), dopamine β-monooxygenase (DβM), tyramine β-monooxygenase (TβM) and monooxygenase X (MOX), all of which share high sequence similarity and a conserved active site.[64-66]

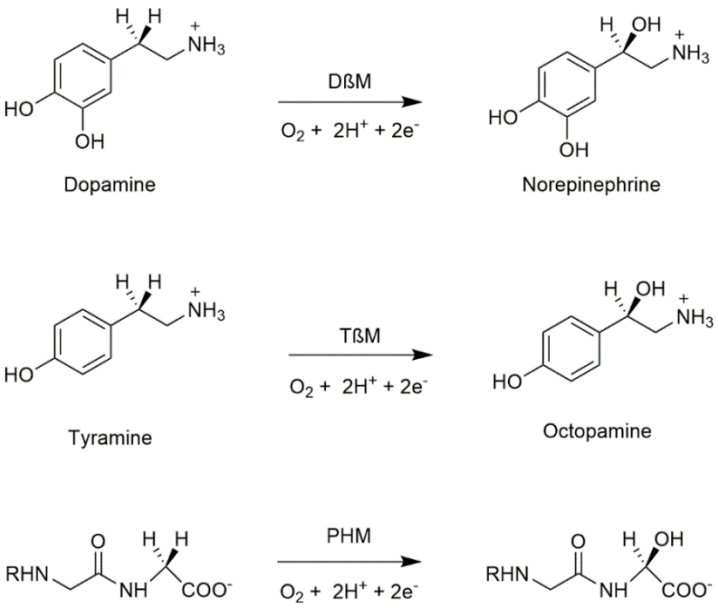

Figure 20. The general reaction schemes of the oxidations carried out by non-coupled binuclear copper monooxygenases. Reproduced from Walton et al.[18]

The active site of these enzymes consists of two mononuclear centres, the Cu_H site and the Cu_M site, which are separated by approximately 11 Å[67] and, as a result of this distance, they do not electronically couple. The two sites fulfil two different roles: the Cu_H site acts as an electron transfer site and the Cu_M is the site where substrate oxidation occurs. [68-70] The two sites are coordinately distinct, as in the Cu_H site the Cu ion is ligated by three histidine side chains while the Cu_M site is a single copper ion ligated by two histidine side chains and a methionine side chain, (Figure 21). In the Cu(II) resting state the coordination sphere is completed by a H_2O molecule and both sites adopt a tetrahedral geometry.[71-72]

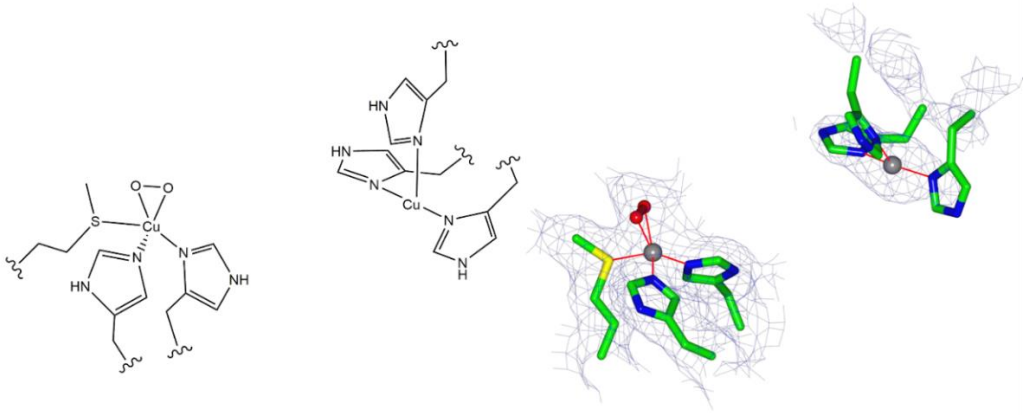

Figure 21. The active site of a PHM from Rattus norvegicus in complex with peroxide (PDB 4E4Z): left, line diagram; right, electron density map at 1 e/Å^3 Reproduced from Walton et al.[18]

1.2.5.4 Tyrosinase and Catechol oxidase

Tyrosinase and catechol oxidase enzymes are binuclear coupled copper proteins (Type 3) which oxidise phenols and catechols. These enzymes perform the two electron oxidation of *o*-catechols to *o*-quinones, where tyrosinases possess additional reactivity and can catalyse the oxygenation of phenols to *o*-catechols. [36-38, 73] The active site of these enzymes is a classical type 3 copper site in which two Cu ions are coordinated by three histidine side chains (Section **1.1.3**).

The reaction mechanism of the two electron oxidation of *o*-catechols to *o*-quinones proceeds *via* the initial binding of O_2 to the di-nuclear site forming a dicopper μ-η^2:η^2-peroxo. Following this the catechol binds to one of the Cu centre *via* the loss of a proton, which is then oxidised to form the quinone coupled with the generation of a water molecule. This results in the formation of a di-Cu bridged hydroxo which can then bind a second molecule of substrate that is then oxidised to a *o*-quinone. (Figure 22). The oxygenation of phenols to *o*-catechols by tyrosinases occurs via a similar mechanism and

then can be further oxidised to *o*-quinones in an overall four electron process (Figure 22).[16, 74]

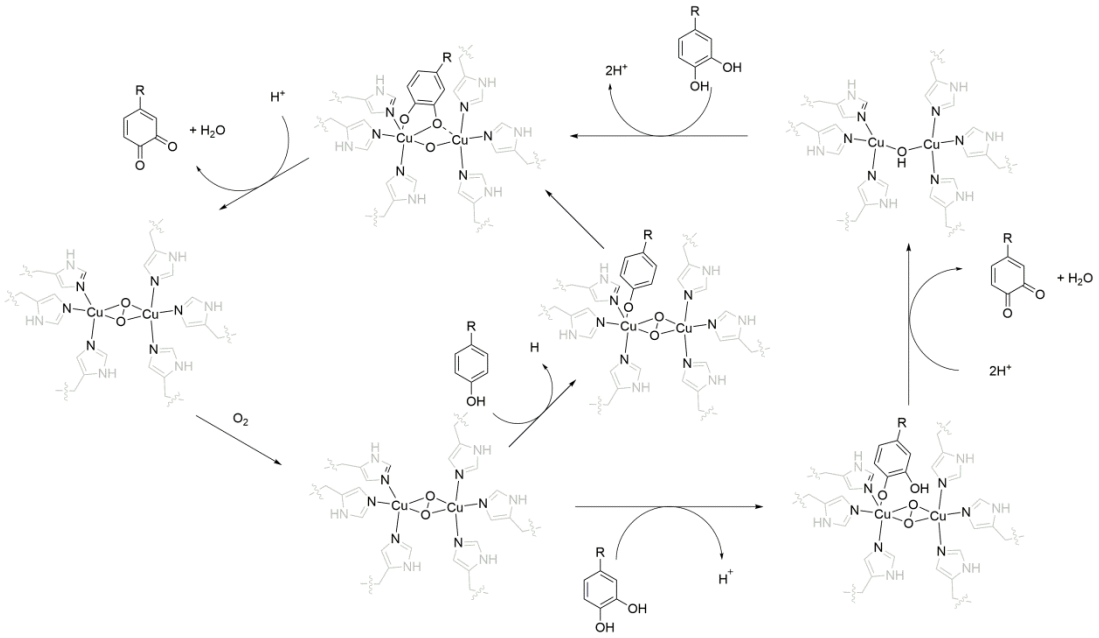

Figure 22. The proposed catalytic mechanism for the oxidation of o-catechols to o-quinones by Tyrosinase and Catechol oxidase (Outer) and the proposed mechanism for the oxidation of phenols to o-catechols by tyrosinases adapted from Decker et al. [16]

1.2.5.5 Formylglycine-Generating Enzyme

The formylglycine-generating enzyme is a recently discovered class of mono copper enzymes which oxidise cysteine or serine to formylglycine in the presence of O_2 (Figure 23).[75] This class of enzymes is unique as the Cu ion is coordinated in the resting state of the protein by two cysteine residues in a linear arrangement. During catalytic turnover the substrate is thought to bind to the Cu centre resulting in a distorted trigonal planar coordination sphere which is then able to react with molecular oxygen (Figure 24) [75-76]

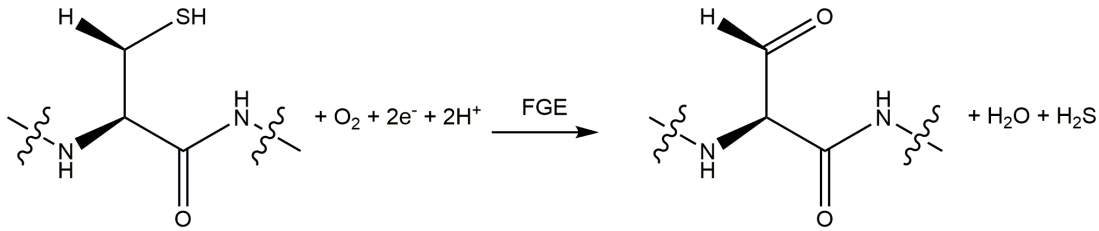

Figure 23. The oxidation of cysteine residues carried out by Formylglycine generating enzymes. Reproduced from Walton et al.[18]

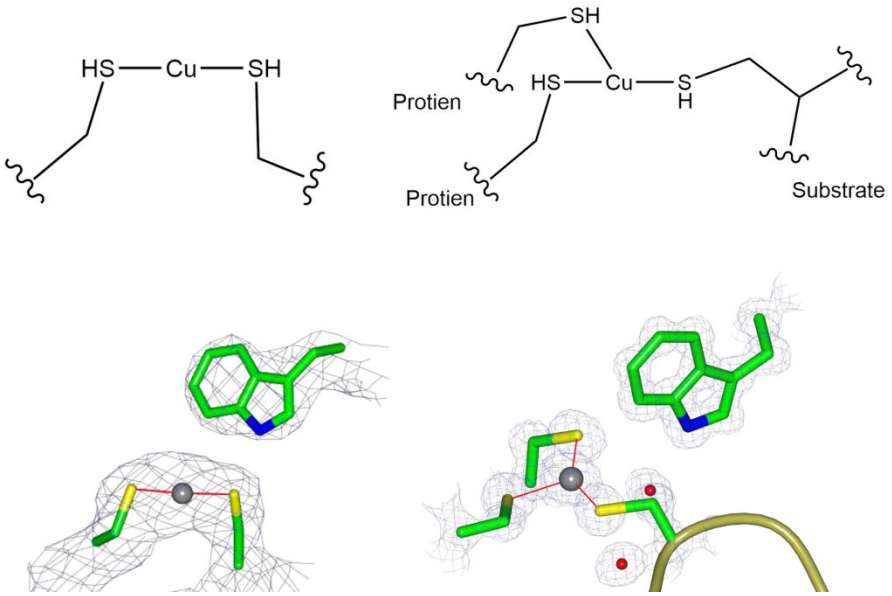

Figure 24. The structure of the active site of Formylglycine generating enzyme from Streptomyces coelicolor and Thermomonospora curvata (PDB 6MUJ and 6S07). Top, schematic diagram of the resting and substrate bound structures respectively with the gold chain representing substrate. Bottom, the corresponding electron density maps at 0.27 e/Å^3 and 0.7 e/Å^3 respectively. Reproduced from Walton et al.[18]

1.2.6 Copper Dioxygenases

1.2.6.1 Quercetin 2,3 dioxygenases

The quercetin 2,3 dioxygenases, also known as quercetinases, are a class of enzymes which breakdown quercetin and other flavanols to depsides coupled with the release of carbon monoxide (CO) (Figure 25).[77-78] The mechanism of these enzymes remains unclear as the oxidising intermediate is unknown, but the general reaction mechanism is generally agreed upon. The reactive intermediate is formed on reaction of O_2 with a Cu(I) substrate radical complex which is transiently formed on substrate binding. Following the oxidation of the substrate an endoperoxo is formed on the substrate which immediately undergoes O-O bond cleave resulting in the release of CO.[31, 79]

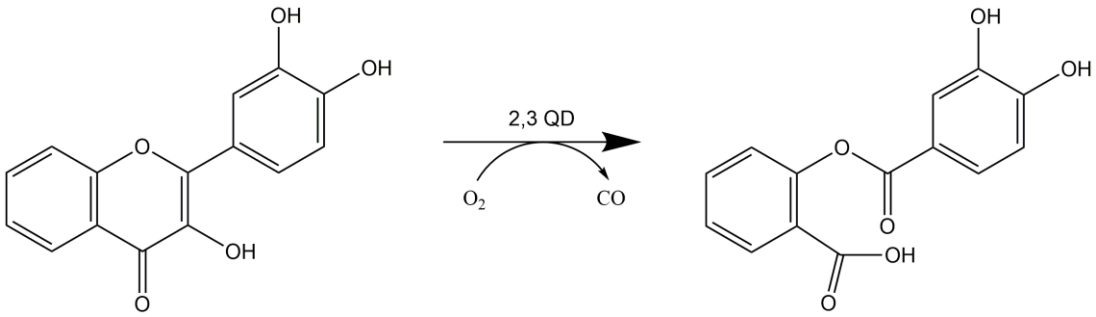

Figure 25. The reaction scheme of the oxidation carried out by quercetin 2,3 dioxygenases Reproduced from Walton et al.[18]

The resting state of these enzymes has been shown to occupy two forms both spectroscopically and cystallographically. In both of these forms the mononuclear Cu ion is coordinated by three histidine side chains; the difference between these forms is the coordination of a nearby glutamate side chain, the major form (70%) is where glutamate side chain is unbound and the minor form (30%) where the glutamate is bound to the Cu centre (Figure 26). The coordination sphere is completed in an overall trigonal bipyramidal geometry.[80] On the binding of substrate the protein fully adopts the glutamate bound form which forms a hydrogen bond with the substrate (Figure 26).[81]

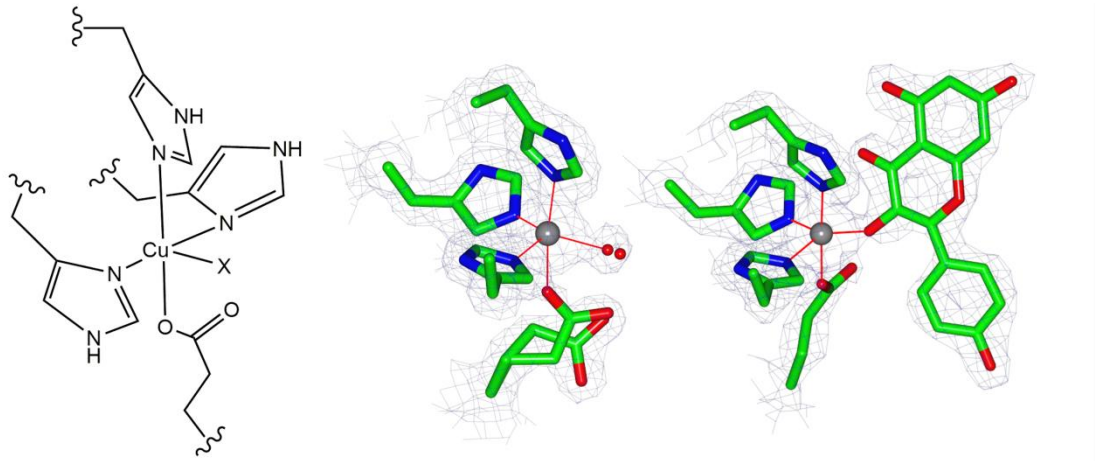

Figure 26. The structure of the active site of quercetin 2,3 Dioxygenase from Aspergillus japonicas: left, schematic diagram, middle, right, resting state (PDB 1JUH) electron density map at 0.5 e/ Å,[3] *the Asp and water molecule is modelled in two conformations with 0.5 occupancy, right, Kaempferol bound (PDB 1H1M) electron density map at 0.6 e/ Å*[3]*. Reproduced from Walton et al.*[18]

1.3. Lytic Polysaccharide Monooxygenases

The copper oxygenases are a wide class of intensely studied enzymes. There is specific interest in LPMO as this class of enzymes was only recently discovered; hence there are many unanswered questions about these enzymes within the literature.[82-83] [84]Furthermore, the abundant nature of their substrate, polysaccharides, and the potential application of these as a biofuel source have resulted in great scientific interest in the field. LPMOs are the focus of the study described in this thesis.

1.3.1 Lignocellulose as a Potential Biofuel

Lignocellulosic biomass has the potential to be converted into a mixture of sugars which can then be turned into biofuels *via* fermentation, therefore being a potentially abundant and carbon-neutral source of fuel. Thus, the utilisation of biomass in the form of bioethanol or biodiesel presents a suitable and renewable alternative to liquid fossil fuels. Lignocellulosic biomass can be defined as a second generation biofuel, a biofuel that is generated from a non-food feedstock, as opposed to a biofuel generated directly from a sugar based feedstock (e.g. sugarcane or corn), which are known as first generation biofuels. The use of second generation biofuel eliminates the food *versus* fuel criticism of first generation biofuels[85-86] as lignocellulostic biomass can be obtained from the dedicated non-food crops, grown on land not suitable for traditional food crops, or agricultural, forestry or food waste.[85-86] The chemical composition of lignocellulose is a mixture of cellulose, hemicellulose and lignin which are closely packed due to an extensive hydrogen bonding between the polysaccharide chains and the cross links between the lignin components.

The use of lignocellulostic biomass as a biofuel is hindered by its innate recalcitrance to degradation. This recalcitrance is due an extensive network of hydrogen bonds between the polysaccharide chains which results in a high level of crystallinity within the structure. This results in unique technological challenges that must be overcome in order to exploit this resource at an industrial scale which is financially viable. In order to overcome the innate recalcitrance of lignocellulose, industrial processes use either thermochemical or enzymatic methods to break down the cellulose structure.[86]

The thermochemical method consists of converting the biomass to an intermediate gas or liquid using a non-biological catalyst reactor, typically a first or second row transition metals, at high temperatures.[87] The thermochemical method allows for full conversion of

the feedstock into ethanol or other biofuels v*ia* either gasification or pyrolysis. During gasification the biomass undergoes full depolymerisation to syngas at 800 – 1000 °C at 2-3 MPa. Pyrolysis occurs at lower temperatures (400 – 600 °C) under oxygen free conditions to depolymerise the biomass into liquid intermediates. As the thermochemical methods used to breakdown biomass require high heat and pressure, this methodology is extremely energy intensive, limiting the scope for this process as an alternative green energy source.[88]

The enzymatic methodology used by a biorefinery to degrade cellulose is more complex and requires multiple steps to efficiently breakdown biomass compared to the thermochemical method, however it can occur at significantly lower temperatures and pressures. Therefore, the enzymatic method has the potential to be significantly less energy intensive than the thermochemical method. The first of these steps is a pre-treatment in which the biomass is treated by chemical, physical and/or mechanical methods to make the cellulose and hemicellulose more accessible. The next step is the enzymatic hydrolysis in which the pre-treated biomass is subjected to enzymatic hydrolysis and depolymerisation using a diverse combination of enzymes, known as an enzymatic cocktail.[89] These enzymatic cocktails consist of a wide range of glycoside hydrolases and auxiliary activity enzymes to allow for the effective degradation of what is chemically a diverse starting material. Following the enzymatic hydrolysis step, monosaccharides of the relevant sugar are obtained. In the final step, these monosaccharides are then converted to ethanol *via* fermentation by bacteria or yeast or can be used directly for the production of value added carbohydrate based products.[88]

1.3.2 The Discovery of LPMOs

In the 1950s Reese *et al.*[90] reported the degradation of cellulose by cellulolytic and non-cellulolytic organisms. From this study the authors proposed that the degradation of cellulose is a two-step process, in which the first step is the conversion of crystalline cellulose to shorter and more accessible polysaccharide chains. This step is then followed by the degradation of the modified cellulose into oligomers and monomers. They proposed that the first step was performed by a component "C_1" which only the cellulolytic enzymes possessed, while the second step was performed by a component known as "C_x" which was possessed by both the cellulolytic and non-cellulolytic organisms. Hence, rationalising that despite the non- cellulolytic organisms possessing cellulases, the C_x component, they were unable to efficiently breakdown cellulose for use as a food source.

The first indication that an oxidative processes was contributing to the degradation of cellulose was obtained in 1974 when Eriksson *et al*.[91] reported the effectiveness of cellulose degradation by the fungus *Sporotrichum pulverulentum.* The degradation of cellulose was found to be dependent on the presence of oxygen. This indicates that an oxidative process is carried out by an enzyme produced by the fungus during the degradation of cellulose which enhances the effect of the cellulases. Thus, it can be assumed that this enzyme is fulfilling the role of the "C_1" component described by Reese *et al.*.[90]

The nature of this oxidative component was first identified in 2010 by Vaaje-Kolstad *et al.*[92] when they revealed the oxidative action of an enzyme, CBP21, excreted by the chitinolytic bacterium *Serratia marcescens.* This enzyme had previously been identified and classified as a carbohydrate binding module (CBM) in the CAZy database and thought to have no enzymatic function. The authors demonstrated that the enzyme could perform oxidative cleavage of the glycosidic bond in chitin *via* the use of molecular oxygen in the presence of reducing agent (Figure 16). This activity was coupled with a boosting effect on the degradation of chitin by other secreted chitinases. However, this study reported the activity to be dependent on the presence of Mg^{2+} or Zn^{2+} ions, which are not known to activate molecular oxygen. This same reactivity was replicated in similar enzymes active on cellulose, (previously classified as GH61 in CAZy) which cleaved the glycosidic bond *via* oxidation of the C1 or C4 position.[93]

Following these findings, the nature of the metal ion responsible for the observed catalysis remained unknown with crystal structures reporting Zn^{2+},[94] Ni^{2+},[95] and Na^{2+}[92] present in the metal binding site of the enzyme. The redox active metal was definitively identified by Quinlan *et al*.[45] who identified the metal as a Cu^{2+} centre using a combination of EPR spectroscopy and X-ray diffraction. The confusion surrounding the identity of the metal is thought to be due to the extremely high affinity of the enzymes active site to Cu (K_d > 1 nM)[93] which makes it difficult to fully remove the Cu from the active site in metal dependency studies. This work identified and characterised the active site of the enzyme known as the "histidine brace" which will be discussed in section **1.3.4**. Further work by Phillips *et al.*[44] confirmed that the activity of these enzymes was exclusively dependant on Cu and no other metal ions.

These discoveries led this class of enzymes to be renamed as lytic polysaccharide monooxygenases (LPMOs) and reclassified in the CAZy database as an auxiliary activity (AA) family, where the fungal GH61 family) and the bacterial CBM33 were reclassified as AA9s and AA10s respectively. Since their discovery, the LPMO field has been the subject of large scientific interest, which has resulted in the identification of LPMOs across the tree of life in organisms such as fungi, bacteria, molluscs, insects and some animals.[52] The substrates scope has also increased with LPMOs found to be active on a wide variety of polysaccharides including cellulose, hemicellulose, short chain oligosaccharides, chitin, starch, xyloglucan, glucomannan, lichenan, xylan and β-glucan.[49, 93, 96-99] This now large field has resulted in additional AA families being identified. At the time of writing there are seven such families described: AA9 -11[45, 100-101] and AA13-AA16.[50-53]

1.3.3 LPMOs and the Breakdown of Biomass

Traditionally, the breakdown of cellulose was thought to be carried out hydrolytically by an enzymatic class known as glycoside hydrolases, which were thought to be exclusively responsible for cellulose degradation. Glycoside hydrolases can be further divided into several distinct classes. The first of these classes are the exoglycanases which attack the ends of carbohydrate chains and processes along them releasing cellobiose units. The endoglucanases bind to the polysaccharide indiscriminately and hydrolytically cleave the 1-4 glycosidic bond. The *β*-glucosidases hydrolyse the cellobiose units into the respective monomers. The action of the first two classes has been shown to be synergistic as activity when both are present is higher than the sum of each enzyme in isolation. This is thought to be due to the generation of new chain ends by the endoglucanases which generate additional binding sites for the exoglycanases. However, recent studies have indicated that the synergistic effect arises from the endoglucanases attacking amorphous regions in the cellulose that exoglycanases are unable to pass through during processive action.[102]

These enzymes use acid/base catalysis to cleave the 1-4 glycosidic bond *via* an S_N2 mechanism which can result in the retention or inversion of the anomeric conformation. The catalysis requires two residues for function: a proton donor (glutamate or aspartate) and a nucleophilic or basic residue (glutamic or aspartic acid).[103]

The mechanisms of these cleavages are shown in Figure 27. The inverting mechanism proceeds *via* a single nucleophilic substitution at the anomeric carbon from a water molecule, which results in an inversion of the stereochemistry of the sugar. Alternatively, the retaining mechanism proceeds *via* a two-step pathway, the first step known as

"glycosylation" where the nucleophilic residue of the protein attacks the anomeric carbon to form a covalent glycosyl-enzyme intermediate. In the second step, "deglycosylation", a water molecule performs a second nucleophilic attack at the anomeric carbon resulting in breaking of glycosyl-enzyme bond and regeneration of the active site. The two inversions of these nucleophilic substitutions result in the net retention of the stereochemistry. Despite the differing mechanisms both precede through an oxocarbenium-ion like transition state which is stabilised by electron donation of the oxygen atom.[89, 104] These active sites are located in grooves or tunnels within the enzyme which only accommodate a single polysaccharide chain. Therefore, the chain must be separated from the bulk polysaccharide in order to undergo hydrolysis by these types of enzymes.[89]

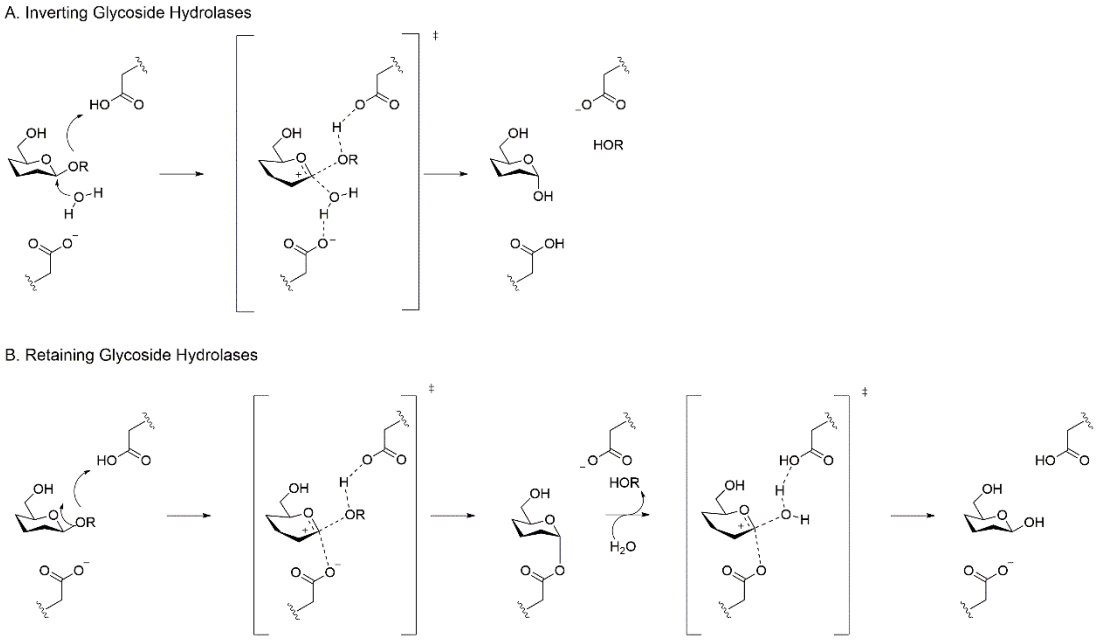

Figure 27. A generalised mechanism for glycoside hydrolysis by (a) Inverting glycoside hydrolases, (b) retaining glycoside hydrolases

Unlike the glycoside hydrolases, the active site of LPMOs is located on the flat surface of the enzyme (Section **1.3.4**) allowing LPMOs to bind to the crystalline surface of cellulose. This binding has been experimentally demonstrated by a study by Ciano *et al.*[105] in which two LPMOs were shown to semi-orientate on a crystalline substrate *via* the use of semi-orientated EPR spectroscopy. Furthermore, the action of LPMOs has been shown to decrease the crystallinity of the substrate surface.[106] The inclusion of LPMOs into enzymatic cocktails containing glycoside hydrolases has been shown to have a large synergistic effect, the inclusion of LPMOs in aerobic conditions boosted cellulose production by 60% compared to anaerobic conditions.[107] This is thought to be due to the generation of new

chain ends within the polysaccharide and the reduction of substrate surface crystallinity which can be exploited by the hydrolytic enzymes.[86]

1.3.4 The Structure of LPMOs

The structure of LPMOs is markedly different to other enzymes active on polysaccharides, like the glycoside hydrolases. Rather than having the active site located within a pocket in the enzyme, the active site of LPMOs is located on a relatively flat, solvent exposed face.[45, 108] This feature allows LPMOs to position themselves for activity on the surface of crystalline polysaccharides which are unavailable for attack by either endo- or exo-glycoside hydrolases. However, some LPMOs have substrate specific contours or grooves in order to facilitate binding of oligosaccharides[109] or branched[16, 49, 110] substrates to the surface.

The tertiary structure of LPMOs is characterised by an immunoglobulin-like fold consisting of a distorted β-sandwich, shown in Figure 28. Despite the similarity in the tertiary structure between LPMOs, the overall amino acid sequence similarity is low, both within the same and between AA families.[111] The variability of the amino acid sequence occurs predominantly in the N-terminal region, which is thought to be involved in substrate binding, while the C-terminal region has a higher degree of similarity and is thought to maintain the overall 3-dimensional core of the enzyme.[111]

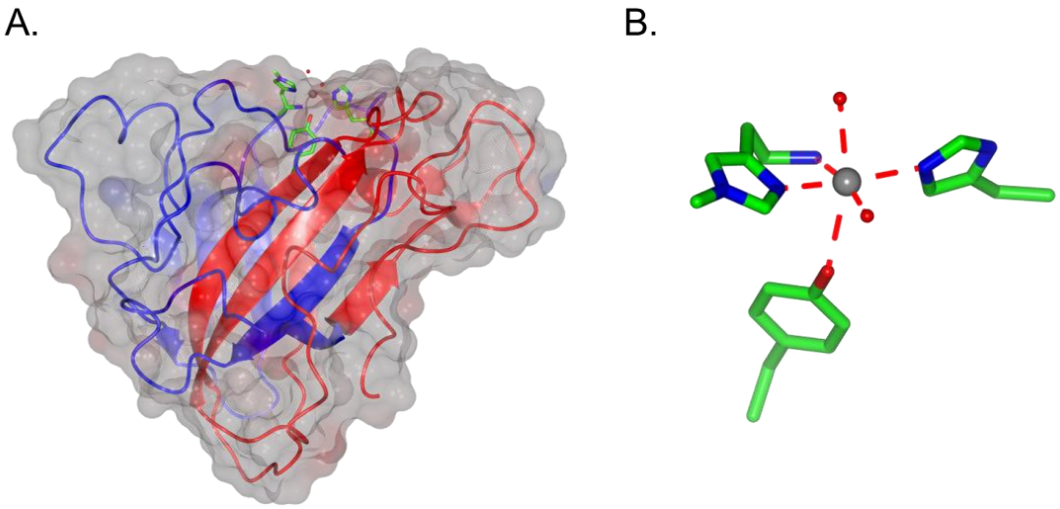

Figure 28. The X-ray structure of an AA9 LPMO from Thermoascus aurantiacus (PDB 2YET). The N terminal region is displayed in blue and the C-terminal region is displayed in red. B. The active site of 2YET

While the substrate specificity between these enzymes varies, the active site of all LPMOs is conserved across all families. This active site is known as the "histidine brace" and consists of a Cu ion coordinated by three nitrogen atoms. Two of these atoms are from the N-terminal histidine, the N_π from the imidazole side chain and the primary amine of N terminus of the protein, and the third nitrogen is provided by a second histidine, the N_T from the imidazole side chain. In the resting state the Cu ion is found in the Cu^{2+} oxidation state and is coordinated by a water or hydroxide molecule in a Jahn-Teller distorted octahedral or square pyramidal coordination geometry. In crystal structures it is found that the coordinated imidazole rings are at a ~ 60° torsion angle to one another as opposed to being planar.[82] An additional characteristic of some LPMOs is the methylation of the N-terminal histidine residue, which has been reported for AA9s and AA13s. Other fungal enzymes, however, such as those characterised for the AA11 and AA14 families, do not present this amino acid modification, although this difference could be due to the expression system (*P. pastoris*) used for protein production, which lacks the necessary methyltransferases required to perform this modification.[112-113] The role of this modification is largely unknown however the presence of the methylation has been shown to protect the enzyme from auto-oxidative damage.[114]

Analysis of the Cu coordination sphere based on crystallographic data alone is hindered by photo-reduction of the Cu in the X-ray beam, which results in the dissociation of the exogenous ligands.[115] Except for the His-brace, the coordination sphere of the Cu can vary between different enzymes (Figure 29). In the reported LPMO structures in which the copper is likely in the Cu(II) state, the coordination geometry is described as Jahn-Teller distorted octahedral for AA9s and distorted square pyramidal for some AA10s. The latter coordination geometry is highly distorted and is likely to be caused by the presence of a highly conserved alanine residue blocking the axial position of the Cu.[116] The axial position below the Cu coordination plane is occupied by a tyrosine in all LPMO families except some AA10s (Figure 29). However, the bond distance between the metal and tyrosine oxygen atom is too large (2.5-3.0 Å)[82] to be considered coordinated in the resting state.

This tyrosine is conserved in all characterised AA10s which are active on cellulose, while the phenylalanine is present in all characterised LPMOs active on chitin, which suggests that it may play a functional role in the oxidation of cellulose.[82, 117] Indeed, it has been demonstrated by Paradisi *et al.*[118] that some LPMOs on reaction with H_2O_2, in the absence of substrate, form a Cu(II)–tyrosyl radical. The formation of such a species has been hypothesised by the authors to be a result of a protection mechanism in which the tyrosine acts as part of a hole hopping pathway, consisting of other tryptophan and tyrosine residues, between the active site and another point on the protein surface. This is thought to prevent oxidative damage to the protein during uncoupled turnover as a positive hole can be transported to the active site and quench reactive intermediates.[118]

As the histidine brace is conserved across all LPMO families, and there is little variation in the bond angles and distances between the coordinating atoms and copper centre, it has been suggested that the reactivity of the histidine brace is tuned by the secondary coordination sphere. This is reflected by specific residues which are always conserved within a LPMO family (Figure 29)[82]. Indeed, these conserved residues have been shown using computational studies to be involved in the stabilisation of various reactive intermediates *via* a network of hydrogen bonds.[119] Furthermore the effect of the secondary coordination sphere has also been probed by Span *et al.*[120] who demonstrated that the ability of LPMOs to oxidise polysaccharides was dependent on the presence of specific amino acid residues close to the active site using mutagenesis studies.

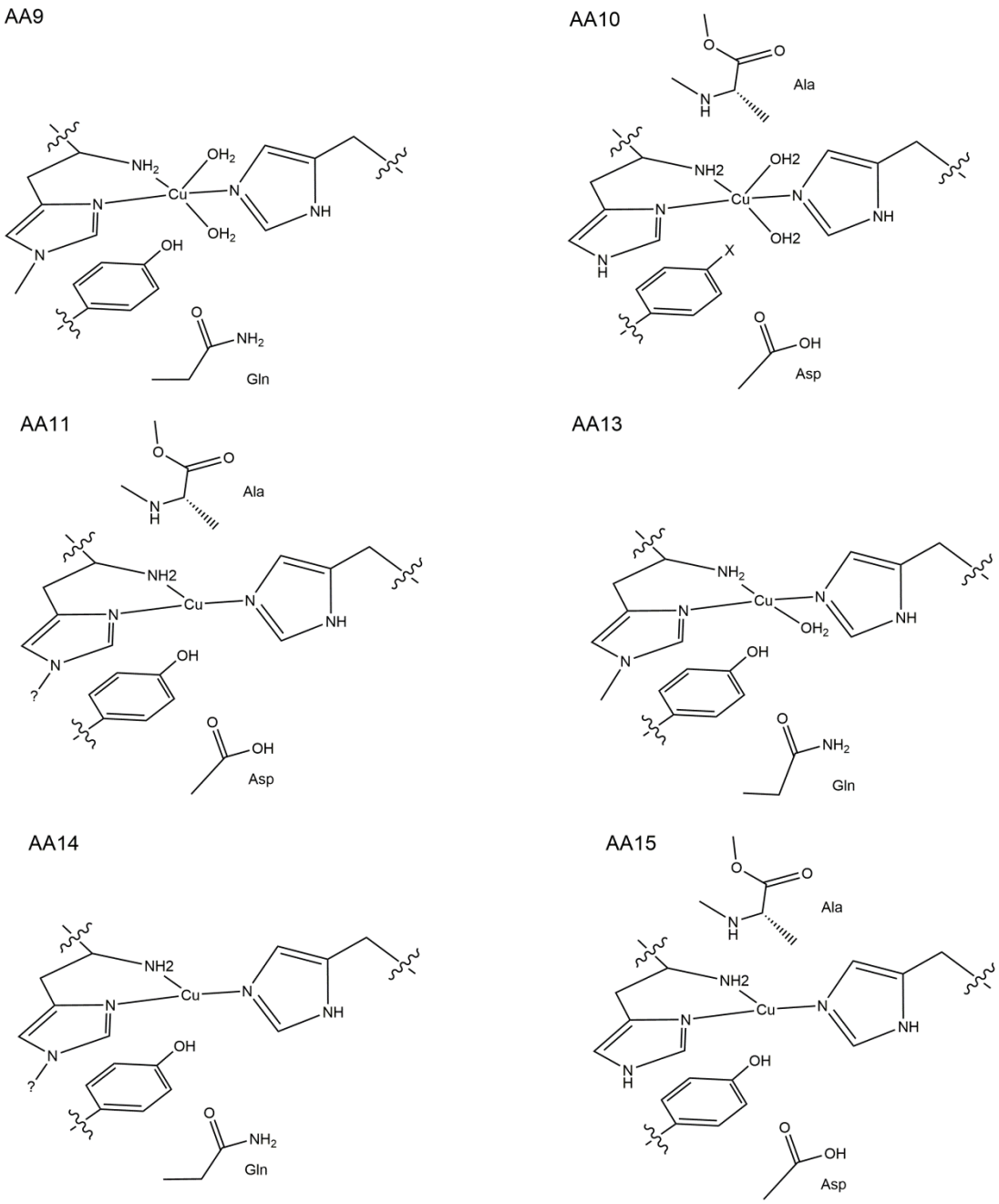

Figure 29. Schematic structures of the active sites in the crystal structures of the different classes of LPMOs as classified by the CAZy database including conserved residues in the coordination sphere[45, 49, 52, 101, 116]

1.3.5 Molecular Mechanism of LPMOs

The molecular mechanism and the nature of the reactive intermediate of LPMOs remains unclear despite extensive studies using both computational and experimental methods.[119, 121-126] Within the literature there is a debate on the nature of the external oxidant. Reactivity was originally reported with O_2 by Vaaje-Kolstad *et al.*[46] while recent reports by Bissaro *et al.*[47] dispute this claim and suggest that H_2O_2 is the relevant oxidant. Both of these studies are supported by the relevant isotopic labelling experiments where the use of either $^{18}O_2$ and $H_2{}^{18}O_2$ resulted in the incorporation of the labelled oxygen into the polysaccharide substrate. The two possible general reactions are shown in Figure 30. The potential mechanisms of these two reactions will now be discussed.

$$O_2 + 2e^- + 2H^+ + R{-}H \xrightarrow{\text{Cu(II)-LPMO}} R{-}OH + H_2O$$

$$H_2O_2 + R{-}H \xrightarrow{\text{Cu(I)-LPMO}} R{-}OH + H_2O$$

Figure 30. General reaction scheme of substrate oxidation by either O_2 or H_2O_2

For the reaction with molecular oxygen, the nature of the species which performs C-H abstraction is disputed, however the initial steps of the reaction with molecular oxygen are generally agreed upon. The initial step of the reaction is the reduction of the Cu(II) resting state to Cu(I). This step is followed by the binding of molecular oxygen to the Cu(I) centre, which results in the formation of a Cu(II)-superoxide species (**Cu(II)-OO^{-}**). Initial studies suggested that this could be the active species which performs C-H atom abstraction (HAA) on the substrate,[44] however further computational studies demonstrated that the HAA step is extremely high (> 150 KJ mol^{-1}) and thus energetically unfavourable.[121, 124] As such, these studies suggest that a more reactive intermediate, such as a Cu(II)-Oxyl (**Cu(II)-O$^{-\bullet}$**), must be responsible for the HAA abstraction, but the mode of formation of such an intermediate remains unknown.[121]

In the absence of experimental data, various calculations have been performed on the active sites of LPMOs, with a view to determining the reaction cycle, particularly the nature of the oxidising intermediate. Initial computational studies placed the reactive oxygen species (ROS) in the axial position of the copper coordination sphere,[42] a highly unlikely scenario because of the Jahn-Teller distortion in Cu(II). Indeed, later structural studies showed that this axial site is blocked upon substrate binding and so is not accessible for the formation of a reactive species.[109] As such, further computational studies of reactions with both O_2 and H_2O_2 were carried out based on the substrate bound LPMO models using both

quantum mechanics/molecular mechanics (QM/MM) and density functional theory (DFT) calculations.[119, 123-124] In the case of computational studies using O_2 as the substrate the lowest energy reaction pathway was found to be two proton coupled electron transfer (PCET) steps to form a **Cu(II)-O$^{-\bullet}$** and a water molecule which is held by the enzyme in a pocket within H-bonding distance of the active site. The **Cu(II)-O$^{-\bullet}$** is then able to perform HAA which is followed by a hydroxyl rebound step to generate the hydroxylated product and to regenerate the Cu(I) active form of the enzyme.[124] This reaction pathway is shown in Figure 31.

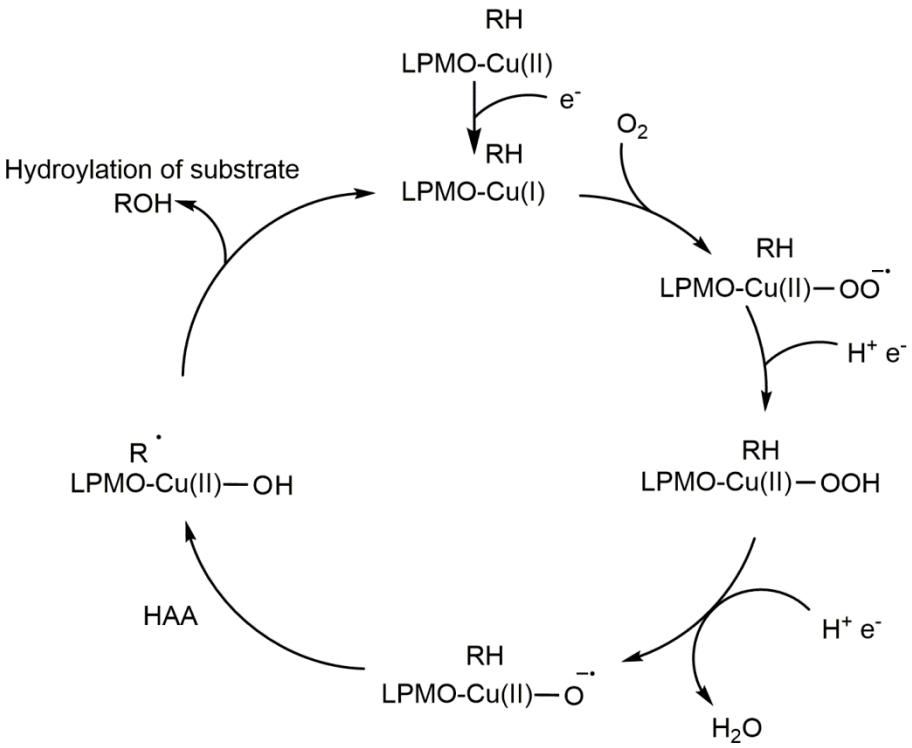

Figure 31. Schematic summary of the proposed mechanism for hydrogen atom abstraction by an LPMO in the presence of O_2 and an external reducing agent

After the identification of H_2O_2 as a potential oxidant Bissaro *et al.*[47] proposed several potential mechanisms for the reaction of LPMOs with H_2O_2. Thus the reaction mechanism of LPMOs with hydrogen peroxide was examined *in silico* by Wang *et al*.[119] The lowest energy pathway was also found to occur *via* a **Cu(II)-O$^{-\bullet}$** intermediate performing the HAA step.[119] The formation of this intermediate is markedly different from the reaction with molecular O_2, as it is generated *via* a "caged hydroxide intermediate". During this process, the copper(I)-hydrogen peroxide (**Cu(I)-H_2O_2**) intermediate undergoes homolytic cleavage to form a copper(II) hydroxide (**Cu(II)-OH**) and OH$^{\bullet}$). The "free" hydroxyl radical, is in fact stabilised by a hydrogen bonding network within the protein (as for the H_2O in the O_2

mechanism), which is then able to deprotonate the Cu(II)-OH to form the **Cu(II)-O$^{-\bullet}$** which is then able to carry out the HAA step.[119] A subsequent study by Bisaaro *et a.l*[127]*.* on a chitin active LPMO*, Sm*AA10, which found a similar result wherein the generated OH radical was orientated by hydrogen bonds in order to perform the HAA step to form the **Cu(II)-O$^{-\bullet}$.** The proposed mechanism from both of these studies is shown in Figure 32.

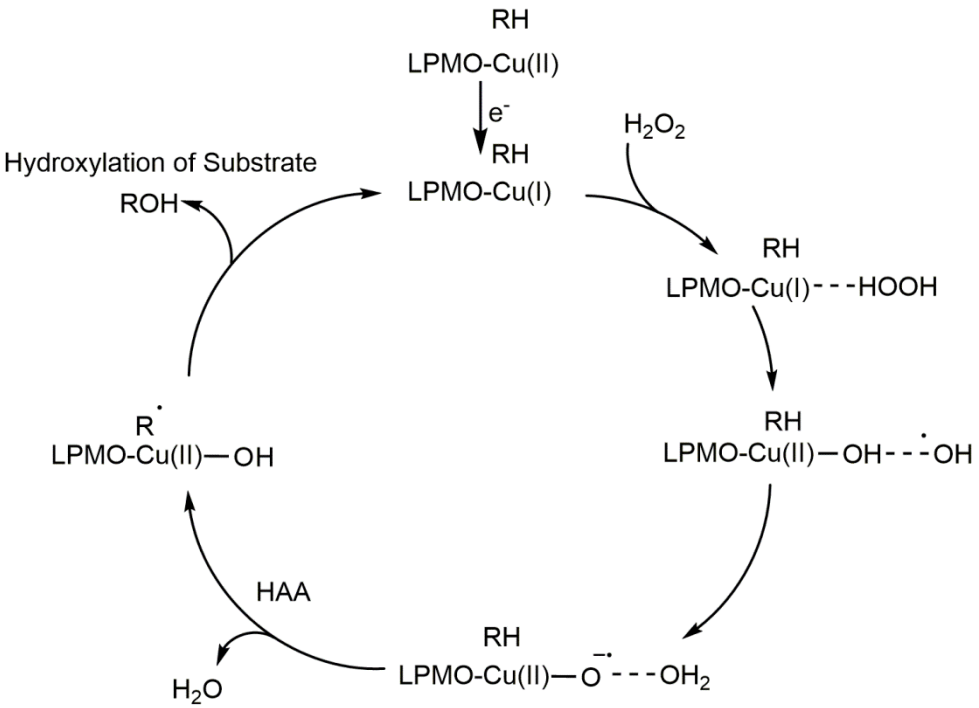

Figure 32. Schematic summary of the proposed mechanism for hydrogen atom abstraction by an LPMO in the presence of H_2O_2

A further computational study linked the O_2 and H_2O_2 pathways together (Figure 33).[123] The study demonstrated that **Cu(II)-OO$^-$** is capable of abstracting a hydrogen atom from ascorbic acid (asc), a common reducing agent used in LPMO activity assays,[45-46, 50] to form a copper(II)-hydroperoxo (**Cu(II)-OOH$^-$**)**.** At this point the proximal oxygen can undergo PCET from asc to form Cu(I)-H_2O_2. This species can then enter the H_2O_2 pathway discussed above.[123]

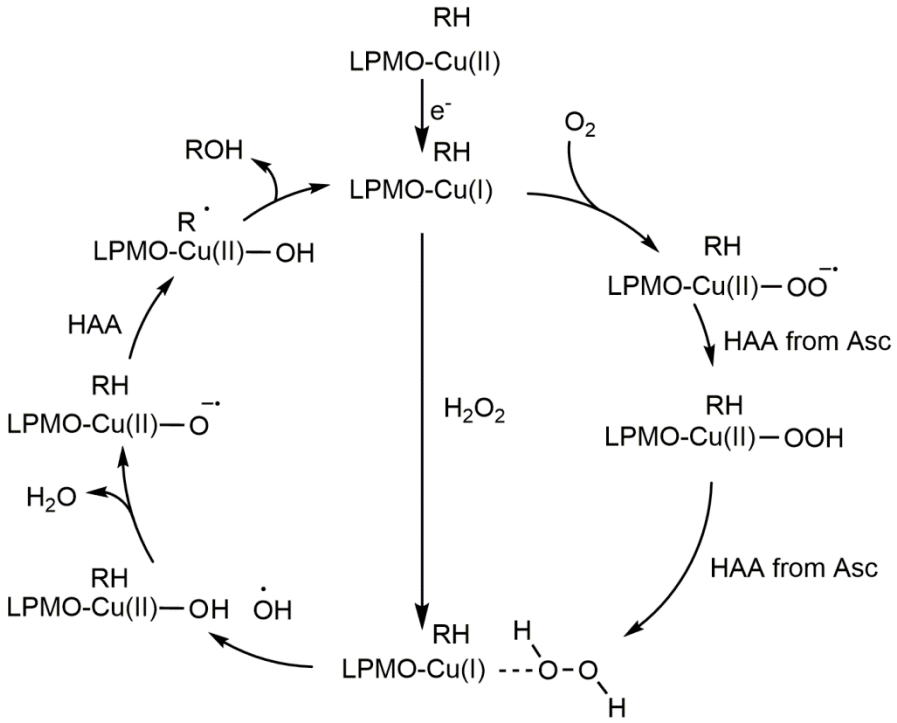

Figure 33. The proposed catalytic cycles of LPMOs on reaction with O_2 or H_2O_2

To conclude, the theoretical studies suggest that the ROS is a copper based oxyl. This has been demonstrated to be the preferred intermediate on reactions with both H_2O_2 and O_2. This intermediate has not previously been observed across small molecule Cu complexes (Section **1.4**) or Cu enzymes (Section **1.2**). The formation, observation and characterisation of this intermediate is the focus of many research groups within the field. The relevant co-substrate remains contentious within the literature. As uncoupled turnover of LPMOs with O_2 in the presence of a reducing agent results in the generation of H_2O_2 some authors have used the faster kinetics of the LPMO activity with substrate (in the presence of O_2) to argue that it is the only relevant co-substrate for catalysis.[47] However, excess peroxide has been shown to cause damage to the enzyme and even cause inactivation in some cases.[118] This damage is not observed in the O_2 reaction coupled with reactivity in the presence of horseradish peroxidase results in other research groups favouring O_2 as the LPMO co-substrate.[84]

1.3.6 Spectroscopy of LPMOs

1.3.6.1 EPR Spectroscopy

The resting state of LPMOs consists of the copper ion in the Cu^{2+} state and as such has a d^9 configuration which results in an unpaired electron (S = ½) resulting in an EPR active species. Thus, the EPR spectroscopy of LPMOs has been used across the literature to gain insight into the resting state of the enzyme. The spin Hamiltonian parameters obtained for LPMOs reported within the literature can be plotted onto a Peisach–Blumberg plot, Figure 34.[117] This leads to LPMOs in the absence of substrate being grouped into two categories. The first of these is the class made up of the chitin active AA10s which can be characterised by their rhombic *g* values ($g_z > g_y > g_x$) and low $|A_z|$ values. This rhombic distortion is due to the square pyramidal geometry adopted by Cu centre (Section **1.3.3**). The second of these classes is made up of the remaining LPMO families (AA9, AA11, AA13, AA14, AA5 and the cellulose active AA10s). On comparison to the first class this cluster is characterised by more axial spectra ($g_z > g_y \approx g_x$) and higher $|A_z|$ values when compared with the other class. These values are consistent with a Jahn-Teller distorted octahedral geometry of the Cu ion and can be classified as Type 2 copper sites based on their position within the Peisach–Blumberg plot.[128]

It can be observed from this data that the binding of substrate results in a large perturbation to the electronic environment of the Cu site. This is most apparent in the case of AA10s on binding chitin, where there is a radical change in spin Hamiltonian parameters ($|A_z|$ changes from ~ 350 MHz to ~600 MHz) which has been rationalised as a change in geometry from the five coordinate square pyramidal geometry of the resting state of the enzyme to a four coordinate square planar geometry.[129] This perturbation is smaller in AA9s but still occurs, and again is thought to be caused by the loss of the axial water molecule on substrate binding which has been demonstrate both *in crystallo*[98] and *in silico*.[119]

Finally, it should be noted that the spin Hamiltonian parameters of LPMOs are remarkably diverse for the enzymes which are structurally very similar.[82] Particularly, when the primary coordination sphere remains constant, which is broadly true of enzymes within the same family of LPMOs have a significant differences in EPR parameters. This indicates that the secondary coordination sphere significantly influences the Cu environment. This hypothesis has been experimentally demonstrated by Span *et al.*[130] who demonstrate that point

mutations to amino acid residues close to the Cu active site of *Mt*AA9 resulted in changes to the EPR spectrum of the LPMO.

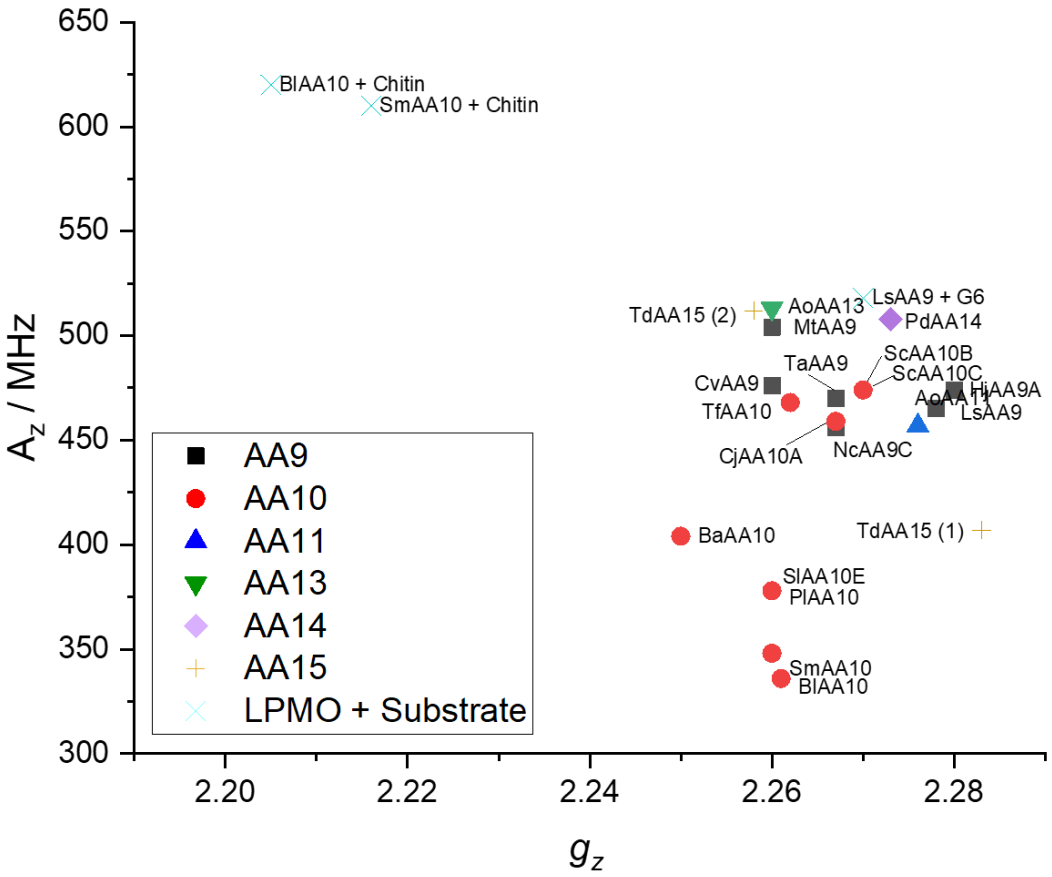

Figure 34. Peisach–Blumberg plot of the published EPR data of LPMOs[128]. Data and reference are listed in Table 1, (X) refers to when multiple Cu species were observed within the same enzyme

Table 1. Published EPR data of LPMOs used for the Peisach–Blumberg plot shown in Figure 34

Family	LPMO	gz	Az	Reference
AA9	*Cv*AA9	2.26	476	*Simmons et al.*[131]
AA9	*Ta*AA9	2.267	470	*Quinlan et al.*[93]
AA9	*Nc*AA9C	2.267	456	*Borisova et al.*
AA9	*Mt*AA9	2.26	504	*Span et al.*[120]
AA9	*Hj*AA9A	2.28	474	*Hansson et al.*[132]
AA9	*Ls*AA9	2.278	465	*Frandsen et al.*[58]
AA10	*Sl*AA10E (1)	2.26	378	*Chaplin et al.*[133]
AA10	*Sl*AA10E (2)	2.23	523	*Chaplin et al.*[133]
AA10	*Tf*AA10	2.262	468	*Forsberg et al.*[134]
AA10	*Cj*AA10A	2.267	459	*Forsberg et al.* [134]
AA10	*Bl*AA10	2.261	336	*Courtade et al.*[129]
AA10	*Sc*AA10C	2.267	459	*Forsberg et al.*[134]
AA10	*Sc*AA10B	2.27	474	*Forsberg et al.*[134]
AA10	*Ba*AA10	2.25	404	*Courtade et al.*[129]
AA10	*Sm*AA10	2.26	348	*Forsberg et al.*[134].
AA11	*Ao*AA11	2.276	457	*Hemsworth et al.*[101]
AA13	*Ao*AA13	2.26	513	*Lo Leggio et al.*[135]
AA14	*Pd*AA14	2.273	508	*Courtier et al.*[51]
AA15	*Td*AA15 (1)	2.283	407	*Sabbadin et al.*[52]
AA15	*Td*AA15 (2)	2.258	512	*Sabbadin et al.*[52]
AA10 + SUB	*Bl*AA10	2.205	620	*Courtade et al.*[129]
AA9 +SUB	*Nc*AA9 + sub	2.226	525	*Borisova, et al.*[136]
AA9 +SUB	*Ls*AA9	2.27	518	*Frandsen et al.*[98]
AA10 + SUB	*Sm*AA10 + Sub	2.216	610	*Bissaro et al.*[137]

1.3.6.2 Electronic Spectroscopy

The study of the electronic spectrum of LPMOs is limited to the Cu(II) state which exhibits a broad weak absorbance at λ_{max} = 615 - 650 nm ($\varepsilon \approx 0.037–0.113\ mM^{-1}\,cm^{-1}$).[138] In the Cu(I) state the ion is d^{10} and hence no *d-d* transitions occur. The reason for the weak *d-d* transition is that these are Laporte forbidden transitions and as such are low intensity. The appearance of the *d-d* band has been used within the literature to monitor the reaction of Cu(I) with O_2 in *Ta*AA9.[45]

Detailed analysis on the *d-d* transition in *Hj*AA9a using circular dichroism and magnetic circular dichroism allowed for three of the four possible d-d transitions to be resolved.[139] These were defined as follows: the $d_{xz/yz} \rightarrow d_{x^2-y^2}$ transition at ~760 nm, the $d_{xy} \rightarrow d_{x^2-y^2}$ transition at ~710 nm and the $d_{xz/yz} \rightarrow d_{x^2-y^2}$ transition at ~640 nm. It was not possible to define the $d_{z^2} \rightarrow d_{x^2-y^2}$ transition from the data.[139]

1.4 Molecular modelling of enzymes

The development of small Cu complexes to model enzymes capable of activating O_2 is a well explored and useful strategy to investigate reaction mechanisms and reactive intermediates. Indeed, small molecule complexes can be produced easily on a large scale and often allow for the use of low temperatures and aprotic solvents in order to trap and spectrally study reactive species.[140] As with enzymes, the reactivity of the Cu complex is dictated by the coordination of the designed ligand, which must be able to support the Cu ion through its reactive cycle (including changes in oxidation state), as well as preventing side reactions and disproportionation.[141] Thus, an examination of literature complexes must be carried out before embarking on novel ligand design.

The field of small molecule Cu complexes is extremely diverse. Ligands use donors including sulphur, oxygen and nitrogen in various coordination environments with coordination numbers from 2 to 5.[141] As the aim of the project is to model the structure and reactivity of LPMOs which is a tridentate N_3 ligand system, only tridentate ligand systems using nitrogen donors will be considered in the following discussion.

1.4.1 Bridgehead Nitrogen-Type Ligand Systems

Bridgehead nitrogen-type ligands are the largest class of N_3 ligands; however, the nature of the coordinating atoms and ligand backbone remains similar across the class. This general class has been well studied and as a result there are a large number of ligands of this type found within the literature (Figure 35). These ligands coordinate copper *via* a bridgehead nitrogen and two heteroaromatic nitrogen atoms which are (connected by an alkyl link) in a square planar or square pyramidal geometries, depending on the counter ion and solvent. Generally structural modifications to these ligands include changes to: the chain length between the bridgehead N and the two coordinating heteroaromatic rings (**L_7**), the nature of the heteroaromatic rings themselves (**L_5**) and the substituents on the heteroaromatics, and the nature of the third substituent on the bridgehead nitrogen. These modifications have been shown to affect the chemistry of the Cu Centre and will be discussed herein. It should be noted demonstrated using due to the relatively recent discovery of LPMOs the modelling of the histidine brace was not the intended purpose for the majority of these ligands.

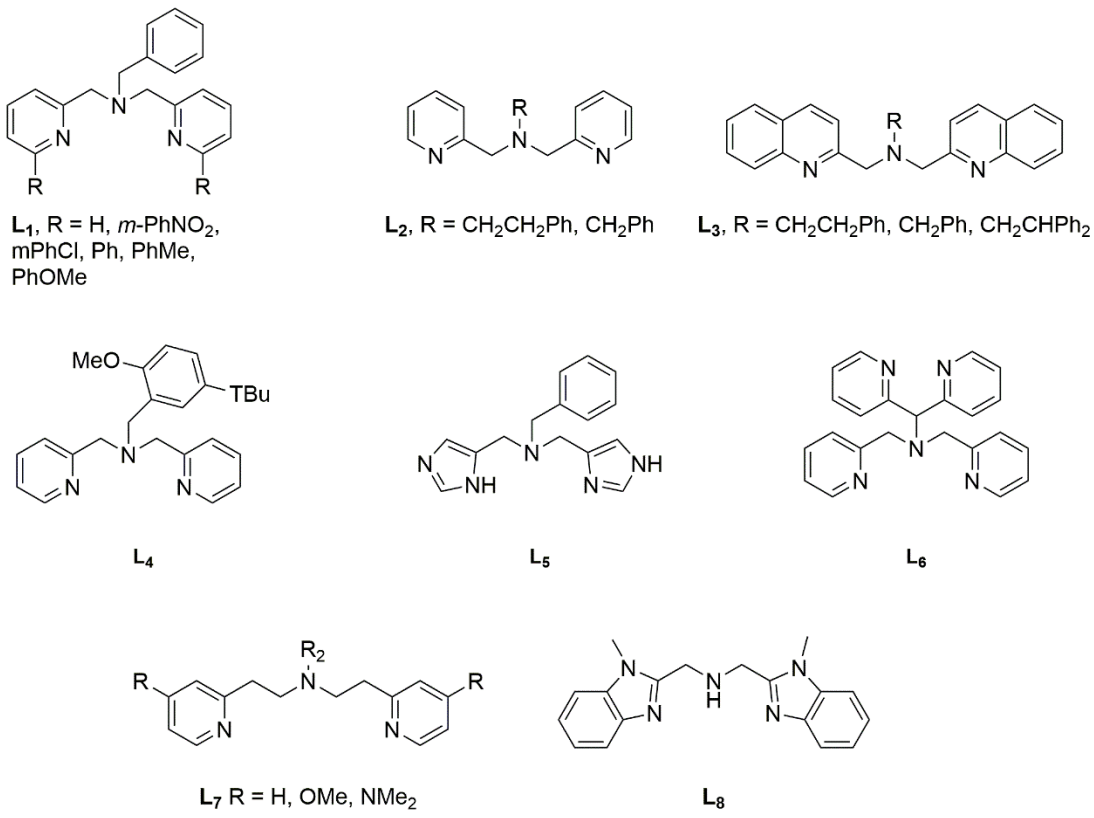

Figure 35. Schematic structures of N-bridgehead ligands, adapted from Elwell et al.[141]

These ligands are able to support both Cu(I) and Cu(II) oxidation states with a vacant coordination site and thus are capable of reacting with O_2 or H_2O_2 . However, on reaction

with O_2 and H_2O_2 they commonly form (μ-η^2:η^2-peroxo)- or bis(μ-oxo)-dicopper centres, as shown in Figure 36, as opposed to monocopper oxygen species such as a Cu superoxide.[142] The formation of (μ-η^2:η^2-peroxo)- or bis(μ-oxo)-dicopper reactivity has been demonstrated to be effected by the ability of the ligand to donate electrons to the Cu centre.[143-144] It was shown *via* UV/Visible spectroscopy that if the ligand can provide additional electron density, formation of the higher oxidation state of the bis(μ-oxo)-dicopper(III)centre is favoured over the formation of the (μ-η^2:η^2-peroxo) dicopper(II) centre as the additional electron density stabilises the higher oxidation state. This electron density is typically provided by modifications to the pyridine rings *via* the addition of electron donating groups such as NMe_2. The inverse is also the case where the use of electron withdrawing groups favours the formation of a (μ-η^2:η^2-peroxo) dicopper(II) centre.

Figure 36. The (μ-η^2:η^2-Peroxo)- and bis(μ-oxo)-dicopper centres

To prevent the formation of a dicopper centres, discussed above, it was hypothesised that the addition of steric bulk could prevent the approach of a second copper centre and hence favour the formation of a mono-copper species. This has been experimentally demonstrated by Kunishita *et al.*[145] using a **CuL_1** type complexes *via* the inclusion of steric bulk on the pyridine rings where the substituent on the pyridine ring is a phenyl group (Figure 37). Following the modification the complex was able to react with alkyl peroxides in a 1:1 Cu to alkyl peroxide ratio, to form an alkylperoxo copper(II) complex.[145] The same reaction with the unmodified complex was instead shown to occur *via* a *bis*-copper species, as the reaction stoichiometry was shown to be in a 2:1 **$[Cu(L_1)]^+$** complex to peroxide ratio.[145] This steric effect has been applied generally across the nitrogen bridgehead ligands, for **L_1** **L_2** and **L_3**, where the inclusion of steric bulk has been shown to stabilise monocopper intermediates.[141]

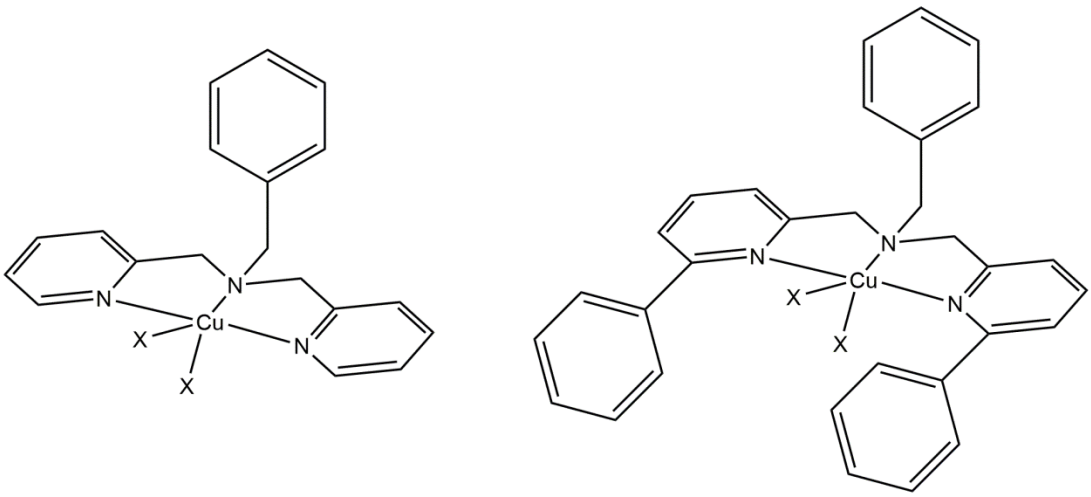

Figure 37. Schematic structures of pyridyl alkyl complexes with and without added steric bulk to inhibit formation of dicopper species. X denotes solvent molecules[145]

However, the use of steric bulk to prevent the formation of dicopper centres can present problems if using the complex as a catalyst as the generated reactive intermediates can react with the additional steric bulk, as seen in a study by Itoh and co-workers[146] in which, upon reaction with H_2O_2, the aromatic steric bulk of **[Cu(L_1, R = Ph)]$^+$** has become hydroxylated (Figure 38). The newly formed hydroxyl group has been shown to be able to coordinate the Cu centre and thus prevent the coordination of additional oxidant and hence can result in the inactivation of the catalyst. This reactivity demonstrates that these complexes can perform C-H activation, but this intramolecular reactivity may cause inactivation of the catalyst towards oxidation.

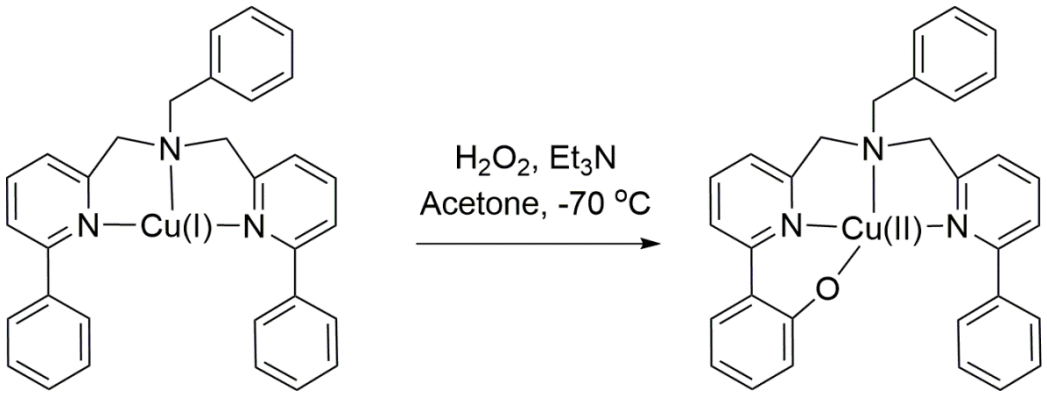

*Figure 38. Formation of a phenolate complex via the reaction of [Cu(**L_1**, R= Ph)]$^+$ with H_2O_2*

A ligand system designed to model LPMOs using a bridgehead nitrogen type ligand is a di-benzimidazolyl ligand, **L_8** Figure 35, has been developed by Castillo *et al.*[147-148] This complex adopts a trigonal bipyramidal geometry where the bond lengths and angles closely model the AA10 LPMOs. The spin Hamiltonian parameters of this Cu complex are markedly different from LPMOs with a g_z of 2.160, which is significantly lower than that reported for LPMOs, even the square pyramidal chitin active AA10s, Table 1. In terms of reactivity this complex was shown to be reactive with a polysaccharide substrate, cellobiose, in the presence of H_2O_2, KO_2 and O_2 and a reducing agent. However, like other bridgehead nitrogen type ligands (without steric bulk), the authors predict that the reactive species responsible for this oxidative cleavage is a bis Cu(μ-η^2:η^2-peroxo) species rather than a monocopper species. [147-148] Therefore while **Cu(L_8)** is able to closely model the structure of the histidine brace, it is unable to replicate both the electronics of the Copper centre and reactivity of the enzyme.

1.4.2 Diamine Containing Ligand systems

Diamine containing ligands coordinate Cu by either a cyclic[149] or linear[150] tertiary diamine and a heteroaromatic nitrogen provided by a pyridyl arm in a N_3 tridentate arrangement, as shown in Figure 39. In the linear diamine complexes, the chain length between the two amines is either two or three atoms however this modification does not appear to affect the reactivity with O_2.[151-152] These ligands have been further derivatised with modifications introduced into the *para* – position of the pyridine ring, similar to the pyridyl alkyl complexes. In the cyclic diamines the ring size has been varied, (six to eight atoms) which modifies the distance between the two amines. Unlike the linear diamines, the variation of distance between the two amides (N-N) in the cyclic diamines has been shown to have a profound effect on the ability of the complex to react with O_2.[149]

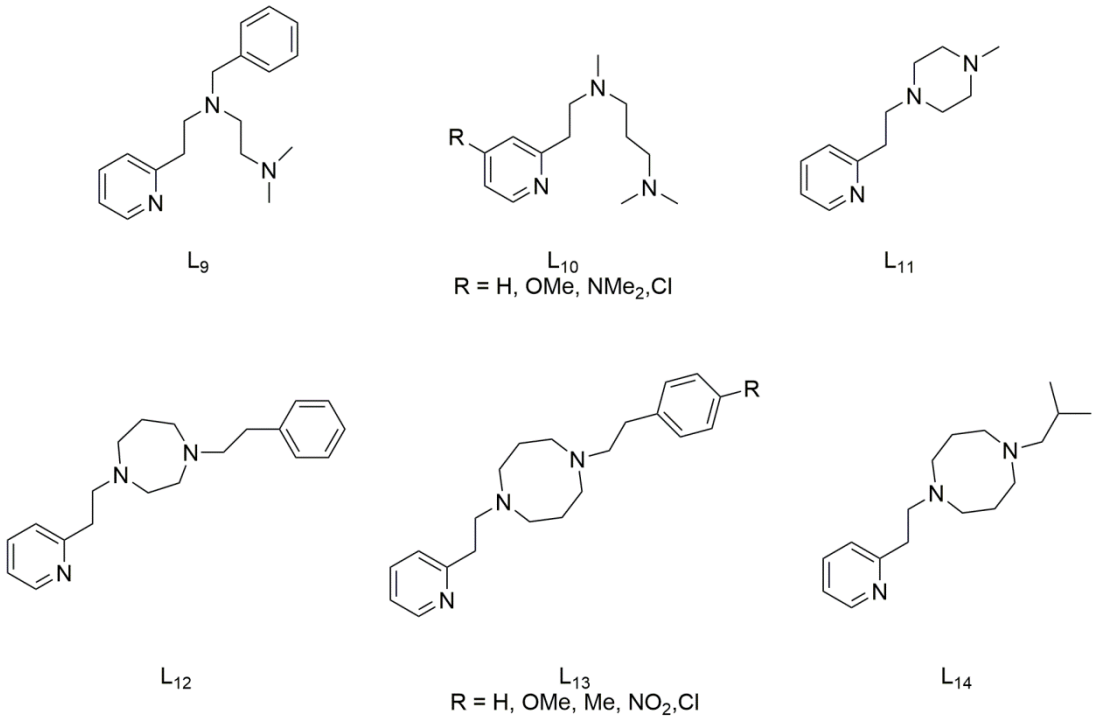

Figure 39. Schematic structures of Diamine containing ligands, adapted from Elwell et al.[141]

The geometries of the Cu complex with linear diamines are closer to tetrahedral than square planar, with all N-Cu-N bond angles greater than 101°. The cyclic diamine ligand was initially developed as an eight membered ring,[153] which the authors claim imparts flexibility to the system in comparison to the linear diamines which are significantly more rigid. This is reflected in the geometry of the complex which allows for the complex to adopt a T-shaped arrangement in the Cu(I) state and a distorted four coordinate geometry upon reoxidation to Cu(II). As this geometry is neither square planar nor tetrahedral, it can be

evaluated using the geometric parameter (τ_4) which is calculated *via* the equation shown below,

$$\tau_4 = \frac{360° - (a + b)}{141°}$$

where *a* and *b* are the two largest angles, *Θ,* present within the complex.[154] For a perfect tetrahedral species this value will be 1.00 and for a perfect square planar complex this value will be 0.00. For the eight membered diamine the τ_4 value of the complex was found to be ~0.5 indicating that the geometry is significantly distorted between these two states.[154]

These ligands are able to support both Cu(I) and Cu(II) oxidation states and possess an exogenous ligand binding site. Therefore they are able to react with O_2 and various peroxides. On the reaction of the linear diamine type complexes (**$CuL_{9/10}$**) with O_2 and H_2O_2 either (μ-η^2:η^2-Peroxo)- or bis(μ-oxo)-dicopper centres are formed. Again, this reactivity has been shown to be modulated by the electron donating ability of the substituents present on the pyridyl ligand.[155] This type of study has not been carried out on the cyclic diamine ligand systems so this effect of altering the pyridine electronics is unknown. Despite the differences in geometry this reactivity is similar to the chemistry observed for the nitrogen bridgehead type copper complexes on reaction with H_2O_2 or O_2.

Steric bulk was employed to prevent the formation of dicopper species on the reaction with oxidants for the cyclic diamines in a study by Kunishita, *et al*.[153] in which steric bulk was provided by a phenethyl group bound to the terminal amine, **L_{13}**. The intermediate formed on the reaction of this complex with O_2 was characterised as an end-on superoxide bound to the Cu centre, shown in Figure 40. The **Cu(II)OO^-** formed is unstable and rapidly reacts with the phenethyl side chain displaying the ability for the reactive intermediate to activate C-H bonds.[153] However, the alcohol formed from this reaction was able to coordinate to Cu centre. This results in inactivation of catalyst to further oxidations. The formation of such a species is similar to what has previously been observed for the N bridgehead complexes on reaction with O_2 (Figure 38).[146] This indicates that care must be taken when incorporating steric bulk to minimise or prevent intramolecular oxidation.

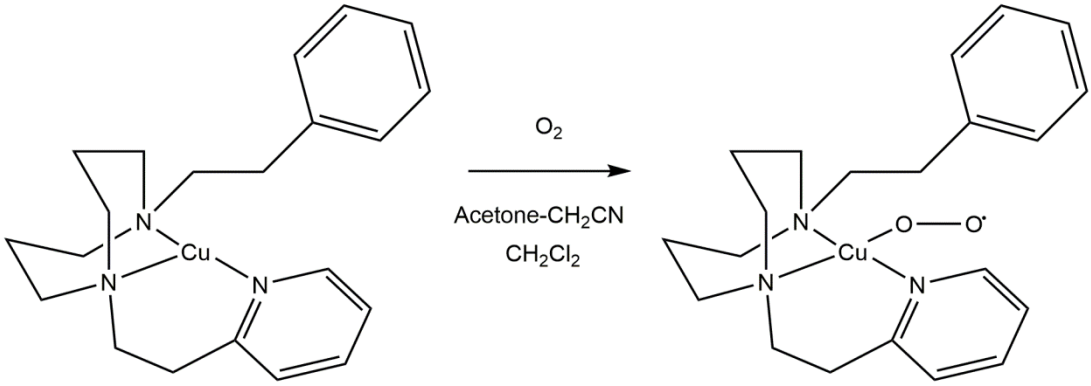

Figure 40. The formation of the Cu(II) superoxide complex on reaction of a cyclic diamine copper complex on reaction with O_2

The N-N atom distance in the cyclic diamine has been shown to be important for O_2 reactivity.[149] The size of the cyclic diamine ring was modified to contain 6, 7 or 8 atoms (**L_{11}**, **L_{12}** and **L_{13}** respectively). This variation of ring size resulted in profound changes to the complexes' reactivity with O_2. The complex formed on reaction of **L_{11}** with Cu, **$[Cu(L_{11})(H_2O)]^{2+}$** was able to undergo a reaction with O_2, but the reactive intermediate was so unstable that it could not be characterised. The complex containing the ligand with the 7 membered ring, **$[Cu(L_{12})(H_2O)]^{2}$,** formed a bis(μ-oxo)dicopper species on reaction with O_2. Finally, **$[Cu(L_{13})(H_2O)]^{2+}$** formed an observable Cu(II) superoxide species on reaction with O_2.

This difference in reactivity has been rationalised, by the authors, as an effect of altering the bite angle and bond distance between the N atoms in the cyclic diamine.[149] The structural parameters of the complexes discussed above were compared with other Cu complexes within the literature known to form bis(μ-oxido)dicopper(III) complexes on reaction with O_2.[156] Within the structure of **$[Cu(L_{12})]^{+}$** it was found that the distance between the two coordinating nitrogen atoms was 2.678 Å with a bite angle, *L*N-Cu-N, of 80.56°. As the N-N distance was fixed due to the rigid nature of the diamine the authors calculated that if the bite angle was increased to 89 ° on reaction with O_2, the N-Cu bond distances were similar to that of the literature structure of the bis(μ-oxido)dicopper(III) complex, 1.97 Å.[156]

The same methodology was used for the analysis of **$[Cu(L_{13})]^{+}$** which has a N-Cu-N angle of 90°, and a N-N distance of 2.9 Å and Cu-N distance of 2.20 Å. In order to reduce the length of the Cu-N bond to 1.97 Å, as in the literature bis(μ-oxido)dicopper(III) complex, the N-Cu-N angle must increase to 95°. This large bite angle is geometrically unfavourable for the formation of a bis(μ-oxido)dicopper(III) complex. In other words, the 8 membered diamine ring is unable to adopt the geometry required to support a bis(μ-oxido)dicopper(III) species

and hence forms the observed **Cu(II)-O-O**$^{-}$ species.[149] This study highlights the importance of the geometry of the copper centre with regard to the reactivity with various intermediates as in some cases the steric constrains of the ligands appear to control the reactivity with oxidants.

1.4.3 Deprotonated Amide Containing Ligand Systems

A further variation of the N_3 ligand type is represented by systems containing deprotonated amides. This type of ligand system generally features two deprotonated amide nitrogen atoms *trans* to one another and a pyridine nitrogen *trans* to the vacant coordination site in a T-shaped geometry, where in the Cu(II) form the vacant site is occupied by a solvent, shown in Figure 41.[157] Therefore, in the Cu(II) state the complex adopts an overall square planar coordination geometry.

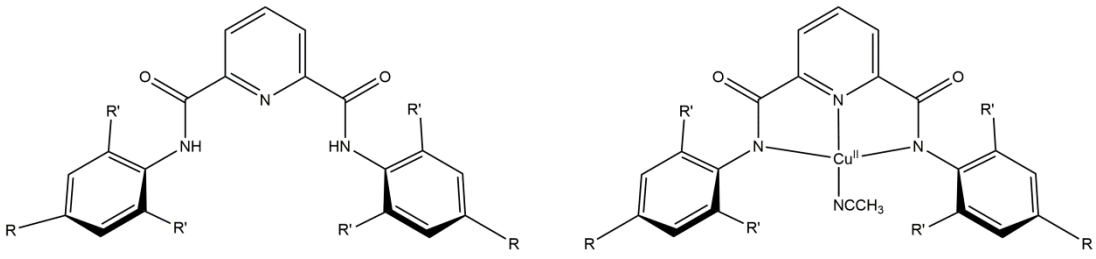

Figure 41. The schematic structure of a deprotonated amide containing ligand and its corresponding Cu complex.R = H, NO_2 R' = iPr, Me

Unlike the ligands discussed above, these complexes stabilise Cu(II) and Cu(III) oxidation states, as opposed to the Cu(I) and Cu(II) oxidation state as seen for the previously discussed complexes. The Cu(III) oxidation state is stabilised *via* the sigma donating power of deprotonated amide ligands. These Cu complexes have been shown to stabilise a mononuclear Cu(III) hydroxide (**Cu(III)(L_{15})OH**) which is able to perform C-H abstraction on a wide variety of substrates.[158-159] This type of ligand has been extensively studied and it has been shown that the reactivity of the **CuL_{15}(III)OH** is dependent on the basicity of the corresponding Cu(II) hydroxide rather than electron withdrawing or donating effects present on the ligand, in contrast to the observed reactivity for the pyridylalkyl or diamine complexes.[159] Interestingly, unlike either the diamines or N-bridgehead ligands, no intramolecular reactivity for these compounds was observed despite possessing steric bulk in the form of aromatic groups.

This ligand set is also able to stabilise a Cu(II) superoxide species *via* a reaction of the Cu(II) form of the complex with potassium superoxide (KO_2) in the presence of 18-crown-6.[160] Further work by Pirovano *et al*. demonstrated that the Cu(II) superoxide complex was shown to be capable to react with acyl chlorides and aldehydes where it was believed that the Cu(II) superoxide species was acting as a nucleophile.[161] However, recent work by Bailey *et al*.[162] has demonstrated that the reactive pathway **Cu(II)-OO$^-$** acts instead as a base to form a **Cu(II)-OOH$^-$**. The **Cu(II)-OOH$^-$** then decays to a **Cu(II)OH** which can then act as the nucleophile. This was demonstrated by modifying the counter ion which allowed for the preparation of **Cu(II)-OO$^-$** in the absence of excesses KO_2, which was then demonstrated to be inert towards 2-phenylpropionaldehyde except in the presence of H_2O, as the latter facilitates the deprotonation of the benzylic C-H bond and subsequent formation of the **Cu(II)-OOH$^-$**. [162]

The reactivity of this type of model complex has been used to suggest the possibility of a different reactive intermediate in LPMOs,[82] in which the mechanism involves the stabilisation of a high oxidation state in the form of Cu(III) *via* the deprotonation of the amino terminus in the protein. This deprotonation allows for the formation of a **Cu(III)OH$^-$**, which can be described as the formally protonated **Cu(II)O$^{-\bullet}$**, shown in Figure 42.[82] This species would likely be able to undergo the first HAA from the substrate, however this would be unlikely to undergo rebound to form the hydroxylated product, making this reaction mechanism unlikely. Within the LPMO literature there is some evidence in support of the deprotonated amino terminus, nominally in the form of a neutron structure showing less proton density on the amino terminus.[163] However, these data are unclear and are not supported by additional spectroscopic data such as EPR and NMR spectroscopies.[163] There have been no other reports of Cu(III) in nature at the time of writing.

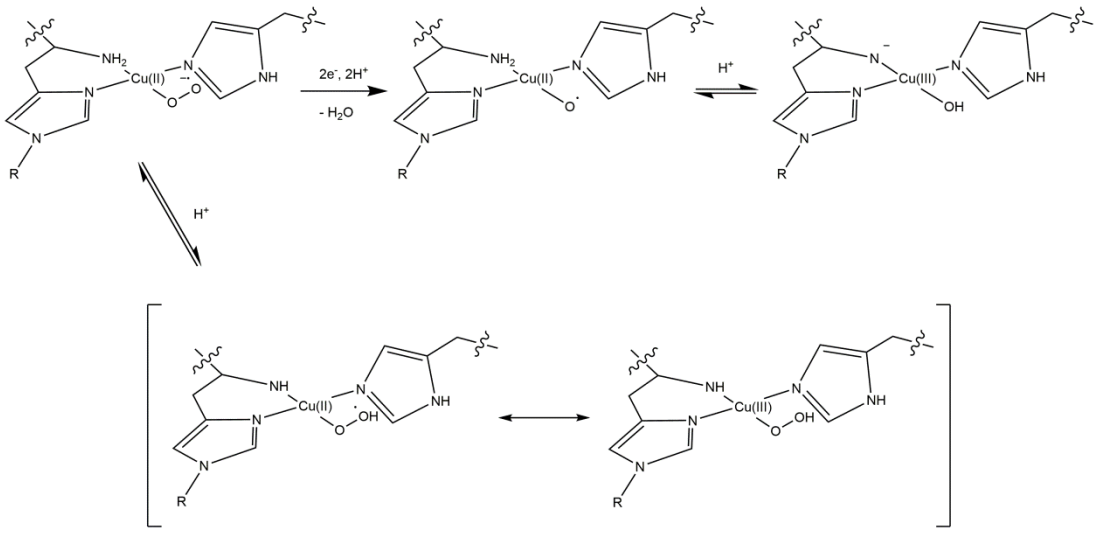

Figure 42. The proposed intermediates stabilized by the deprotonated amino terminus. Reproduced from Ciano et al.[82]

1.4.4 Asymmetric Complexes to Model LPMOs

Recent work by Concia *et al*.[164] use a modified bridgehead type ligand and the corresponding Schiff base to model LPMOs. Unlike the bridgehead designs discussed previously, the two alkyl arms are of differing lengths and the ligand consists of two differing aromatics (a pyridine and imidazole) (Figure 43). On the coordination to $Cu(ClO_4)_2$ these complexes adopt a Jahn-Teller distorted octahedral geometry, where the plane consists of the three ligating nitrogen atoms and a molecule of solvent and the axial ligands are the perchlorate counter ions with similar bond distances to those seen in AA9 LPMOs. However the amine Cu bond is significantly shorter (**CuL_{17}** Cu-N_{am} = 2.0 Å, Cu-N_{Pyr} = 1.97 Å, AA9 LPMOs: Cu-N_{im} ~ 2.0 Å, Cu-N_{amine} ~2.2 Å).[82] Furthermore, the spin Hamiltonian parameters of the Cu are similar to that of AA9 LPMOs (g_z = 2.258, $|A_z|$ = 535 MHz) which is consistent with a Peisach–Blumberg Type 2 Cu centre.

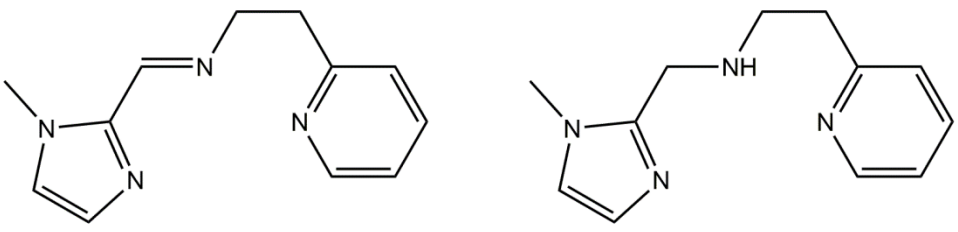

L_{16} **L_{17}**

Figure 43.A. N-[(E)-(1-methyl-1H-imidazol-2-yl)methylidene]-2-(pyridin-2-yl)ethanimine and N-[(1-methyl-1H-imidazol-2-yl)methyl]-2-phenylethanamine ligands developed by Concia et al.[164]

These complexes have been shown to react with a polysaccharide mimic, *p*-nitrophenyl-β-D-glucopyranoside, in the presence of H_2O_2. However, there is no reported reactivity of the complexes with these substrates in the presence of O_2 and an electron donor as observed for LPMOs. Computational and UV/Visible studies of the reactive intermediate observed following the reaction of these complexes with H_2O_2 predict that a **Cu(II)–OOH**$^-$ is responsible for the observed oxidative chemistry. However, a di-Cu(I) species with two ligands bridging between two Cu^+ ions (Figure 44), was obtained upon crystallisation of the reaction mixture. This species would be primed for the formation a *bis*-Cu peroxo, on reaction with H_2O_2 which brings some doubt on the authors' claims of a monomeric active species being responsible for the observed reactivity.

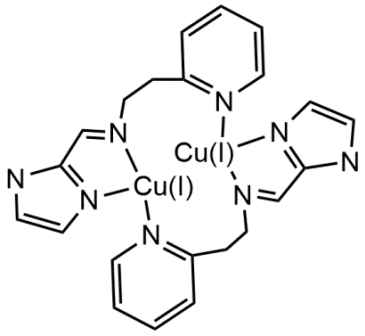

Figure 44. Schematic structure of the crystal structure obtained by Concia et al.[164] *of the reaction mixture of N-[(E)-(1-methyl-1H-imidazol-2-yl)methylidene]-2-(pyridin-2-yl)ethanimine and Cu(I)(PF_6)*

This type of ligand backbone had been previously investigated by Scarpellini *et al.*[165] who developed the bis-imidazole analogue [(2-(imidazol-4-yl)ethyl)(1-methylimidazol-2-yl)methyl)imine (Figure 45) for the investigation of phosphate diester hydrolysis. The spin Hamiltonian parameters of **CuL_{17}** and **CuL_{19}** were found to be very similar (g_z = 2.258 for both the **CuL_{17}** and **CuL_{19}**, A_z = 445 and 482 MHz, respectively). This indicates in this case that the replacement of pyridine by imidazole does not greatly affect the electronic environment of the copper ion.

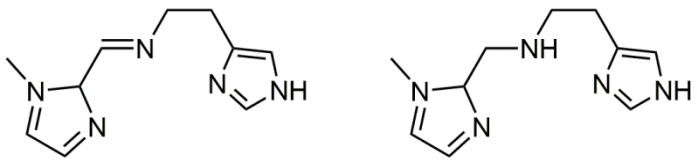

L_{18} **L_{19}**

Figure 45. Schematic structures of 2-(imidazol-4-yl)ethyl)(1-methylimidazol-2-yl)methyl)imine) and the analogous (N-[(1-methyl-1H-imidazol-2-yl)methyl]-2-phenylethanamine) complexes

As previously discussed in **Section 1.3.3** the active site of LPMOs features an angle of ~60° between the two imidazole rings. Until recently this twist had not been achieved in small molecule complexes.[82] Recent work by Fukatsu *et al.*[166] developed a ligand system which incorporated a twist angle between the imidazolyl groups of 75° shown in Figure 46. The Cu ion is coordinated by two imidazoles *trans* to one another and a secondary amide which adopts a square planar geometry. The twist angle is facilitated by a larger chelate ring, seven opposed to five or six typically used in small molecule complexes (Section **1.4.1**). This facilitates additional flexibility within the ligand backbone.[82]

The complex was shown to be active for the oxidation of *p*-nitrophenyl-β-D-glucopyranoside using H_2O_2 at pH 10 and the oxidation of cyclohexane using H_2O_2 in MeCN. The catalysis of the oxidation of *p*-nitrophenyl-β-D-glucopyranoside was shown to have a turnover number (TON) of 58 after 24h. The TON of this reaction is similar to that of the complexes developed by of Concia *et al*. (50) for the same reaction. This similar reactivity indicates that the incorporation of an imidazole twist angle does not significantly increase reactivity with H_2O_2. However, reactivity with O_2 has not been explored currently and as such the benefit of this twist may be unknown.

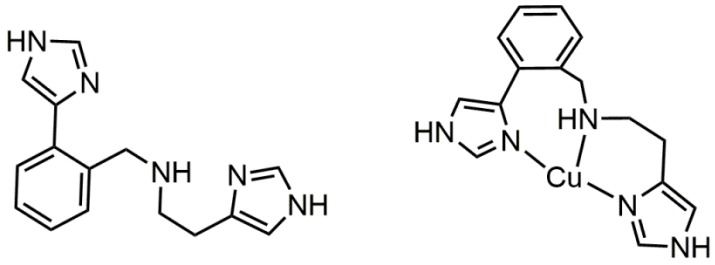

L_{20} **CuL_{20}**

Figure 46. Schematic structure of 2-(1H-imidazol-4-yl)-N-[2-(1H-imidazol-4-yl)benzyl]ethanamine and the corresponding Cu complex

1.4.5 Polyimizadole based Ligands

Small molecule Cu complexes which use exclusively imidazole based ligands as tridentate ligand have been explored by Place *et al.*[167] (Figure 47) in an effort to model biological type 2 copper sites. In this ligand the Cu ion was reported to be coordinated to each of the imidazoles where the coordination sphere is completed by methanol and Cl in a distorted square pyramidal geometry. However, one of the Cu-N bonds is extremely long (2.980 Å) indicating that the one of the nitrogen atoms is not coordinating the Cu centre, placing doubt on the authors claim about the coordination geometry.

L_{21} $[Cu(L_{21})(MeOH)Cl]Cl$

Figure 47. Schematic structure of 2-(Imidazol-2-ylmethyl)-4-(imidazol-4-ylmethyl)imidazole and the corresponding copper complex obtained by Place et al.[167]

For these complexes no activity with molecular oxygen was reported and hence the ability for this complex to form a reactive intermediate or to oxidise substrates is unknown. The EPR parameters for this complex are reported and will be discussed in the following section.

1.4.6 EPR Spectroscopy of Small Molecule Cu complexes

The small molecule complexes discussed within this section are diverse both in coordinating ligands, coordination geometry and counter ions. The effect of this diversity becomes apparent when plotting the spin Hamiltonian parameters in a Peisach–Blumberg plot, Figure 48. Unfortunately, most of the N-bridgehead type complexes were prepared in the Cu(I) state, to allow for the reaction with oxidants. As Cu(I) is d^{10} it lacks the unpaired e^- required for EPR activity.

From the Peisach–Blumberg plot the square planar complexes with tridentate N_3 complexes cluster together, the deprotonated amide Cu complexes and the cyclic diamine complex all cluster separately. Of these complexes the tridentate N_3 complexes developed by Concia, Scarpellini, Place and Fukatsu have similar parameters to that of AA9 LPMOs which is expected as they adopt square planar or distorted square pyramidal geometries and as such can be described by their position on the plot as a Type 2 Cu site. The difference in g_z and A_z values between these ligands and the cyclic diamine can be rationalised in terms of geometry. This is because the cyclic diamines are significantly distorted towards a tetrahedral geometry (Section **1.4.2**) and as such is reflected in the EPR parameters which would be expected to be more rhombic.

The deprotonated amide containing ligands cluster with significantly higher A_z and lower *g* values (g_z = ~2.17 compared to g_z = ~2.25 and A_z = ~600 MHz compared to ~475 MHz). This decrease in *g* value can be rationalised as due to the large increase in the energy of the $d_{x^2-y^2}$ resulting in a larger energy gap and as such a decrease in *g* and as *g* and A values are

anticorrelated there is a resultant increase in A value. The position of these complexes on the Peisach–Blumberg -plot is consistent with similar Cu complexes with deprotonated ligands as previously reported by Peisach *et al.*. [168]

This limited study indicates that the EPR of a given Cu complex is sensitive to counter ion, coordination geometry and ligand type.

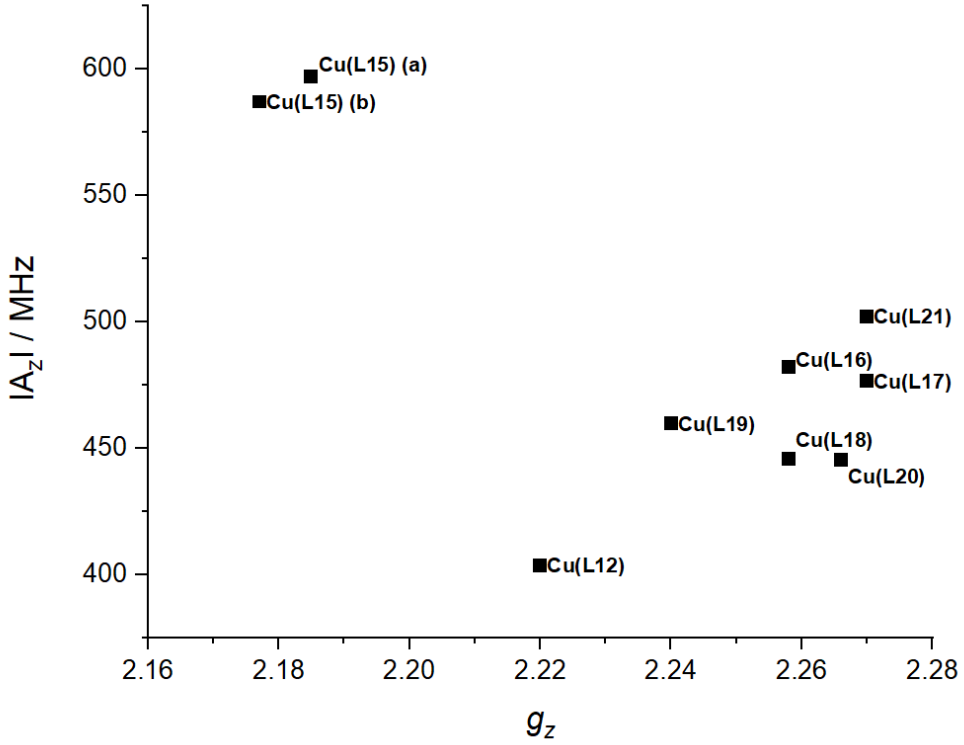

Figure 48. Peisach–Blumberg plot of the published EPR data of N_3 Cu complexes. Data and reference are listed in Table 2.(a) $[Cu(L15)OH]^-$ (b)$[Cu(L15)Cl]^-$

Table 2. Published EPR data of N_3 Cu complexes used for the Peisach–Blumberg plot shown in Figure 48

Complex	g_z	A_z / MHz	References
Cu(**L_{20}**)(tfa)$_2$	2.266	445	*Fukatsu et al.*[166]
Cu(**L_{16}**)(H_2O)(ClO_4)$_2$	2.258	482	*Concia et al.*[164]
Cu(**L_{17}**)(H_2O)(ClO_4)$_2$	2.270	476	*Concia et al.*[164]
Cu(**L_{18}**)Cl_2	2.258	446	*Scarpellini et al.*[165]
Cu(**L_{19}**)Cl_2	2.240	460	*Scarpellini et al.*[165]
Cu(**L_{15}**)OH	2.185	597	*Tolman et al.*[159]
Cu(**L_{15}**)Cl	2.177	587	*Tolman et al.*[159]
Cu(**L_{12}**)H_2O	2.220	404	*Kunishita et al.*[153]
Cu(**L_{21}**)(ClO_4)$_2$	2.27	502	*Place et al*[167]

1.4.7 General Conclusions from Small Molecule Literature Review

Within the literature there are no ligands which incorporate a tridentate N_3 coordination sphere in which there are two aromatic nitrogen donors *trans* to one another with a primary amine *trans* to the vacant coordination site, in an overall T-shaped coordination geometry at the copper ion.[82, 141]

The small molecule model complexes are generally planar due to short rigid backbones, with the torsion angles between the two aromatic rings regularly below 20°.[82] The exception is the complex developed by Itoh *et al.*[166] which uses an seven membered chelate ring to facilitate a twist in the ligand backbone. The interplanar angle between the two imidazole rings observed in LPMOs is believed to help stabilising highly reactive species,[169] and as such this twist in model complexes may explain why a **Cu(II)$O^{-\bullet}$** has not been observed in small molecules despite extensive studies of reactive intermediates as they used H_2O_2 as the oxidant.[141] However, the incorporation of the twist does not appear to improve small molecule complexes ability to oxidise substrates when H_2O_2 is used as the oxidant. This was demonstrated experimentally as the rate of reaction and TON of *p*-nitrophenyl-β-D-glucopyranoside oxidation in the presence of H_2O_2 did not increase when compared with complexes lacking this twist.[164, 166]

It should also be noted that dimerisation of small molecule model complexes to form either (μ-η^2:η^2-peroxo)- or bis(μ-oxo)-dicopper centres on reactions with oxidants presents a significant problem in most small molecule complexes. However, the formation of these species can be prevented by the incorporation of steric bulk to prevent dimerization. However the use of steric bulk must be carefully employed as any ROS generated may be able to react with this steric bulk and be able directly coordinate the Cu ion resulting in inactivation.[153]

1.5 Stabilization of Metal Oxyls

While small molecule Cu complexes have not been able to generate an oxyl intermediate, there are several small molecule structures of other metal-oxyls reported in the literature. The chemistry of these metal oxyls and the stabilisation provided by their ligands and the insights from these complexes can be applied to LPMOs and subsequent ligand designs. A metal oxyl species can be defined as an oxygen atom bound to a metal where an unpaired electron or hole is located almost entirely on the oxygen. The corresponding metal centre is nearly one electron reduced compared to its equivalent metal oxo complex, in which a double bond is formed between the oxygen and the metal, shown in Figure 49.[169-170]

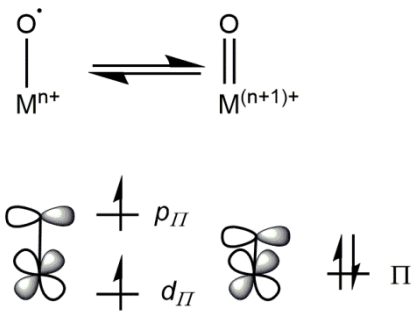

Figure 49. Schematic description of metal-oxyl (left) and metal-oxo right

Computational studies of the frontier orbitals of a fully characterised ruthenium(III)-oxyl complex, shown in Figure 50 left,[171] reveal the role of the coordination sphere in stabilizing the reactive species. The bipyridine (bpy) ligand acts as a π acceptor and as such allows for the unpaired electron of the oxyl to delocalise across the π network increasing stability. A N-heterocyclic carbene (NHC) provides a strong σ donation effect in the *trans* position to the oxyl favouring it over the metal-oxo. This effect occurs as the strongly σ-donating ligand weakens the Ru-O bond and the resultant elongation favours the Ru-oxyl over the Ru-oxo.[169, 171]

Similar donor and acceptor type ligands are utilised in a different ruthenium(II)-oxyl complex developed by Tanaka *et al.*[172], shown Figure 50 right. The 2,2‘:6‘,2‘ ‘-terpyridine (trpy) ligand acts as a π acceptor, similar to bpy, while the semiquinone ligand in the *trans* position acts as a π donor. However, unlike the ruthenium(III) complex, the orbitals involved in these interactions have not been confirmed by computational analysis.

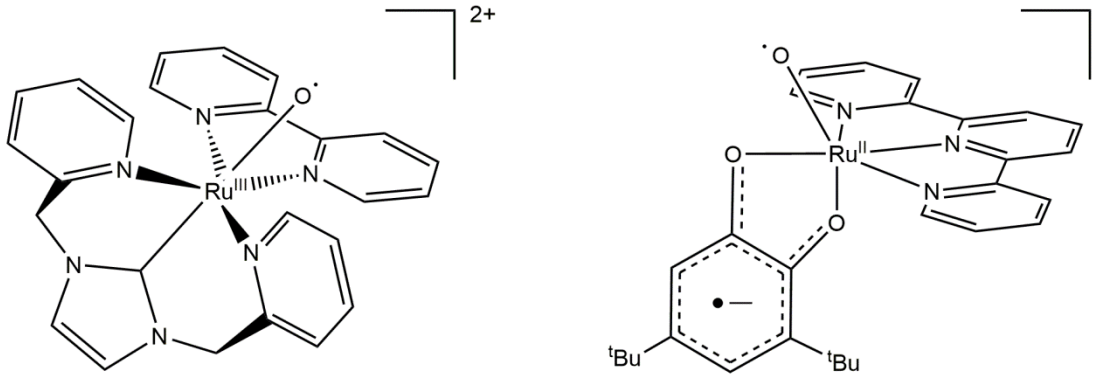

Figure 50. The ligand set of a Ru(III)-Oxyl developed by Kojima et al.[171] and *a Ru(II)-Oxyl developed by Tanaka et al.*[172]

The 'histidine brace' of LPMOs contains features compatible and necessary for the stabilisation of a reactive oxyl intermediate. For instance, it contains a potential π-acceptor in the form of the imidazole ring from the coordinated histidine. As described in section **1.1.1.2**, this ring is consistently twisted in LPMO structures. Thanks to this twist, the unpaired electron of the oxyl could delocalise through the d orbitals on the copper into the π network. Meanwhile, a strong σ donation *trans* to the site of ROS formation is provided by the amino terminus, both effects are shown in Figure 51. These features support the hypothesis that LPMOs are able to generate an oxyl intermediate to break the glycosidic bond in polysaccharides.

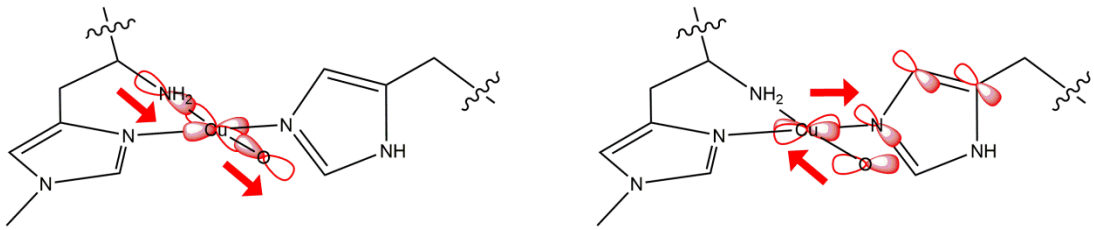

Figure 51. Proposed electron flow in the histidine brace for stabilisation of a Cu-oxyl. Left. The σ donation effect from the amino terminus trans to the oxyl. Right. The π accepting effect of the coordinated histidine

1.6 Electron Paramagnetic Resonance Spectroscopy (EPR)

Copper in the 2+ oxidation state has a d^9 configuration and therefore possesses an unpaired electron. This unpaired electron can be studied by electron paramagnetic resonance (EPR) spectroscopy. EPR spectroscopy is similar to any other spectroscopy in which it is dependent on the absorption of electromagnetic radiation, in this case microwaves. The absorption of energy causes a transition from a lower energy state to a higher energy state. This energy difference can be measured as according to Planck's law, electromagnetic radiation will be absorbed if,

$$\Delta E = hv$$

where ΔE is the energy gap between the two states, *h* is Planck's constant and *v* is the frequency of radiation.

The energy difference studied in EPR spectroscopy is due to the interaction of an unpaired electron with an external magnetic field, B_0, known as the Zeeman Effect. Since an electron has both a charge and an intrinsic angular momentum (spin), μ, this particle acts as a magnet with its own intrinsic magnetic moment. When placed in a magnetic field this produces two energy levels for the magnetic moment of the electron, the lowest energy state where *μ-(½)* is aligned with the magnetic field and the highest energy state where *μ(+½)* is aligned against the magnetic field. The two states induced by a magnetic field are designated as +½ and -½ for the antiparallel and parallel states, respectively, as electron is a spin half particle (Figure 52). The energy of these states is given by the equation,

$$E = m_s g_e \beta$$

Where β is the Bohr magneton and g_e is the spectroscopic g-factor of the free electron.

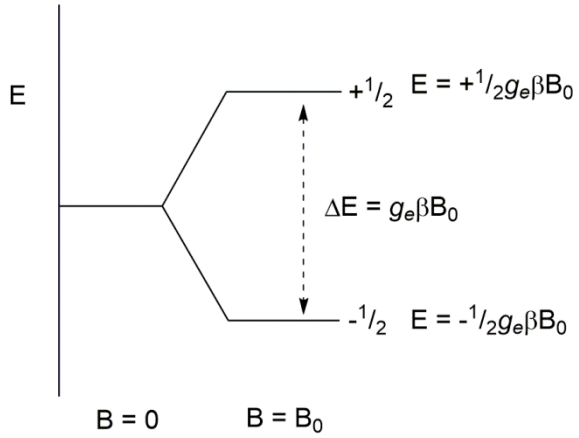

Figure 52. Spin state energies induced by a magnetic field, B_0.

In a molecule, as opposed to a free electron, there is a change in the total angular momentum of any unpaired electron as it now possesses orbital angular momentum, *L,* in addition to the spin angular momentum, *S*. The contribution of the orbital angular momentum is relatively small in the pure spin ground state. However the coupling of orbital angular momentum and spin angular momentum (spin orbit coupling) results in significant mixing between the angular momenta. As such the magnetic moment of the electron can now be expressed as,

$$\mu \propto g_e S + Spin - orbit\ coupling\ contribution$$

Therefore,

$$\Delta E = g\beta B_0$$

Where *g* contains contributions from both electron spin and spin angular momentum. Experimentally, as the energy gap is measured, *g* can be calculated by the following equation,

$$g = \frac{hv}{\beta B_0}$$

As both h and β are constant the *g* value can, to first order, be calculated as it is linearly dependant on the magnetic field. Due to this dependence, the magnetic field is varied in an EPR experiment as opposed to the frequency of radiation which is typical in other forms of spectroscopy. This is due to the fact that radiation sources, used for EPR, can only produce a limited spectral window which makes continuous wavelength variation impossible.

The equations discussed above concern a single molecule in a single orientation within a magnetic field. The *g* value is dependent on the contribution of orbital angular momentum

to the spin only momentum. The degree of angular momentum contribution is a function of d-orbital ordering. As such there is a direct connection between the g value and the d-orbital splitting within a metal complex. This is the essential link in anisotropic EPR spectroscopy.

Molecular orbitals, by definition, are orientated with respect to a magnetic axis, as such *g* is inherently anisotropic. Each molecule therefore has a unique axis system known as the principal axis system. The *g* values measured along these directions are known as the principal g-factors and are labelled as g_x g_y and g_z based on their alignment with the principal axis system. In solution this anisotropy is averaged out by rapid tumbling of the molecule, hence most inorganic EPR spectra are carried out in frozen solution as this fixes the molecule in all possible orientations. The EPR spectrum of such a frozen state gives rise to a typical powder spectrum absorption envelope. The shape of the absorption envelope in an EPR experiment is dependent on the symmetry of the environment of the molecule. For a molecule which is totally symmetric (e.g. $[Cu(H_2O)_6]^{2+}$) all of the *d* orbitals have an equal interaction in all directions and as such $\mu_z = \mu_y = \mu_x$ *so* $g_z = g_y = g_x$, which would give rise to a single Gaussian-shaped peak in the absorption spectrum due to the super positioning of the individual components (which have a Lorentzian line shape) to give a Gaussian absorption profile. When moving away from a totally symmetric system the magnetic moment within the system can vary along any of the principal axes. For example, in a system where $g_z > g_y = g_x$ the spectral envelope is that shown in Figure 46.

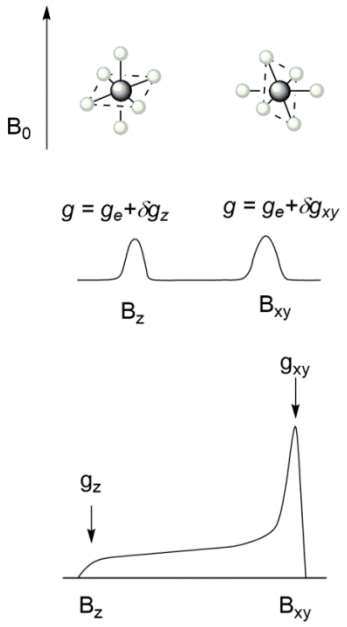

Figure 53. Top. The dependency of the g *value on the orientation of the molecule. Bottom. The dependency of the g value on orientation in a powder spectrum.*

Generally, there are two different classes of anisotropy and the absence of it. The absence of any anisotropy is known as isotropic where all of the principal *g*-factors are the same *(g_z = g_y= g_x)*. The second class are called axial and these occur when there is one unique axis that differs from the other two ($g_z \neq g_y = g_x$). The final class is classed as rhombic where all three *g*-factors differ ($g_z \neq g_y \neq g_x$).

The electron can be represented by a bar magnet and as such will be influenced by interactions with neighbouring magnets. Within an EPR experiment, there are two main types of interaction which can occur. These interactions are due to the magnetic coupling between the unpaired electron and the magnetic moment of nuclei. The first of these is the nuclear hyperfine interaction, A, which is the interaction between the nuclei from which the unpaired electron originates and the unpaired electron itself. In inorganic systems the second is the super hyperfine interaction, A_{SHF}, which is the interaction between neighbouring nuclei and the unpaired electron. These interactions are much smaller than the Zeeman interaction and as such can be treated as perturbations to it; the resonance condition then becomes,

$$hv = g\beta B_0 + hAm_i$$

where *A* is the hyperfine coupling constant and m_i is the magnetic quantum number of the nucleus. For the values for m_i there are 2I + 1 possible value and as such the hyperfine interaction splits the Zeeman transition into 2I+ 1 lines (m = +L, +L-, …,-L) of equal intensity, known as the 2I+1 rule. This can then be repeated by any nearby magnetic nuclei via the super hyperfine coupling, shown in Figure 54.

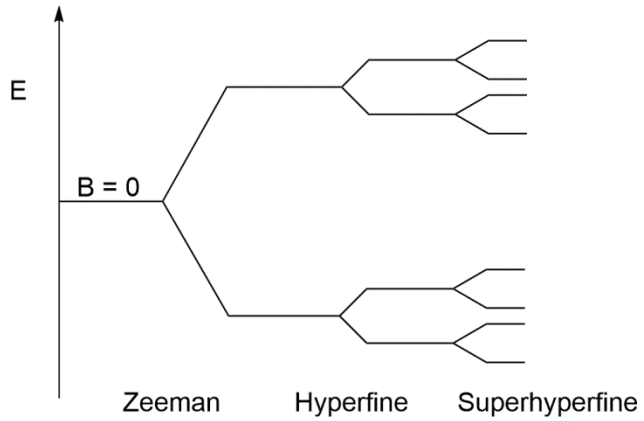

Figure 54.Coupling diagram showing the perturbation caused by the Zeeman, hyperfine and super hyperfine coupling in a magnetic field.

The hyperfine component can be broken down into three different interactions, the Fermi contact term, A^{Fermi}, the spin-dipolar coupling, A^{SD} and the orbit-dipolar coupling term A^{SO}. Of these A^{Fermi} occurs due to direct overlap of the nuclear and electronic wavefunctions, and is restricted to the s-orbital content of the electronic wavefunction—this is an isotropic interaction. The two other interactions involve the dipolar coupling of the electron through space to the either the nuclear spin or the orbital momentum of the nuclei and are hence orientation dependent and therefore anisotropic.

Standard equations for the calculation of the hyperfine values from d-orbital coefficients have been determined already by previous workers.[173] In particular, in terms of a Cu(II) d^9 complex, the most accurately determined experimental value is that of A_z, the hyperfine coupling in the z direction of the so-called A-tensor. Accordingly, the full equation for the hyperfine A_z value in a complex with D_{2h} geometry is given by,

$$A_z = P_{\mathrm{d}}\left[-K - \frac{4}{7}\alpha_{\mathrm{GS}}^2(a^2 - b^2) + \Delta g_z + \frac{\Delta g_y(3a - \sqrt{3}b)}{14(a + \sqrt{3}b)} + \frac{\Delta g_x(3a + \sqrt{3}b)}{14(a - \sqrt{3}b)}\right]$$

in which P_{d}=$g_e g_{Cu} \mu_e \mu_{Cu}$ the quasi-atomic parameter (1180 MHz), α_{GS}^2 is the covalency of the ground state and a and b are the coefficients for the contributing ground state orbitals, K is the dimensionless constant, known as the Fermi contact parameter and Δg is the change in g value from the free electron value. This equation can be split into the three terms contributing to the hyperfine values, described above. The isotropic Fermi contact term (A^{Fermi}) is represented in blue, the spin-dipolar term (A^{SD}) represented in green and the spin–orbit term (A^{SO}) represented in red. During this project, this relationship will be used to determine the covalency of the SOMO of any Cu(II) complexes.

1.7 Aims of the Project

Within the current literature biomimetic models of lytic polysaccharide monooxygenases are unable to carry out C-H activation on polysaccharide substrates. This may be due to the models lacking the features required to stabilise highly reactive species such as the Cu-oxyl which is suspected to be the intermediate in AA9s. The aim of this project is to design, synthesise and test a new ligand system based on the active site of LPMOs. The design, synthesis and characterisation of these new ligands and the corresponding Cu complexes are described in **Chapter 2**.

Both the primary and secondary coordination spheres have been shown to be important for enzymatic function (Section **1.3.4**). Therefore, an additional aim is to probe the role of the secondary coordination sphere of LPMOs using an artificial enzyme approach. This strategy is used since a purely synthetic approach cannot be used effectively to probe the secondary coordination sphere. This is due to the considerable synthetic difficulty of incorporating atoms capable of hydrogen bonding while preventing coordination in a N_3 system. The synthetic modification of the ligand for use in a biotin-streptavidin system, the characterisation of the free ligand and the corresponding artificial enzyme are detailed in **Chapter 3**.

Finally, the reactivity of both the free complex and corresponding artificial enzymes are explored with both polysaccharide substrates, using stopped-flow kinetics and biological assays. The results of these activity tests are detailed in **Chapter 4**.

Chapter 2 – Synthesis and Characterisation of a Primary Amine Containing Ligand and its Corresponding Copper Complexes

2.1 Ligand Design and Synthesis

The objective of the work described in this chapter is to design, synthesise and characterise a novel ligand system and its respective Cu complexes. The complexes are required to address shortcomings of current model complexes within the literature in an effort to more successfully model both the structure and spectroscopy of the histidine brace. In order to do this the ligand must fulfil the following criteria,

1. Two heteroaromatic nitrogen donors *trans* to one another in the Cu coordination sphere
2. A primary amine *trans* to an exogenous ligand coordination site
3. A torsion angle of ~40° between the two planes of the aromatic residues
4. Be water soluble

2.1.1 Nomenclature and Numbering

All non-literature compounds within the thesis are numbered with an **X.Y** scheme, where **X** is the chapter number and **Y** is a progressive number based on order of appearance.

Metal complexes are labelled in a **M(X.Y)Z** scheme where **M** is the Metal ion, **(X.Y)** is the synthetic compound number and **Z** is the respective counter ion.

2.1.2 Ligand Design

In order to effectively model the active site of LPMOs, three key features of the histidine brace were identified as essential for the ligand design, listed in **Section 2.1**. Histidine methyl ester, shown in Figure 55, was selected as the starting point for the ligand design, as it is both readily available and already possesses some of the key features needed for the ligand. Furthermore, the methyl ester can be reduced to the alcohol or cleaved to give the carbonyl to allow for further functionalisation thus serving as a convenient synthetic handle.

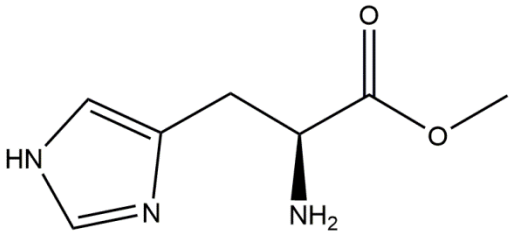

2.1

Figure 55. L-Histidine methyl ester.

The coordination chemistry of histidine to Cu has been well studied.[174-176] In solution, histidine can adopt numerous different coordination modes dependent on pH, metal to ligand ratio and temperature. This is due to the various protonation states available to histidine coupled with a relatively large number of atoms, present within histidine, that are capable of coordinating to the Cu ion. Both the mono- and bis- *L*-histidine Cu complexes have been identified and characterised along with the percentage of each present in solution over a range of pHs, shown in Figure 56.[174]

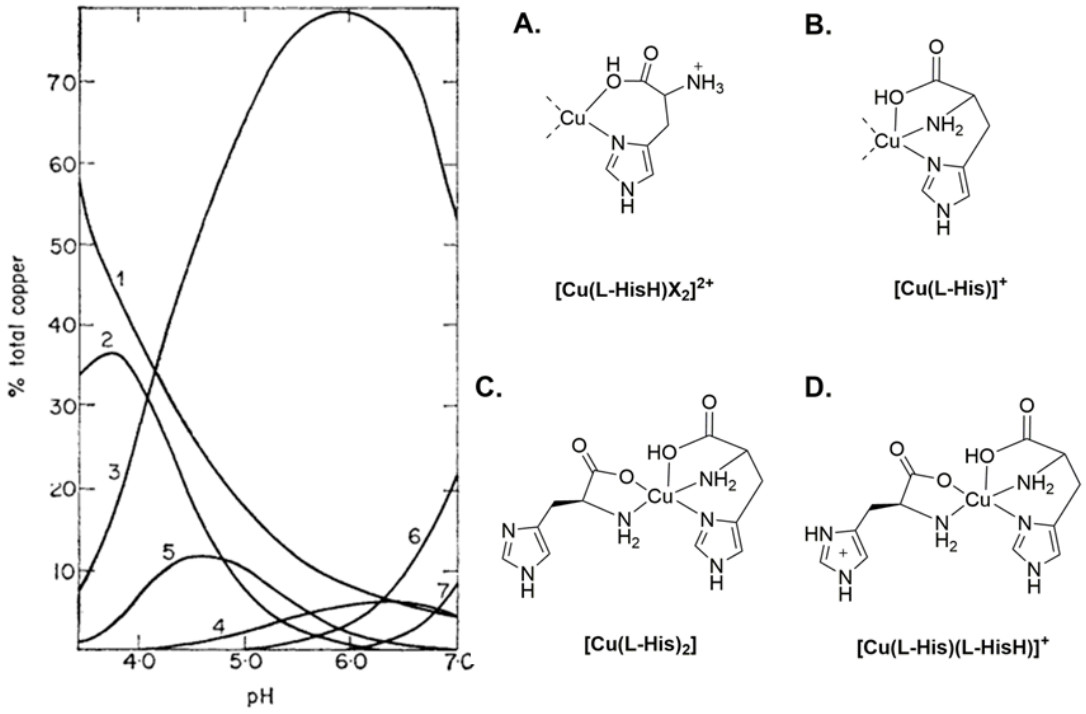

Figure 56. ***Left.*** *Calculated variation with pH of the composition of a Cu(II) - histidine system with a 1:1 ratio adapted from V. S. Sharma et al.*[177] ***1. Cu^{2+} 2. $[Cu(L\text{-}HisH)]^{2+}$ 3. $[Cu(L\text{-}His)]^{+}$ 4. $[Cu(L\text{-}His)_2]$ 5. $[Cu(L\text{-}His)(L\text{-}HisH)]^{+}$ 6. $[Cu(L\text{-}His)OH]$ 7. $[Cu(L\text{-}His)_2(OH)_2]$. Right.*** *A Schematic representation of the predicted structure of* ***$[Cu(L\text{-}His)]^{2+}$*** *based on IR data****. B.*** *A Schematic representation of the crystal structure of* ***$Cu(L\text{-}His)^{+}$. C*** *A Schematic representation of predicted structure of* ***$Cu(L\text{-}His)_2$. D.*** *A Schematic representation of the crystal structure of* ***$Cu(L\text{-}His)(L\text{-}HisH)^{+}$.***

As the ligand which is being designed is focused on a 1:1 Cu : ligand ratio, complexes with the analogues Cu : histidine ratio will be the primary focus of this discussion. Below pH 6 $[\mathbf{Cu(L\text{-}HisH)X_2}]^{2+}$ is the predominant species in solution, however, this is not the only species present and a significant amount of free copper and ligand are present in solution at this pH, shown in Figure 56. The exact coordination geometry of $\mathbf{[Cu(L\text{-}HisH)X_2]^{2+}}$ is unknown as there are no solved crystal structures available for this complex. Thus the coordination geometry has been elucidated using spectroscopic methods. IR spectroscopy of the $\mathbf{[Cu(L\text{-}HisH)]^{2+}}$ complex in solution indicates that the histidine coordinates to the Cu centre *via* the imidazole nitrogen and carbonyl oxygen, as such the predicted structure is shown in Figure 56A.[178]

At pH 6 the $\mathbf{[Cu(L\text{-}His)X_2]^{+}}$ is the dominant species present in solution. However, the exact coordination geometry of $\mathbf{[Cu(L\text{-}His)X_2]^{+}}$ is unknown as there is no crystallographic structure available for $\mathbf{[Cu(L\text{-}His)X_2]^{+}}$. Thus the coordination geometry has been elucidated using spectroscopic methods. The IR spectroscopic data of the solution state complex indicate that both the amine and imidazole nitrogen atoms, along with the carboxyl oxygen coordinate to the Cu centre. The predicted structure is shown in Figure 56B.[178]

It should be noted that above pH 6 both $\mathbf{[Cu(L\text{-}His)OH]^{+}}$ and $\mathbf{[Cu(L\text{-}His)_2(OH)_2]}$ are formed but neither have been fully characterized in the literature. These complexes have been speculated to retain the same geometry as observed for $\mathbf{[Cu(L\text{-}His)X_2]^{+}}$ and $\mathbf{[Cu(L\text{-}His)_2]^{2+}}$ respectively.[174]

It must also be noted that the *bis*-histidine Cu complexes are present in the solution at low concentrations. The crystal structures of both $\mathbf{[Cu(L\text{-}His)_2]^{2+}}$ and $\mathbf{[Cu(L\text{-}His)(L\text{-}HisH)]^{2+}}$ have been characterised *via* X-ray crystallography.[179] The complexes adopt a square pyramidal geometry at the copper where one histidine coordinates the Cu as a tridentate ligand through the carbonyl oxygen, the amine nitrogen and the imidazole nitrogen. The coordination sphere is completed by a second histidine which coordinates the Cu as a bidentate ligand through the carbonyl oxygen and amide nitrogen, shown in Figure 56C and Figure 56D respectively.

In all of the complexes, histidine was shown to coordinate through the carboxyl oxygen, in both bidentate and tridentate coordination modes. Therefore, in order to obtain the desired coordination mode of the ligand (through both the amine and imidazole nitrogen) the carbonyl must undergo further functionalisation or be removed entirely to prevent its coordination. The carbonyl group can be removed either *via* reduction to an alcohol or

aldehyde or used in either an amide or ester synthesis. Of these options, reduction to an alcohol is preferable as it allows for increased flexibility within the molecule due to the loss of the sp^2 carbon. The alcohol can also be used as a nucleophile in an ether synthesis or can be easily converted to an electrophile *via* a halogenation reaction. This allows for greater flexibility in synthetic steps when synthesising the ligand as the alcohol can be modified to form either a nucleophile or an electrophile while a carbonyl almost exclusively acts as an electrophile.

Within the literature pyridines are widely used as alternatives to imidazoles in small molecule models of enzymes, shown in **Section 1.4**. Pyridine and its synthetic derivatives are more readily available than imidazoles and they fulfil the same requirement of a heteroaromatic ring for the ligand design. As such, a pyridine derivative was chosen as the second coordinating aromatic moiety.

Space filling (CPK) models were used to understand ligand sterics. The length of the carbon chain between the ether oxygen atom and the pyridine ring were assessed, shown in Figure 57. The models suggest that steric hindrance prevents molecules with one carbon atom between the pyridine ring and the oxygen (compound **2.2** in Figure 57) from coordinating the metal ion. Methyl and ethyl chains (**2.3** and **2.4,** respectively) provide the best compromise between the size of the chelate ring and the ability for the pyridine to coordinate the metal ion. Both chain lengths are long enough to allow for the pyridine to position itself in such a way to allow for coordination while minimizing the size of the ring formed on coordination. These models also revealed the possibility of an intermolecular hydrogen bond forming between the ether oxygen atom and the NH_2 which may allow for the ligand to orientate itself for coordination. Serendipitously, the use of a longer linker may also allow for the increased torsion angle between the two rings, as these models indicate that on coordination the two aromatic rings are non-planar with respect to one another. Thus compounds **2.3** and **2.4** were selected as initial ligand targets for synthesis.

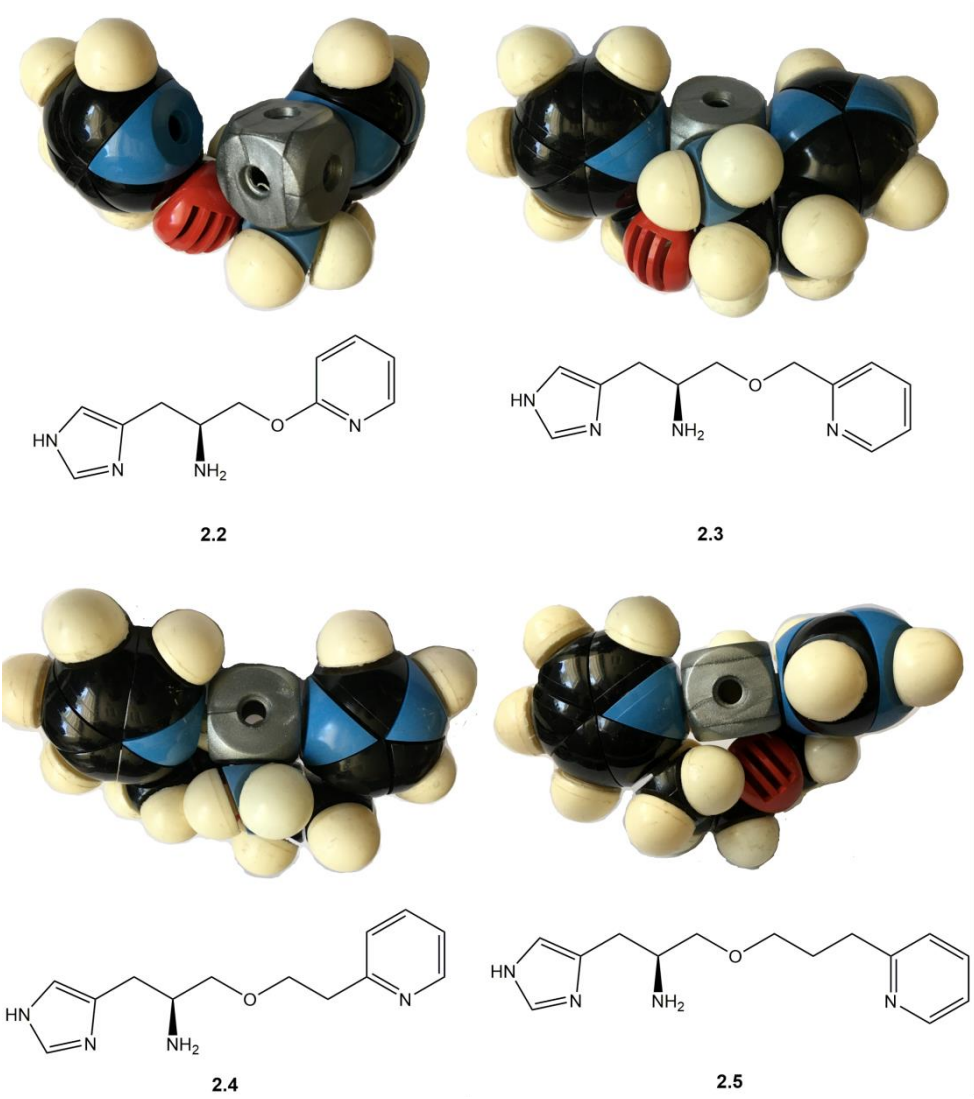

Figure 57. Schematic structure of initial target ligands and CPK models of their respective Cu complexes

2.1.3 Synthesis and Characterisation

This section will detail the synthetic design, synthetic route and subsequent characterisation of the target compounds **2.3** and **2.4.**

2.1.3.1 Design of Ether Synthesis

There are several potential synthetic methods to form ether linkages.[180] These methods include the Williamson ether synthesis,[181] bimolecular dehydration,[182] the Ullman ether synthesis [183] and the Mitsunobu reaction.[184]

The Williamson ether synthesis is a versatile reaction capable of forming both symmetrical and asymmetrical ethers using either aryl or alkyl substituents.[185] These reactions occur *via* the use of an inorganic base to form the alkyl metal salt of the alcohol, which is then able

to act as a nucleophile, as it can be deprotonated to form a negatively charged alkoxide. The electrophile in this case is a primary carbon centre with a good leaving group, (LG) (*e.g*. Cl^-, Br^-, tosylates (OTs), mesylates (OMs), OSO_2R). This reaction occurs *via* a bimolecular nucleophilic substitution (S_N2) type mechanism, shown in Figure 58A.[186] As with all S_N2 reactions, the competing E2 elimination must be considered, in which the alkoxy group, instead of acting as a nucleophile, acts as a base, abstracting a proton with the subsequent loss of the leaving group and formation of an alkene, as shown in Figure 58B.

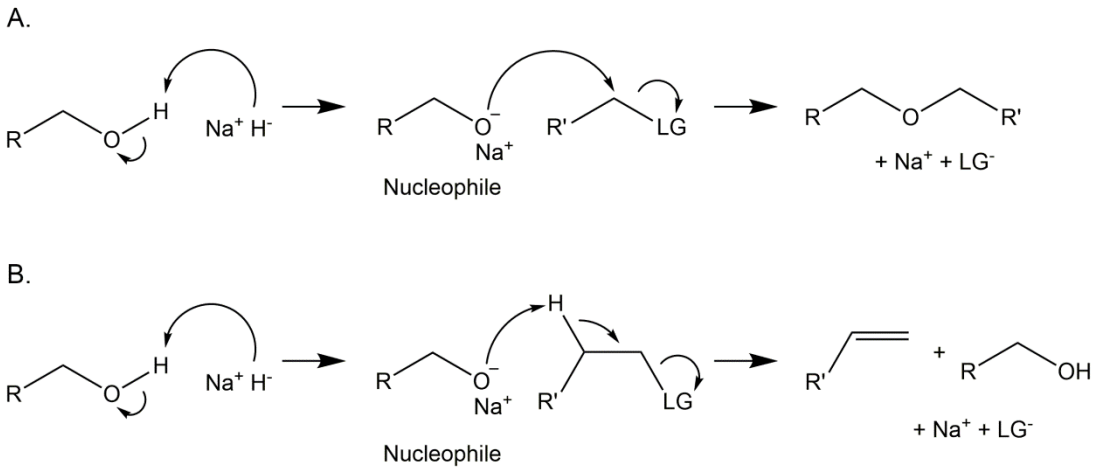

Figure 58. Williamson ether synthesis. A .Ether formation via a S_N2 Reaction mechanism. B. The competing E2 reaction mechanism for the formation of an alkene. Leaving group (LG) = Cl^-, Br^-, -OTs, -OMs, -OSO_2R

The formation of ethers *via* a bimolecular dehydration reaction occurs under acidic conditions, with two molecules of an alcohol reacting together with the loss of water to form an ether. This type of reaction is widely used by the chemical industry to synthesise simple ethers.[180] However, this reaction is unsuitable for the synthesis of asymmetric ethers as when two different alcohols are used, the homocoupling reaction competes with the heterocoupling reaction resulting in a mixture of isomers, shown in Figure 59A. The reaction also competes with the unimolecular dehydration to give an alkene, shown in Figure 59B.

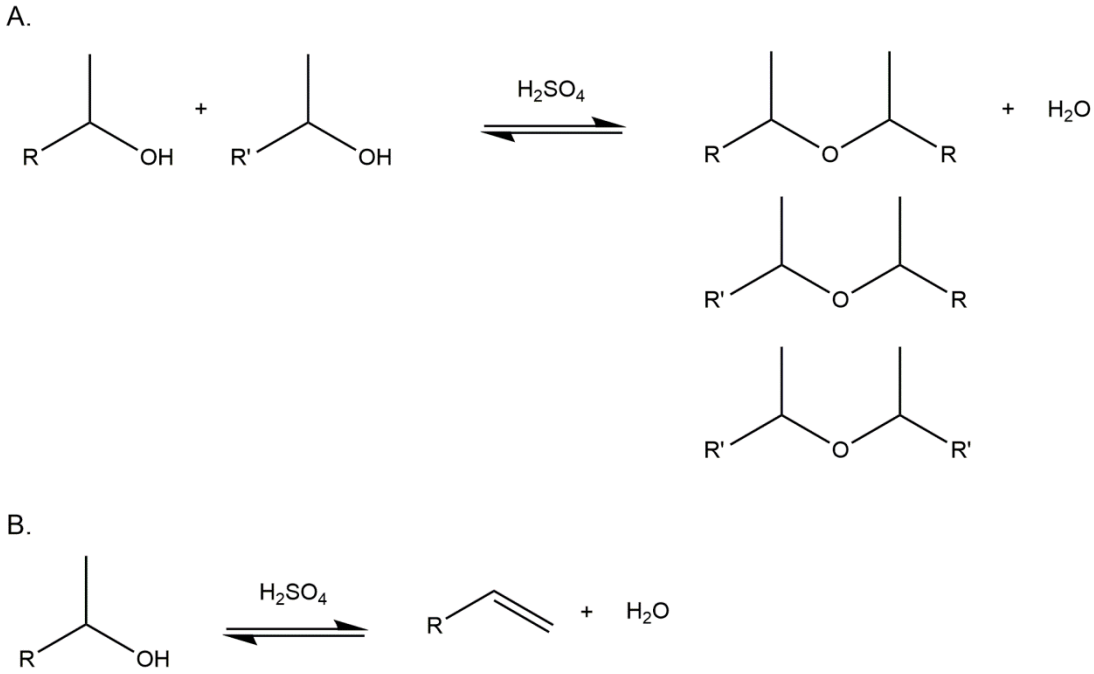

Figure 59.A. An example of reaction scheme for bimolecular dehydration. B. An example of reaction scheme for unimolecular dehydration.

The Ullman ether synthesis occurs *via* a Cu-catalysed coupling reaction between phenols and aryl halides, shown in Figure 60.[187] These reactions require for both substituents to be aromatic. The Ullman ether synthesis is tolerant to heteroaromatics and functionalisation of the said aromatics but may result in decreased yields.[188] Various ligands for the Cu catalyst have been shown to improve the yields and rates of reaction.[188]

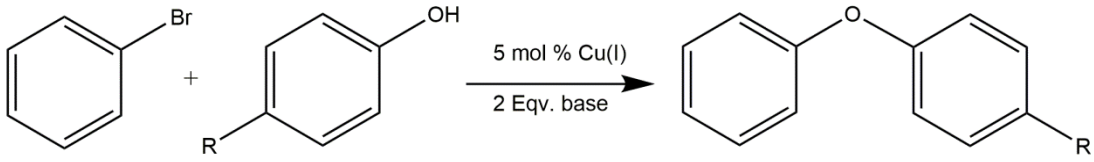

Figure 60. An example of an Ullman ether synthesis.

The Mitsunobu reaction occurs using what is known as a "redox" condensation using triphenylphosphine and a diethyl azodicarboxalate (DEAD), shown in Figure 61. In the first step of the reaction the triphenylphosphine combines with DEAD to generate a phosphonium intermediate. The phosphonium intermediate is then able to activate the alcohol converting it to a good leaving group. The activated alcohol is then able to undergo attack from the second alcohol to form the desired product and triphenylphosphine oxide.

The Mitsunobu reaction allows for the formation of alkyl aryl ethers, enol ethers and cyclic dialkyl ethers *via* reactions with phenols, β-ketoesters and intermolecular coupling (in the presence of mercuric bromide) respectively.

Figure 61. The general reaction scheme of a Mitsunobu reaction used to form aryl alkyl ethers.

Considering the variety of synthetic methodologies employed to produce ethers, an analysis of the target compounds **2.3** and **2.4** is needed to choose the best synthetic strategy. Retrosynthetic analysis of compound **2.4** gives an indication of possible starting materials, shown in Figure 62. Both of the starting materials have alkyl chains and the final ether is asymmetric. As both the Mitsunobu and Ullman ether syntheses require the alcohol to be aromatic or the desired product to be cyclic (Mitsunobu), which is not the case for the formation of compounds **2.3** and **2.4**, these methodologies are unsuitable. The asymmetric nature of the ethers present in **2.3** and **2.4** prevents the use of a bimolecular dehydration reaction to avoid homocoupling. Therefore, the Williamson ether synthesis is the most suitable methodology for the formation of the ether bond in this case, as it allows for formation of asymmetric ethers when neither substituent is aromatic.

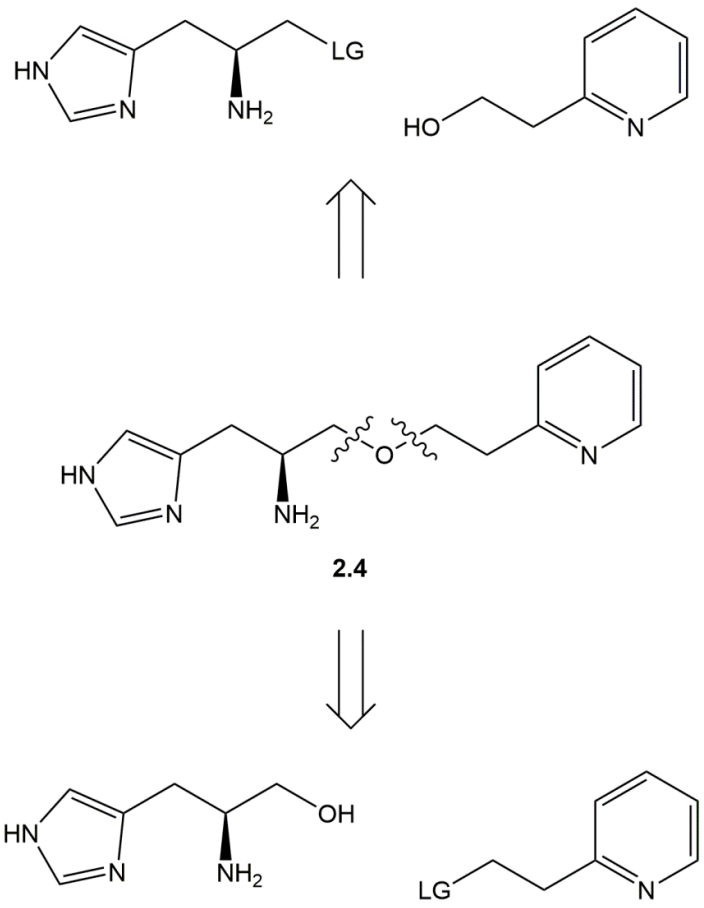

*Figure 62. The disconnection of the ether linkage in compound **2.4** to its respective synthetic equivalents*

2.1.3.2 Initial synthetic route targeting 1-(1*H*-imidazol-4-yl)-2-[2-(pyridin-2-yl)ethoxy]ethanamine **2.4**

The histidine brace mimic targeted for synthesis was **2.4**. Having considered the synthesis and disconnection of the ether linkage, shown in Figure 62, it was decided to introduce the linkage using a Williamson ether synthesis.[180, 185] As such the synthetic route for compound **2.4** was planned as shown in Figure 63.

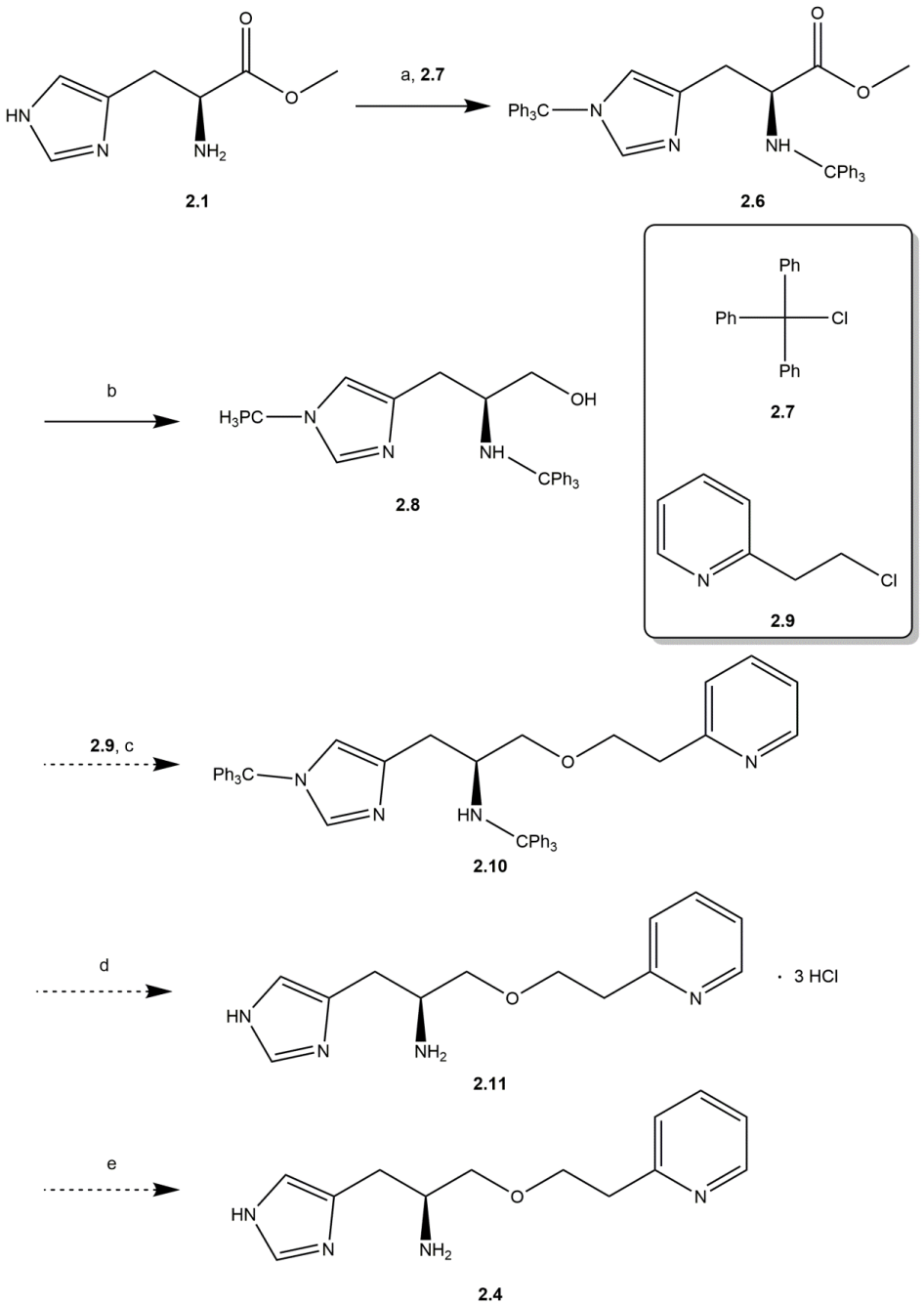

*Figure 63. Initial synthetic route towards compound **2.4**. (a) MeCN, 2.5 eq **2.7**, 5 eq Et_3N (b) N_2 atm., Dry THF, 5 eq $LiAlH_4$ (c) N_2 atm., Dry THF, NaH, **2.9** (d) 1:1 THF / 3M HCl, Δ .(e) Dowex® MSA-1 resin.*

Compound **2.8** can also be used for the synthesis of the other target compound **2.3** through the use of a different electrophile, 2-(chloromethyl)pyridine **2.12**. Thus, the planned synthesis of compound **2.3** from **2.8** is shown in Figure 64.

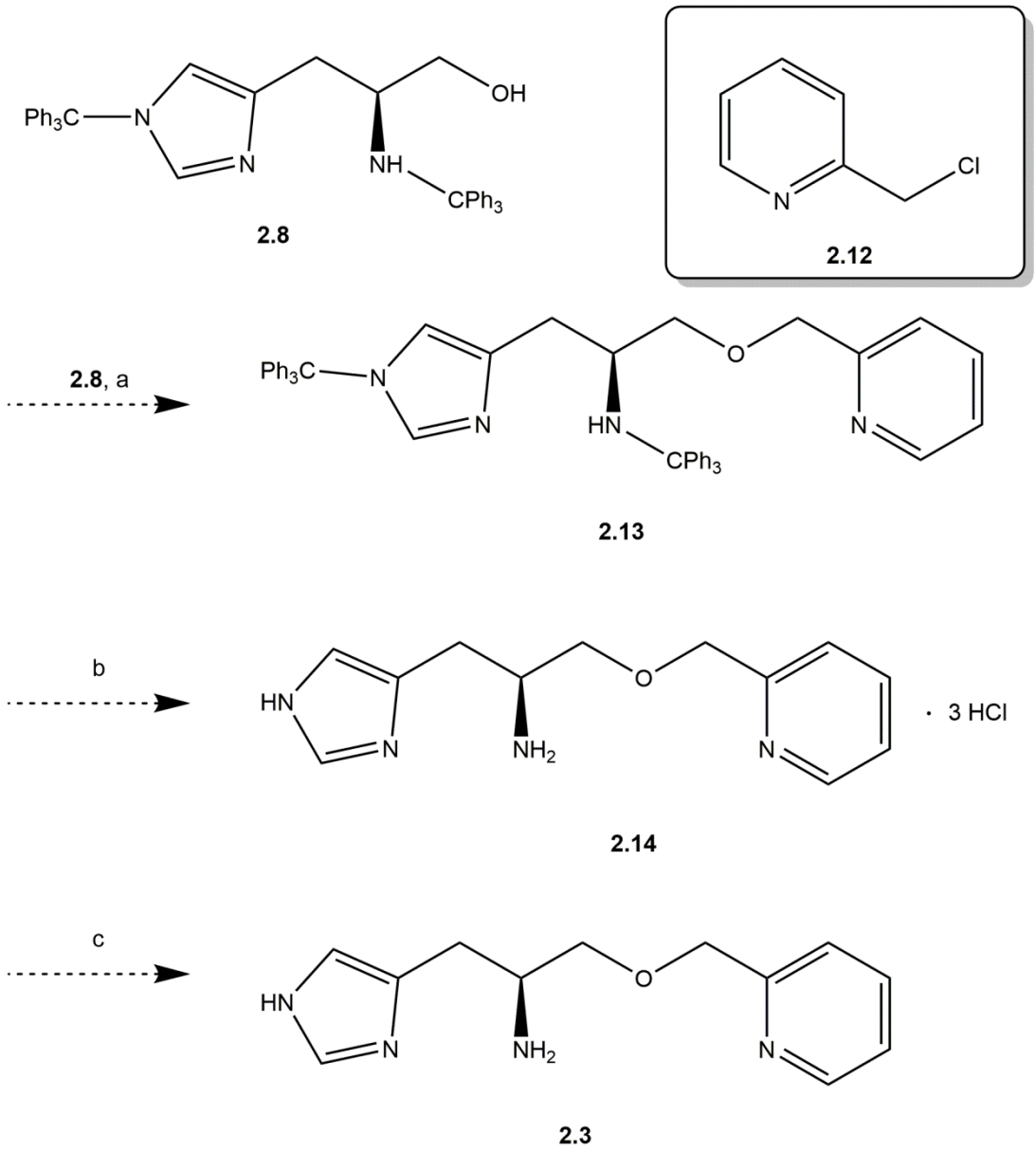

*Figure 64. Initial synthetic route towards compound **2.3**. (a) N_2 atm., Dry THF, NaH, **2.8** (b) 1:1 THF / 3M HCl, Δ. (c) Dowex® MSA-1 resin.*

The initial step in the synthesis was the protection of both the primary amine and τ-nitrogen of the imidazole ring of histidine methyl ester, **2.1**. This protection was carried out to prevent unwanted side reactions in the subsequent reactions in the synthetic route, such as the nucleophilic coupling of the primary amine to the electrophile. Furthermore, the incorporation of the protecting group can be used to significantly reduce the polarity of the molecule. By reducing the polarity of the molecule the solubility of the molecule in

organic solvents is improved, which in turn facilitates various purification steps such as flash column chromatography. A triphenylmethyl (trityl) group was selected as the protecting group because, despite requiring more activating conditions as opposed to a other protection groups,[189] its additional steric bulk prevents racemisation *via* the deprotonation of the α-carbon under basic conditions. The use of this group also allows for the protection and deprotection of both nitrogen atoms simultaneously.

To protect the amine and imidazole nitrogen atoms, triphenylmethyl chloride was added dropwise to a slurry of histidine methyl ester **2.1** in MeCN with the addition of base, shown in Figure 65. Compound **2.6** was isolated in 80% yield after an organic-aqueous extraction and was characterised using ^{1}H and ^{13}C NMR spectroscopy, infrared spectroscopy and ESI mass spectrometry. The formation of **2.6** is supported by the appearance of two new quaternary resonances at 75.21 and 70.98 ppm in the ^{13}C spectrum. In the Heteronuclear Multiple Bond Correlation (HMBC) spectrum these resonances share cross peaks with the imidazole hydrogens and the chiral carbon's proton, respectively, indicating bond formation between the two reagents. In addition, the ESI-MS analysis showed a molecular ion peak $[M+H]^+$ at *m/z* 654.3115, which is consistent with a compound of formula $C_{45}H_{40}N_3O_2$ the expected molecular formula of **2.5**. The peaks in ^{1}H NMR spectra match those found in the literature for compound **2.6**.[190]

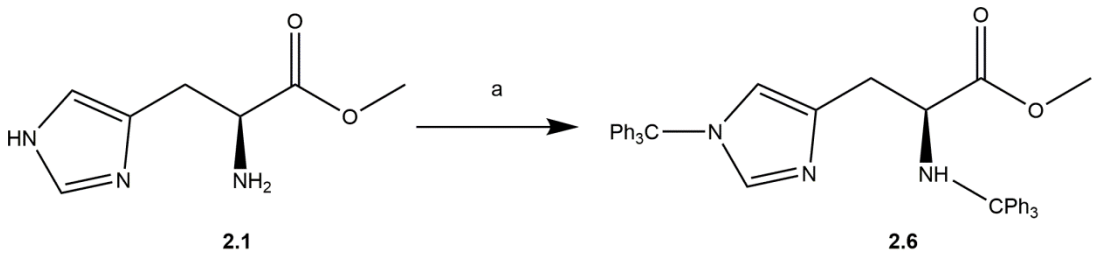

2.1 **2.6**

*Figure 65. Formation of the dityrityl protected L-histidine methyl ester **2.6** from **2.1** (a) MeCN, 2.5 eq **2.7**, 5 eq Et_3N*

After protection, the alcohol required for reactivity in the Williamson ether synthesis can be produced without the risk of side reactions *via* the reduction of L-histidine methyl ester to the corresponding alcohol, shown in Figure 66. Under a N_2 atmosphere dityrityl-protected L-histidine methyl ester, **2.6**, was added dropwise to a suspension of $LiAlH_4$ in dry THF. The reaction mixture was purified using a modification to a protocol developed by Guichard *et al.*[191] in which the reaction was quenched with a saturated NaOH solution, further diluted with ethyl acetate (EtOAc) and filtered to remove the insoluble lithium/aluminium salts. The filtrate was dried and purified *via* flash column chromatography to give pure **2.8** in 78%

yield. The product **2.8** was characterised using ^{1}H and ^{13}C NMR spectroscopy, infrared spectroscopy and ESI mass spectrometry. The formation of **2.8** was supported by the ^{1}H NMR spectroscopy, as the singlet resonance with relative integration three at 3.04 ppm present in the starting material spectrum which corresponds to the methyl ester, is no longer present in the ^{1}H NMR spectrum of the product. Furthermore, the appearance of two new diastereotopic protons of relative integration one at 3.47 and 3.00 ppm, with J coupling values of 3, 11 Hz and 6, 11 Hz respectively which correspond to the newly formed methylene group, also supports the formation of **2.8**. The ^{13}C NMR also supports successful reduction with the loss of the characteristic resonance of the carbonyl carbon at 175 ppm after purification. In addition to NMR evidence the ESI-MS analysis gave a molecular ion peak $[M+H]^{+}$ for **2.8** at *m/z* 626.3161, which is consistent with a compound of formula $C_{44}H_{40}N_3O$, the expected molecular formula of **2.8**.

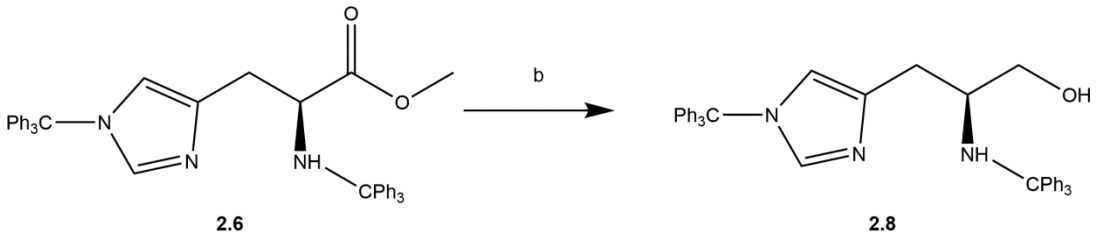

*Figure 66. Formation of the dityrityl protected histidinol ,**2.8,** from **2.6**. (b) N_2 atm., dry THF, 5 eqv $LiAlH_4$*

Initially, 2-(2-chloroethyl)pyridine (**2.9**) was selected as the electrophile for the Williamson ether synthesis due to its commercial availability and relative low cost (£10 per gram).[192] However, this reagent was found to be unstable during storage as, under an N_2 atmosphere the reagent formed a dark brown residue which when analysed by NMR the peaks corresponding to **2.9** had been lost and replaced by an uninterpretable spectrum therefore an alternative reagent was identified. Literature indicated that 2-(2-bromoethyl)pyridine (**2.15**) could be a suitable alternative as it had been previously used in an ether synthesis within the literature, shown in Figure 67.[193] Due to the high cost of **2.15** (£500 per gram)[194] this compound was synthesised in-house.

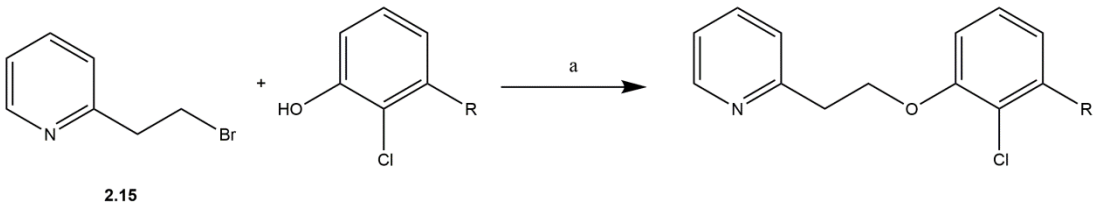

Figure 67. Example of ether synthesis carried out by Scola et al.[193](a) HBr, Cs_2CO_3, acetone. Δ

A number of methods to synthesise 2-(2-hydroxyethyl)pyridine **2.15** are reported in the literature, shown in Figure 68.[195,196] The first of these methodologies is an Appel reaction in which carbon tetrabromide (CBr_4) and PPh_3 are used to form the brominated product. [197] The reaction occurs as follows: the triphenylphosphine attacks the CBr_4 to form CBr_3^- and $BrPPh_3^+$. The CBr_3^- can then deprotonate the alcohol to form the corresponding alkoxide. The alkoxide in turn attacks the $BrPPh_3^+$ to form a phosphonium ion with loss of Br^-, the phosphonium ion can then undergo tautomerisation to form the corresponding oxonium ion. The Br^-attacks the oxonium ion forming the brominated product with the loss of triphenylphosphine oxide ($OPPh_3$), shown in Figure 69. The second of these methodologies is direct bromination, in which HBr is used to form the conjugate acid of the alcohol, R-OH_2^+, which is a good leaving group, followed by nucleophilic attack of the Br to form the brominated product.

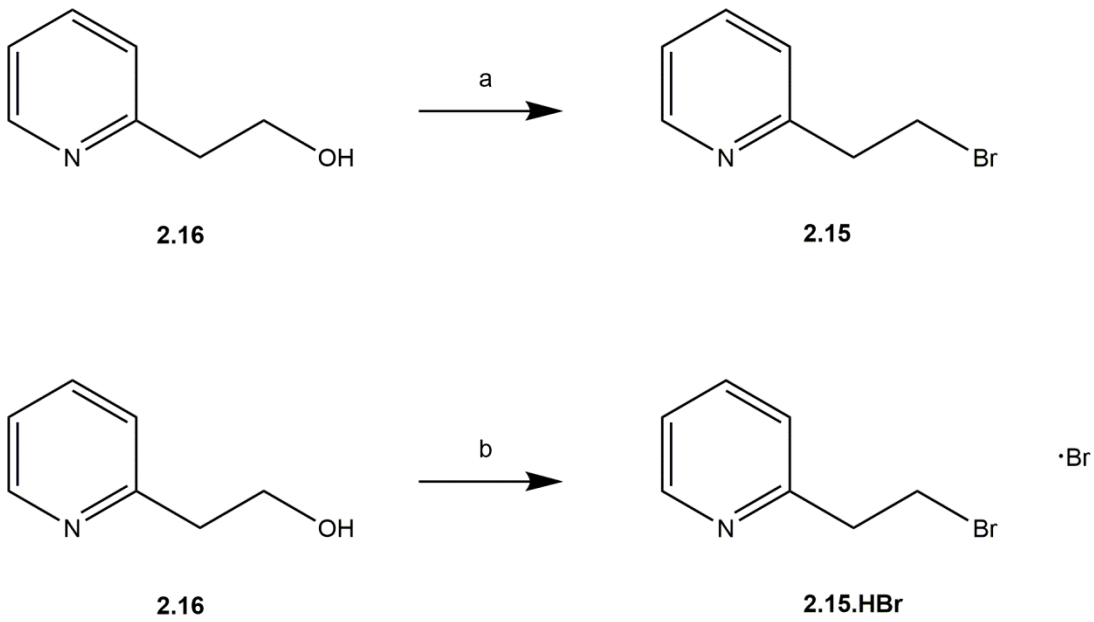

*Figure 68. Synthetic procedures used to produce **2.15**. A. An Appel reaction developed by Asai et al.[195]. B. A direct substitution method developed by Hejchman et al..[196] (a) CBr_4, PPh_3, THF, N_2 atm., 0 °C (b) 48% HBr in H_2O.*

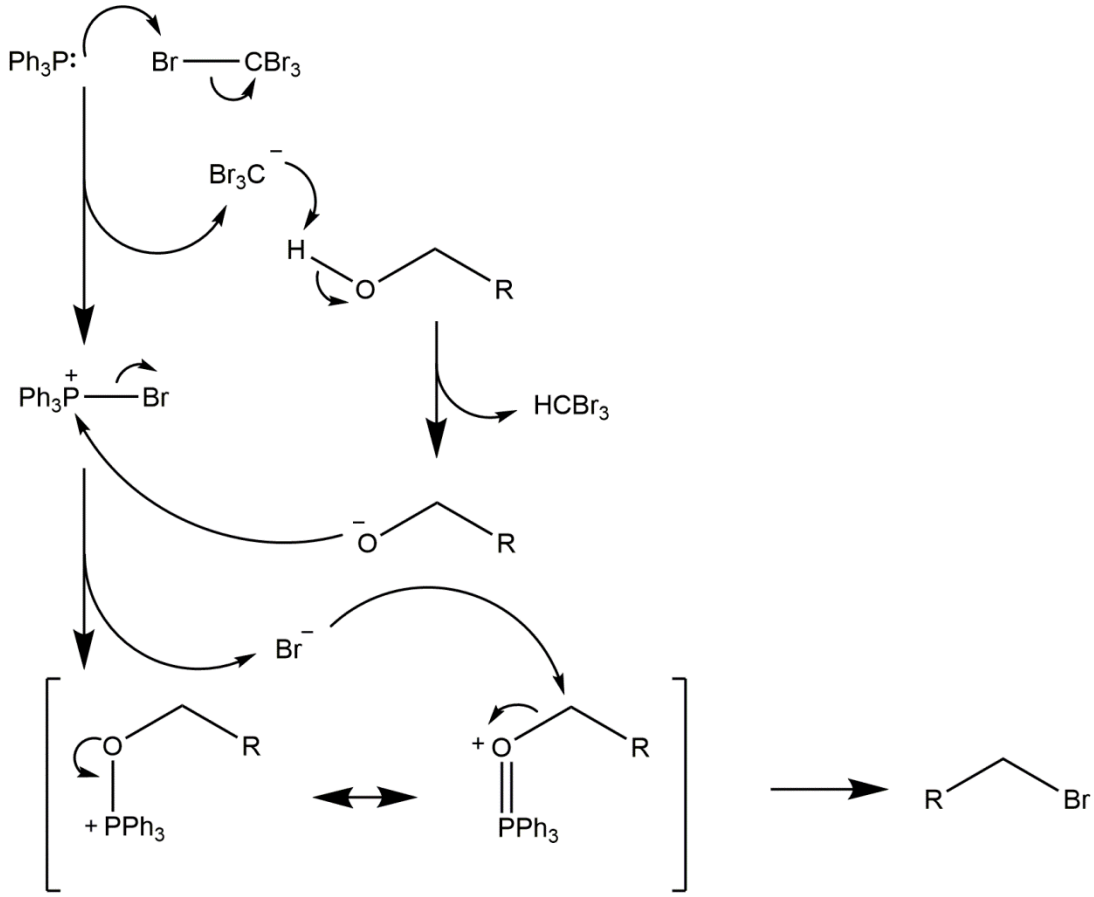

Figure 69. The general reaction mechanism of an Appel Reaction

The formation of **2.15** was carried out using a modified procedure developed by Asai *et al.*[195], shown in Figure 68. Under a N_2 atmosphere, PPh_3 and CBr_4 were stirred in DCM for 30 minutes to form $BrPPh_3^+$ and CBr_3^-. To the reaction mixture 2-(2-hydroxyethyl)pyridine **2.15** was added dropwise at 0 °C. The reaction was allowed to warm to room temperature and stirred for an additional 12 hours. The reaction mixture was filtered, dried and analysed by NMR spectroscopy, which, on comparison with chemical shifts of **2.15** in the literature, indicated a crude yield of 20%, from the appearance of the upfield shifted protons at 3.78 ppm from 4.05 ppm corresponding to the protons adjacent to the Br group. Attempts to purify the reaction mixture using flash column chromatography were unsuccessful. Analysis of the collected fractions by ^{1}H NMR showed that the peaks corresponding to the product in the crude of the reaction were lost and the starting material, **2.16**, had been regenerated as 95% of the starting material was recovered. This indicates that compound **2.15** is susceptible to acid-catalysed hydrolysis of the C-Br bond during the flash column chromatography step. The reaction was repeated and purification was attempted using a neutral alumina as opposed to silica as the stationary phase. However, the use of alumina

did not prevent the breakdown of **2.15** with the same appearance and loss of the peak at 3.78 ppm following purification.

Therefore, the direct synthesis of **2.15·HBr** *via* addition of HBr developed by *E Hejchman et al.*[196] was explored, as this procedure uses recrystallization as the purification method rather than column chromatography thus avoiding degradation on attempted purification. Compound **2.15·HBr** was synthesised *via* the addition of HBr to a solution of 2-(2-hydroxyethyl)pyridine which was heated to reflux for 3 hours in THF. After cooling, excess HBr and solvent were removed *in vacuo* and the mixture was recrystallized from isopropanol to give **2.15·HBr** in 90% yield. The compound was characterised by ^{1}H and ^{13}C NMR spectroscopy, infrared spectroscopy and ESI mass spectrometry. The ^{1}H NMR resonances for the obtained compound matched those reported in the literature data indicating the successful synthesis of **2.15·HBr**.[198] The ESI-MS showed the presence of a molecular ion peak $[M+H]^+$ at 185.9915 *m/z* with the characteristic bromine isotopic pattern, consistent with a molecular formula of C_7H_9NBr.

Having a reliable synthesis for compound **2.15** allowed for the next step in the synthesis route to proceed. The attempted synthesis of compound **2.10** was carried out using 2-(2-bromoethyl)pyridine·HBr, **2.15·HBr**, and the dityrityl protected histidinol **2.8**, as shown in Figure 70. Under a N_2 atmosphere sodium hydride was suspended in anhydrous THF and a solution of dityrityl protected histidinol, **2.8**, in anhydrous THF was added slowly to the suspension, which was stirred for 45 minutes. 2-(2-bromoethyl)pyridine·HBr **2.15·HBr** was then added to the solution, which was stirred for a further 12 hours at room temperature. After an organic-aqueous work up of the reaction mixture there was no evidence of the formation of compound **2.10**. ^{1}H NMR analysis of the organic fraction indicated the recovery of dityrityl protected histidinol **2.7** with no presence of peaks corresponding to pyridine. ^{1}H NMR analysis of the aqueous layer gave an indication of the reason for the unsuccessful outcome: resonances appeared at 5.00 ppm with a relative integration of 2, which is characteristic of the formation of an alkene. This result indicates that under these conditions the E2 elimination, described in Figure 59B, is favoured compared to the formation of the S_N2 product, **2.10**. This reaction proceeds *via* an E2 mechanism as opposed to the E1 elimination as the E1 mechanism would have to form a primary carbocation which is energetically unfavourable.

This reaction was repeated in a range of polar aprotic solvents, DCM, MeCN and EtOAc, in an attempt to favour S_N2 reactivity over E2 reactivity. Analysis of the reaction mixtures did not provide any evidence for the formation of the desired S_N2 product. As a result of this finding other synthetic avenues were explored.

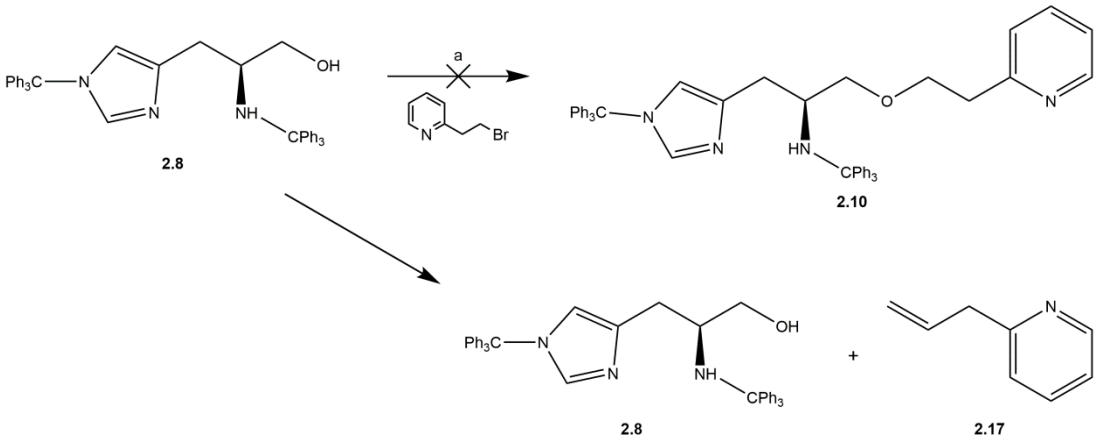

*Figure 70. Attempted synthesis of **2.9** (a) N_2 atm., Dry THF, NaH, **2.15***

The favourability of the elimination reaction could not be overcome when using **2.15** as the electrophile. As such new synthesis to form **2.10** was devised, shown in Figure 71. This synthetic route swapped the roles of the electrophile and nucleophiles for this reaction. This option was identified as a possible solution as the steric bulk provided by the trityl group has been shown to prevent the deprotonation of the C2 carbon during peptide synthesis and thus may potentially hinder the E2 elimination.[189] However, the additional steric bulk of the trityl may also hinder the approach of the nucleophile, it was hoped that S_N2 reactivity would be favoured.

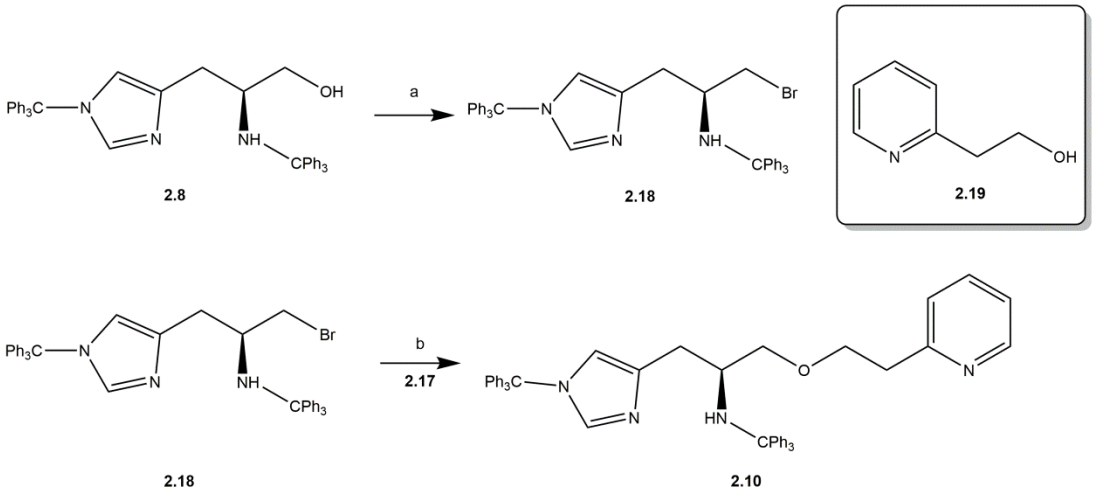

*Figure 71. Alternative synthetic route for the formation of **2.10** (a) CBr_4, PPh_3, THF (b) N_2 atm., Dry THF, NaH, **2.19***

The synthesis of compound **2.18** was carried out using Appel conditions, under a N_2 atmosphere, using the same procedure as was used to synthesise compound **2.15**. The reaction mixture was dried *in vacuo* and purified by flash column chromatography. The product was characterised by ^{1}H NMR and ESI MS. ^{1}H NMR spectroscopy supports the successful synthesis of **2.18**. Analysis of the ^{1}H NMR spectrum revealed a shift downfield of a resonance at 2.91 ppm in **2.8** to 4.55 ppm in the product. This resonance corresponds to the protons adjacent to the heteroatom, oxygen in **2.8**, the downfield shift indicates the introduction of a stronger electron withdrawing group, in this case the bromide. The two diastereotopic methylene protons appear now as a doublet at 3.16 ppm with a relative integration of two, with a J coupling of 7 Hz. The formation of **2.18** is also supported by ESI MS analysis, showing a molecular ion peak $[M+H]^+$ at 688.2334 *m/z*, containing the characteristic Br isotopic pattern which corresponds to the molecular formula $C_{44}H_{39}N_3Br$, which is expected for **2.18**.

The synthesis of compound **2.10** was carried out using 2-(2-hydroxyethyl)pyridine **2.19** and 1-bromo-3-[N-(triphenylmethyl)-1H)-H-imidazol-4-y]-(1-triphenylmethyll)propan-2-amine **2.18**, shown in Figure 72. Initial analysis of the reaction mixture by ESI-MS showed a molecular ion $[M+H]^+$ peak at 731.3793 *m/z* (chemical formula $C_{51}H_{46}N_4O$, consistent with the expected molecular formula for **2.10**), indicating the formation of the desired product, albeit as a minor peak. After purification by flash column chromatography, the fractions were characterised *via* ^{1}H NMR spectroscopy, which gave evidence for the formation of the desired product *via* the disappearance of a resonance at 4.55 ppm indicating the loss of the Br. This suggests the formation of the E2 product (Figure 72). The assignment was supported by ESI MS analysis, which showed a molecular ion peak $[M+H]^+$ at 608.3063 *m/z* which corresponds to the expected mass of **2.20**. This reaction was repeated in a range of polar aprotic solvents, DCM, MeCN and EtOAc, in an attempt to favour S_N2 reactivity. These experiments appeared to only increase the rate of formation of the E2 product as NMR analysis of the reaction mixture showed an increase in rate of loss of the resonance at 4.55 ppm corresponding to the starting material, **2.18**. However, the loss of the resonances corresponding to the starting material did not correspond to the appearance of any resonances which could be assigned to compound **2.10**..

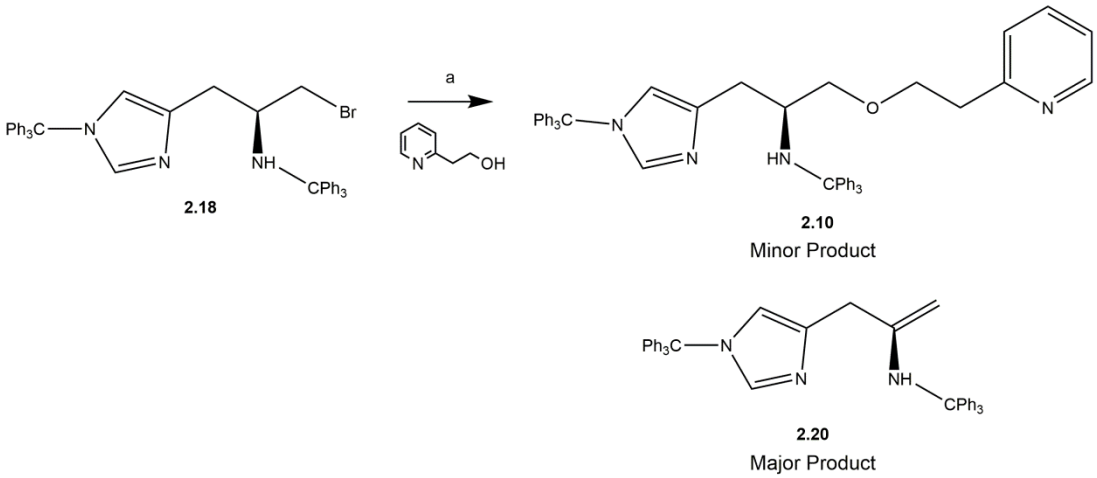

*Figure 72. Adapted synthesis of compound **2.9.** (a) N_2 atm., Dry THF, NaH, **2.18***

Due to the competing elimination reaction the maximum crude yield for synthesis of **2.10** never exceeded 5%, despite surveying various solvents and conditions. As such, the synthesis of **2.3** was not pursued any further.

2.1.3.3 Initial synthetic route targeting (2S)-1-(1H-imidazol-4-yl)-3-[(pyridin-2-yl)methoxy]propan-2-amine

The competing elimination reaction prevents the formation of **2.4** as such the synthesis of **2.3** was examined as the shorter chain length present in chloromethylpyridine, **2.12**, prevents the elimination reaction from occurring. This is because the deprotonation required for E2 reactivity cannot occur as there is no hydrogen present on the C2 carbon, shown in Figure 73. Thus, the desired nucleophilic substitution can occur without the problems described in the synthesis of **2.4**.

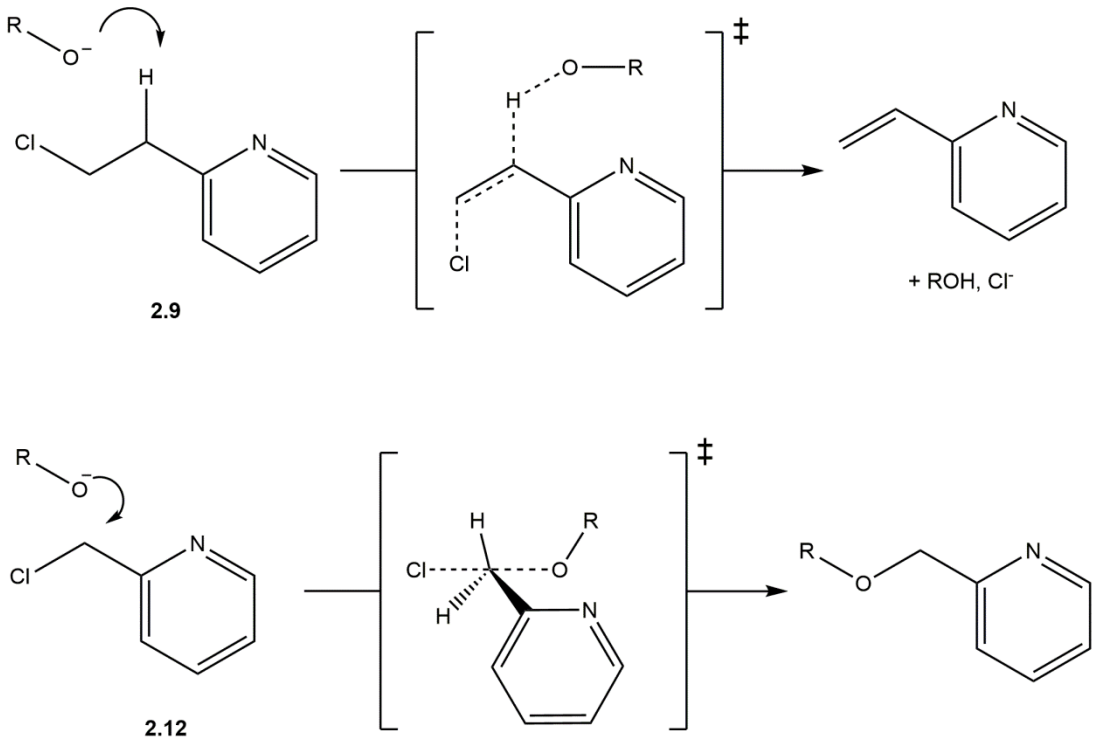

*Figure 73.Top. The transition state required to form for an E2 elimination on compound **2.9**. Bottom The transition state required for an S_N2 nucleophilic substitution on compound **2.12**.*

The synthesis of compound **2.13** was carried out using 2-chloromethylpyridine **2.12** and dityrityl protected histidinol **2.8**, as shown in Figure 74. Under an N_2 atmosphere in anhydrous THF, dityrityl protected histidinol **2.7** was stirred with NaH, for 45 minutes, 2-chloromethylpyridine was added and the reaction mixture was stirred for 24 hours. The reaction mixture was monitored by ^{1}H NMR and ESI-MS, and while the resonances corresponding to the most downfield pyridine proton did shift, the ESI-MS showed no appearance of a new molecular ion peak. Unfortunately, after an organic aqueous work-up only the starting materials **2.7** and **2.11** could be recovered, as confirmed by ^{1}H NMR spectroscopy. As such, a modification to the reaction was required to facilitate the reactivity.

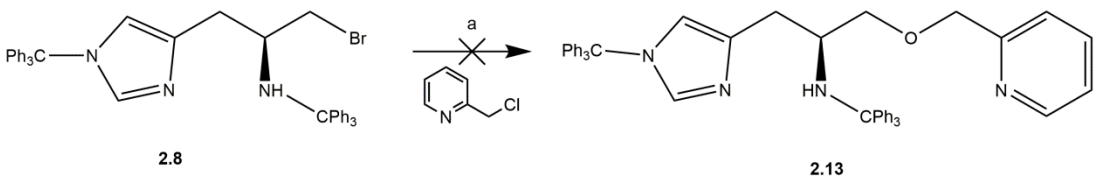

*Figure 74. Initial synthesis of compound **2.13.** (a) N_2 atm, Dry THF, NaH, **2.12***

S_N2 substitution reactions are governed by both the strength of the carbon-leaving group (C–LG) bond in the electrophile and the nucleophilicity of the nucleophile. Although the alkoxide **2.7** is likely a poor nucleophile, it is not possible to alter it in an ether synthesis. Therefore, in order to increase reactivity the strength of the C–LG bond must be reduced.

This modification can be carried out by altering the nature of the leaving group, as the C-LG bond becomes weaker with increasing the size of the halogen (Cl > Br > I). This halogen exchange can be carried out *in situ* using a Finkelstein halogen exchange reaction, shown in Figure 75.[199] This reaction will be able to proceed catalytically in conjunction with the S_N2 reaction as NaI is regenerated after each of the nucleophilic substitution, shifting the equilibrium towards the desired product due to Le Chatelier's principle.

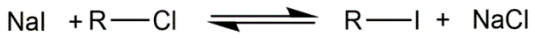

Figure 75. Finkelstein halogen exchange.[200]

The synthesis of **2.13** was repeated using the conditions described above, with the addition of 20 mol% of NaI to the reaction mixture before stirring for 8 hours. Analysis of the aromatic region of the crude reaction mixture *via* ^{1}H NMR spectroscopy indicated the appearance of two new resonances with relative integration to each other of 1H (Figure 76). These new resonances correspond to the C_4 H on the imidazole ring with a resonance of 6.38 ppm as opposed to 6.31 ppm in the starting material and the ortho hydrogen of the pyridine ring from 8.59 ppm in the starting material to 8.49 ppm. The reaction mixture was purified using flash column chromatography yielding the desired product **2.13** in a 20% yield, which is commensurate with the relative integrations of the previously discussed peaks present in the crude reaction mixture. The purified compound **2.13** was characterised by ^{1}H and ^{13}C NMR spectroscopy, 2D NMR techniques (HMBC, HSQC and DEPT NMR), infrared spectroscopy and ESI mass spectrometry. The purified ^{1}H NMR spectrum shows the loss of the peaks corresponding to the starting material and the methyl pyridine protons shift upfield from 5.07 to 4.35 ppm indicating the loss of the chloride. The ESI MS confirmed the presence of a molecular ion $[M+H]^+$ peak at 717.3588 *m/z* (chemical formula $C_{50}H_{45}N_4O$), consistent with the expected molecular formula of compound **2.13**. The reaction was optimised by increasing the reaction time to 24 hours and NaI to 25 mol% resulting in an optimised yield of 85%.

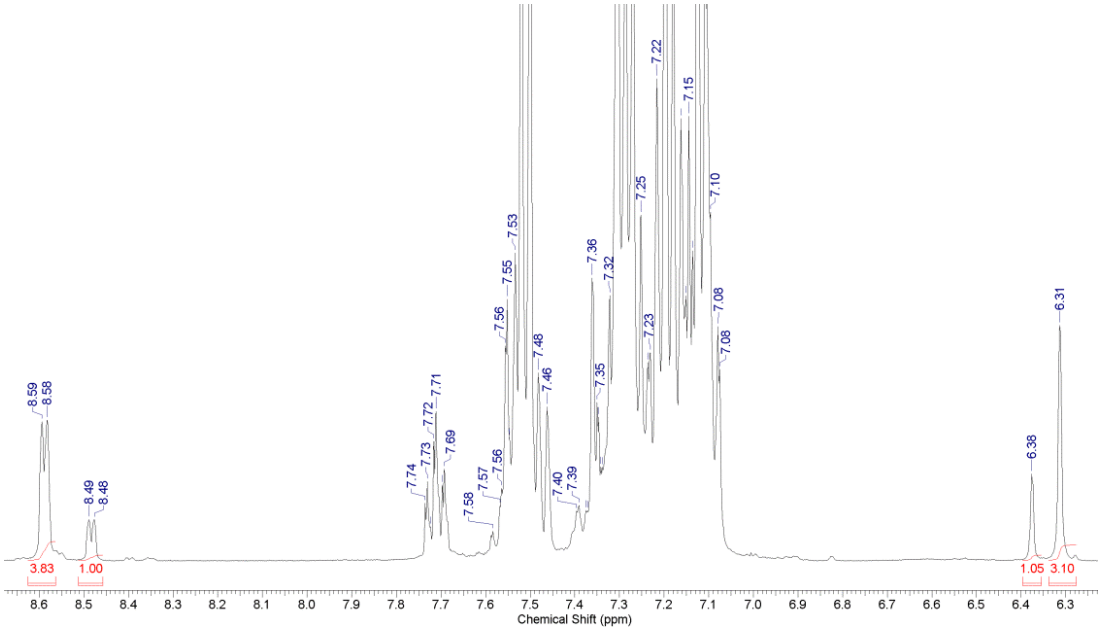

*Figure 76. Part of ^{1}H NMR spectrum (400 MHz) of the protected ligand **2.12** in $CDCl_3$, the region between 6.30 and 8.60 ppm is shown for simplicity.*

With compound **2.13** successfully synthesised, deprotection to give **2.14** was explored, shown in Figure 77. Compound **2.13** was dissolved in THF and 3 M HCl was added until the solution was 1:1 *v/v* THF: 3 M HC. The solution was heated to 70 °C for 1 hour and, on cooling, a white precipitate formed, this was identified as Ph_3CH by ^{1}H NMR spectroscopy. The solution was filtered to remove Ph_3CH and the reaction mixture was dried *in vacuo*. The crude solid was dissolved in H_2O and washed with DCM (5 X 20ml) to remove residual Ph_3CH. The aqueous phase was dried to give 2-([3-(1H-imidazol-4-yl)-2-methylpropoxy]methyl)pyridine 3HCl, compound **2.14** in 75% yield. The formation of **2.14** was supported by ^{1}H NMR spectroscopy, which showed with the disappearance of the multiplet resonances corresponding to the phenyl- protecting groups. Furthermore, ESI-MS analysis gave a molecular ion peak $[M+H]^+$ for **2.13** at 233.1394 *m/z*, consistent with a molecular formula $C_{12}H_{16}N_4O$, as expected for **2.14**.

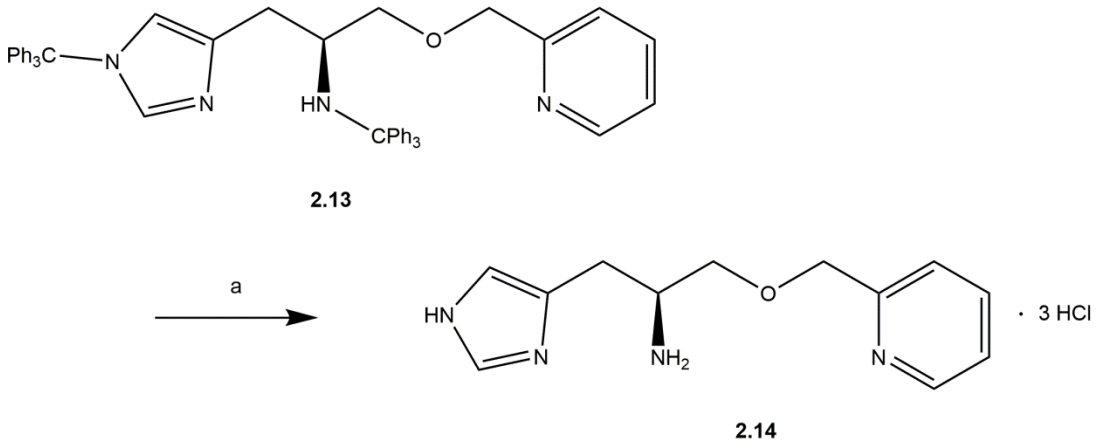

*Figure 77. Deprotection of compound **2.13** using acid hydrolysis to give the deprotected compound **2.14** (a) 3 M HCl, THF*

A side effect of the acid deprotection of **2.12** is that the nitrogen atoms present in **2.14** become protonated. As the nitrogen atoms are required to coordinate the Cu centre they must be returned to the free base state to allow for coordination to occur. The formation of the free base from the HCl salt was carried out by a DOWEX™ anion exchange resin shown in Figure 78. Compound **2.14** was passed down the DOWEX™ anion exchange column and the basic fraction was recovered. On removal of the solvent *in vacuo* a pale brown solid, compound **2.3**, was obtained in an 80% yield.

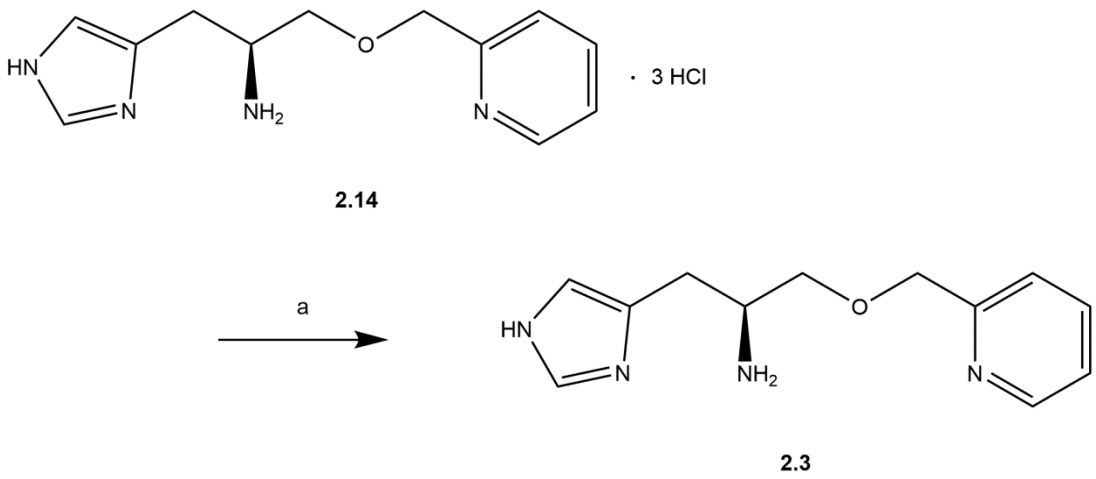

*Figure 78. Conversion of the trihydrochloride salt **2.14** to the equivalent free base compound **2.3**.(a) Dowex anion exchange resin.*

2.1.3.4 Characterisation of (2S)-1-(1H-imidazol-4-yl)-3-[(pyridin-2-yl)methoxy]propan-2-amine, **2.3**

The characterisation of the final product, compound **2.3**, shown in Figure 79, is presented herein. The NMR assignments of **2.3** were carried out using primarily 1D and 2D NMR techniques coupled with mass spectrometry, with specific examples used throughout the chapter to illustrate compound formation. Full characterisation data for all compounds are detailed in the experimental chapter.

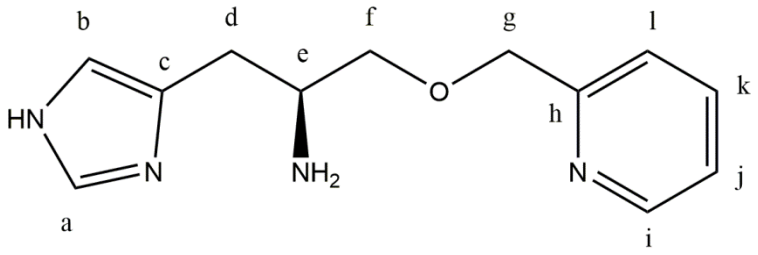

*Figure 79. (2S)-1-(1H-imidazol-4-yl)-3-[(pyridin-2-yl)methoxy]propan-2-amine **2.3***

The aromatic region of the ^{1}H NMR spectra contains six resonances each with a relative intensity of 1H, the expected number for compound **2.3**, shown in Figure 80. The two singlet resonances, at 8.97 and 7.65 ppm, are diagnostic of the imidazole proton environments **a** and **b** as they couple to no hydrogen atoms. These signals can be assigned on the basis that proton **a** is significantly more deshielded than proton **b** due to its positioning between the two electron withdrawing nitrogen atoms. Thus environment **a** can be assigned to the resonance at 8.97 ppm and environment **b** can be assigned to the resonance at 7.65 ppm.

The remaining four resonances in the aromatic region correspond to the pyridine protons **i-k**. These signals can be fully assigned using the *J* coupling values and 2D NMR. The two doublet resonances at 8.90 and 8.17 ppm correspond to proton environments **i** and **l** as they are only able to couple with one other proton environment, **j** and **k** respectively, thus due to the (n+1) rule result in their appearance as doublets. Environment **i** is significantly deshielded by its proximity to the nitrogen atom and thus can be assigned the 8.90 ppm resonance while **l** can be assigned to the resonance at 8.17 ppm.

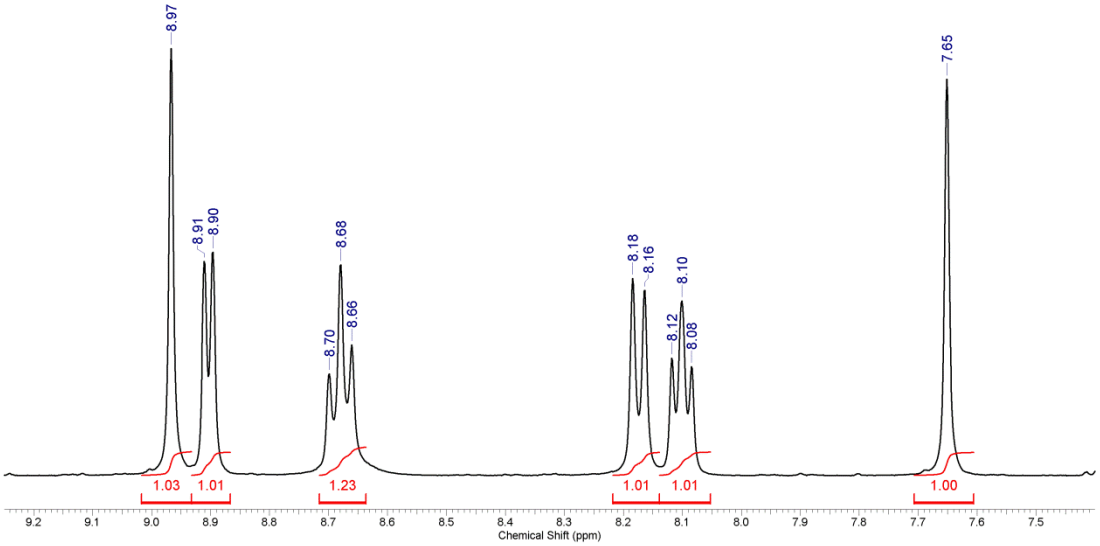

*Figure 80. Part of ^{1}H NMR spectrum of **2.2** in d_4-MeOH (400 MHz). Only the aromatic region, 7.00 – 9.00 ppm, is shown for clarity.*

The two remaining resonances appear as apparent triplets at 8.68 and 8.10 ppm. These resonances must correspond to protons **j** and **k**. However, these resonances should appear as a doublet of doublets as there are two distinct proton environments, **i/k** and **l/k**, that are coupling with each proton. This phenomenon can be explained by the presence of two protons with similar *J* coupling values, resulting in an apparent triplet, as shown in Figure 81. As such it is not possible to definitive assignment of these resonances using exclusively *J* couplings so must be derived with the use of 2D NMR techniques.

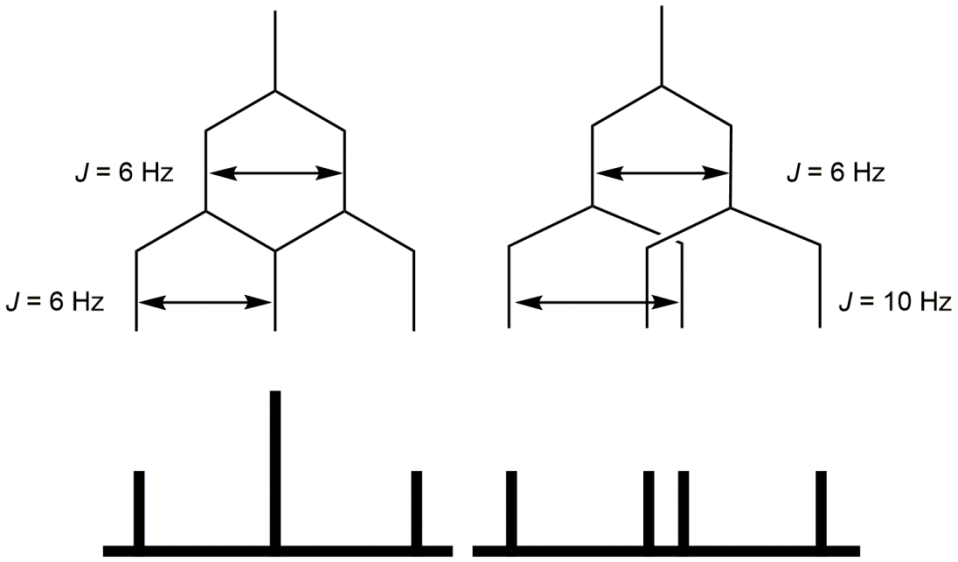

Figure 81. J couplings resulting in different coupling patters. Left. Two similar or equivalent J couplings resulting in an apparent triplet. Right. Two different J couplings resulting in a doublet of doublets.

The alkyl region of the spectrum presents five resonances, consistent with what expected for **2.3,** shown in Figure 82. This number of environments is due to the chiral centre present in the molecule, which causes the proton environments **d** and **f** to become diastereotopic and hence each proton has its own corresponding NMR signal and *J* couplings. However, as these signals have similar chemical shifts, they overlap significantly, causing the appearance of a multiplet, as shown in Figure 82. As one resonance overlaps with the H_2O signal in the MeOD solvent, 2D NMR techniques were needed to complete the full characterisation.

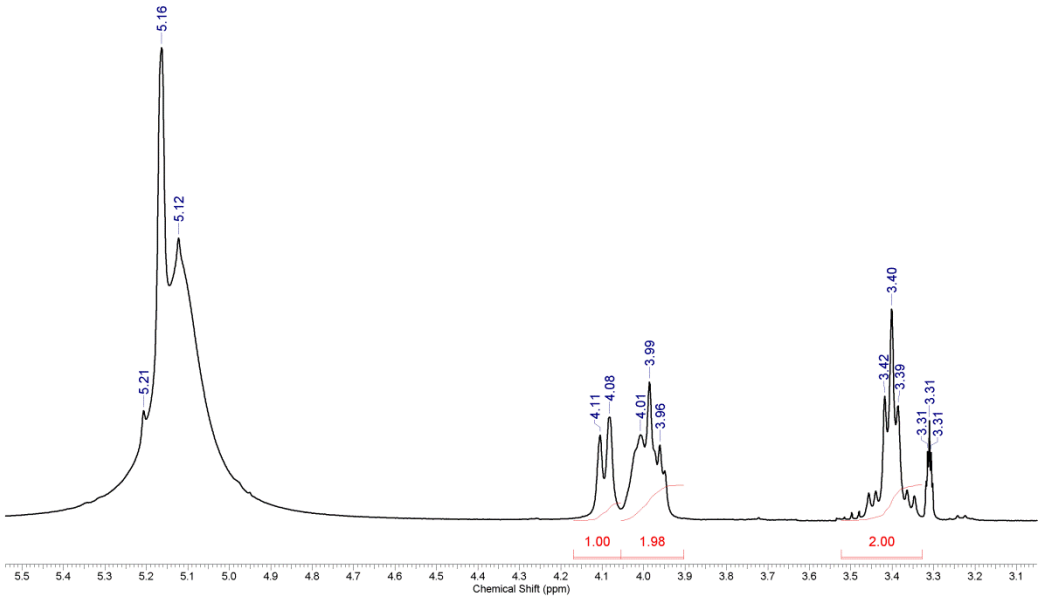

*Figure 82. ^{1}H NMR spectrum of **2.2** in d_4-MeOH. The alkyl region 3.00 – 5.50 ppm is shown for clarity.*

Using Heteronuclear Single Quantum Correlation (HSQC) and Heteronuclear Multiple Bond Correlation (HMBC) NMR it is possible to assign these protons and their respective carbon environments. The HSQC NMR spectrum allows the assignment of each proton resonance to the carbon they are directly bonded to by analysis of the cross peaks, shown in Figure 83. The two resonances corresponding to quaternary carbons **c** and **h** can also be identified at 153.38 and 129.13 ppm as they possess no cross peaks in the HSQC spectrum. The four remaining pyridyl carbon environments can also be identified at 153.38, 142.25, 127.50 and 126.75 ppm as these possess cross peaks with the pyridyl protons, at 8.48, 8.91, 8.10 and 8.18 ppm respectively. This same process can be carried out on the alkyl region of the spectrum which allows for the assignment of diastereotopic protons to the carbon they are directly bonded to. Therefore, the ^{13}C resonance at 51.35 ppm can be assigned to environment **e** as it possesses a single cross peak with the multiplet at 3.66-3.68 ppm.

Thus, proton **e** can be assigned as one of the two protons contributing to the multiplet at 3.66-3.68 ppm. A full list of cross peaks is given in Table 3.

*Table 3 List of cross-peaks found in HSQC spectrum of **2.3***

F1 Chemical shift	F2 Chemical shift
25.63	3.40
51.75	3.95-4.01
69.13	5.16
70.88	4.11, 3.95-4.01
119.5	7.65
126.75	8.18
127.38	8.10
129.13	
135.63	8.97
142.25	8.91
148.13	8.68
153.38	

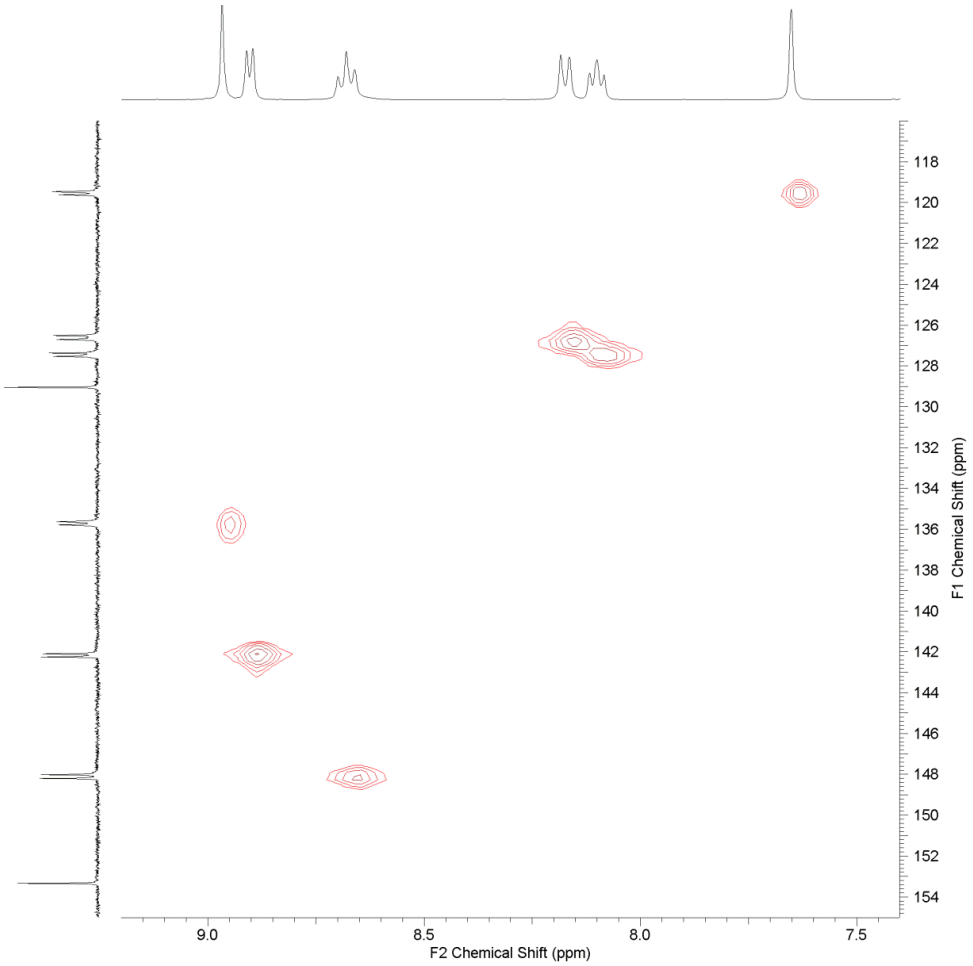

*Figure 83. HSQC NMR spectra of **2.3** in d_4-MeOH, the aromatic region only is shown for clarity. F1 ^{13}C NMR chemical shift. F2 ^{1}H NMR chemical shift.*

Analysis of the HMBC NMR spectrum allows for full assignment of the remaining resonances following the cross peaks which indicate multiple bond correlations between ^{1}H and ^{13}C. The quaternary carbon resonance at 153.38 ppm can be assigned to carbon **h** as it possesses cross peaks with the pyridine protons. This signal also possesses a cross peak with the alkyl protons at 5.18 ppm, which can therefore be assigned as proton **g**, shown in Figure 84. Therefore, the second quaternary carbon at 129.13 ppm can be assigned to environment **c**, and, from the cross peak with the proton signal at 3.30 ppm, the latter can be assigned as proton **d**.

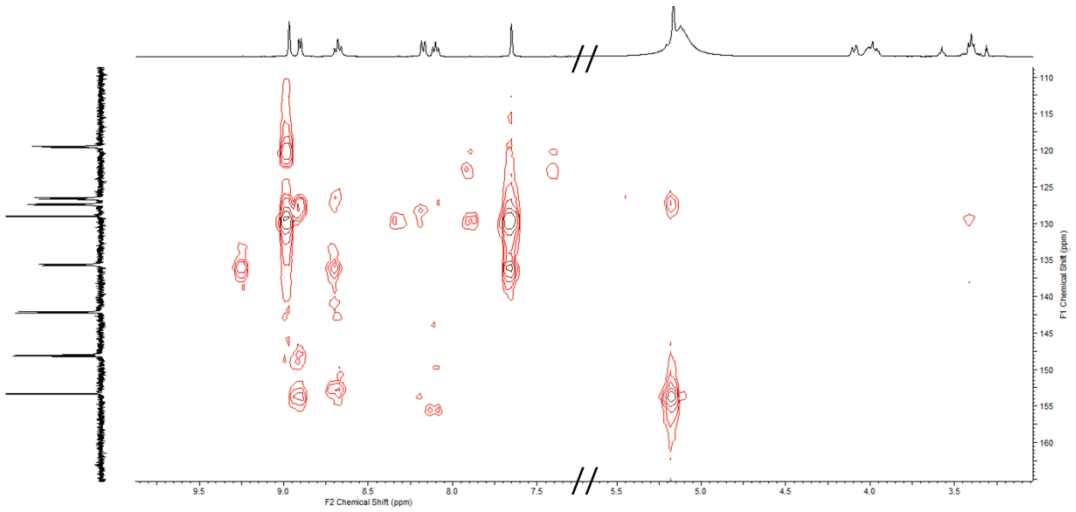

*Figure 84. HMBC NMR spectra of **2.3** in d_4-MeOH. F1 ^{13}C NMR chemical shift region between 142-162 ppm. F2 ^{1}H NMR chemical shift between 7.5–9.5 and 3.0 - 5.5 ppm.*

The remaining alkyl environment **f** can therefore be assigned to the final ^{13}C resonance at 70.88 ppm. On examination of the alkyl region of the HSQC spectra (Figure 85) the corresponding proton environments can also be assigned as the resonances at 4.11 ppm and one of the two protons in the multiplet at 3.95-4.01 ppm. As the ^{13}C resonance at 70.88 ppm features two proton cross peaks.

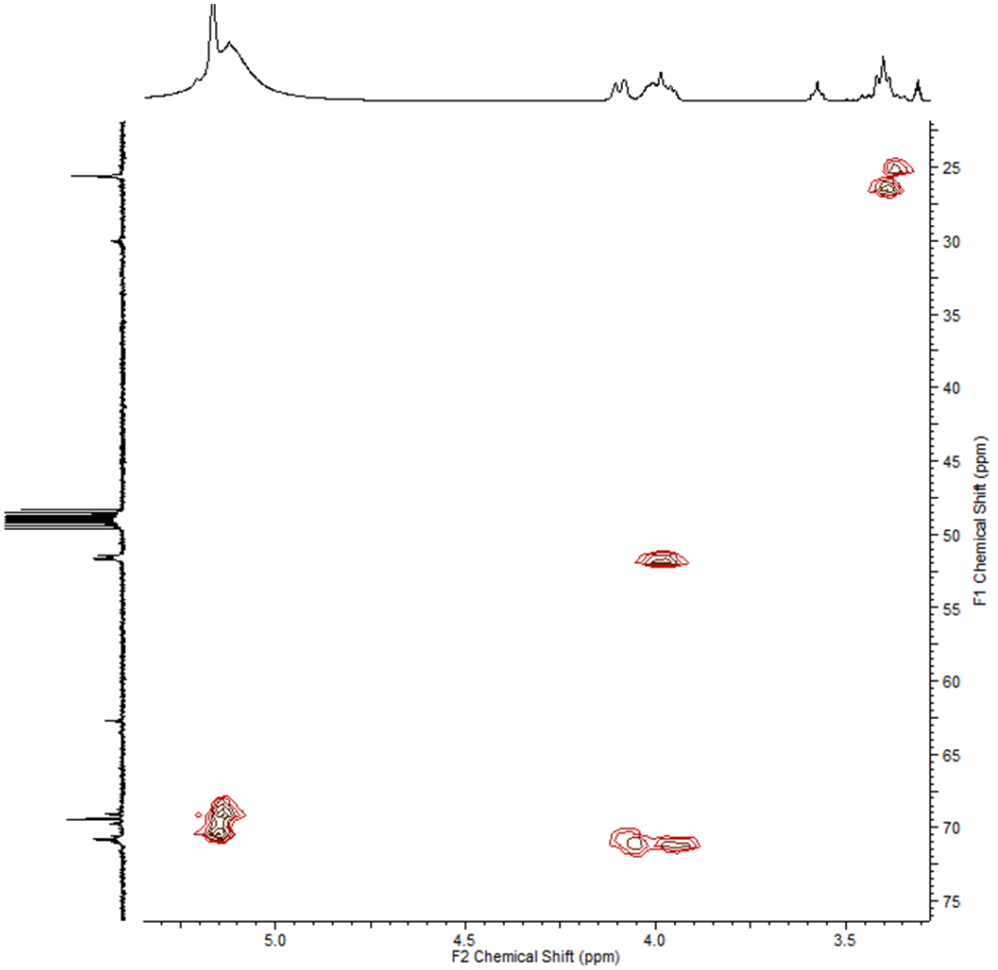

*Figure 85. HSQC NMR spectra of **2.3** in d_4-MeOH. F1 ^{13}C NMR chemical shift region between 20-75 ppm. F2 ^{1}H NMR chemical shift between 3.5 - 5.5 ppm.*

Analysis of the multiplet at 3.40 ppm is complex due to non-first order coupling. Therefore, more complex coupling effects must be occurring; as the two protons, $\mathbf{d_1}$ and $\mathbf{d_2}$ are non-equivalent, as shown in Figure 85. These will have a *J* coupling to one another *via* a $^{2}J_{HH}$ coupling and a coupling to proton **e** *via* a $^{3}J_{HH}$. As proton environment **e** is well separated from $\mathbf{d_1}$ and $\mathbf{d_2}$ the coupling scheme can be described as an ABX system for assigning coupling. In an ABX system both the magnitude and sign of *J* coupling must be considered to properly assign the couplings and the *J* couplings from X and AB must be extracted in order to perform the analysis. As the resonance **e** is masked by one of the protons from environment **f**, it is not possible to carry out a *J* coupling analysis on this peak. The apparent splitting pattern is likely caused by the superposition of the middle two AB lines. Thus while the proton environments can be unambiguously assigned it is not possible to elucidate all of the relevant *J couplings.*

Despite many attempts no crystal structure of **2.3** was obtained. The crystallisation efforts were significantly hindered by limited solubility. Elemental analysis was used to confirm the purity of the compound. The elemental analysis of **2.3** gave %C, 62.03, %H, 6.92; %N, 24.10, which is consistent with a compound with the molecular formula of $C_{12}H_{16}N_4O$ (Calculated %C, 62.05; %H, 6.94; %N, 24.12.). Furthermore, the MP of 73-74 °C also indicates high purity of compound **2.3** as it is possesses a sharp melting point. The successful synthesis of 2.3 occurred over five steps in 32 % yield. The successful synthesis of these compounds allows for the reaction with copper salts to form their respective Cu Complexes, hereafter **Cu(2.2)** and **Cu(2.3)**.

2.2 Copper complexes of **2.3**

2.2.1 Synthesis of (2S)-1-(1H-imidazol-4-yl)-3-[(pyridin-2-yl)methoxy]propan-2-amine copper complexes, **Cu(2.3)X_2**

(2S)-1-(1H-imidazol-4-yl)-3-[(pyridin-2-yl)methoxy]propan-2-amine,**2.3**, and its corresponding Tri-HCl salt **2.14** were used to synthesise the corresponding copper(II) complexes **Cu(2.3)** as shown in Figure 86. Compound **2.3** was added dropwise to a solution of **$CuCl_2$** in methanol and the reaction was stirred for 1 hour. The reaction of **2.3** with Cu(II)Cl_2 occurred immediately as the pale blue solution turned a brilliant emerald colour on addition of **2.3**. On addition of **2.14** to Cu(II)Cl_2 no colour change occurred indicating that no complexation had occurred. This is likely due to the protonation of the coordinating atoms therefore three equivalents of base were added to the solution at which point the solution immediately turned an emerald colour indicating the complex formation.

Addition of diethyl ether to both of the solutions caused the precipitation of a dark green solid, which was isolated by filtration yielding **Cu(2.3)Cl** in 80% from the reaction with **2.3** and 40% from the reaction with **2.14**. Hence, further syntheses were carried out exclusively from the free base.

This reaction was repeated with a number of Cu(II) salts to vary the counter ion and hence improve the chances of successful crystallisation of the complex. The details of this procedure are given in chapter **6**.

The elemental analysis of **Cu(2.3)$(NO_3)_2$** gave %C, 29.23, %H, 5.14; %N, 17.07, which is consistent with a compound with the molecular formula of $C_{12}H_{16}N_6O_{11}Cu$ + $2H_2O$ (Calculated %C, 29.22; %H, 5.12; %N, 17.05.)

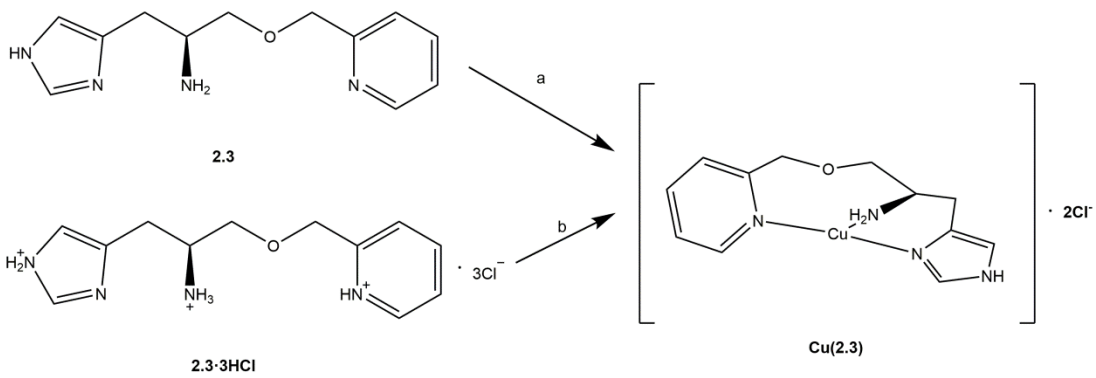

Figure 86. Synthetic scheme for the formation of Cu(II)(2.2)Cl_2 complex. (a) $CuCl_2$, MeOH. (b) $CuCl_2$ MeOH, Et_3N.

2.2.2 Characterisation of (2S)-1-(1H-imidazol-4-yl)-3-[(pyridin-2-yl)methoxy]propan-2-amine copper complexes, **Cu(2.3)X_2**

2.2.2.1 Speciation of [Cu(2.3)]X_2

In the predicted structure of compound **$[Cu(2.3)]^{2+}$ Cl_2** there are two chelate rings, one of which is a six membered ring featuring the imidazole N and the primary amine and the second consisting of an eight membered ring with the pyridine and the primary amine. Increasing the size of the chelate ring has been shown, by Ngwenya *et al.*[201] , to decrease the stability of the resulting complex.[201] As such, the ligand may be able to form the *bis*-**(2.3)** copper complex, where two equivalents of **2.3** coordinate the Cu ion as bidentate ligands *via* the imidazole Nτ and the primary amine resulting in **$[Cu(2.3)_2]^{2+}Cl_2$** as opposed to the desired tridentate coordination of **$[Cu(2.3)Cl]^+$ Cl ,**shown in Figure 87.

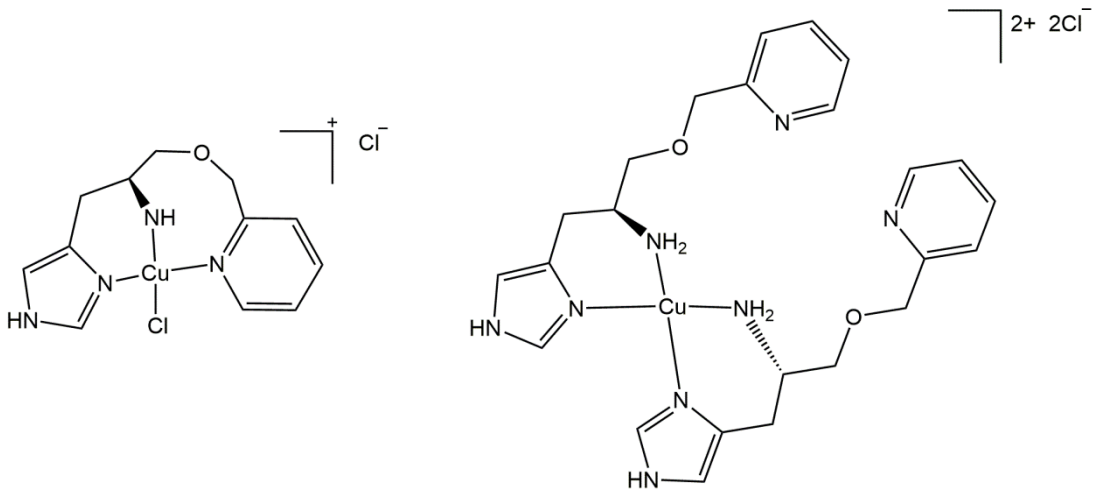

$Cu(2.3)Cl_2$ **$Cu(2.3)_2Cl_2$**

*Figure 87. The expected structures of the mono-**(2.3)** and the bis-**(2.3)** copper complexes.*

As expected for a d^9 Cu^{2+} system, the ^{1}H NMR spectrum of **$Cu(2.3)Cl_2$** was featureless due to the paramagnetism of the Cu ion. The ESI-MS showed the presence of the singly charged ion with the charge derived from the metal centre for compound **$Cu(2.3)Cl_2$** at *m/z* 295.0615, which is in agreement with the molecular formula $C_{12}H_{17}N_4OCu^+$ expected for **$Cu(2.3)^+$.** There was no presence of a peak corresponding to the doubly charged $[M]^{2+}$ ion expected to occur at *m/z* 147.53075. Furthermore, no peak was found at the predicted *m/z* for **$Cu(2.3)_2^+$** , *m/z* 527.1944 for the singularly charged ion or at 263.5972 *m/z* for the

doubly charged ion. On the basis of these data, the predicted structure from ESI-MS is shown in Figure 88.

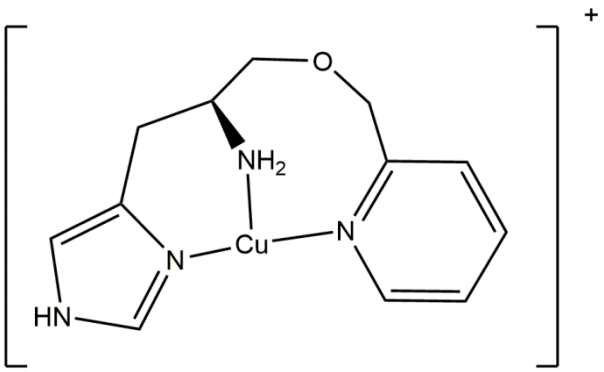

Figure 88. Proposed structure for the molecular ion peak of observed in the ESI-MS spectrum of compound ***Cu(2.3)***

The presence of the peak at *m/z* 295.0615 as opposed to the presence of a peak with an *m/z* suitable for an exogenous ligand could be explained as a result of reduction of the Cu(II) species to Cu(I) by electron capture in the electrospray ionization source. This resulting oxidation state change would result in the change of favoured geometry from the four coordinate square planar, favoured by Cu(II), to 3 coordinate T-shaped, favoured by Cu(I), and thus results in the loss of the exogenous ligand. This has previously been observed by *Hoppiliard et al.*[202] where on performing the ESI MS of Cu(II)-peptide complexes the ratios of peaks corresponding to Cu(I) or Cu(II) complexes differed depending on the nozzle voltage of the instrument.

2.2.2.2 UV/Visible studies of **Cu(2.3)X_2**

It is possible to assess the stoichiometry of the reaction between the copper and ligand using a method of continuous variation, otherwise known as a Job plot. The method keeps the total concentration of the two substituents constant but the relative proportions to one another are varied over the course of the experiment. This variation is then plotted against a varying physical property to give plots which are characteristic of the stoichiometry of the reaction, shown in Figure 89.

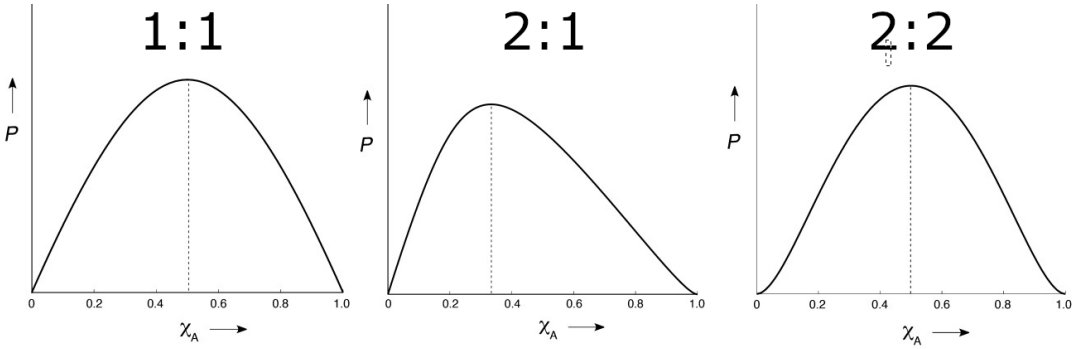

Figure 89. Example of Job plots of 1:1, 2:1 and 2:2 binding stoichiometry. Adapted from Collum et al.[203]

The UV-Vis spectrum of **Cu(2.3) Cl_2** in MeOH shows a broad band at 678 nm, which can be used as the resonance from which the Job's analysis was carried out. The molar ratios of **$CuCl_2$** and **(2.3)** were varied during the experiment and plotted against the absorbance at 678 nm, as shown in Figure 90. Before performing any analysis a background correction is required as both **$CuCl_2$** and **(2.3)** have their own corresponding molar extinction coefficients at 678 nm. Therefore, this must be removed so that any change in intensity can be attributed exclusively to the formation of a new species.

The background correction is carried out as follows,

As,

$$A_{exp} = l(\varepsilon_{CuCl2}[CuCl_2] + \varepsilon_{(\mathbf{2.3})}[\mathbf{2.3}] + \varepsilon_{Cu(2.3)}[(Cu(\mathbf{2.3}))]$$

Assuming the following holds,

$$\Delta\varepsilon = \varepsilon_{Cu(\mathbf{2.3})} - \varepsilon_{CuCl2} - \varepsilon_{(\mathbf{2.3})}$$

This equation can be rewritten as

$$\Delta A = A_{exp} - A_o = Y\Delta\varepsilon[C_o]$$

Where,

$$A_o = (\varepsilon_{CuCl2} - \varepsilon_{(\mathbf{2.3})})\,\chi + \varepsilon_{(\mathbf{2.3})})l[C_o]$$

$A_o$is the absorbance of the mixed constituents, χ is the mol fraction of the constituents, [C_O] is the prepared concentration of the stock solutions and Y is the molar fraction of the complex at equilibrium, which is then used to correct the baseline.[204]

The plot of ΔA as a function of molar ratio is shown in Figure 90, which clearly indicates the formation of **Cu(2.3)Cl_2** in a 1:1 ratio in solution as opposed to **Cu(2.3)$_2$$Cl_2$** as the peak of

the Job's plot occurs at 0.5 χ and the overall shape of the plot is characteristic of the 1:1 ratio, rather than the 2:2 ratio shown in Figure 89. The Job's plot is not completely symmetrical and thus suggests that the formation of the **$Cu(2.3)_2Cl_2$** species may occur at a higher concentration of **(2.3)**.

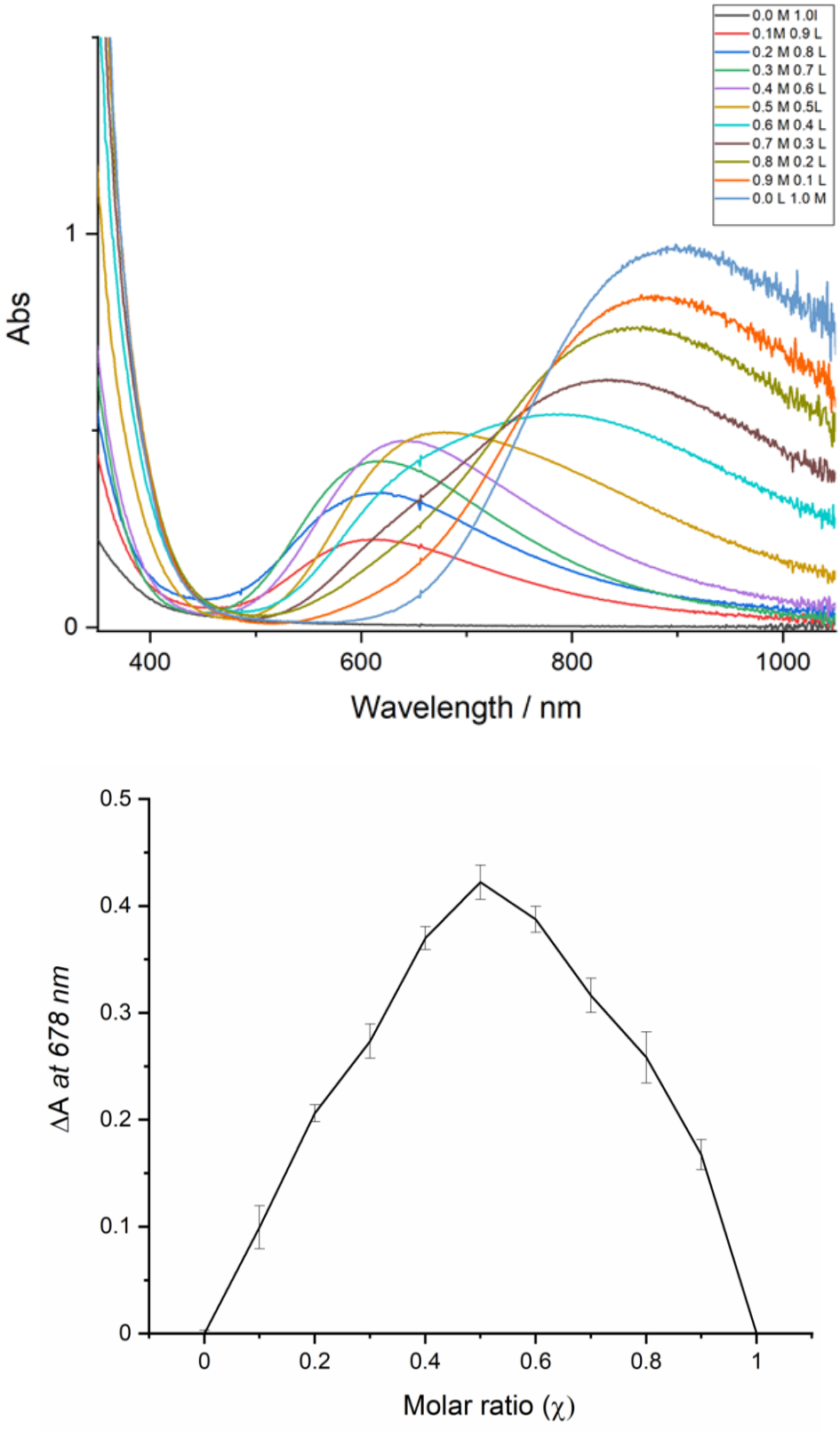

Figure 90. Top. UV-Vis spectra of ***$CuCl_2$*** *and* ***(2.3)*** *in varying molar rations. Bottom. Job's plot of* ***$Cu(2.3)Cl_2$*** *using absorbance at 678 nm indicating a 1:1 stoichiometry. Error bars show standard deviation from triplicate experiment.*

From the Job plot it is possible to gain an estimate of the equilibrium constant for the formation of **Cu(2.3)** using an initial tangent method, using the background-corrected spectra (Figure 90).[204] For a reaction of 1:1 stoichiometry the following equation is valid,

$$K_{eq} = \frac{[AB]}{([A]_i - [AB])([B]_i - [AB])}$$

Where $[A]_i$ and $[B]_i$ are the intial concentrations of A and B. The nature of the continuous variation experiment where aliquots of A and B are mixed at a constant volume allows $[A]_i$ and $[B]_i$ to be expressed as,

$$[A]_i = [C_o] \times \chi$$

$$[B]_i = [C_o] \times (1 - \chi)$$

This gives,

$$m = \frac{Y}{(\chi - Y)(1 - \chi - Y)} = K_{eq}[C_o]$$

Where,

$$Y = \frac{[AB]}{[C_o]}$$

From this it is possible to calculate an estimate of the equilibrium constant of the binding. This method uses the intersection of initial tangents at χ = 0 and χ = 1, (Y_1) and the experimental maximum of the Job's Plot (Y_{max}). Given *d* is the ratio between the top of the two tangents and the experimental data at χ =0.5,

$$d = \frac{Y_1 - Y_{max}}{Y_1} = \frac{(1 + 2m)^{\frac{1}{2}}(1 + m) - 2m - 1}{m^2} = f(logm)$$

The value of *d* can therefore be calculated from the experimental data graph and is found to be from the initial value of *d* = 0.44. By solving the equation for m the equilibrium constant K_{eq} could then be derived from the equation below:

$$m = K_{eq}[C_o]$$

$$K_{eq} = 948 \pm 350 \text{ mol}^{-1} \text{ dm}^3$$

The calculated value of K_{eq} for the formation of the **$[Cu(2.3)X]^{2+}Cl_2$** was found to be 948 ± 350 mol^{-1} dm^3.[204] This equilibrium constant is similar to that of a **$[Cu(NH_3)_3(H_2O)_3]^{2+}$** complex which has a stability constant of 955 $mol^{-1}dm^{-3}$. This indicates that the chelate

effect is not providing any additional stability to the complex. However, this study was carried out in water and it has been shown that pH has an effect on the equilibrium constant of the coordination of amines to copper.[205] The competing formation of **Cu(2.3)$_2$** may also have hindered this analysis as the Job Plot is not perfectly symmetrical, Figure 90.

2.2.2.3 Electron Paramagnetic Resonance Spectroscopy Studies of Cu(2.3)Cl_2

Initially MeOH was used as the solvent for EPR analysis as it removes potential pH effects as well as forming a more effective glass when compared to aqueous equivalents. For the **Cu(2.3)Cl_2** complex it was possible to obtain a frozen solution spectrum (150 K) at both X- and Q- band frequencies in methanol, as shown in Figure 91.The g_z region of the spectra contains three equally spaced resonances in the X-band spectrum and four in the Q-band spectrum. These resonances are caused by the hyperfine coupling of the unpaired electron to the Cu nucleus of which the common isotopes (^{63}Cu and ^{65}Cu) both have a nuclear spin of $I = {}^3/_2$ resulting in four resonances *due* to the 2nI+1 rule. The presence of three well defined peaks in the parallel *(g_z)* region of the X-band spectrum is expected as the fourth resonance overlaps with the perpendicular (g_{xy}) region in the X-band spectrum and is therefore not resolved. The absence of shoulders or additional peaks in this region is indicative of a single copper environment present within the sample.

It should be noted that all EPR spectra in the section are of frozen solution. Therefore, the spectrum is a statistically weighted average of all orientations available to the molecule, known as powder spectra. In solution this anisotropy is lost due to rapid tumbling in the sample leaving only the isotropic effects. (This is discussed in **Chapter 1 Section 1.5**).

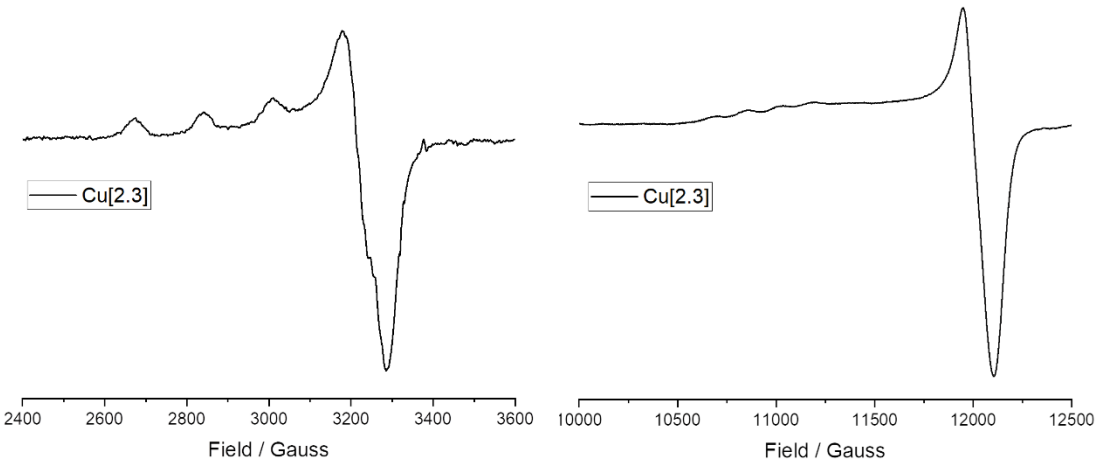

Figure 91. Left. Frozen solution continuous wave X-band EPR spectrum of Cu(2.3). Right. Continuous wave Q-band EPR spectrum of Cu(2.3). Conditions: MeOH, 10% glycerol,. X-band at 130 K, Q band at 77 K.

The g_z *and* A_z values can be measured directly from the experimental data, however, in order to obtain the full set of spin Hamiltonian parameters for **Cu(2.3)Cl_2** simulations of the experimental spectrum must be carried out. The use of in depth simulations allows information about any potential SHF coupling from coordinating atoms and precise values of g_{xy} to be obtained. All simulations were carried out using EasySpin 5.2.28[206] integrated into MatLab R2019b.[207] Spin Hamiltonian parameters were individually adjusted by hand and the fit of the simulation to the experimental data was assessed after each change. The methodology which is described here was used to simulate all subsequent spectra.

In order to obtain certainty of the spin Hamiltonian parameters of **Cu(2.3)** the Q- and X-band spectra were simulated simultaneously with a single set of spin Hamiltonian parameters. This is because in the X-band spectrum the fourth resonance of g_z overlaps with the g_x/g_y region of the spectra and g_x/g_y values are very close to each other and not easily resolved. The higher frequency and magnetic field of a Q-band spectrometer results in a higher resolution spectrum and as such separates the resonances. The higher resolution is due to the Zeeman Effect which states that the energy gap is proportional to the applied magnetic field. Therefore, at higher magnetic fields there is a larger energy gap between the ground and excited states and as such a corresponding increase in frequency is required to promote the electron to the excited state. This increase in frequency results in a larger separation between the *g* values. However, due to the increased size of the Zeeman contribution lower order contributions such as super hyperfine couplings are supressed or even lost.[208] Hence a combination of both frequencies gives the most certainty on the obtained values.

Close inspection of the first derivative spectrum X-band EPR spectrum of **Cu(2.3)Cl_2** , Figure 91, reveals weak super hyperfine coupling (SHFC) to other nuclei observed at *ca.* 2500 G (xy region of the spectrum). In order to better observe and simulate this SHFC, the second derivative spectrum of **Cu(2.3)Cl_2** was obtained *via* differentiation, shown in Figure 92. This makes the SHFC more obvious and hence easier to simulate accurately. In order to identify the nuclei responsible for SHFC simultaneous simulations of both the first and second derivative spectra can be carried out.

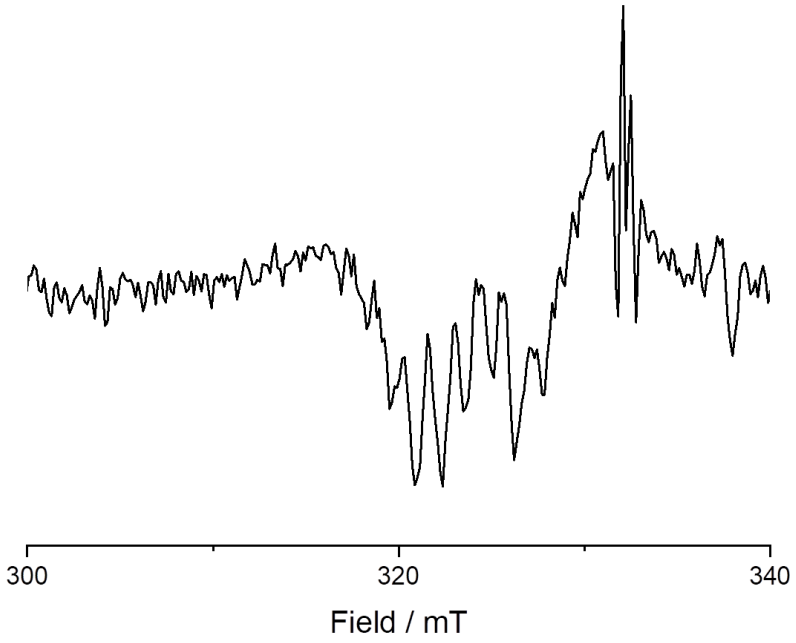

*Figure 92. Second derivative spectrum of the X-band EPR spectrum of **Cu(2.3)** between 300 and 400 mT at 130 K.*

The process of simulating these spectra began with the fitting of the g_z and A_z parameters as these are generally separated from the g_{xy} region of the spectrum. These values were unambiguously assigned using simultaneous fitting of both the X- and Q- band spectra as g_z *=2.271* and $|A_z|$= 523 MHz. As the g_{xy} region of the spectra is more complex as it contains *g* and A values and potentially SHFC this region of the spectrum was simulated using a more rigorous process which is described below.

In order to identify the origin of the SHFC, ligating nuclei were included in the simulation to assess their impact on the fit of simulated spectrum to the experimental data. The number of resolved peaks is determined by the nuclear spin of the coupled nuclei as well as the experimental line width, whilst the size of the splitting depends on the SHFC values assigned to them.

It should be noted that these spectra a fitted by hand as opposed to an automated least-squares fitting which is common for anisotropic copper spectra within the literature. [117] An automated approaching using the Easyspin function 'simplex' was attempted. However, this methodology of fitting was unable to reach a convergence point after 1000 cycles with an average cycle length of >10 minutes this methodology was not suitable for the simulation of this type of spectrum. Future investigation may be able to employ a cluster in order to reduce computing times and allow for an automated approach to be feasible.

The expected coordination sphere of **Cu(2.3)Cl_2** contains three N atoms and either a solvent or a Cl^- ion in the remaining equatorial position. Therefore, the potential nuclei responsible for the appearance of SHFC could be any combination of Cl and N atoms. As a result of this these nuclei will be the primary focus for inclusion in the simulations. The typical A_N for nitrogen atoms coupling to Cu centres has previously been identified by Electron Nuclear DOuble Resonance spectroscopy (ENDOR). The A_N value is dependent on the hybridisation of a particular N atom, for sp^2 environments this is typically between 30-45 MHz and for sp^3 environments this has been found to be between 15-25 MHz.[109, 209] The greater coupling size for sp^2 is attributed to the relative increase in *s*-orbital character in the donor orbital, boosting the Fermi contact contribution of the A_{iso} term. As such, a range of SHF coupling values (A_N = 15 – 45 MHz) were used when simulating the spectrum.

Initial simulations were carried out using a single isotropic coupling to a nitrogen atom in order to avoid overparameterization. An example of one such simulation is shown in Figure 93, using a value of A_N = 30 MHz. These simulations failed to simulate both the line shape of the overall spectrum and also featured an intense SHFC not observed in the experimental spectra. The line width, a parameter which governs broadening within the simulated spectrum, was also varied in an attempt to supress the intense super hyperfine coupling. The use of this broadening effect supressed the SHFC but did not improve the overall line shape of the simulation. Thus the simulation requires more parameters to simulate the experimental spectrum with an acceptable fit.

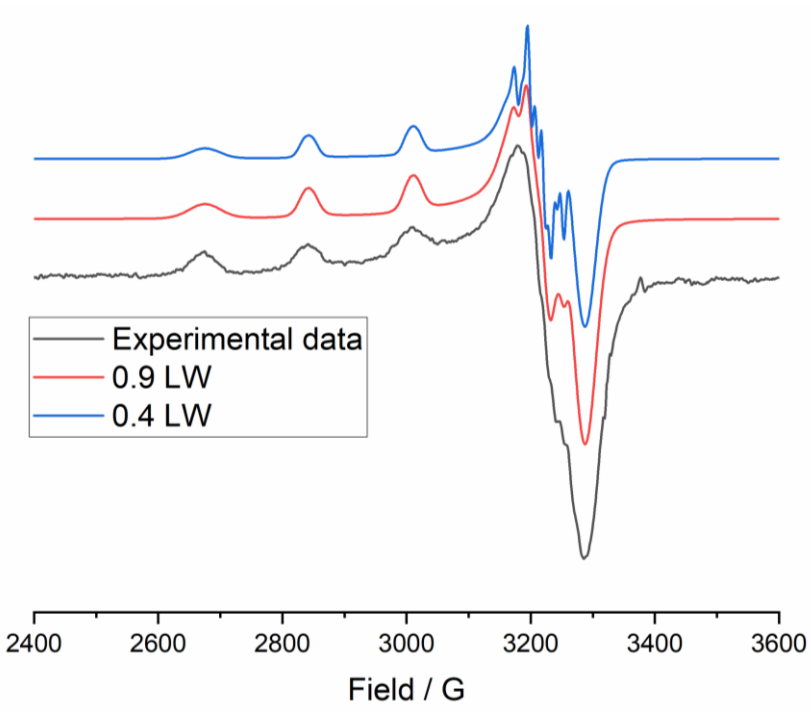

Figure 93. First derivative *X-band EPR spectrum of* ***Cu(2.3)Cl$_2$*** *and simulated spectra using a single A_N SHFC coupling. Parameters used are given in Table 4 Blue = Simulation 1 Red = Simulation 2*

The addition of more parameters improved the simulation dramatically. A simulation using a SHFC to Cl and N was able to closely match the line shape of the first derivative spectrum of **Cu(2.3)Cl$_2$** , shown in Figure 94. However, this simulation required the use of a high line width to fit the experimental spectrum. When these same parameters are used to simulate the second derivative spectrum the resultant simulation is clearly missing resonances, shown in Figure 95. This indicates that the line shape seen in the first derivative simulation is due to excessive broadening caused by the selected line width rather than the correct combination of the varying parameters. To confirm this theory a lower value for line width was selected and the spectrum was simulated using the same parameters. The resultant simulated spectrum has a large number of resonances due to super hyperfine coupling in the g_{xy} region of the spectrum which are not present in the experimental spectrum, shown in *Figure 94*. In order to probe the possible combinations of Cl and N atom coupling, the A_N values were modified between 15-45 MHz for the N atom and 40-50 MHz for the Cl atom couplings. These modifications did not result in an increased number of peaks in the second derivative spectrum or a decrease in the hyperfine coupling observed in the spectrum simulated with a 0.4 line width. As such other combinations of SHF coupling nuclei were explored and the line width was deliberately kept low in subsequent simulations to prevent the loss of any resolution in the simulations.

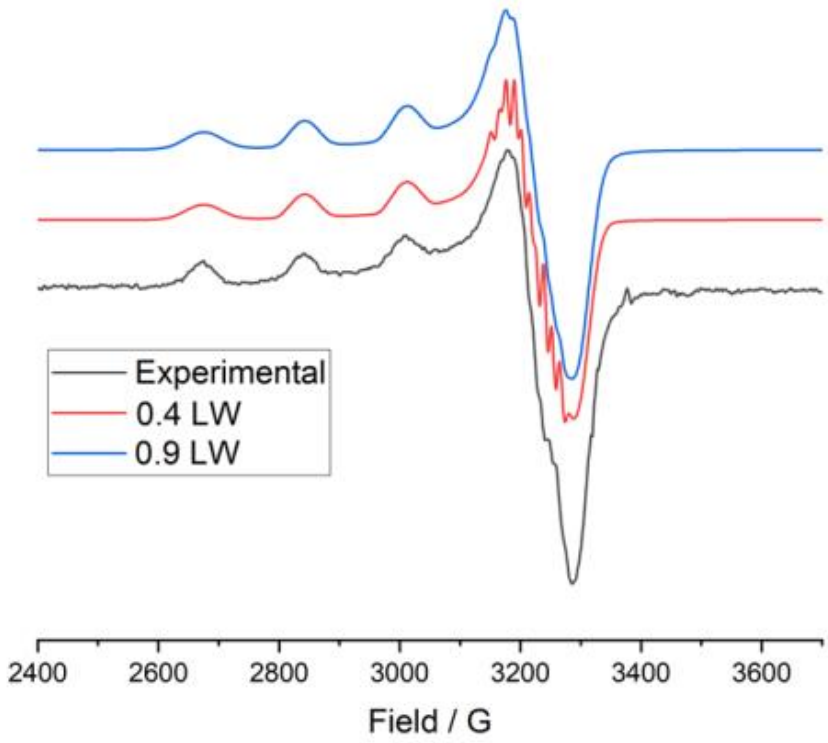

Figure 94. Top. First derivative X-band EPR spectrum of ***Cu(2.3)Cl$_2$*** *and simulated spectra with varying line widths and A_N = 30 MHz and A_{Cl} = 43 MHz. Parameters used are given in Table 4 Blue = Simulation 3 Red = Simulation 4*

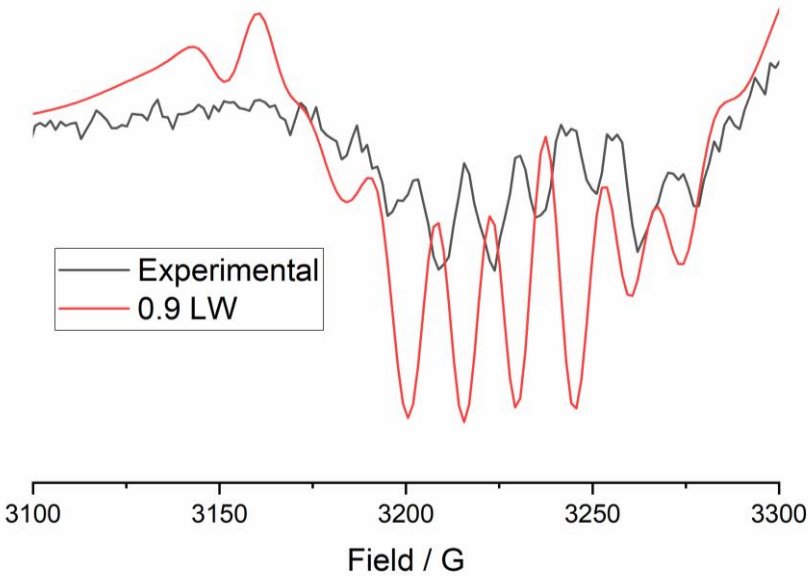

Figure 95. Second derivative *X-band EPR spectrum of* ***Cu(2.3)Cl$_2$*** *and corresponding simulation, parameters used are given in Table 4. Simulation 4.*

The alternative combination of SHFC nuclei is two nitrogen atoms. The two possible combinations are either two sp^2 nitrogen atoms or a sp^3 and sp^2 nitrogen atom based on the structure of the ligand. Therefore, these combinations were explored before adding additional coupling nuclei to the simulation. When both A_N couplings to nitrogen correspond to sp^2 environments, (A_N = 30 – 45 MHz) the resultant simulations feature intense SHF coupling. The intensity of the SHF is significantly reduced when using A_N parameters which correspond to a sp^3 and sp^2 environment (A_N = 30 – 35 MHz and 10 –20 MHz). However, these parameters result in the appearance of a large feature at ~3250 G in the simulation not present in the experimental spectrum. The full range of A_N values was tested in an attempt to improve the simulations. This did not result in the suppression of the super hyperfine or the loss of the feature at ~3250 G in either case, Figure 42 shows two examples to highlight this effect.

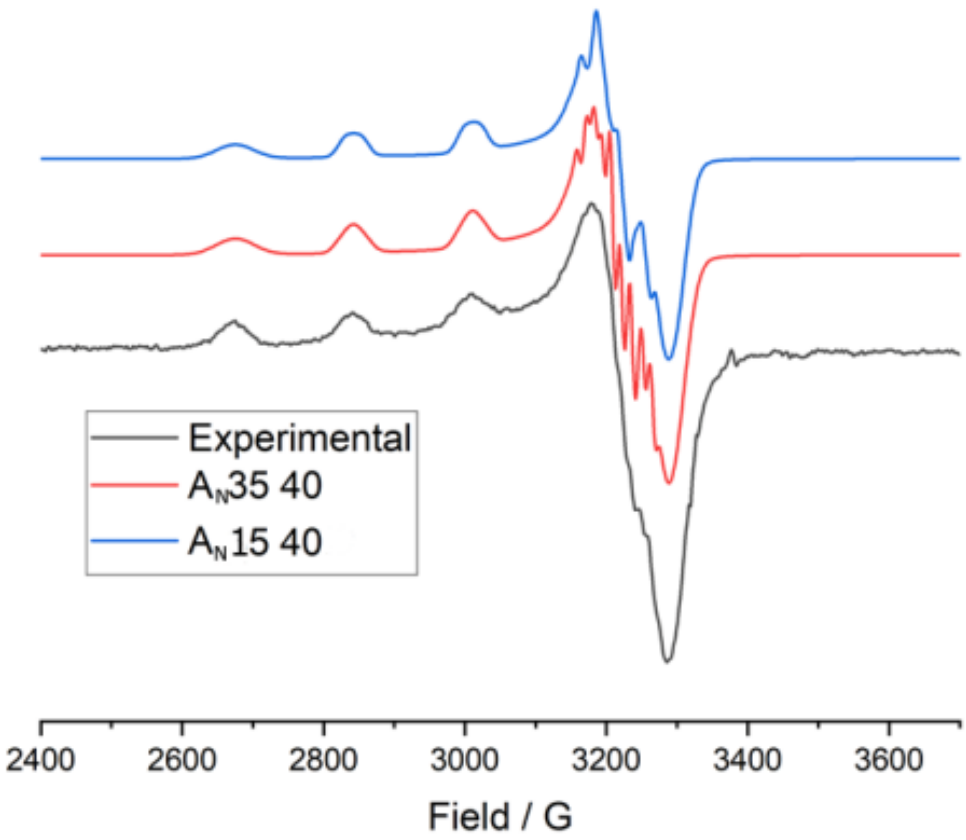

Figure 96. First derivative *X-band EPR spectrum of* ***Cu(2.3)Cl$_2$*** *and simulated spectra with varying A_N coupling. Parameters used are given in Table 4 Blue = Simulation 5 Red = Simulation 6*

The previous simulations were unable to successfully simulate the experimental spectrum. As such, an additional coupling to a third nitrogen atom, corresponding to the primary amide, was added in an effort to improve the simulation. This resulted in a drastic improvement in the line shape of the simulated spectrum and the disappearance of the feature at ~3250 G, shown in Figure 97. The simulation was then refined by simulating the first and second derivative spectra simultaneously by adjusting both the A_N of the N atoms within the A_N values for sp^3 and sp^2 nitrogen atoms. All possible combinations of A_N parameters were tested and the best fit observed was A_N = 35, 39 and 18 MHz which corresponds well to two sp^2 and one sp^3 nitrogen atoms, which would be expected for compound **2.3**. Attempting to simulate the spectrum with super hyperfine coupling to a Cl as opposed to a N atom resulted in SHF coupling appearing below 3150 G in the simulated spectrum which is not present in the experimental spectrum therefore SHFC to Cl was not included in the final simulation. In order to improve the fitting of the resonances in the second derivative spectrum small adjustments were also made to the g_x/g_y values, shown in Figure 98, after this adjustment the simulation was deemed a good fit.

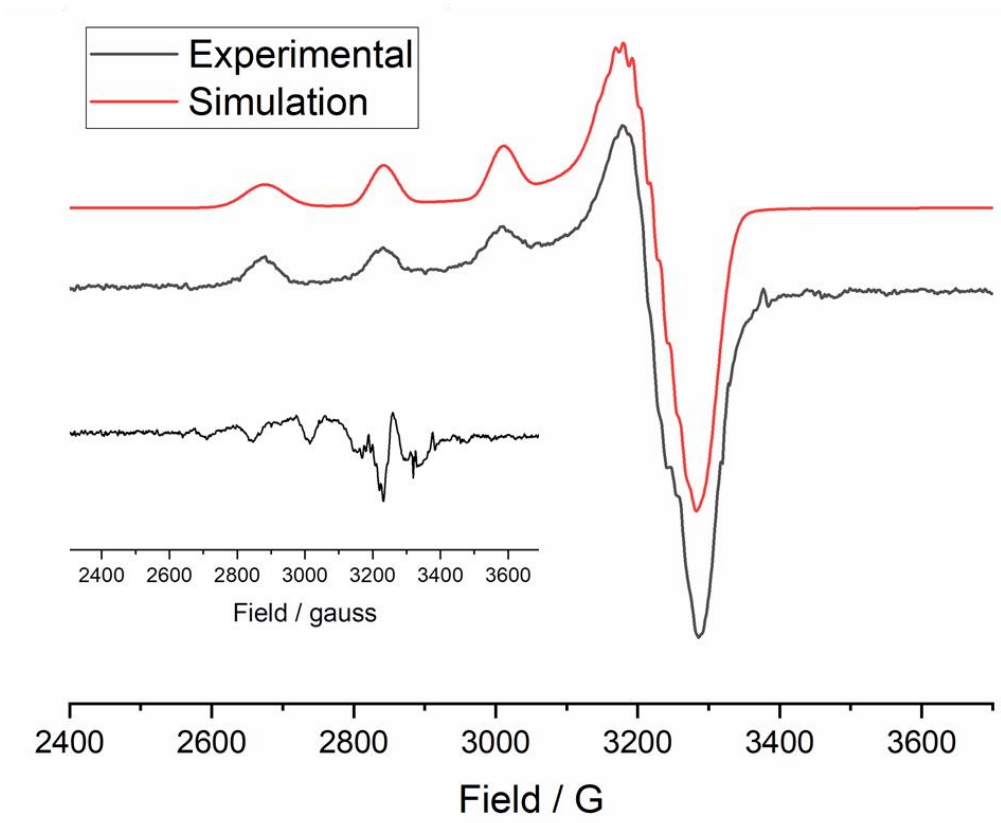

Figure 97. First derivative *X-band EPR spectrum of* ***Cu(2.3)Cl$_2$*** *and simulated spectra with three A_N couplings to Nitrogen atoms. Inset shows subtraction spectrum of experimental vs simulation. Parameters used are given in Table 4 Simulation 7*

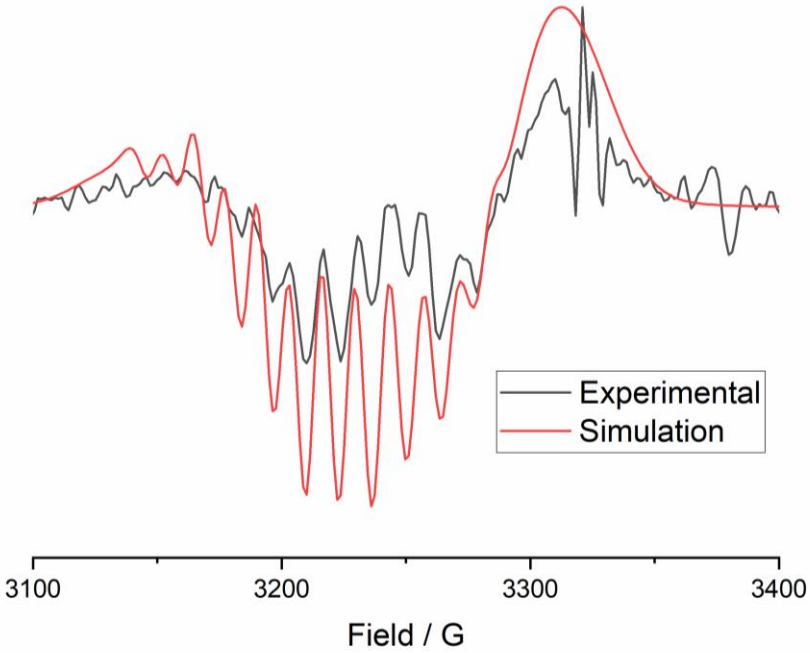

Figure 98. Second derivative *X-band EPR spectrum of* ***Cu(2.3)Cl$_2$*** *and simulated spectra with three A_N coupling to nitrogen atoms. Parameters used are given in Table 4 Simulation 7*

Table 4. The simulated Spin Hamiltonian parameters for various simulations of ***Cu(2.3) Cl$_2$*** *(MeOH, 10% glycerol).G = Gaussian L = Lorentzian*

Simulation	g			A_{Cu} / MHz			A_N	A_{Cl}	Line Width / Gauss	
	g_z	g_y	g_x	$\|A_z\|$	$\|A_y\|$	$\|A_x\|$			G	L
1	2.271	2.075	2.053	523	40	30	30	-	0.4	0.4
2	2.271	2.075	2.053	523	40	30	30		0.9	0.9
3	2.271	2.075	2.053	523	40	30	37	43	0.4	0.4
4	2.271	2.075	2.053	523	40	30	37	43	0.9	0.9
5	2.271	2.075	2.053	523	40	30	15, 45	-	0.4	0.4
6	2.271	2.075	2.053	523	40	30	35, 40	-	0.4	0.4
7	2.271	2.079	2.051	523	40	30	35,39,21	-	0.4	0.4

The spin Hamiltonian parameters obtained *via* the simulations allow for the ground state and overall coordination geometry to be determined as follows. Examination of the spin Hamiltonian parameters shown in Table 4 indicates that g_z is larger than g_{xy} and, therefore, the unpaired electron can be assigned to the $d_{x^2-y^2}$ orbital. However, the spectrum is not perfectly axial (as $g_x \neq g_y$) hence in order to confirm the nature of the ground state the asymmetry parameter, η, can be determined via the following equation,[210-211]

Where $g_z > g_y > g_x$,

$$\eta = \frac{g_y - g_x}{g_z - g_y}$$

$$\eta = \frac{2.079 - 2.051}{2.271 - 2.079} = 0.146$$

As η is closer to 0 than 1, where $0 < \eta < 1$, where 0 designates axial and 1 rhombic symmetry, the ground state can be confidently assigned to the $d_{x^2-y^2}$ orbital.[211] Hence, the coordination geometry of **Cu(2.3)Cl$_2$** can be assigned as square planar or Jahn-Teller not elongated octahedral as these have $d_{x^2-y^2}$ orbitals as the singular occupied molecular orbital (SOMO) in Cu(II), as shown in Figure 99.

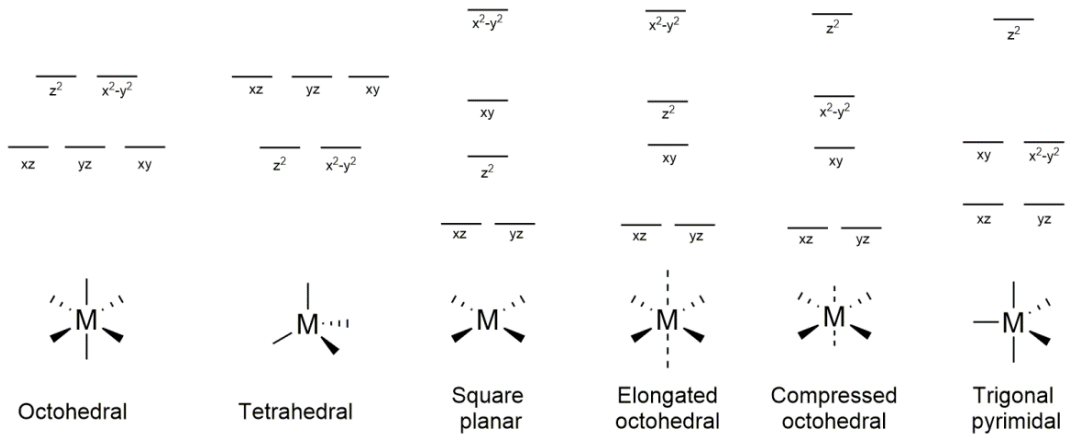

Figure 99. Orbital splitting diagram of Cu(II) in various different coordination geometries

The energy gap between these orbitals and thus the geometry of the complex can be related directly to the *g* values *via* the following equations,

$$g_z = 2.0023 \pm \frac{8\lambda_{Cu}k}{E(d_{x^2-y^2}) - E(d_{xy})}$$

$$g_y = 2.0023 \pm \frac{2\lambda_{Cu}k}{E(d_{x^2-y^2}) - E(d_{yz})}$$

$$g_x = 2.0023 \pm \frac{2\lambda_{Cu}k}{E(d_{x^2-y^2}) - E(d_{xz})}$$

where λ_{Cu} the spin orbit coupling constant (-830 cm^{-1}) for Cu(II), *k* is the orbital reduction factor and E_{ij} are the orbital energies. However, these equations are only applicable to perfectly symmetric D_{4h} systems and breakdown when used for a less symmetric system.

This becomes apparent when solving these equations for the *g* values of **Cu(2.3)Cl$_2$** which result in a large separation between the d_{xy} and d_{yz} orbitals. This indicates that the symmetry of this complex is of lower order, likely D_{2h} as $g_x \neq g_y$, therefore these equations must be modified.

Therefore, the *g* values have been redefined by Solomon *et al.*[212] as,

$$\Delta g_z \approx \frac{8\lambda_{Cu}\alpha_{GS}^2\,\gamma_{xy}^2\,a^2}{\Delta E_{xy\rightarrow x^2-y^2}}$$

$$\Delta g_y \approx \frac{2\lambda_{Cu}\alpha_{GS}^2\,\alpha_{xz}^2\,(a+\sqrt{3}b)^2}{\Delta E_{xz\rightarrow x^2-y^2}}$$

$$\Delta g_x \approx \frac{2\lambda_{cu}\alpha_{GS}^2\,\alpha_{yz}^2\,(a-\sqrt{3}b)^2}{\Delta E_{yz\rightarrow x^2-y^2}}$$

where Δg_i is the energy difference from the free electron *g* value $(g_i - 2.0023)$, *a* and *b* are the molecular orbital coefficients of the $d_{x^2-y^2}$ and d_{z^2} orbital respectively where $a^2+b^2 = 1.$, α_{GS}^2 is the covalency of the ground state and α_{yz}^2 is the covalency of the excited state. Using these equations allows for lower order symmetry to be accounted for and as such when solving these equations for **Cu(2.3)Cl$_2$** using a modified rhombicity parameter,

$$R_g = \frac{2(\Delta g_2 - \Delta g_1)}{\Delta g_2 + \Delta g_1} \approx 2\,\frac{\left(a+\sqrt{3}b\right)^2 - \left(a-\sqrt{3}b\right)^2}{\left(a+\sqrt{3}b\right)^2 + \left(a-\sqrt{3}b\right)^2}$$

to obtain the values of a and b. It is found that instead the d_{xy} and d_{yz} orbitals are close in value confirming the square planar geometry.

A comparison of the spin Hamiltonian parameters of **Cu(2.3)Cl$_2$** to ***Ls*AA9**, a well characterised LPMO, are shown in Table 5**.** The *g* values of **Cu(2.3)Cl$_2$** in MeOH are in general in good agreement with both ***Ls*AA9** in the presence and absence of substrate. However, this agreement is greatly improved when comparing to LsAA9 in the presence of substrate. This improvement could be interpreted as due to the loss of the axial water molecule present in the resting state ***Ls*AA9** which is lost on substrate binding resulting in the overall geometry of the Cu centre becoming square planar.[109] It is assumed that there are no axial ligands present in **Cu(2.3)Cl$_2$-MeOH** and as such the complex is in much closer geometric agreement to the square planar geometry of ***Ls*AA9+Substrate** as opposed to ***Ls*AA9** in the resting state. As these values are close in value to LsAA9 this is a good indication that **Cu(2.3)Cl$_2$** mimics the active site of LPMOs well. However, it must also be

able to mimic the spin Hamiltonian parameters in water which will be discussed in the next section.

*Table 5. Spin Hamiltonian parameters of **Cu(2.3)Cl$_2$** and **LsAA9** LPMO in the presence or absences of substrate*[109]

Species	*g* - values			A_{Cu} / MHz		
	g_z	g_y	g_x	A_z	A_y	A_x
Cu(2.3)Cl$_2$	2.271	2.079	2.051	523	40	30
***Ls*AA9**	2.278	2.075	2.051	465	125	50
***Ls*AA9 + Substrate**[109]	2.270	2.064	2.053	518	46	46

2.2.2.4 The effect of pH on the EPR spectra of Cu(2.3)X$_2$

The EPR spectrum of **Cu(2.3)$_2$** was markedly different in H_2O than in MeOH, shown in Figure 100. Initial observation indicates that a change to all of the primary *g* values compared to the same complex in MeOH occurred. While the *g* and A values have changed the overall spectral envelope remained constant (near-axial, $g_z > g_y \approx g_x$). This indicates that while the overall coordination geometry of the complex does not change in an aqueous environment the copper environment of **Cu(2.3)Cl$_2$** has been perturbed.

On close inspection of the g_z region of the H_2O spectra of **Cu(2.3)Cl$_2$** the resonances are revealed to be both broader and asymmetrical. This indicates that these resonances are made up of a mixture of signals corresponding to multiple Cu environments as opposed to a single well defined Cu environment as observed in MeOH. As **Cu(2.3)Cl$_2$** is now in H_2O as opposed to MeOH the most likely cause of these multiple environments is pH as the vacant coordination site is able to bind either H_2O or OH. The equilibrium of this binding would be dependent on the concentration of OH present in solution and as such the pH of the solution. Therefore, the effect of pH on the EPR spectra of **Cu(2.3)Cl$_2$** was examined *via* a pH titration.

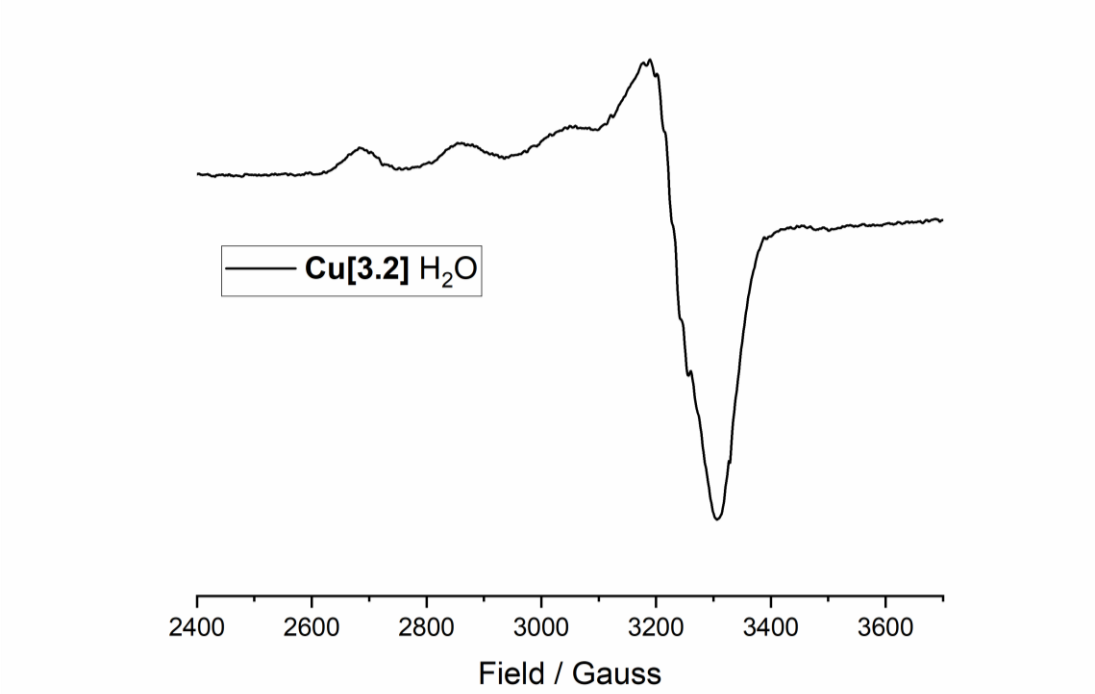

*Figure 100. Continuous wave X-Band EPR spectrum of **Cu(2.3)** in H_2O, 10% glycerol (150 K)*

The pH titration was carried out using the same sample of **Cu(2.3)Cl_2** at 0.2 mM with 10 % glycerol in a mixed buffer solution consisting of MES, CHES, HEPES and sodium phosphate to cover the full pH range. The buffers MES, CHES and HEPES are non-coordinating and as such should not affect the Cu centre; sodium phosphate could potentially coordinate the Cu centre. However, we do not observe this effect as a manually adjusted solution using exclusively HCl to alter the pH results in an identical EPR spectrum. After each spectrum was taken the sample was removed from the sample tube and the pH was manually adjusted using small amounts of 1 – 0.1 mM NaOH and HCl. All of the recorded spectra are shown in Figure 101, it should be noted that below pH 4 and above pH 10.5 there was a significant reduction in signal intensity. Above pH 10.5 this signal reduction was accompanied by significant precipitation. As the signal from an EPR experiment is phase independent this indicates that at this point a new species which is EPR silent has formed. While within the pH range of 4 – 10.5 the species are in a reversible equilibrium with one another as they are able to return to each of the observed states.

It should be noted the total spin integration of each spectrum up to and including pH 10.5 does not change between each spectrum. This indicates that the concentration of Cu present within the sample remains constant throughout. Hence, the apparent decrease in

intensity in the g_z region of the spectra occurs due to the appearance of multiple differing copper environments within the sample as opposed to a loss of Cu signal via the formation of S = 0 species.

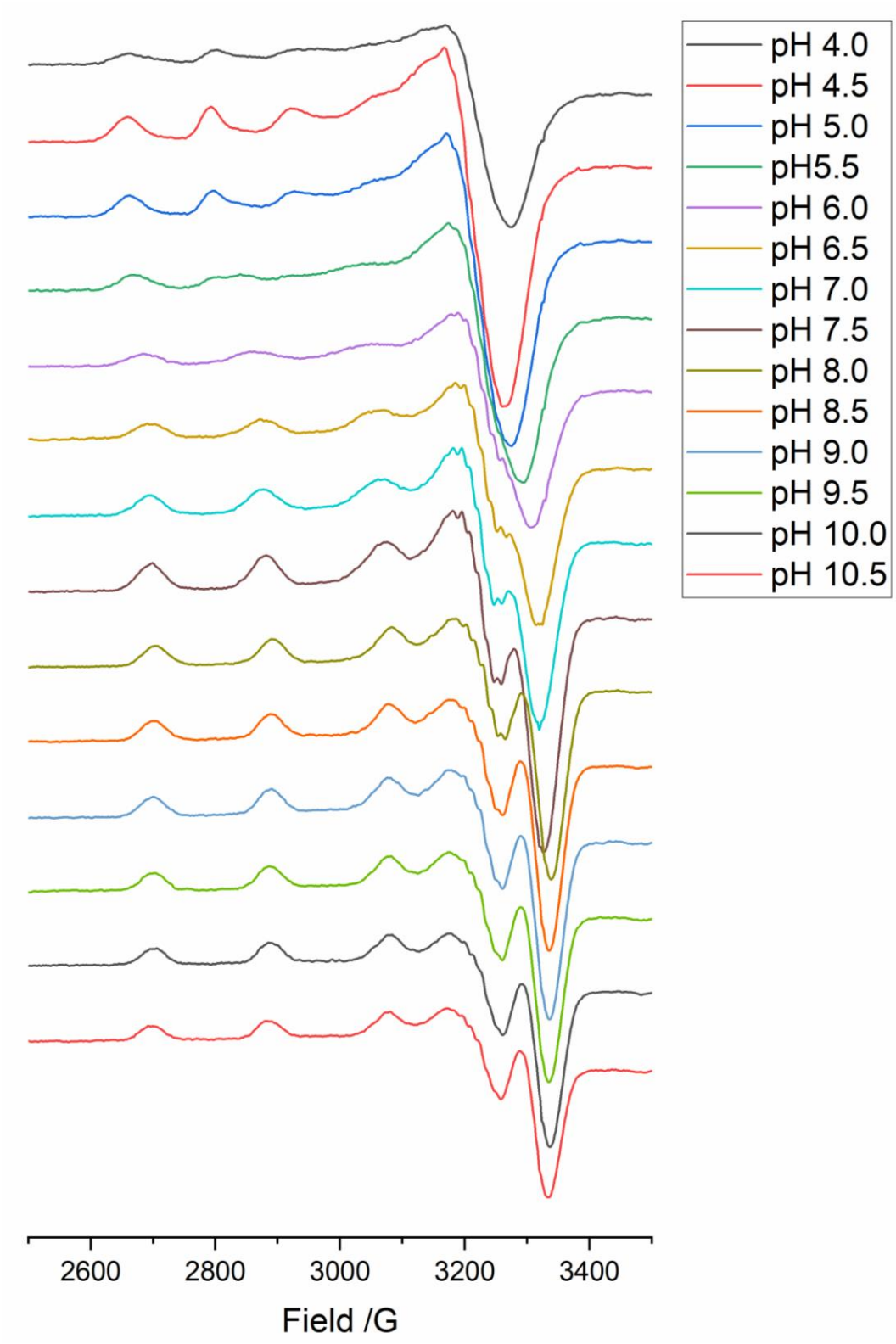

Figure 101. pH titration of 0.2 mM ***Cu(2.3)Cl$_2$*** *with 10% glycerol in a mixed buffer solution (5mM MES, 5 mM HEPES, 5 mM CHES, 5 mM sodium phosphate) .*

Above pH 9 examination of the g_z region of the spectra reveals three symmetrical resonances separated equally, this indicates that there is a single Cu environment present within the sample. The number of resonances is lower than expected *via* the 2nI+1 rule where for Cu, where I = 3/2, there would be four expected resonances. However, this fourth resonance has extended into the g_{xy} region of the spectra and therefore is not observed.

Similar analysis was carried out on all of the spectra across the pH range. From this analysis, it was observed that at pH 6 and pH 4 there were 3 symmetrical resonances with equal separation present in the g_z region of the spectra. On overlaying these spectra with one another, as shown in Figure 102, it can be clearly seen that they have differing g_z and IA_zI values. Hence, it can be concluded that across the pH range there are three Cu species present.

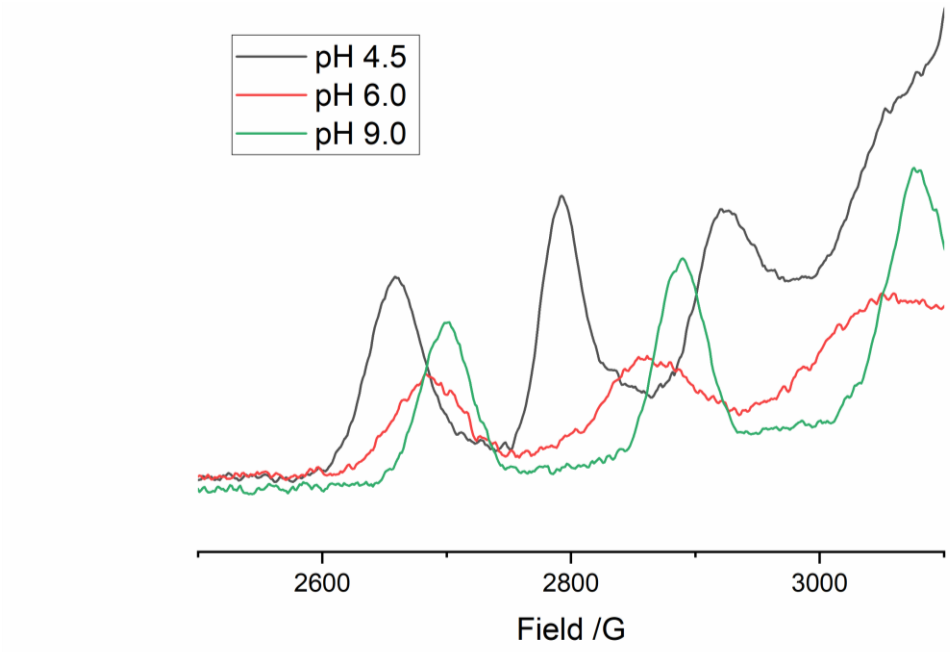

Figure 102. Overlaid X-Band Spectra of ***Cu(2.3)Cl$_2$*** *at pH 4.5, and 9 showing the g_z region between 2500 and 3100 gauss.*

This initial identification of three apparent species was assessed by the use of singular value decomposition (SVD) analysis of the data. SVD is used to determine the principal components of a data set; these principal components are the main vectors for variance in the data set and as such can be interpreted as the number of species present in this case.

SVD uses matrix algebra and eigendecomposition in order to obtain the principal component matrix. This matrix will then be decomposed into three other matrices,

$$\mathbf{A} = \mathbf{U}\boldsymbol{\Sigma}\mathbf{V}^{\mathbf{T}}$$

Where $\mathbf{A}$ is an $m \times n$ matrix, $\mathbf{U}$ is an $m \times m$ orthogonal matrix, $\boldsymbol{\Sigma}$ is an $m \times n$ rectangular diagonal matrix and $\mathbf{V}$ is an $n \times n$ orthogonal matrix. The columns of $\mathbf{U}$ and $\mathbf{V}$ are the left- and right-singular vectors of matrix $\mathbf{A}$, respectively. It should be noted that the diagonal matrix of $\boldsymbol{\Sigma}$ is hierarchically ordered.

The σ values obtained from the solutions of the $\boldsymbol{\Sigma}$ matrix, are the principle vectors of variance found across the data set. On performing this analysis on the pH titration data set the following integer σ values were obtained,

7.3244, 3.2261, 1.0984

It was concluded that all values >1 were too small to warrant a fourth component. The full list of σ values is listed in the experimental section. As there are three integer values of σ this indicates that there are primarily three species present in solution over the pH range. The presence of three interconverting species indicates that over the pH range there are two changes to the Cu environment which are dependent on the pH. The potential causes of these changes to the Cu environment will now be investigated further.

The percentage of each of these species present at any given pH can be calculated by carrying out simultaneous simulations of the g_z region of each spectrum. The weighting of each "pure" spectrum within the simulation are directly correlated to its percentage within each sample. In order to calculate the percentage of each species present in the mixed spectra the different components of the spectrum must first be defined. This was carried out by first defining the spin Hamiltonian parameters for each of the different Cu environments present in solution *via* simulations. As such the species at pH 9 and pH 6 were selected to be simulated as they both appear to only contain a single species, as shown in Figure 103 and Figure 104, respectively. There is no single species available at low pH as below pH 4 precipitation and signal loss occurs and this has begun at pH 4 as noted by the decrease in spin intensity for this sample. Hence, detailed analysis for this change in Cu environment was omitted.

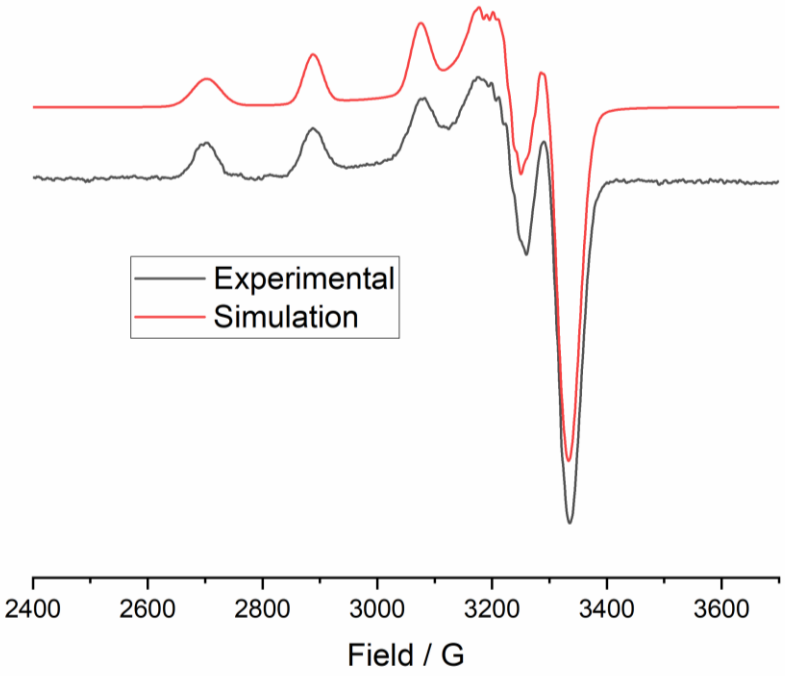

*Figure 103. Continuous wave X-band EPR spectrum of **Cu(2.3)** at pH 9 in a mixed buffer solution (5mM MES, 5 mM HEPES, 5 mM CHES, 5 mM sodium phosphate, 10% glycerol) at 150K*

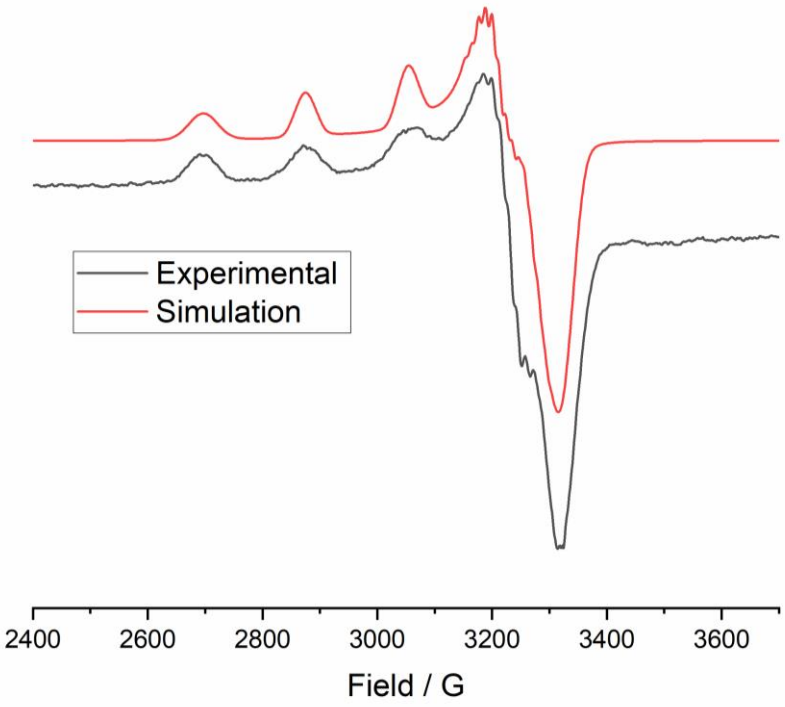

*Figure 104. Continuous wave X-band EPR spectrum of **Cu(2.3)** at pH 6 in a mixed buffer (5mM MES, 5 mM HEPES, 5 mM CHES, 5 mM sodium phosphate, 10% glycerol) at 150K*

The simulations for both of these spectra were carried out using the same general methodology as detailed in **2.2.2.2.** Minimal parameters were used as a starting point to which additional parameters were slowly added while judging the fit of the simulated spectrum to the experimental spectrum by eye, with an effort to prevent over parameterisation. The list of parameters of the full spin Hamilton parameters are given in Table 6.

The simulation of the pH 9 species was aided by the presence of a feature in the g_{xy} region at the spectrum at 3285 G. Attempts to simulate the spectrum using a large separation between g_y and g_x were unsuccessful at simulating the sharp line shape of the feature at 3285 G. Following this, strong SHFC coupling to other nuclei were used in an attempt to simulate this feature which resulted in a spectrum which had intense sharp peaks throughout as opposed to a single distinct feature. This indicates that neither of these methods are suitable for simulating the experimental spectrum. As such this feature was identified as an "overshoot" feature which is caused by an off axis turning point.[117] Off axis turning points arise when the hyperfine splitting, A value, expands faster than the decrease in *g*, during the molecular orbital transition. As such the highest resonance 'overshoots' the *g* value and as such appears as an additional resonance. This effect could have been unambiguously confirmed *via* the use of other frequencies, as a higher frequency would allow for the complete separation of the *g* values and thus the elimination of this feature in the spectrum but it was not possible to obtain a Q- band spectrum of this complex in H_2O due to absorption of the MW by the aqueous sample resulting in loss of signal. Following the assignment of this feature super hyperfine coupling to N atoms was assessed between 15 – 40 MHz and coupling to Cl atoms between 40 -50 MHz. Similar to the simulation of **Cu(2.3)** in MeOH, three nitrogen atoms with super hyperfine coupling corresponding to two sp^2 and one sp^3 nitrogen atoms were identified as the best combination of simulated parameters. The full spin Hamiltonian parameters are given in Table 6.

*Table 6. Spin Hamiltonian parameters of **Cu(2.3)** at various pHs, Line widths: Gaussian 0.3 Lorentzian = 0.3*

	g			A_{Cu} / MHz			A_N
pH	g_z	g_y	g_x	A_3	A_2	A_3	
6	2.245	2.079	2.041	30	38	550	33, 38, 18
9	2.230	2.065	2.037	55	58	570	32, 31, 18

Having obtained the spin Hamiltonian parameters for the two species in equilibrium it is now possible to estimate the percentage of each present within a mixed sample. This is carried out using simultaneous simulations where the spin Hamiltonian parameters of the two species pH 6 and pH 9 are fixed but the relative weighting spectrum within the simulation is modified. The weighting of each species is then modified until a good simulation of the experimental data is reached, which is primarily focused on the g_z region of the spectrum. The relative weighting can then be used as an estimate of the contributions for each spectrum which are shown in Table 10 and Figure 105. The fitting of these double species simulations were carried out and the fit was judged by eye. For each spectrum a range of weightings in which a good level of fit to the experimental spectrum was judged to have been reached are given as error bars.

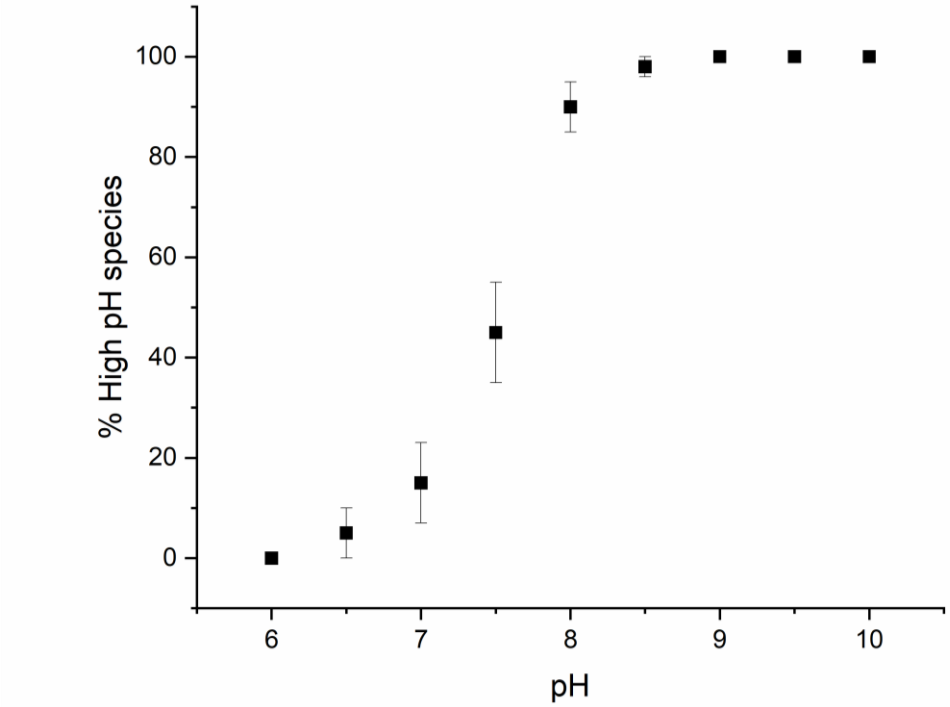

Figure 105. Speciation of ***Cu(2.3)*** *at varying pH. The precise values for these contributions are given in* Table 7

Table 7. Estimated contributions from EPR simulations from high and low species

pH	% High pH species	% low pH species
6	0	100
6.5	5	95
7	15	85
7.5	45	55
8	90	10
8.5	98	2
9	100	0
9.5	100	0
10	100	0

The estimated contribution of each species at each pH is shown in Figure 105. From these data it is possible to estimate the pH of the equivalence point, the point where there is an equal amount of the conjugate acid and conjugate base. By reading from the graph the equivalence point is approximately pH 7.6. From the equivalence point the pK_a of the process can then be estimated based on the Henderson-Hasselbach equation,[213]

$$pH = pK_a + log_{10}\left(\frac{[Base]}{[Acid]}\right)$$

as at the equivalence point concentrations of both the acid and base are equal therefore this term becomes zero, therefore,

$$pH = pK_a$$

Hence the estimated pK_a of the process is 7.6. The pK_a of this process could tentatively be assigned to the deprotonation of a coordinated H_2O molecule to hydroxide. This is in line with literature data where a $[Cu(H_2O)_6]^{2+}$ forming the $[Cu(H_2O)_5(OH^-)]^{2+}$ complex has been shown to have an experimental pK_a of 8.[214]

From the obtained spin Hamiltonian parameters it is possible to carry out some analysis of the spectrum. For both of the spectra $g_z > g_y \sim g_x$ the location of the unpaired electron can be identified as in the $d_{x^2-y^2}$ orbital which can be further confirmed by the μ value which is less than one for both complexes. This indicates that no large geometric change occurs between the two species.

On comparison of the spin Hamiltonian parameters of the two species it can be seen that the largest change occurs to the g_z and A_z values which decrease from 2.245 to 2.230 and increase from 550 to 570 MHz respectively. An in depth analysis of the A values can provide information about the ground state of the complexes. From this analysis it is possible to obtain *via* calculation the spin-orbit contribution, degree of Fermi contact and spin density on the Cu. This can then be used to understand the changes of the electronics at the Cu centre as the pH is raised and may assign a possible cause. This analysis will be carried out as follows using the parameters obtained for the EPR spectrum of **Cu(2.3)** at pH 6 as an example,

The A values of a Cu(II) with a $d_{x^2-y^2}$ can also be defined as,[212]

$$A_z = P_{\mathrm{d}}\left[-K - \frac{4}{7}\alpha_{\mathrm{GS}}^2(a^2-b^2) + \Delta g_z + \frac{\Delta g_y(3a-\sqrt{3}b)}{14(a+\sqrt{3}b)} + \frac{\Delta g_x(3a+\sqrt{3}b)}{14(a-\sqrt{3}b)}\right]$$

$$A_y = P_{\mathrm{d}}\left[-K + \frac{2}{7}\alpha_{\mathrm{GS}}^2(a^2-b^2) - \frac{4\sqrt{3}}{7}\alpha_{\mathrm{GS}}^2(ab) + \Delta g_y - \frac{\Delta g_x(3a+\sqrt{3}b)}{14(a-\sqrt{3}b)}\right]$$

$$A_x = P_{\mathrm{d}}\left[-K + \frac{2}{7}\alpha_{\mathrm{GS}}^2(a^2-b^2) + \frac{4\sqrt{3}}{7}\alpha_{\mathrm{GS}}^2(ab) + \Delta g_x - \frac{\Delta g_y(3a-\sqrt{3}b)}{14(a-\sqrt{3}b)}\right]$$

in which P_{d}=$g_e g_{Cu}\mu_e\mu_{Cu}$ the quasi-atomic parameter (1180 MHz) this equation can be split into the three terms contributing to the hyperfine value. The isotropic Fermi contact term (A^{Fermi}) represented in blue, the spin-dipolar term (A^{SD}) represented in green and the spin – orbit term (A^{SO}) represented in red.

The A^{SO} term can be calculated directly from the orbital coefficients *a* and *b* and the Δg_z from the following equations,

$$A^{SO} = \Delta g_z + \frac{\Delta g_y(3a-\sqrt{3}b)}{14(a+\sqrt{3}b)} + \frac{\Delta g_x(3a+\sqrt{3}b)}{14(a-\sqrt{3}b)}$$

where *a* and *b* are

$$R_g = \frac{2(\Delta g_2 - \Delta g_1)}{\Delta g_2 + \Delta g_1} \approx 2\frac{(a+\sqrt{3}b)^2 - (a-\sqrt{3}b)^2}{(a+\sqrt{3}b)^2 + (a-\sqrt{3}b)^2}$$

on substituting Δg_2 and Δg_1,

$$0.6586 \approx 2\frac{(a+\sqrt{3}b)^2 - (a-\sqrt{3}b)^2}{(a+\sqrt{3}b)^2 + (a-\sqrt{3}b)^2}$$

as,

$$a^2 + b^2 = 1$$

it is possible to solve simultaneously for *a* and *b,*

$$a = \pm 0.9952, b = \pm 0.0973 \; or \; a = \pm 0.2815, b = \pm \; 0.9595$$

as the ground state has been previously assigned to the d_{x2-y2} orbital $a^2 > b^2$ therefore,

$$a = \pm 0.9952, b = \pm 0.0973$$

On substituting for the A^{SO} term gives,

$$A^{SO} = P_d \left[\Delta g_z + \frac{\Delta g_y \left(3a - \sqrt{3}b\right)}{14\left(a + \sqrt{3}b\right)} + \frac{\Delta g_x \left(3a + \sqrt{3}b\right)}{14\left(a - \sqrt{3}b\right)} \right] = 317.25 \; MHz$$

The A_{iso} parameter can be linked directly to the Fermi contact parameter *via* the following equation,

$$A_{iso} = P_{\mathrm{d}} \left[-K + \frac{1}{3} (\Delta g_z + \Delta g_x + \Delta g_z) \right]$$

A_{iso} can be calculated from the experimental data by averaging the experimental A_z, A_y and A_x values. However, the signs of these coupling constants cannot be obtained experimentally using CW-EPR spectroscopy. It is known that for Cu(II) square planar A_z is always negative, while A_y and A_x can be negative or positive therefore there are four possible values for A_{iso} (-160 MHz, -206 MHz,-180 MHz and -186 MHz) all of which were used to calculate A^{Fermi}, A^{SD} and α^2_{GS} which are given in Table 8.[215] These values were calculated using the following methodology where in these example calculations A_{iso} = -160.7 MHz.

Thus by rearranging the equation for the A_{iso} parameter for the Fermi contact term, $-P_dK$, this equation becomes,

$$-P_d K = A_{iso} - P_d \left[\frac{1}{3} (\Delta g_z + \Delta g_x + \Delta g_z) \right]$$

$$-P_d K = \; -301.5 \; MHz$$

Having obtained both the A^{SO} and A^{Fermi} term it is now possible to calculate the A^{SD} term using the following equation,

$$A^{Total} = A^{SO} + A^{Fermi} + A^{SD}$$

$$A^{SD} = A^{Total} - (A^{SO} + A^{Fermi})$$

$$A^{SD} = -565\ MHz$$

From this it is possible to solve the A^{SD} part of the A_Z equation for α^2_{GS},

$$A^{SD} = -565\ MHz = P_d \left[-\frac{4}{7}\alpha^2_{GS}(a^2 - b^2)\right]$$

$$\alpha^2_{GS} = 0.86$$

Table 8. The contributions to the A values used in the determination of α^2_{GS}.

	A_{ISO}		A^{Fermi}		A^{SD}		A^{SOz}		α^2_{GS}	
	pH 6	pH 9.5	pH 6	pH 9.5	pH 6	pH 9.5	pH 6	pH 9.5	pH 6	pH 9.5
AISO (Ax +ve/Ay +ve)	-161	-152	-302	-280	-566	-584	317	294	0.86	0.89
AISO (Ax -ve/Ay-ve)	-206	-228	-347	-356	-520	-509	317	294	0.78	0.77
AISO (Ax -ve /Ay +ve)	-181	-189	-322	-317	-546	-548	317	294	0.83	0.82
AISO (Ax +ve /Ay -ve)	-186	-191	-327	-319	-540	-546	317	294	0.82	0.82

The value of α^2_{GS} can be related to the covalency ground state as follows: a completely ionic system will have a value of 1 and a completely covalent system has a value of 0.5.[212] The calculated values of α^2_{GS} for **Cu(2.3)Cl$_2$** at pH 6 are found to be between 0.75 and 0.86, depending on the signs of A_x and A_y, indicating that the system has both ionic and covalent character. On comparison of the values of α^2_{GS} of **Cu(2.3)Cl$_2$** to the literature values for a LPMO, *BaAA9,* these were found to be very similar, 0.75 - 0.83.[215] This indicates that the ligand set of **Cu(2.3)Cl$_2$** provides a similar electronic environment to that of LPMOs and is therefore a good candidate to mimic the reactivity.

The data shown in Table 8 shows that between the low and high pH species the value for α^2_{GS} does not change significantly. This indicates in all cases that there is no large change to the coordinating atoms, e.g the binding of a more covalent ligand. However, the general trends to the changes of A^{Fermi} and A^{SD} are dependent on the signs of A_{iso}. Therefore, an attempt to determine the signs of A_x/A_y must occur. Within the literature this is carried out by what is known as a density functional theory informed Ligand field theory (DELFT) approach, in which the signs are determined by a density functional theory calculation.[215] This analysis has previously been carried out on *Bl*AA*10* in the presence and absence of chitin. Assuming that as the *g* and *A* values of **Cu(2.3)Cl$_2$** are similar to *Bl*AA10 in the

presence of chitin, Table 9, the signs of A_y and A_x would be similar and as such they were assigned as A_y is negative and A_x is positive.

Table 9. Spin Hamiltonian Parameters of ***Cu(2.3)Cl$_2$*** *and BlAA9 in the presence of chitin. Line widths: Gaussian = 0. 3 Lorentzian = 0.3*

		g			A_{Cu} / MHz	
Species	g_z	g_y	g_x	A_z	A_y	A_x
Cu(2.3)Cl$_2$ pH 6	2.245	2.079	2.041	550	38	30
Cu(2.3)Cl$_2$ pH 9	2.230	2.065	2.037	570	58	50
***Bl*AA10**[215]	2.261	2.095	2.027	336	88	255
***Bl*AA10 + Chitin**[215]	2.205	2.053	2.047	620	95	85

If this assignment is correct the comparison of the values of A^{Fermi}, A^{SO} and A^{SD} for the two species shows that there are no large changes to any of the values. As this is an approximate method and there is no large separation between any of the two values this indicates that the electronic environment of the Cu is relatively unchanged on the formation of the high pH species. However, as α_{GS}^2 remains the same between both species it is possible to relate the Δg_z directly to the *d* orbital energy gaps *via,*

$$\Delta g_z \approx \frac{8\lambda_{Cu}\alpha_{GS}^2\,\gamma_{xy}^2\,a^2}{\Delta E_{xy\rightarrow x^2-y^2}}$$

as it can be assumed that $8\lambda_{Cu}\alpha_{GS}^2\,\gamma_{xy}^2\,a^2$ remains constant between the two species the decrease in Δg_z can be directly correlated to the energy gap. This correlation shows that as the *g* value increases the energy gap decreases.

As α_{GS}^2 has not changed from between the two species this indicates that the Cu ligation remains unchanged. Therefore, a change to one of the ligating atoms must occur in order to facilitate this increase in energy gap. This increase in energy gap can be caused by the following factors, a change in symmetry in the coordination geometry, a change in covalency or an electrostatic effect. The fact A^{Fermi} and α_{GS}^2 remain relatively unchanged indicates that this is not due to either an increase in covalency or change in coordination geometry and therefore this effect could be assumed to be electrostatic. As this change occurs as the pH is raised this change is likely due to a deprotonation. The resulting negative charge would then be able to provide an electrostatic effect close to the nucleus. For this deprotonation there are three potential candidates, H_2O to OH^-, NH_2 to NH^- or a

deprotonation on the imidazole. From the speciation plot it can be ascertained that the pK_a 7.6 which as previously discussed is commensurate with a H_2O to OH^- deprotonation.

This allows for the assignment of the high pH species observed for **Cu(2.3)Cl$_2$** at pH 9 is due to the formation of **[Cu(2.3)(OH)]$^+$ Cl**.

The analysis of the EPR parameters of **Cu(2.3)Cl$_2$** indicate that it is a good electronic mimic of the active site LPMOs, not only are the spin Hamiltonian parameters similar as shown in Table 5. The covalency of **Cu(2.3)Cl$_2$**, α^2_{GS}, is also similar to that of *Bl*AA10, Table 9. Furthermore, The pH titration of **Cu(2.3)Cl$_2$** indicates that an exogenous water molecule is bound to the Cu centre which upon raising the pH become deprotonated. The presence of an exogenous ligand which can be lost on the generation of Cu(I) is a necessary requirement for activity as oxidant needs to bind to the Cu centre in order become activated.

The observed pK_a and analysis of the covalency of the ground state in **Cu(2.3)** provides strong evidence that the observed change to the EPR parameters on raising the pH is due to the exchange of an exogenous ligand with hydroxide. Assuming this assignment is correct this indicates that there is an exchangeable site on the Cu complex. An exogenous ligand capable of disassociation is required for reactivity as the Cu ion must be able to form a reactive intermediate species bound to the Cu centre to facilitate catalysis. As such **Cu(2.3)Cl$_2$** is a promising ligand for reactivity testing.

2.2.2.5 Crystallographic studies of Cu(2.3)X$_n$

Numerous attempts to obtain a crystal structure of **Cu(2.3)X$_n$** using a variety of counter ions (X_2 = Cl, NO_3, PF_6, X_1 = SO_4^{2-}) were made, ultimately crystals suitable for X-ray diffraction were only obtained using SO_4^{2-} as a corner ion. Dark blue crystals suitable for X-ray diffraction were obtained from slow layer diffusion of DMF:MeOH (100:1) into diethyl ether using SO_4^{2-} as the counter ion. On solving the crystal structure it was revealed that instead of the expected a mono-ligand complex a different molecule the di-ligand Cu complex, [**Cu(2.3)$_2$(SO$_4$)**], had formed, shown in Figure 106. In which the Cu centre is coordinated by the imidazole and amide nitrogen of two molecules of **2.3** in a square planar arrangement.

Within the crystal lattice the asymmetric unit is comprised of two molecules of **Cu(2.3)$_2$**, two molecules of MeOH and two SO_4^- counter ions in a $P2_1$ space group. The primary

coordination sphere of **Cu(2.3)$_2$(SO$_4$)** consists of the imidazole rings *trans* to the primary amine of the other molecule of **(2.3)**. The geometry is distorted from square planar towards a seesaw geometry with a τ_4 value of 0.25 (**section 1.4.2)** indicating significant distortion away from square planar geometry.[154] The bond lengths and angles of the first coordination spheres of **Cu(2.3)$_2$** for both asymmetric units are shown in Table 10 and Table 11, respectively. One of the two **(2.3)** ligands appears to have a weak hydrogen bond between the primary amine and ether linkage with a distance of 2.6 Å and N-H…O angle of 103.5 , which indicates a moderate to weak hydrogen bond that is mostly electrostatic. [216]

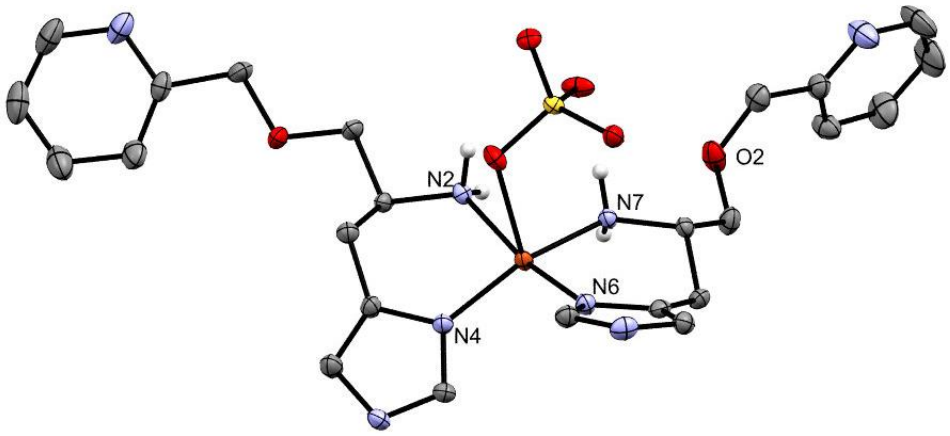

*Figure 106. ORTEP diagram (thermal ellipsoids at 50% probability level) of **Cu(2.3)$_2$.(SO$_4$)** Hydrogen atoms on non-coordinating atoms omitted are for clarity. Nitrogen atoms shown in blue, oxygen atoms shown in red, carbon atoms shown in grey, sulphur atoms shown in yellow, copper atoms shown in orange. H atoms refined using riding coordinates.*

*Table 10. Selected bond lengths of the first coordination sphere of **Cu(2.3)$_2$(SO$_4$)***

Bond		Bond Length / Å
Cu1	N2	2.026(4)
Cu1	N4	1.970(3)
Cu1	N6	1.953(4)
Cu1	N7	2.020(3)
Cu1	O7	2.562(3)
Cu2	N10	2.012(3)
Cu2	N11	1.976(4)
Cu2	N14	1.988(3)
Cu2	N15	2.004(4)
Cu2	O13	2.530(3)

Table 11. Selected bond angles of the first coordination sphere of ***Cu(2.3)$_2$(SO$_4$)***

Bond			Bond Angle /
N7	Cu1	N4	159.1(1)
N2	Cu1	N6	165.7(2)
N7	Cu1	N2	86.2(1)
N2	Cu1	N4	92.9(1)
N4	Cu1	N6	93.1(1)
N6	Cu1	N7	92.7(1)
N11	Cu2	N15	160.1(2)
N14	Cu2	N10	143.2(1)
N14	Cu2	N11	98.0(1)
N14	Cu2	N15	92.8(1)
N15	Cu2	N10	89.8(1)
N11	Cu2	N10	91.5(1)

This structure does not appear to be commensurate with the solution state data as the Job's Plot analysis indicates the formation of 1:1 complexes in methanol. The solution state data was obtained using a coordinating counter anion (Cl^-) while the crystal was obtained using a non-coordinating anion (SO_4^{2-}). While these have the same solution state EPR spectrum the crystal packing may alter the structure.

The anion may have an important role in preventing dimer formation. However, attempts to grow **Cu(2.3)Cl$_2$** crystals failed despite many attempts so this theory is purely speculation. In order to gain insight into the potential role of the anion in potential dimer formation, simple Cu histamine complexes, **Cu(Him)X$_2$**, were crystalized with a range of counter ions. Four anions were selected: SO_4^-, Cl^-, NO_3^- and PF_6^- as these act as a scale of the coordinating ability of the counter ion with $Cl^- > SO_4^-$, $NO_3^- > PF_6^-$. The formation of these complexes is shown in Figure 107. After the synthesis of these complexes, crystals suitable for X-ray diffraction were obtained from slow layer diffusion of MeOH into diethyl ether for Cl^-, NO_3^- and PF_6^-.

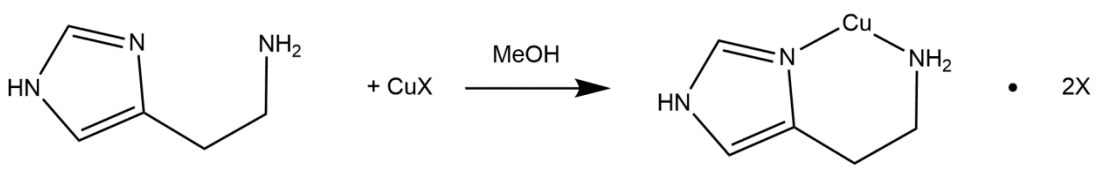

Figure 107. Synthetic route to ***Cu(Him)2X*** *complexes. X = SO_4^- or Cl^- or NO_3^- or PF_6^-.*

The crystal structures of these complexes are shown in Figure 108. The two complexes with non-coordinating anions, NO_3^- and PF_6^-, form **Cu(Him)$_2$** complexes with a Jahn Teller distorted octahedral geometry. The coordinating anion, Cl^-, forms a **Cu(Him)Cl$_2$** complex with a square planar geometry. Interestingly, **Cu(Him)$_2$(PF$_6$)$_2$** produced two crystal forms, one where the N1 of each histamine are *trans* to one another and one where they are *cis*. The overall coordination geometry of both crystal forms of **Cu(Him)$_2$(PF$_6$)$_2$** is Jahn Teller elongated octahedral, however the *xy* plane of the cis-N1-N1 structure of **Cu(Him)$_2$(PF$_6$)$_2$** shows some distortion away from this geometry as shown by its τ_4 value of 0.18. This distortion is not present in the trans-N1-N1 complexes as demonstrated by a τ_4 value of 0.00. In **Cu(Him)$_2$(NO$_3$)$_2$** a single crystal form was obtained, which is an Jahn Teller elongated octahedral with a trans N1-N1 geometry consistent with the reported crystal structure of **Cu(Him)$_2$(NO$_3$)$_2$** with a τ_4 value of 0.00.[217] A similar distortion to cis-N1-N1 **Cu(Him)$_2$(PF$_6$)$_2$** is observed in the crystal structure of **Cu(2.2)$_2$(SO$_4$)**$^-$ where the two N1 molecules are also *cis* to one another and hence the distortion observed away from square planar may be due to sterics of ethyl chain in histidine and histamine crystal form. These experiments indicate that the role of the anion in preventing the formation of the ligand dimer copper appears is significant as all of the crystals were synthesised and grown with the same methods.

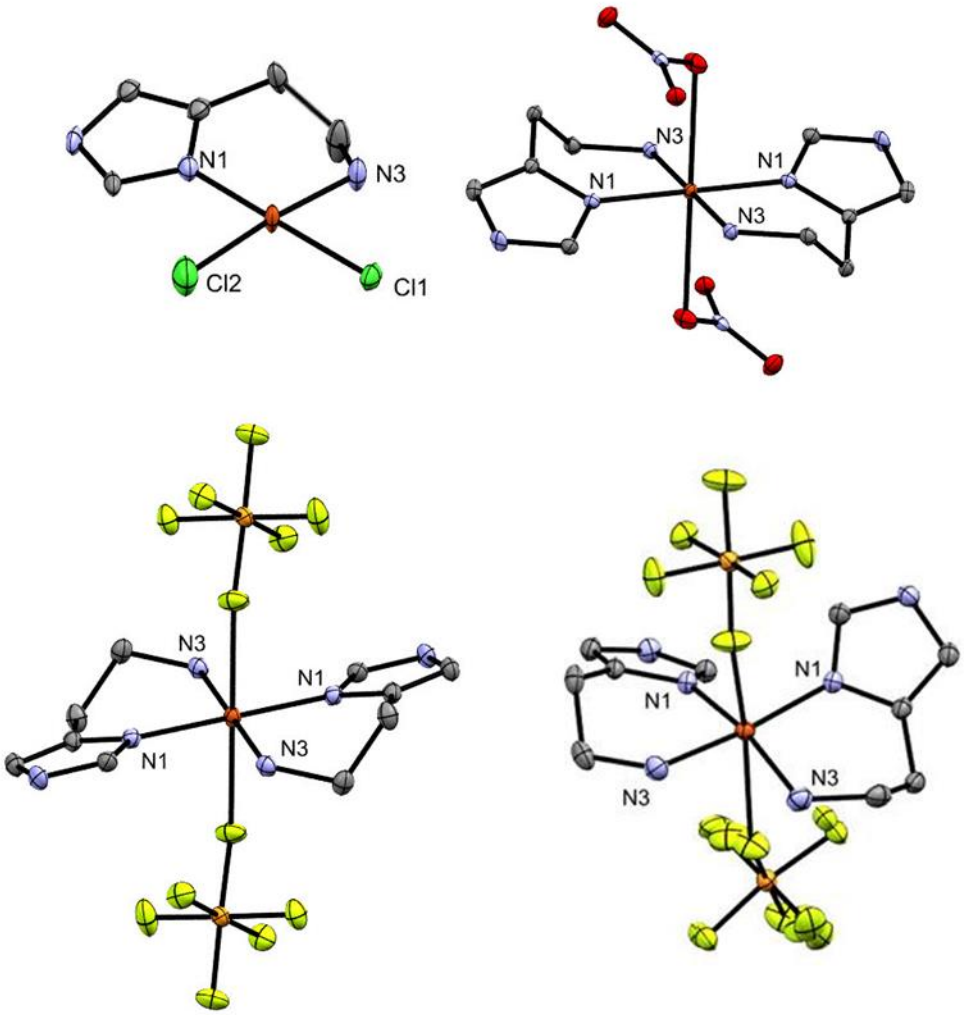

Figure 108. ORTEP diagram (thermal ellipsoids at 50% probability level) of $Cu(Him)_2X_2$ complexes. Top Left: $Cu(Him)Cl_2$; Top Right: $Cu(Him)_2(NO_3)_2$; Bottom left: Trans N1-N1 $Cu(Him)_2(PF_6)_2$; Bottom right: Cis N1-N1 $Cu(Him)_2(PF_6)_2$ Hydrogen atoms omitted for clarity. Nitrogen atoms shown in blue, oxygen atoms shown in red, carbon atoms shown in grey, fluorine atoms shown in yellow, copper atoms shown in copper, phosphorus atoms shown in pale orange.

2.3 Conclusions

The goal of this chapter was to produce a ligand and corresponding Cu complex capable of mimicking the coordination sphere of LPMOs. This required a tridentate ligand featuring a primary amine and two aromatic nitrogen's coordinating to copper.

As such novel ligand containing a primary amine, 2-([3-(1H-imidazol-4-yl)-2-methylpropoxy] methyl)pyridine, **2.3** was synthesised. This ligand featured two nitrogen containing heteroaromatics rings *trans* to one another and the 3rd coordinating atom is a primary amine. This compound was analysed using NMR spectroscopy, mass spectrometry, infrared spectroscopy and melting point analysis. Using multidimensional NMR techniques, the molecule was fully characterised. The formation of the key ether linkage was supported by the upfield shift of the methyl pyridine protons (5.07 to 4.35 ppm) indicating the loss of the chloride during the Williamson ether synthesis.

In order to successfully synthesise **2.3** an *in situ* Finkelstein reaction was used as in the absence of NaI an elimination reaction occurs on the histidinol. This indicates that the leaving group has the greatest effect on reactivity, which is confirmed as reaction yields increase from 20% to 80% on increasing the amount of NaI present in solution by 5%.

The corresponding **Cu(2.3)Cl$_2$** was synthesised and characterised using mass spectrometry, EPR spectroscopy and UV/Vis. In the solution state Job's plot analysis of the formation of **Cu(2.3)Cl$_2$** indicated that the complex formed a 1:1 Cu : **2.3** complex as the greatest change of the $\Delta\lambda_{max}$ occurs at a 1:1 ratio.

The EPR spectra of **Cu(2.3)Cl$_2$** in water showed a pH dependence with a pK_a of 7.6. This was assigned to a water to hydroxide shift. The presence of this shift indicates that there is a vacant coordination site capable of binding an exogenous ligand present in the complex. The spectral envelope of the EPR spectra indicated the coordination environment of the Cu was a square planar geometry and in-depth simulations of the various spectra found that the best simulations featured a Cu nuclei coupling to two $sp^2$and one sp^3 nitrogen atoms.

A single crystal suitable for X-ray crystallography was obtained. The solid state structure is that of the **Cu(2.3)$_2$(SO$_4$)** form, this is likely due to the use of a non-coordinating anion as a simple study using histidine Cu complexes in a 1:1 ratio also exhibited this phenomenon.

Overall, the evidence suggest that **CuX_2** forms a tridentate complex with **(2.3)**. As such the goal of designing and synthesising a ligand which incorporates a primary amine into the coordination sphere of a Cu complex was accomplished.

Chapter 3 – The Synthesis and Characterisation of an Artificial Metalloenzyme based on **Cu(2.3)**

3.1 Introduction

The secondary coordination sphere of lytic polysaccharide monooxygenases has been shown *via* mutagenesis studies to be important for oxidative activity.[120] This work found that two residues, a glutamine and a histidine, close to the active site of an LPMO, from *Myceliophthora thermophile* (*MtPMO3*) are part of a hydrogen bonding network which is thought to stabilise the reactive intermediate involved in polysaccharide degradation.[119, 123] This work showed that the removal of these residues by mutagenesis significantly reduced the catalytic activity of the enzyme demonstrating that the secondary coordination sphere for LPMOs is important for activity.[120]

Reproducing these interactions in small molecules would therefore be very important to understand and/or mimic the mechanism of action of LPMOs. Within the literature there are examples of small molecule complexes that have introduced hydrogen bonding moieties to support reactive intermediates, shown in Figure 109.[218-219] However, the addition of hydrogen bonding groups in positions that would favour the interaction with the intermediates can alter the coordination geometry thus the reactivity of the metal centre and is hence undesirable.

An alternative methodology to incorporate a hydrogen bonding network is to create what is known as an artificial metalloenzyme (ArMs) in which a metal centre is incorporated into a protein host.[220-222] In this case, the amino acid residues close to the metal centre provide a secondary coordination sphere. This methodology also provides the secondary effect of preventing dimerization of the metal centres as they will each have a distinct environment provided by the protein. This chapter will explore the synthetic modification of **2.3** to produce an artificial enzyme system and the characterisation of the corresponding ArMs.

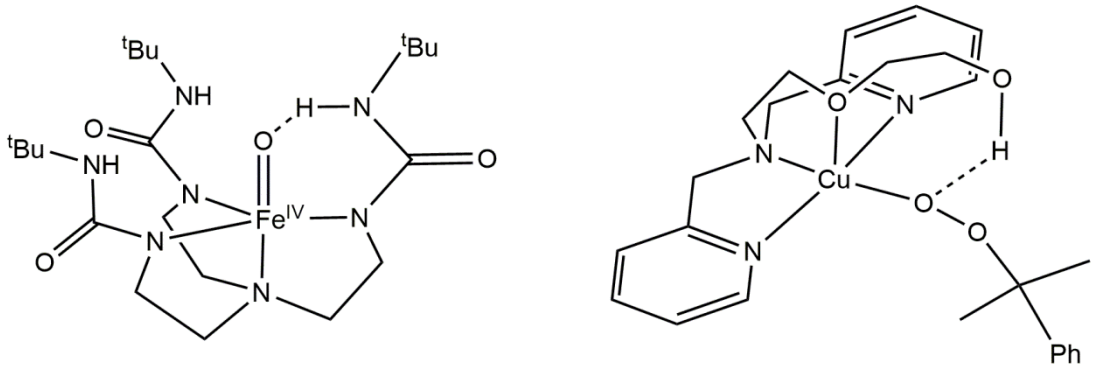

$[Fe^{IV}H_3Buea(O)]^-$ $[Cu^{II}(Pyridyakyl)(OOCumyl)]$

Figure 109. Two examples of small molecule complexes which use intramolecular hydrogen bonds to support reactive intermediates. Left. A Fe-oxo complex developed by A. S. Borovik et al.[218] Right. Cu-alkyl peroxo complex developed by Hong et al.[219]

3.1.1 Artificial enzymes

ArMs result from the incorporation of a catalytic metal site into a protein scaffold allowing for the study of the non-covalent interactions provided by the protein scaffold. There are four differing methodologies of incorporation into the host protein, these are (a) dative coordination to the metal centre from the protein; (b) metal substitution; (c) supramolecular anchoring; and (d) covalent immobilization, all of which are shown in Figure 110. These strategies can be used by themselves or in conjunction with one another, for example using a supramolecular interaction to place the metal centre into a position to coordinate with the desired residue in the protein.[223]

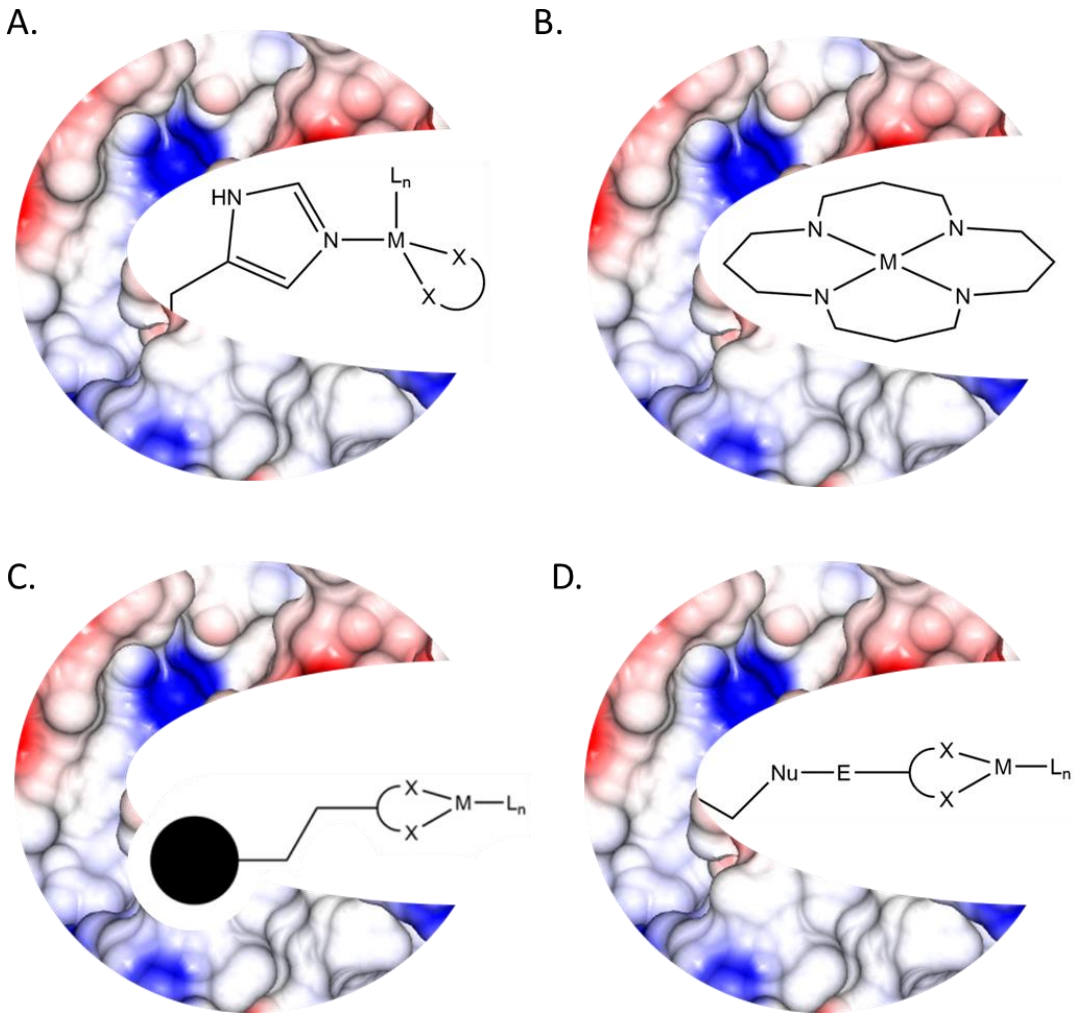

Figure 110. The four anchoring strategies to allow for the incorporation of the metal site into the protein host. (A) Dative coordination of an unsaturated metal complex (B) Metal substitution. (C) Supramolecular anchoring. (D) Covalent immobilization. Adapted from Davis et al.[221]

The dative coordination strategy uses direct coordination of the metal centre by a nucleophilic amino acid residue within the protein. The specific localisation of the metal centre inside the protein is challenging as these residues appear frequently across the amino acid sequence, which can result in many metal sites within the protein.

The main field of study which uses this approach is *de novo* protein design, in which non-natural single chain peptides are used to form three- or four- helical bundles. The inside of these bundles contain specifically placed nucleophilic amino acid residues (His, Cys, Glu, Asp, Ser) to form the coordination environment.[224-225] This methodology solves the multiple site problem as the coordinating residues are only introduced in a single location resulting in a single site. The incorporation of artificial amino acids increases the scope of metals that these constructs can bind and thus can provide unique reactivity. For example the

incorporation of the unnatural amino acid (2,2'-bipyridin-5yl)alanine into a *de novo* designed protein allowed for the protein to bind Co^{2+}.[226]

The supramolecular anchoring strategy relies on the high affinity some proteins possess for certain specific co-factors. The modification of these cofactors to covalently attach a metal binding domain while maintaining the high affinity of the co-factor allows for these conjugates to be selectively localised within the protein. The most common approach for the supramolecular anchoring strategy is biotin-streptavidin(Sav) technology™. This methodology uses the extremely high affinity of Sav for biotin ($K_a \sim 10^{13}$ M^{-1}) to insert a biotin-functionalised metal complex in the protein scaffold. This methodology was originally developed by *G. M. Whitesides et al.*[227] using a rhodium complex for asymmetric hydrogenation. This approach has been further expanded by *Ward and co-workers* whom have demonstrated that the methodology is suitable for a large range of metal complexes and functions.[223, 228-229] Alternatively, a supramolecular metal binding cofactor, *e.g.* a heme, can be modified or replaced, for example studies report the replacement of a Fe-binding heme with a Ir-binding heme in myoglobin. The artificial enzyme was then able to carry out C-H bond functionalisation.[230] This heme based approach is similar to the metal substitution strategy.

The metal substitution replacement strategy involves repurposing the enzyme's own active site by removing the metal ion and replacing it with a non-bioavailable metal. This approach has been shown to induce reactivity not seen before in nature.[230-231] This methodology typically involves the demetalation of the original enzyme followed by the metalation with the desired metal. An example of this methodology is α-carbonic anhydrase where a zinc ion was replaced with manganese.[231] The unmodified enzyme is able to carry out the formation of bicarbonate from CO_2 and the hydrolysis of esters while the Mn-modified enzyme is able to oxidise *o*-dianisidine and the epoxidation of olefins.[231]

The covalent anchoring strategy uses bioconjugation techniques to covalently link a metal binding domain to an amino acid residue in the protein. This methodology typically utilises either cysteine chemistry, to form Cys-maleimide,[232] Cys-α-halocarbonyl,[233] or disulfide bonds,[234]or the incorporation of artificial amino acids into the protein which can then perform a [3+2] cycloaddition to a metal binding domain *via* click chemistry.[235]

As we do not wish to modify the coordination geometry found in **2.3** of the four available methodologies for the formation of artificial metalloenzymes, the covalent or supramolecular anchoring are the most suitable. Of these two approaches the

supramolecular approach using the biotin-streptavidin system is widely studied, with crystallographic examples of the secondary coordination sphere influencing the reactivity of the metal centre.[222] The high affinity of Sav to biotin also allows for quantitative binding as opposed to the potential for incomplete binding from the covalent attachment. Furthermore, covalent anchoring requires the incorporation of a nucleophile into the protein host in order to allow for covalent attachment. These features, coupled with the fact that Sav can be expressed in *E.coli* in good yields and that site specific mutagenesis has been previously carried out, makes this system an excellent candidate for the goals of this chapter.[222]

3.1.2 Biotin Sav Artificial Enzymes

Sav is a homo-tetramer which assembles as a dimer of dimers, where each subunit is able to bind a single biotin molecule, as shown in Figure 111.[236] A key structural aspect of each Sav dimer is the formation of a volume of space between the biotin binding sites, known as the vestibule and shown in Figure 112. In order to position a metal complex into this vestibule a linker between the biotin and the synthetic metal complex must be used. The placement of the metal complex within the vestibule is determined by the length of this linker.[221] The positioning of the metal centre within the vestibule profoundly affects both structural and physical properties of the resultant artificial enzyme, with implications on the reactivity of the incorporated metal centre.[223]

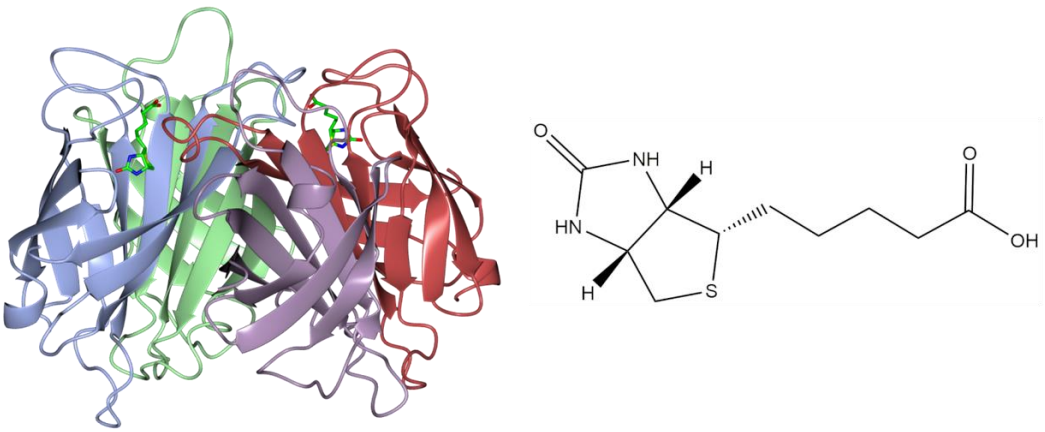

Figure 111. Left. The structure of tetrameric Sav with biotin bound in each subunit (PDB 1STP).[236] Right. Schematic structure of biotin

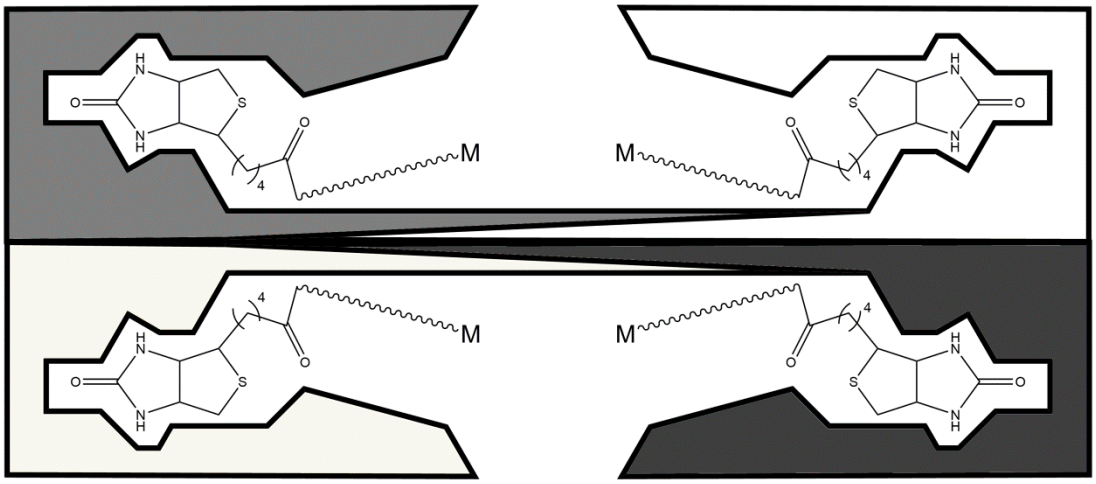

Figure 112. Schematic representation of the Sav dimer of dimers with a metal complex anchored in the vestibule (Chirality excluded for simplicity)

The general synthetic design of the biotinylated metal complexes, suitable for use in a biotin-Sav system, consist of an anchor, linker and metal chelator; an example of such a system which was developed by *Borovik et al.*[223] is shown in Figure 113. As the anchor, biotin, and the metal chelator, **2.3**, are fixed, the linker is the moiety with the most variability. Within the literature both the length and chemical makeup of the linker has been varied. These linkers have ranged from simple alkyl chains of varying lengths (ethyl, propyl, butyl)[223, 229] to more complex linkers such as phenol rings[237] and phenyl groups of N heterocyclic carbenes.[238] As the linker length and chelator length will have an effect on the positioning of the metal centre, the number of atoms between the biotin amide and the metal centre provides a better metric of the positioning within the cavity as opposed to the chemical composition of the linker. From the literature it can be seen that a suitable linker length is between 4-8 atoms including the metal coordinating atom. [223, 229,237, 238]

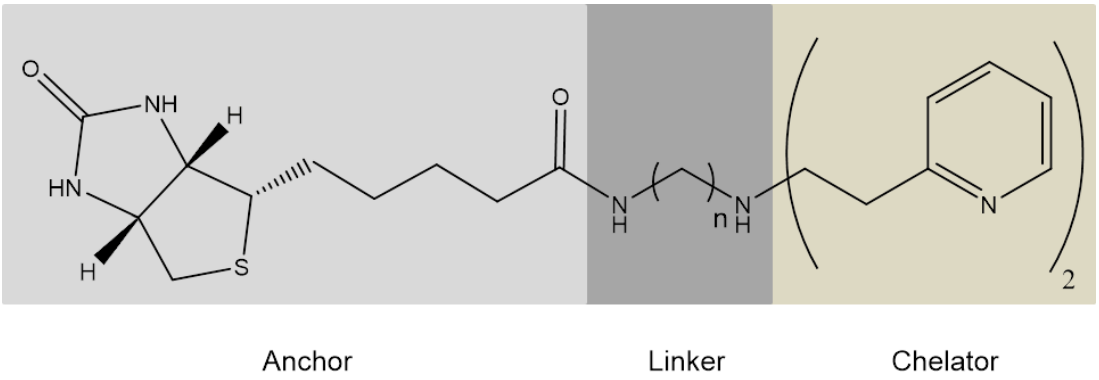

Figure 113. A schematic structure of a biotinylated ligand developed by Borovik et al.[223]

Within the literature it has been demonstrated that a stabilisation effect is provided by the secondary coordination sphere to a reactive oxygen species in a biotin Sav artificial enzyme using a pyridylalkyl Cu complex.[222] This work examined the reaction of Cu(II) with H_2O_2 to form a putative **Cu(II)-OOH$^-$** within the artificial enzyme. Structural characterisation of the **Cu(II)-OOH$^-$** revealed an extensive hydrogen bonding network to both the proximal and distal oxygen atoms of the hydroperoxo which had not been observed previously, shown in Figure 114.

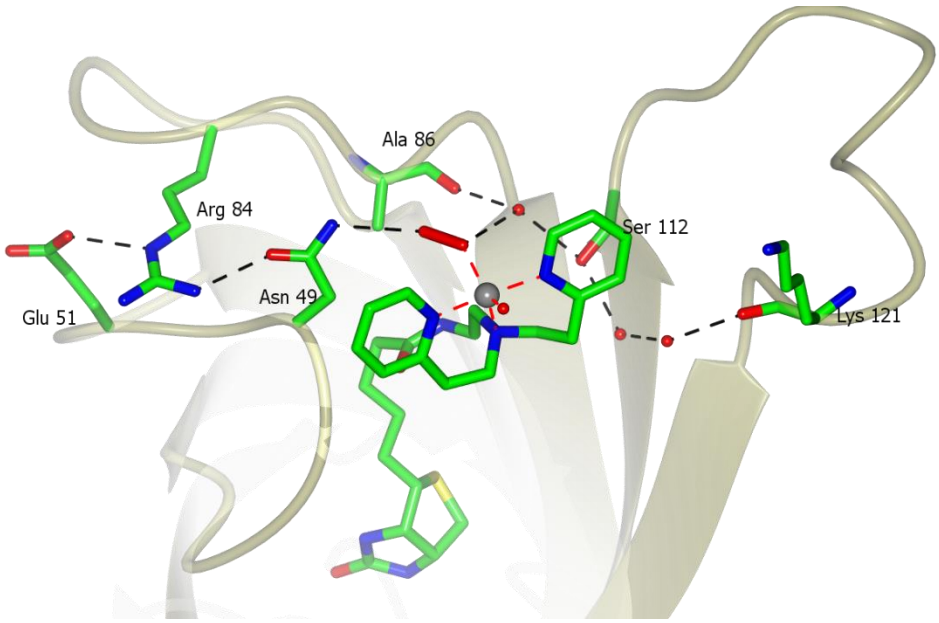

Figure 114. Crystal structure showing the extended hydrogen bond network of the artificial enzyme [Cu(biot-et-dpea)(H_2O)(H_2O_2)]$_2^+$⊂Sav WT (PDB 6ANX) utilised by Borovik et al. to stabilise H_2O_2

The hydrogen bonding network was shown to incorporate a serine and the carbonyl backbone of an alanine residue interacting with a water molecule, which is then perfectly positioned to hydrogen bond to the proximal oxygen. The distal oxygen is hydrogen bonded to a nearby asparagine residue. These interactions clearly demonstrate the ability of neighbouring amino acid residues to stabilise reactive intermediates, as the **Cu(II)-OOH$^-$** species was demonstrated to be transient outside of the streptavidin host. A similar mechanism is thought to be in place in the stabilisation of reactive intermediates in LPMOs.[120]

A further advantage of the biotin Sav system is given by the stability of the protein, which allows for mutagenesis studies of the residues in close proximity to the metal ion. Within the same study the system described above was investigated using mutagenesis studies to

determine the effect of the secondary coordination sphere on the stability of the Cu(II)-OOH^- species. [222]

The serine residue (Ser 112 in Figure 6, mutant defined as S112A) was replaced with an alanine to disrupt the hydrogen bonding network. After this mutation the water molecule responsible for H-bonding to the proximal O of **Cu(II)-OOH^-** was significantly reduced in occupancy in the solved structure. This modification also resulted in a decrease in the half-life of the hydroperoxo species when monitored *via* UV/Vis spectroscopy, highlighting the strong link between the hydrogen bonding network and the stability of the ROS. A second mutant was produced in which the asparagine was replaced with an alanine (Asn49 in Figure 6, mutant defined as N49A) to probe the role of H-bonding to the distal O of Cu(II)-OOH^- and this resulted in a similar structure and stability in solution to the WT protein. These results indicate that the stability of the Cu(II)-OOH^- depends primarily on the stabilisation of the proximal rather than the distal O atom. This study would not have been possible in a conventional small molecule complex due to the complexity of building an extensive H-bonding network such as the one shown in Figure 114.

The stability of **Cu(II)-OOH^-** intermediate has been shown to be directly related to the reactivity of the artificial enzymes. The catalytic competency of the various streptavidin mutants was monitored using the oxidation of 4-chlorobenzylamine to the corresponding aldehyde which then undergoes a schiff-base condensation to form N-(4-chlorobenzyl)-1-(4-chlorophenyl)methanimine, shown in Figure 115. On testing the reactivity of various ArMs it was found that the wild type streptavidin and the N49A mutant had minimal reactivity with 4-chlorobenzylamine in these conditions. However, the S112A mutant was shown to form N-(4-chlorobenzyl)-1-(4-chlorophenyl)methanimine effectively. From these data it can be seen that reactivity decreases based on increasing stability of the **Cu(II)-OOH^-** which indicates that **Cu(II)-OOH^-** is likely the reactive species for this oxidation.

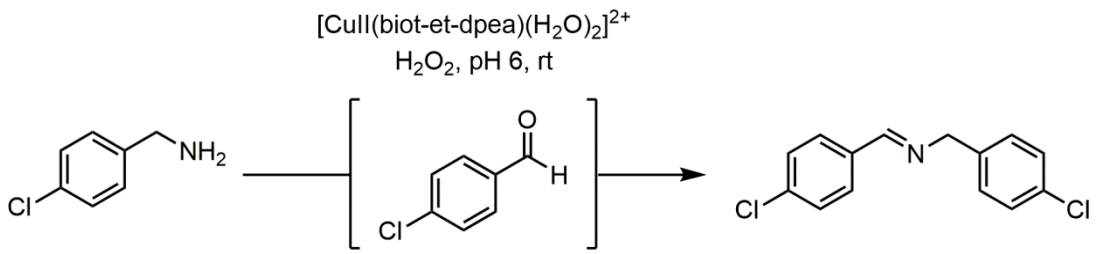

Figure 115. Oxidation of 4-chlorobenzylamine by [CuII(biot-et-dpea)(H_2O)(H_2O_2)$_2$]$^+$⊂Sav WT and H_2O_2

It has been established that the coordination environment provided by the vestibule can also affect the stereoselectivity of a reaction through steric effects, this has been extensively demonstrated by Ward and co-workers.[239-241]. In their studies the enantioselectivity of various hydrogenation and hydroxylation reactions, shown in Figure 116, was controlled by the positioning of the metal complex within the vestibule, either by modification of the linker length between the biotin and metal complex[239] or *via* modifications to the amino acid sequence which can alter the positioning of the complex within the biotin vestibule.[240]

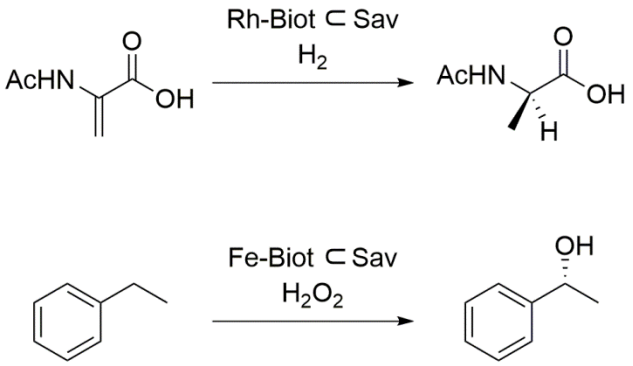

Figure 116. Enantioselective reactions carried out using artificial metalloenzymes

The studies discussed above demonstrate a diverse range of applications of a supramolecular anchoring strategy to support a variety of metal complexes and that the streptavidin host plays a non-innocent role in the resultant reactivity of the incorporated metal centres. Therefore it is a good candidate for the development of an artificial enzyme containing **2.3**.

3.2 Ligand Design and Synthesis

This section describes the synthetic modification of compound **2.3** to allow for the attachment of biotin and subsequent incorporation into streptavidin to generate a novel biotin-Sav metalloenzyme.

3.2.1 Initial Synthetic Design

As previously discussed in **Chapter 2**, compound **2.7** which acts as the nucleophile for the formation of the ligand **2.3** has an easy and enantio-pure synthesis from low-cost starting materials. Therefore, any synthetic alterations to allow for the addition of the biotin-linker moiety will occur on the pyridine moiety of **2.3.** The available positions for functionalisation are either the pyridine ring or the pyridine α-carbon shown in Figure 117.

Modification of the pyridine ring raises some concerns, as it has been shown that in small molecule copper complexes the inclusion of different electron withdrawing or donating groups on the coordinating heteroaromatic rings can affect the reactivity of the metal centre, as discussed in section **1.4.1**. Therefore, the linker to biotin was initially designed to be incorporated onto the alkyl backbone of the ligand as opposed to the pyridine ring.

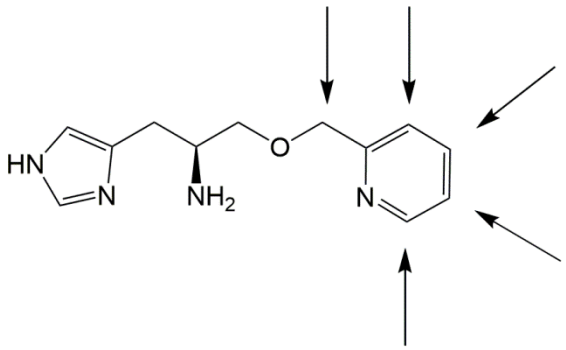

*Figure 117. The points available for derivatization of **2.3***

As previously discussed in section **3.1.2**, the linker length between the biotin domain and the metal centre has been shown to have a profound effect on the reactivity. Analysis of the literature and the reported structures allows for the design of the optimal linker chain for these compounds hence, the synthetic ligands used by *Borovik et al.*[222-223] in their studies are shown in Figure 118. It is worth noting that, unlike the ligands shown in Figure 118 where the terminus of the linker (tertiary amine) coordinates the Cu centre, in compound **2.3** the coordinating atoms are further away from the linker. Therefore, to ensure optimal positioning within the vestibule, the linker used to attach biotin to **2.3** will

be required to be shorter, in order to maintain the same number of atoms between the coordinating atom and the biotin moiety.

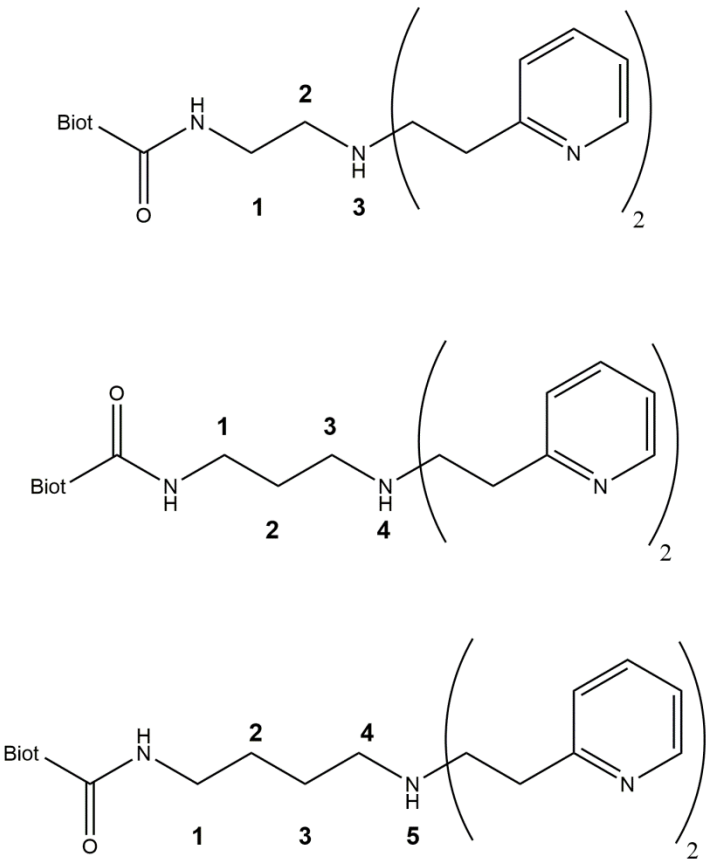

Figure 118. Biot-et-dpea, prop-et-dpea and but-et-dpea], from Borovik et al.[223] showing the lengths of simple alkyl linkers from the biotin amide to the closest coordinating atom.

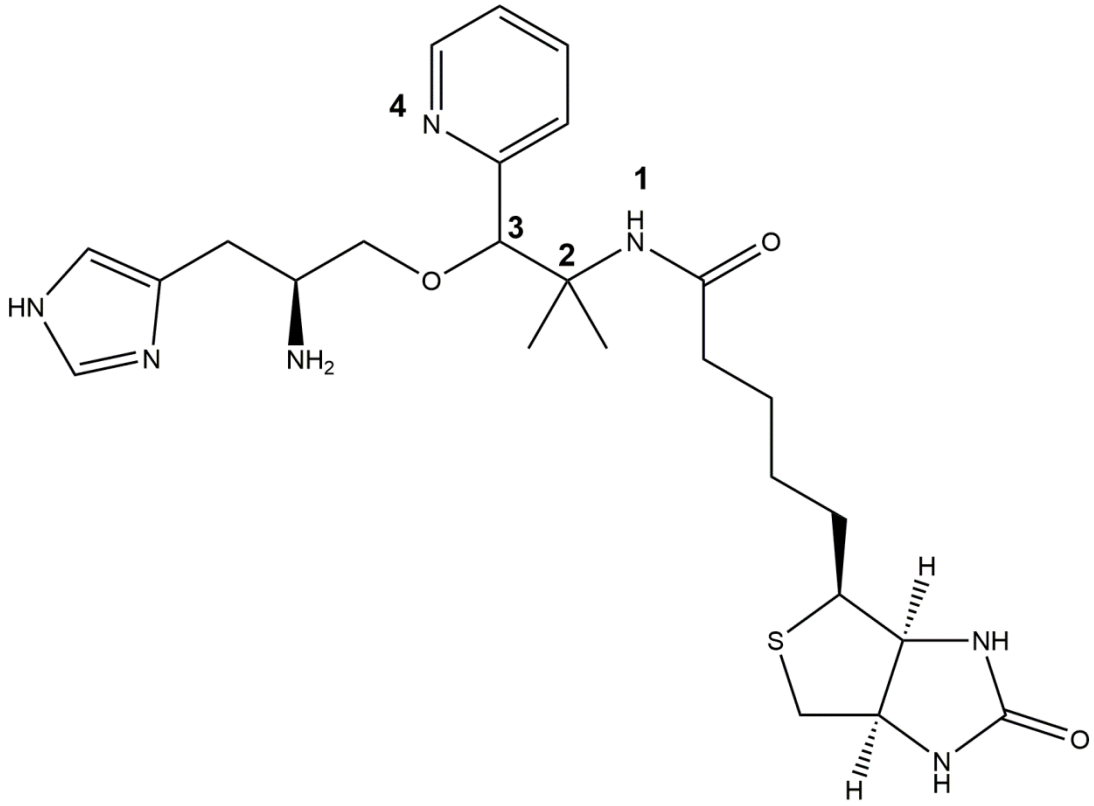

3.1

Figure 119. The schematic structure of N-[1-[[(2S)-2-amino-3-(1H-imidazol-4-yl)propyl]oxy]-2-methyl-1-(pyridin-2-yl)propan-2-yl] (5-(2-oxohexahydro-1H-thieno[3,4-d]imidazol-4-yl)pentanamide, ***3.1***

The modified design of **2.3** to allow for the incorporation of both a linker and biotin (compound **3.1**) is shown in Figure 119. The linker between the biotin amide and coordinating atom is four atoms long which is the same as the Biot-et-dpea molecule studied by *Borovik et al.*[222-223] The resulting synthetic strategy to obtain the target molecule is shown in Figure 120.

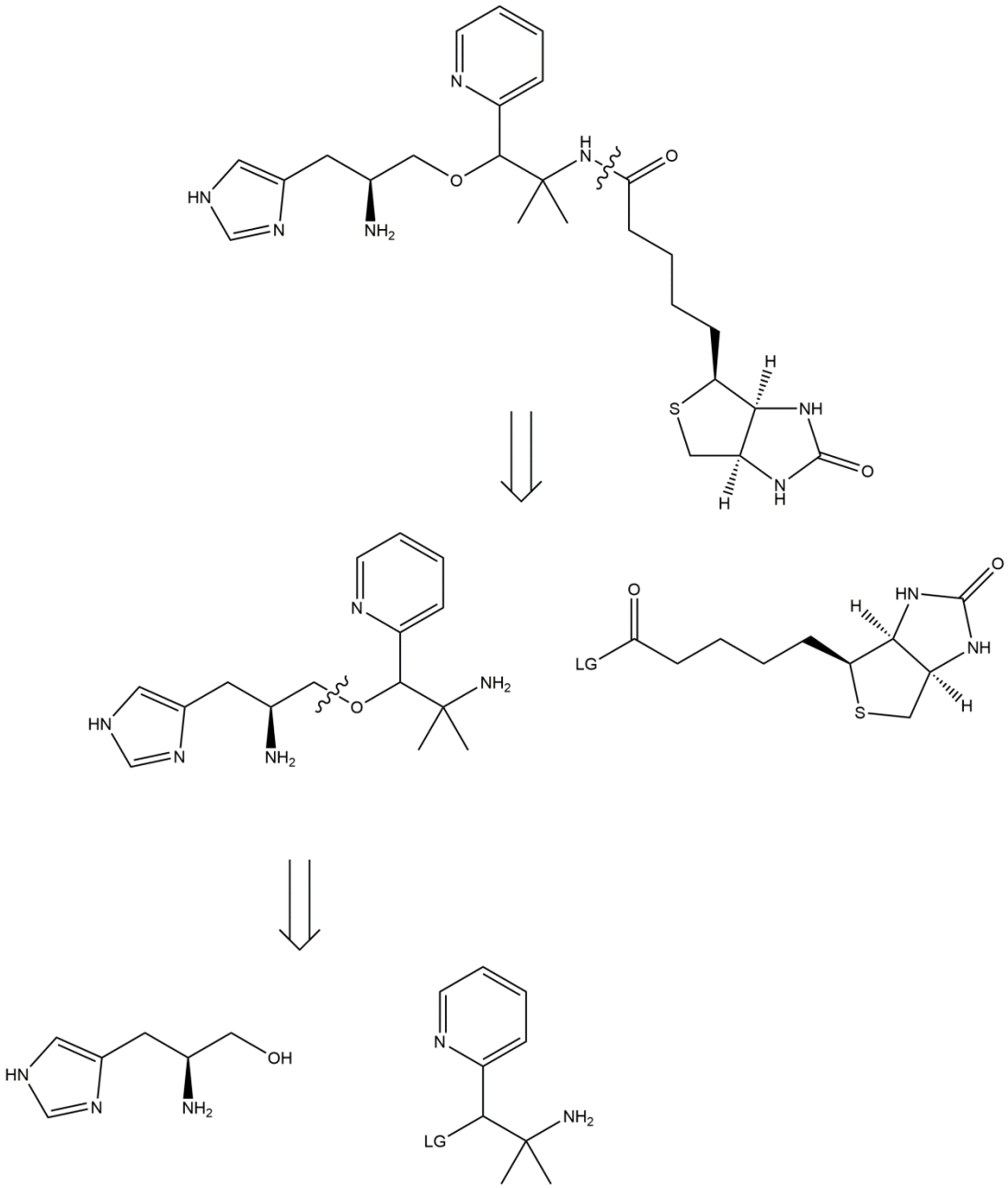

*Figure 120. Synthetic disconnections of **3.1** into its respective synthetic equivalents*

Within the literature, the final synthetic step for forming a biotinylated ligand is the biotinylation step and hence this will also be the case in the devised synthetic route for **3.1**.[222-223, 229, 242] This strategy stems from the polar nature of the biotin group, which hinders the use of non-polar organic solvents commonly used for synthesis and purification. This step involves the formation of an amide bond between a primary amine which terminates the linker and biotin-pentafluorophenyl ester (Biotin-PFP), where in the PFP moiety acts as an excellent leaving group.

The formation of the ligand backbone has been explored in **Chapter 2** for the synthesis of **2.3** and will remain the same in the formation of **3.1**. This step relies on a Williamson ether synthesis which occurs *via* nucleophilic substitution. However, the carbon on which the leaving group is located is now secondary as opposed to primary which was the case for the formation of **2.3**. This presents a problem as the competing elimination reaction will now be favoured over the desired nucleophilic substitution. To prevent this elimination reaction occurring on **3.2,** two methyl groups were incorporated on the β-carbon thus removing the protons required for the elimination reaction to occur.

The use of a Henry (Nitro Aldol) reaction, shown in Figure 121, allows for the incorporation of two functional groups simultaneously, an alcohol and a nitro group.[243] The alcohol can be transformed into a leaving group *via* a halogenation reaction and the nitro group can be reduced to a primary amine, making the Henry Aldol product of the corresponding pyridine desirable (Figure 122).

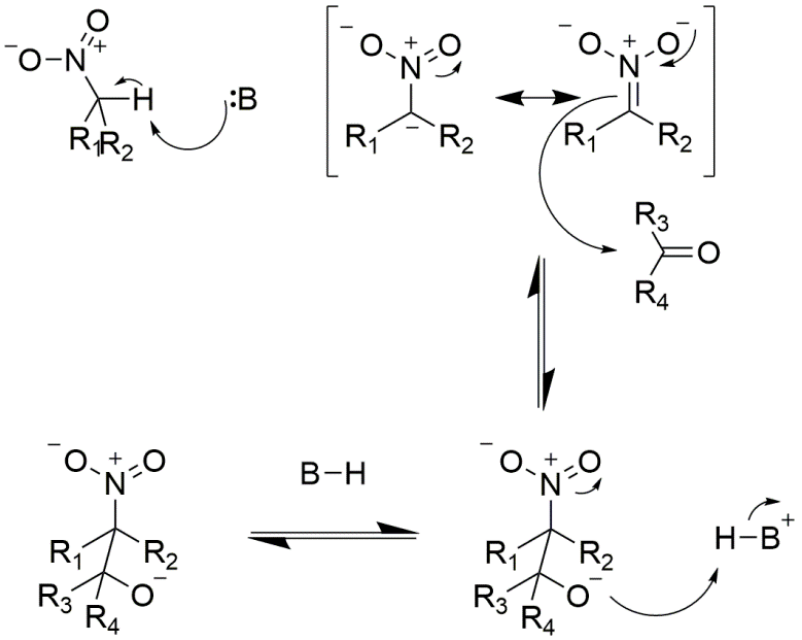

Figure 121. The general reaction mechanism of a Henry reaction

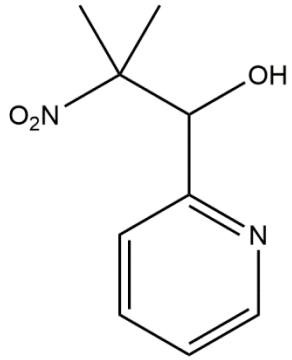

3.2

*Figure 122. The Henry Adol product, compound **3.2***

3.2.2 Initial synthetic route targeting 3.1

Having considered the synthetic disconnections of **3.1** shown in Figure 120, the full synthetic route for its synthesis was planned. The Henry Aldol product **3.2** was selected as an initial target followed by the conversion of the alcohol to a suitable leaving group. This leaving group would then be used in the Williamson ether synthesis followed by the reduction of the nitro group and subsequent biotinylation and deprotection. The full synthetic scheme is shown in Figure 123.

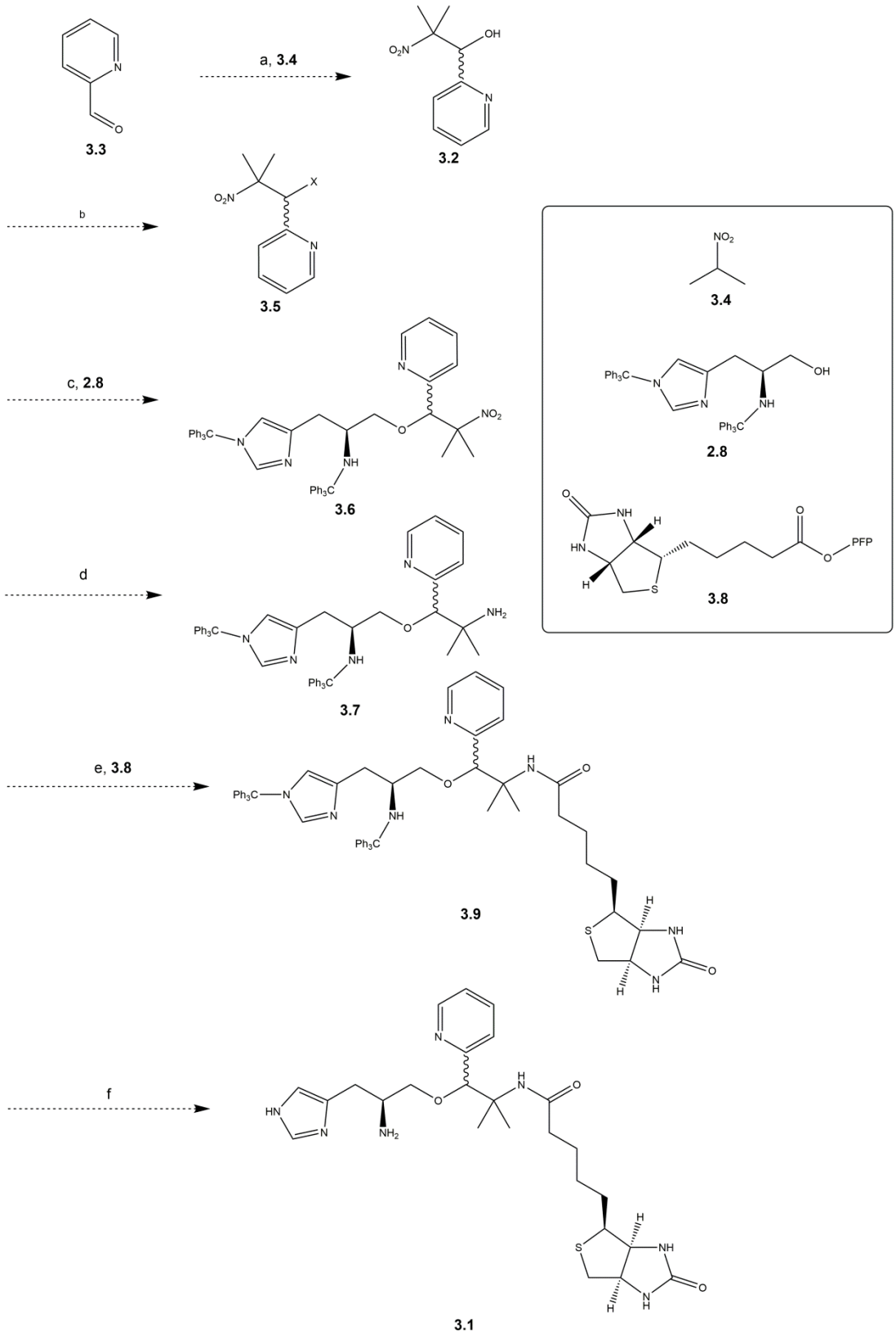

Figure 123. Initial synthetic route to form the biotinylated ligand, ***3.1*** *(a) P(i-PrNCH$_2$CH$_2$)$_3$N,MgSO$_4$,* ***3.4*** *(b) X = Tosyl, X = Br, PPh$_3$, CBr$_3$/HBr (c)* ***2.8****, NaH, NaI (d) Raney nickel, H$_2$ (e)* ***3.8****, Et$_3$N, DMF (f) 1:1 THF / 3M HCl, Δ*

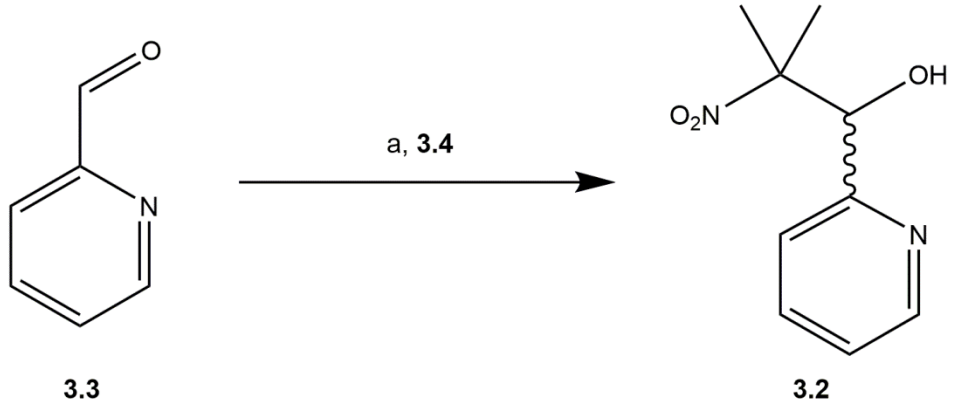

*Figure 124. Formation of 2-methyl-2-nitro-1-(pyridin-2-yl)propan-1-ol **3.2** from 2-Pyridinecarboxaldehyde **3.3**.(a) 2-nitropropane **3.4**, P(*i*-PrNCH$_2$CH$_2$)$_3$N, MgSO$_4$*

The initial step of the synthesis is the formation of the Henry Aldol product, 2-methyl-2-nitro-1-(pyridin-2-yl)propan-1-ol **3.2**, shown in Figure 124. This transformation was carried out using a modification of the procedure developed by *J. G. Verkade et al.*[244] The first step of this reaction is the formation of a slurry from 2-nitropropane **3.4** and $MgSO_4$. To this 2-pyridine-carboxaldehyde, **3.3**, was added dropwise and the reaction mixture was stirred for 5 minutes, during which time Mg^{2+} is thought to have activated the aldehyde. Following this a catalytic amount of a proazaphosphatrane base, P(i-PrNCH$_2$CH$_2$)$_3$N, was added to the solution and stirred for 12 hours. The reaction mixture was subjected to an organic/aqueous work up and dried *in vacuo* to give **3.2** as a brown solid. The product was characterised *via* ^{1}H NMR and ESI mass spectrometry. The formation of **3.2** is supported by the loss of a singlet peak at 10.09 ppm which corresponds to the aldehyde proton. Furthermore, two new singlet resonances appear in the spectrum at 1.60 ppm and 1.42 ppm with a relative integration of three; which corresponds to the two new methyl environments present in the product. In addition, the ESI-MS analysis gave a molecular ion peak $[M+H]^+$ for **3.2** at *m/z* 197.0920 which is consistent with a compound of formula $C_9H_{12}N_2O_3$, the expected molecular formula of **3.2**.

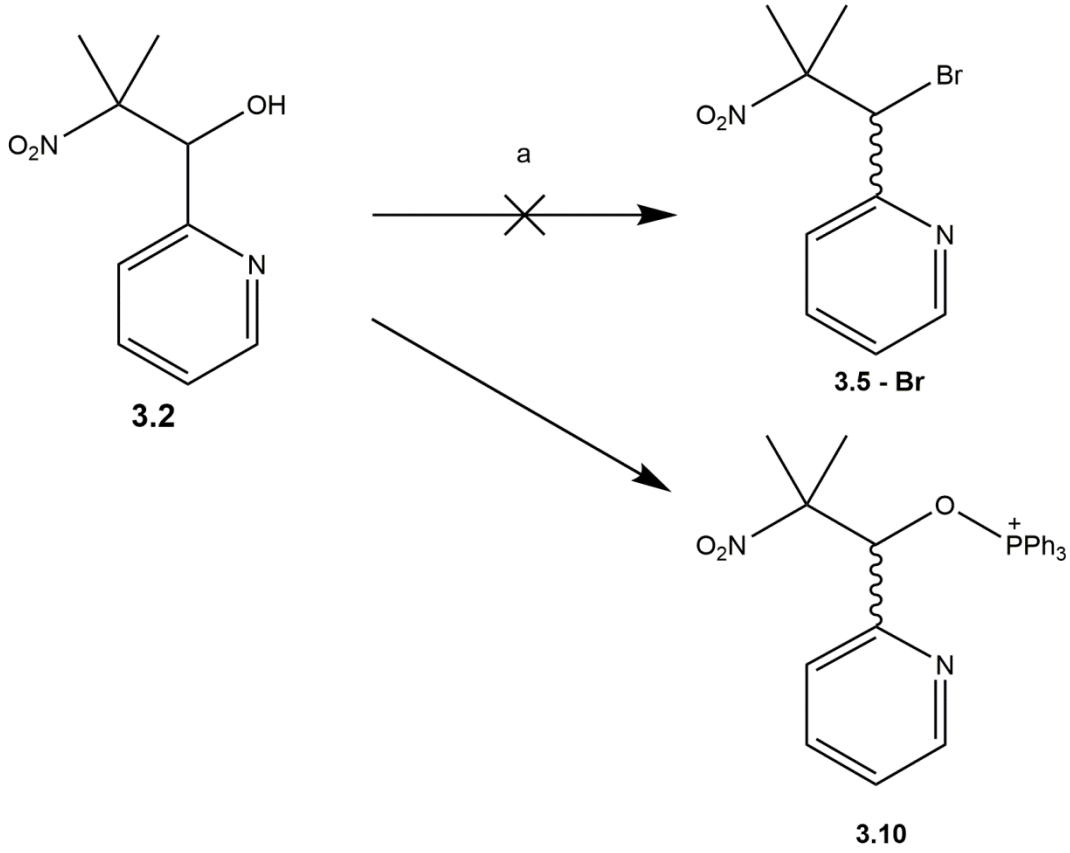

*Figure 125. Attempted formation of 2-(1-bromo-2-methyl-2-nitropropyl)pyridine **3.5-Br** from 2-methyl-2-nitro-1-(pyridin-2-yl)propan-1-ol **3.2** (a) Br, PPh_3, CBr_3, DCM*

In order to use **3.2** in a Williamson ether synthesis an appropriate leaving group must be introduced in place of the alcohol group. It has been previously shown in **Chapter 2** that an *in situ* Finkelstein reaction followed by the Williamson ether synthesis allows for the formation of the desired product. Therefore, a halogen is the preferred leaving group in this case.

The introduction of a halogen in the place of the alcohol can be carried out using several methodologies. The first of these to be explored was bromination *via* an Appel reaction.[245] Under a N_2 atmosphere, PPh_3 and CBr_4 were stirred in DCM for 30 minutes, followed by the addition of 2-methyl-2-nitro-1-(pyridin-2-yl)propan-1-ol **3.2**. After 12 hours the reaction mixture was filtered and subjected to an organic/aqueous work up and dried. ^{1}H NMR analysis of the crude reaction mixture revealed, upon comparison with the chemical shifts of the starting material, that a reaction had occurred due to the change in chemical shift of H_5 on the pyridine ring (from 8.69 ppm to 8.53 ppm). However, the spectrum also contains signals corresponding to phenyl protons with a relative integration of >26, indicating that either the triphenylphosphine oxide has not been removed from the reaction mixture or

that triphenylphosphine is still bound to the oxygen atom in the final step of the reaction, giving the corresponding phosphonium ion, **3.10**.

The formation of the phosphonium ion, **3.10**, is supported by the ESI-MS analysis of the crude reaction mixture which gave a molecular ion peak $[M+H]^+$at 457.1676 *m/z* which is consistent with a compound of formula $C_{27}H_{26}N_2O_3P$, the expected molecular formula of **3.10**. Attempts to purify the reaction mixture in order to remove the excess triphenylphosphine *via* column chromatography resulted in the degradation of the compound into a complex mixture. This reaction was repeated adding KBr to the reaction mixture after the apparent formation of **3.10** in order to increase the concentration of Br^- in solution in an attempt to push the reaction to the desired product, **3.5**, using Le Chatelier's principle. However, this modification to the reaction resulted in no visible changes to either the crude ^{1}H NMR spectrum or the ESI-MS spectrum. Therefore, this methodolgy to incorporate a halogen into **3.2** was discarded.

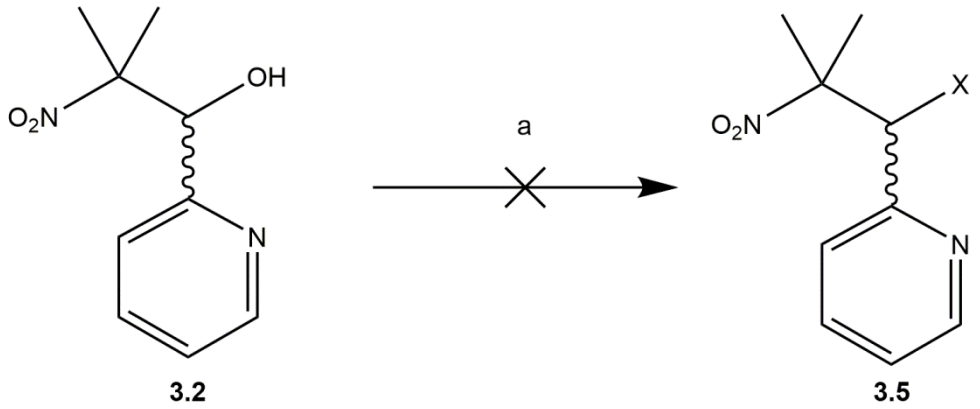

*Figure 126. Attempted formation of 2-(1-X-2-methyl-2-nitropropyl)pyridine **3.5** from 2-methyl-2-nitro-1-(pyridin-2-yl)propan-1-ol **3.5** (a)X = Cl, $SOCl_2$, DCM, X = Br, HBr, DCM*

The alternative to the Appel method is direct halogenation. Attempts to use direct halogenation methods such as thionyl chloride and HBr, shown in Figure 126, were carried out, but were unsuccessful. The ^{1}H NMR spectra of the reaction mixture in both cases remained unchanged even after long reaction periods and heating. As direct halogenation of the alcohol was found to be nonviable, the use of other potential leaving groups was explored.

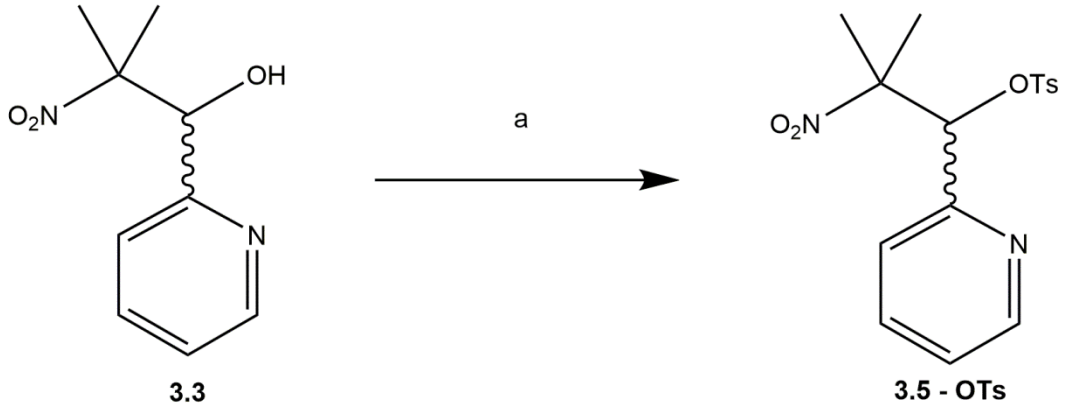

3.3 **3.5 - OTs**

*Figure 127. Synthesis of 2-methyl-2-nitro-1-(pyridin-2-yl)propyl 4-methylbenzenesulfonate **3.5-OTs** from 2-methyl-2-nitro-1-(pyridin-2-yl)propan-1-ol **3.3** (a) 4-Toluenesulfonyl chloride, 4-dimethylaminopyridine, Et_3N, DCM*

P-toluenesulfonyl groups (OTs) are able to act as good leaving groups as the negative charge on the oxygen atom after substitution is stabilized by the resonance forms on the aromatic ring and sulfonate group. The synthesis of 2-methyl-2-nitro-1-(pyridin-2-yl)propyl 4-methylbenzenesulfonate, **3.5-OTs**, is shown in Figure 127**.** 2, 2-dimethyl-2-nitro-1(2-pyridyl)-1-propanol and 4-toluenesulfonyl chloride were dissolved in DCM and to this Et_3N was added along with a catalytic amount of 4-dimethylaminopyridine to facilitate the reaction. The reaction mixture was stirred for 12 hours, dried *in vacuo* and purified *via* flash column chromatography to give **3.5-OTs** as a pale brown solid in 20% yield. The compound was then characterised *via* ^{1}H NMR spectroscopy and ESI mass spectrometry. The formation of **3.5-OTs** is supported by the appearance of two new multiplets of relative integration three at 7.77 and 7.72 ppm, corresponding to both the remaining pyridine proton and the protons from the OTs group. Furthermore, a new resonance at 2.39 ppm of relative integration three assigned to the methyl group of OTs, is present in the spectrum. ESI-MS analysis of the crude reaction mixture gave a molecular ion peak $[M+H]^+$at *m/z* 351.1009, which is consistent with a compound of formula $C_{16}H_{19}N_2O_5S$, the expected molecular formula of **3.5-OTs**.

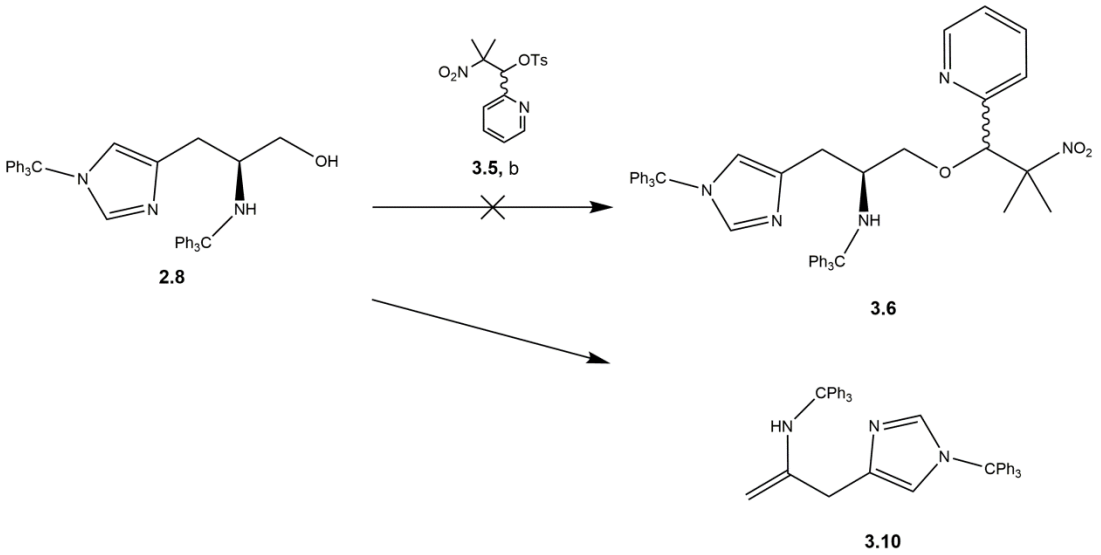

*Figure 128. Attempted synthesis of (2S)-N-tribenzyl-1-(1-tribenzyl-imidazol-4-yl)-3-[2-methyl-2-nitro-1-(pyridin-2-yl)propoxy]propan-2-amine **3.6** (a) N_2 atmosphere, Dry THF, NaH, 2-methyl-2-nitro-1-(pyridin-2-yl)propyl 4-methylbenzenesulfonate **3.5-Ots***

Having successfully synthesised compound **3.5-OTs**, the Williamson ether synthesis of **3.6** was attempted (Figure 128). Under an N_2 atmosphere in anhydrous THF, dityrl protected histidinol, **2.8**,was stirred with NaH for 45 minutes. To this slurry **3.5-OTs** was added and the reaction mixture was stirred for 24 hours. After 24 hours there had been no reaction as observed by ^{1}H NMR and ESI-MS of the crude reaction mixture, therefore the reaction was left to precede for a further 48 hours, at which point a change to the reaction mixture was observed by NMR, ESI MS and TLC. Initial purification of the reaction mixture was carried out by an organic aqueous extraction. On examination of the aqueous layer by ^{1}H NMR the presence of **3.3** in quantitative yield was identified, hence the desired product,**3.6**, had not formed. The ^{1}H NMR of the organic layer could not be fully characterised, ESI MS indicated the presence of a compound with a molecular ion $[M+H]^+$ peak of *m/z* 608.3063, which corresponds to a molecular formula of $C_{45}H_{37}N_3$,which could be tentatively assigned to the elimination product of compound **2.8**: N-tribenzy-1-(1-tribenzy-1*H*-imidazol-4-yl)-*N*-(2,2-dimethylpropyl)prop-1-en-2-amine **3.5b**

As described above, the backbone of the ligand could not be formed successfully. The lack of the desired reactivity is likely caused by the carbon, which the leaving group is located on becoming secondary as opposed to primary (**Chapter 2**). This results in increased steric crowding and as such results in a decrease in reactivity towards S_N2 reactions due to the steric bulk hindering the attack of the nucleophile. It is likely that over time the alcohol present on **2.8** was regenerated due to the presence of water which would then be able to undergo an E2 elimination reaction as previously observed in **Chapter 2**. The use of a tosyl

group also prevented the use of the *in situ* Finkelstein reaction which was shown to be necessary for reactivity observed in **Chapter 2**. As such this methodology for incorporating a linker to biotin was abandoned and the linker design was re-examined.

3.2.3 Modified Synthetic Design towards 3.12

The direct attachment of the linker into the ligand backbone *via* the Williamson ether synthesis was shown to be unfeasible and hence a new approach was required. As previously discussed (Figure 117), the pyridine ring was the alternative target for derivatization. Given that the Williamson ether synthesis had thus far shown to be the most challenging step, it was decided that this would be carried out first followed by any derivatization attempts.

Addition of any type of new linker onto the pyridine moiety would require the formation of a new C–C bond between the aromatic pyridine and the alkyl linker. The most common methodology within the literature for the formation of aromatic – alkyl bonds is the use of palladium cross-coupling, shown in Figure 129A. These cross-coupling reactions are categorized by the nature of the activated, R^2–Y group but generally occur *via* the same mechanism in which the active catalyst is a Pd(0) species. In the initial step of the reaction the aryl halide, R^1–X, undergoes oxidative addition to the metal centre. This step is followed by transmetallation of the activated alkyl group, R^2–Y, to the Pd centre followed by reductive elimination to give the desired product, R^1–R^2, shown in Figure 129B.[246]

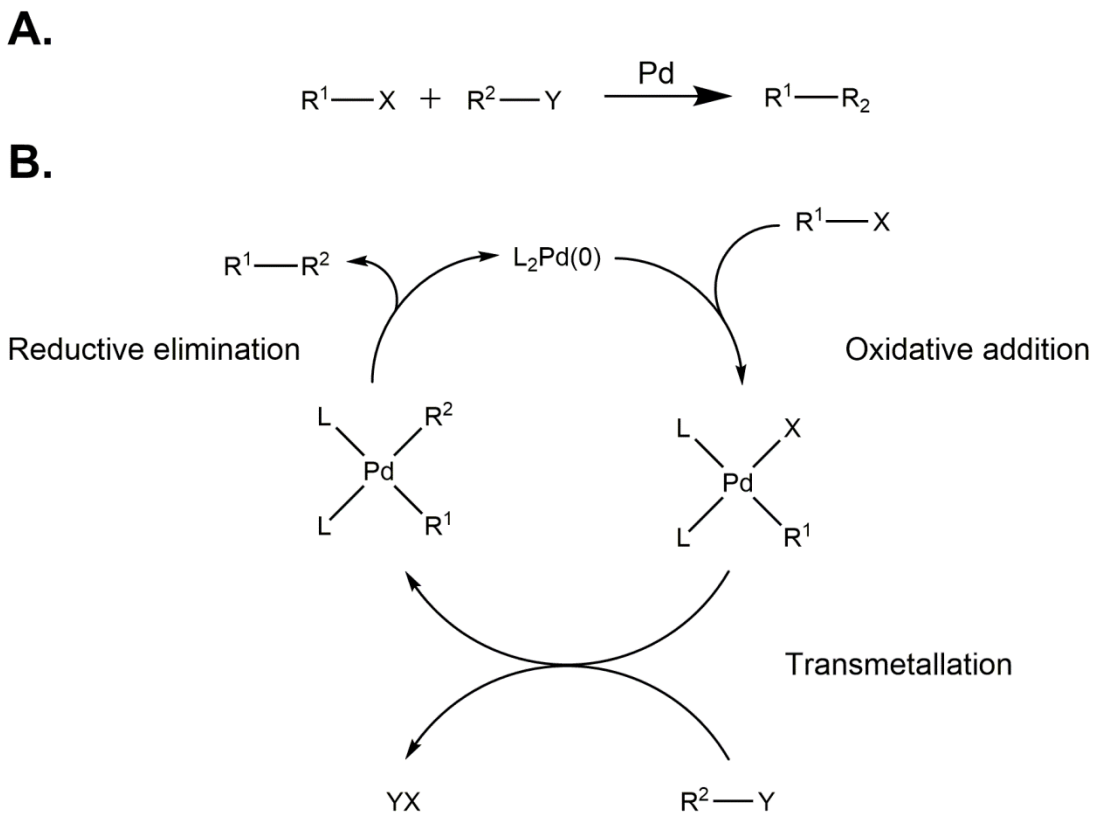

Figure 129. A. General reaction scheme for Pd cross-coupling. X = halide, triflate, tosylate. Y = -$B(OR)_2$, -SNR_3, -ZnR, -MgX, -SnR_3, Cu. B. General catalytic cycle for cross-coupling reactions

As halogenated pyridines are available for commercial purchase, the linker will fulfil the role of the activated alkyl group for transmetallation. There are several differing methodologies for the formation of C-C bonds using palladium cross-couplings described in the literature. These are Suzuki,[247] Stille,[248] Negishi,[249] Kumada,[250] Heck[251] and Sonogashira[252] reactions. Each of which perform the transmetallation step using different reagents. These procedures were examined to determine the most suitable for the system under investigation.

The Suzuki-Miyaura reaction uses organoboroic acid reagents to generate C–C bonds *via* the reaction with an organohalide in the presence of a palladium catalyst, shown in Figure 130. In the literature the Suzuki-Miyaura reaction is most commonly used for the rapid formation of bi-aryls under mild conditions.[253-254] While there are examples of sp^2-sp^3 bond formation within the literature using these conditions, they require pseudo aryl halides or activated alkyl chlorides.[255]

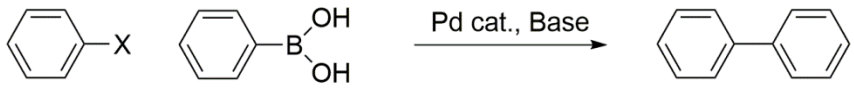

Figure 130. General reaction scheme of Suzuki-Miyaura cross-coupling. X = Cl, Br

The Stille cross-coupling reaction generates C–C bonds *via* the reaction of tributyl-tin ($SnBu_3$) with an organohalide in the presence of a palladium catalyst (Figure 131).[248] These reagents have been shown to be active for complex heterocyclic compounds and are able to perform, sp^2-sp^2 and sp^2-sp^3 couplings.[256-257] The organostannes are relatively tolerant to water and oxygen allowing for harsh conditions to be used. However, there is an inherent toxicity of tin compounds so care must be taken in both purification and handling of these reagents.

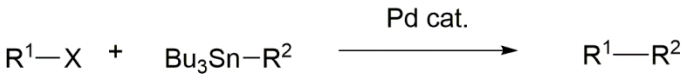

Figure 131. Reaction scheme of Stille cross-coupling. X = I, Br, Cl. R^1= aryl, hetaryl. R^2 = aryl, hetaryl, alkenyl, alkyl

The Negishi cross-coupling reaction generates C–C bonds *via* the reaction of an organozinc compound with an organohalide in the presence of a palladium catalyst, shown in Figure 132.[249] The formation of organozinc reagents is halide selective and as such allows for selective insertion into a molecule possessing multiple halides. Furthermore, transmetallation has been shown to occur faster in Negishi cross-couplings than both Stille and Suzuki cross-couplings resulting in higher yields and faster rates of reaction. However,

the reactive nature of the organozinc reagent make Negishi cross-couplings sensitive to both air and water.[249]

Figure 132. Reaction scheme of Negishi cross-coupling. R^1 = Ar. R^2= Ar. X = Cl, Br

Kumada cross-couplings generate C–C bonds *via* the reaction between a Grignard reagent and an organohalide in the presence of a palladium catalyst, shown in Figure 133.[250] These reactions are capable of forming sp-sp^2, sp^2-sp^2 and sp^3-sp^2 bonds.[258] Due to the highly reactive nature of the Grignard reagent, Kumada cross-couplings have limited functional group tolerance as they are susceptible to protonolysis under mild conditions and may attack other reactive centres across the molecule.

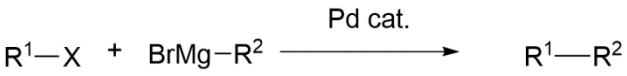

Figure 133. Reaction scheme of Kumada cross-coupling. R^1 = aryl, hetaryl, vinyl. R^2 = aryl, hetaryl, alkenyl, alkyl

Sonogashira cross-couplings generate C–C bonds *via* the reaction between an alkyne and an organohalide, in the presence of a catalytic amount of copper iodide (CuI), palladium catalyst and base, shown in Figure 134. This reaction is capable of forming sp-sp bonds from sp^2 or sp^3 organohalides and an alkyne.[259] In this reaction the transmetalation agent forms *in situ via* the reaction of Cu^+ with the alkyne. Sonogashira couplings are tolerant to water and oxygen to some degree. However, if the transmetallation step in the reaction is slow, the build-up of activated alkyne can result in homocoupling and the formation of by-products. [259]

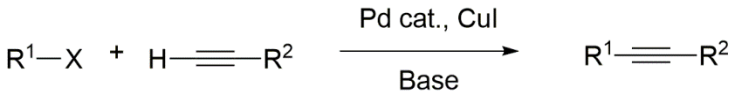

Figure 134. Reaction scheme of Sonogashira cross-coupling. X = I, Br, Cl. R^1 = aryl, hetaryl, vinyl. R^2 = aryl, hetaryl, alkenyl, alkyl, SiR_3

The Heck reaction forms C–C bonds *via* the reaction of an alkene with and an organohalide in the presence of a palladium catalyst, shown in Figure 135.[251] The Heck reaction forms sp^2-sp^2 carbon bonds from sp^2 or sp^3 organohalides and an alkene. Unlike the other Pd-catalysed crossed couplings described so far the Heck reaction is thought to occur *via* a carbometallation step rather than the transmetallation step (Figure 129B). This is followed by β-hydride elimination instead of reductive elimination to give the desired product.[260]

However, the regioselectivity of the addition is affected by both the electronics of the palladium complex and the sterics of the alkene which can result in addition to both of the alkene carbon resulting in the formation of undesired side products .[246]

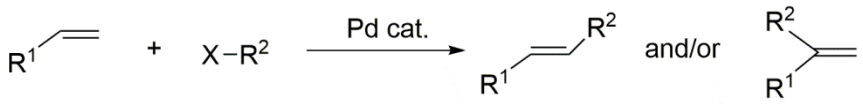

Figure 135. Reaction scheme of a Heck cross-coupling. R^2 = aryl, alkyl, hetaryls. R^1 = aryl, alkyl, hetaryls. X= I, Br, Cl, OTf.

Considering the variety of synthetic methodologies to produce new C–C bonds, an analysis of the new bond forming must be carried out. The linker is required to be an alkyl chain terminated by an amino group; therefore aryl-aryl coupling is unsuitable for this purpose. Of the remaining cross-coupling methodologies, Sonogashira cross-coupling was selected as it is selective for an alkyne and halogen, which prevents undesirable side reactions (as seen for Kumada and Heck reactions) and avoids the use of toxic reagents (used for the Stille cross-coupling).

Following the selection of Sonogashira as the methodology to perform the cross coupling reaction the design of the linker can now be examined. The linker must contain an alkyne for the Sonogashira cross coupling and an amine group for attachment to the biotin moiety. To prevent unwanted reactivity of this amine, it will have to be protected. The protecting group must have suitably different deprotection conditions than the trityl protecting groups used for the synthesis of **2.8** in order to obtain selective deprotonation of this amine prior to the desired biotinylation reaction. Trityl protecting groups are unstable under acidic, reductive and oxidative conditions, thus traditional amino protecting groups such as *tert*-butyl carbamates (BOC) or benzyl carbamates cannot be used as these require acidic conditions for removal.[261] Phthalimides (Phth) provide an excellent alternative to BOC or benzyl carbamates as they are readily deprotected under hydrazinolysis conditions for which trityl groups are stable allowing for selective deprotection to occur.[261] There are also many Phth-protected amines which are commercially available. In addition, the presence of Phth protecting groups increase the solubility in non-polar organic solvents, allowing for easier purification.[261] Therefore a Phth protected amine was selected as the terminus of the linker.

The commercially available N-propargylphthalimide, **3.16**, was selected as the basis of the linker to biotin and the resulting target molecule **3.12** is shown in Figure 136.

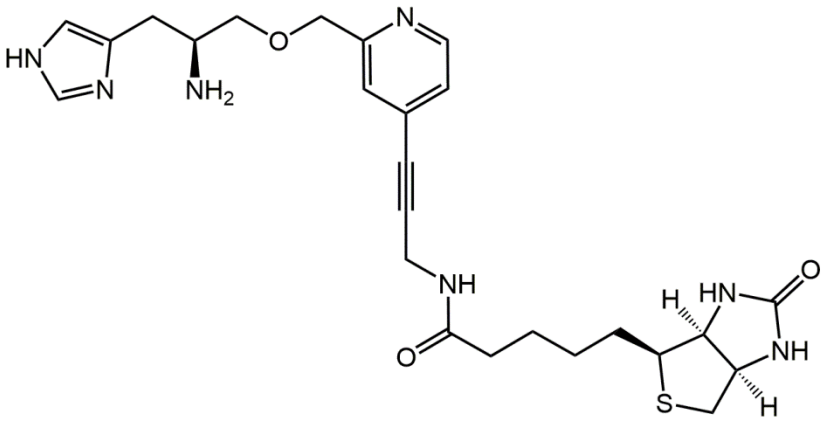

3.12

*Figure 136. Chemical structure of the modified ligand N-[(2-([2-amino-3-(1H-imidazol-4-yl)propoxy]methyl)pyridin-4-yl) pro-2-yn-1-yl)-2-(2-oxohexahydro-1H-thieno[3,4-d]imidazole-4-yl)pentamide **3.12***

3.3.4 Modified synthetic route

After establishing the target molecule **3.12**, the appropriate synthetic disconnections were assessed as shown in Figure 137 and the full synthetic route was planned as shown in Figure 138.

The initial step of the synthesis was the formation of 4-bromo-2-(chloromethyl) pyridine, **3.14**, in order to introduce a leaving group for the subsequent Williamson ether synthesis with reaction of the protected histidine **2.8** as described in **Chapter 2**.

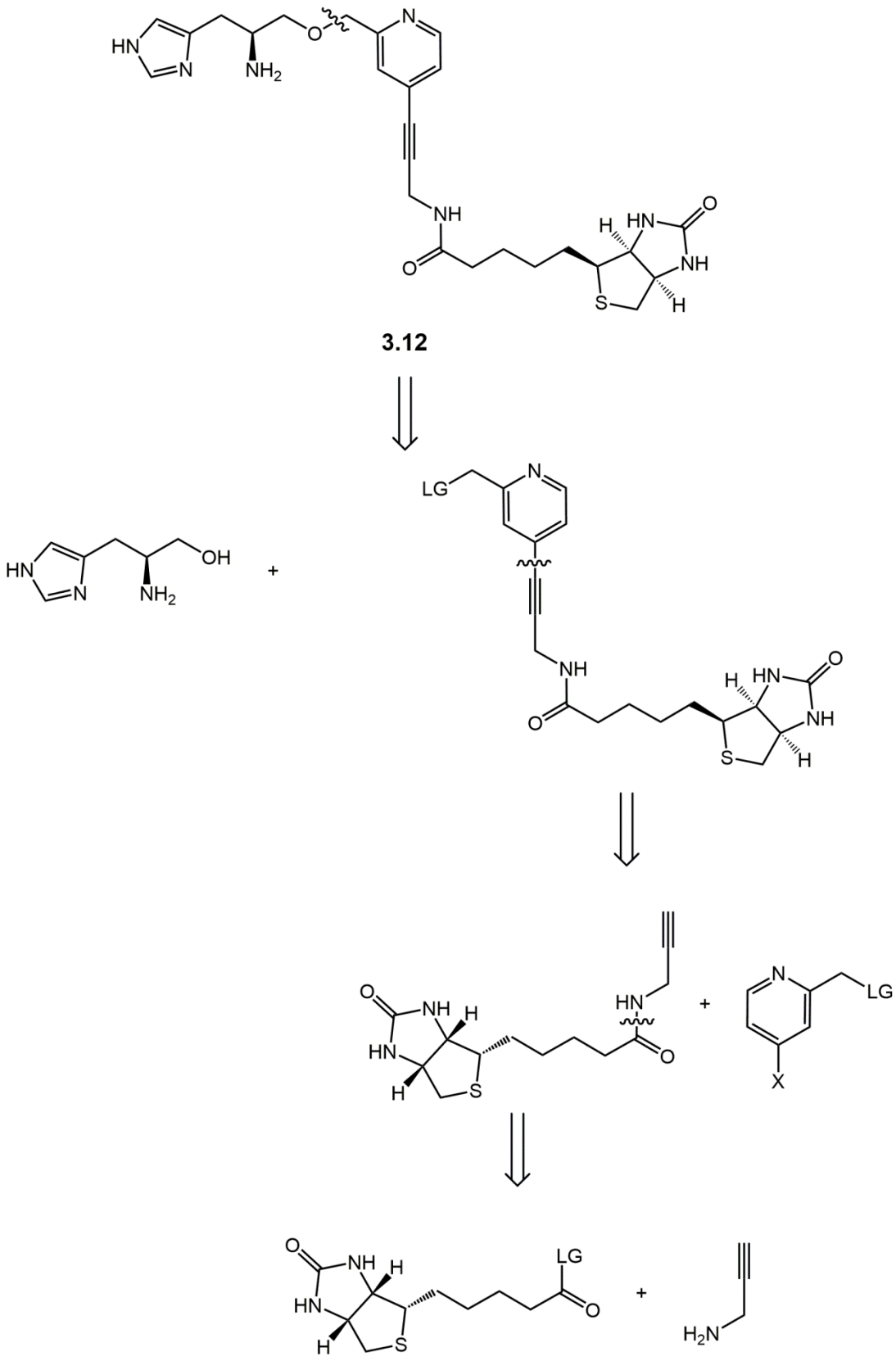

*Figure 137. Synthetic disconnections of **3.12** into its relative synthetic equivalents*

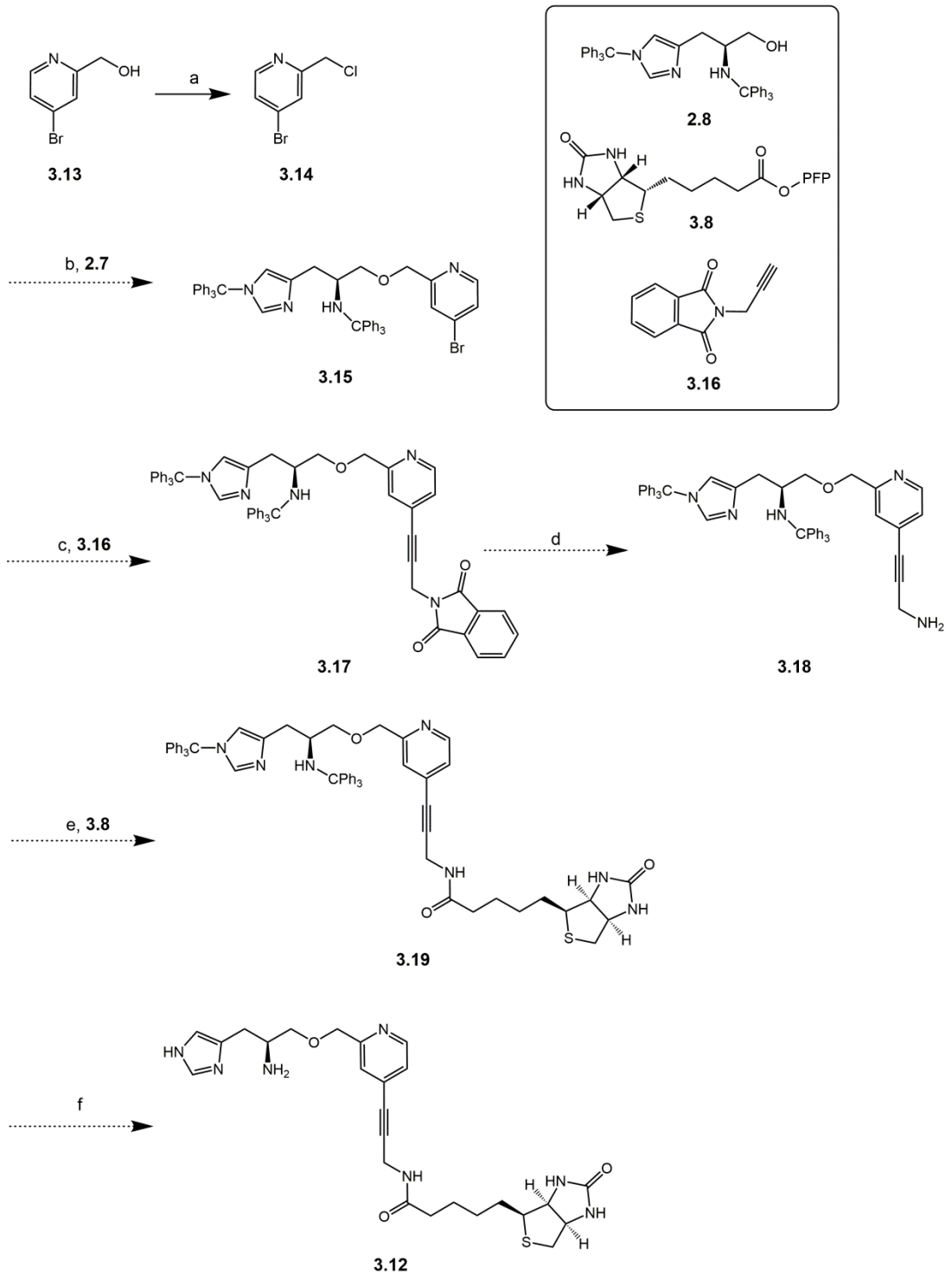

Figure 138. Initial synthetic route to form the bitionylated ligand, ***3.12*** *(a) $SOCl_2$, DCM (b) N_2 atm., Dry THF,* ***2.8****, NaH, NaI (c) N_2 atm., Dry THF, $Pd(PPh_3)_2Cl_2$, CuI* ***3.16*** *(d) EtOH, N_2H_4 (e)* ***3.8****, Et_3N, DMF (f) 1:1 THF / 3M HCl, Δ*[45]

The initial step of the synthesis involves the chlorination of 1-(4-bromopyridin-2-yl)methanol, **3.13**, which was selected as Br is known to be more reactive towards Sonogashira cross-coupling than its chloride counterpart. To carry out this reaction, **3.13** was dissolved in DCM and cooled to 0 °C, to this solution thionyl chloride was added dropwise, which was allowed to warm to room temperature and stirred for 45 minutes. The reaction was rapidly quenched with saturated sodium carbonate and immediately separated *via* the addition of DCM. This was to prevent the breakdown of **3.14** as it is prone to hydrolysis. Compound **3.14** was isolated as a dark brown oil which was characterised by ^{1}H and ^{13}C NMR spectroscopy, infrared spectroscopy and ESI mass spectrometry. The formation of **3.14** was supported by ^{1}H and ^{13}C NMR spectroscopy with the upfield shift of both the resonances corresponding to the methylene protons and the carbon, from 4.73 to 4.64 ppm and from 63.91 to 45.79 ppm, respectively. This shift was coupled with the loss of the broad singlet with relative intensity of one, which was assigned to the alcohol. In addition, the ESI-MS analysis showed a molecular ion peak $[M+H]^+$ for **3.14** at *m/z* 205.9358, consistent with a compound of formula C_6H_6NBrCl and possessing the expected isotopic pattern. In the IR spectrum the loss of the signal corresponding to the hydroxide peak in **3.13** also indicates product formation.

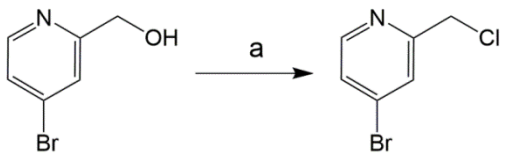

3.13 **3.14**

*Figure 139. Formation of 4-bromo-2-(chloromethyl) pyridine, **3.14** from **3.13**. (a) $SOCl_2$, DCM*

The synthesis of compound **3.15** was carried out using 1-(4-bromopyridin-2-yl)methanol **3.14**, and dityrityl protected histidinol **2.8** in the presence of NaH and NaI using the same methodology developed in **Chapter 2**, shown in Figure 140. On purification using flash column chromatography, an off-white foam was obtained in 60% yield. The compound was characterised by ^{1}H and ^{13}C NMR spectroscopy, infrared spectroscopy and ESI mass spectrometry. The formation of **3.15** was supported by ^{1}H NMR spectroscopy as the resonance corresponding to the methyl pyridine proton shifts upfield from 4.64 to 4.29 ppm, alongside the upfield shift of the protons adjacent to the alcohol in **2.8** from 3.52 to 3.20 ppm, indicating the successful formation of the ether. In addition, the ESI-MS analysis showed a molecular ion peak $[M+H]^+$ for **3.15** at *m/z* 795.2682 with the expected isotopic pattern for the presence of Br, consistent with a compound of formula $C_{50}H_{43}N_4OBr$.

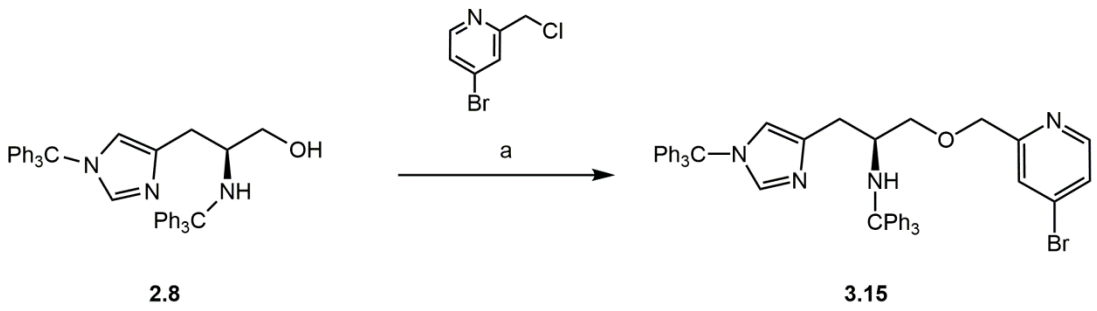

*Figure 140. Formation of 1-[(4-bromopyridin-2-yl)methoxy]-N-methyltriphenyl-3-(1-methyltriphenyl-1H-imidazol-4-yl)propan-2-amine **3.15** from ditriyl protected histidinol **2.8** (a) NaH, NaI, N_2 Atm., Dry THF*

The synthesis of **3.17** was carried out *via* a Sonogashira cross-coupling between compound **3.15** and N-propargylphthalimide, **3.17**, in the presence of $Pd(PPh_3)_2(Cl)_2$ and CuI, shown in Figure 141. In an inert atmosphere **3.15**, N-propargylphthalimide and $Pd(PPh_3)_2(Cl)_2$ were dissolved in a 1:1 mixture of Et_3N and THF and stirred for 30 minutes. CuI was added to the reaction mixture, which was heated to 80 °C for 12 hours. The reaction mixture was cooled, filtered and purified *via* flash column chromatography to give a pale yellow foam in 22% yield. This was then characterised using ^{1}H and ^{13}C NMR spectroscopy, infrared spectroscopy and ESI mass spectrometry. The formation of **3.17** was supported by the appearance of a singlet resonance at 4.66 ppm with a relative intensity of 2 which corresponds to the protons adjacent to the triple bond (shifted downfield from the starting material where the same protons have a resonance at 4.47 ppm). Two new doublets of doublets with relative integration of two also appear in the purified ^{1}H NMR spectrum at 7.90 and 7.75 ppm (J =3, 5 Hz) which is commensurate with the expected chemical shift of a phthalimide group. In addition, the ESI-MS analysis showed a molecular ion peak $[M+H]^+$ for **3.17** at *m/z* 900.3897, which is consistent with a compound of formula $C_{61}H_{50}N_5O_3$, the chemical formula of **3.17** and the peak no longer possesses the expected isotopic pattern for Br.

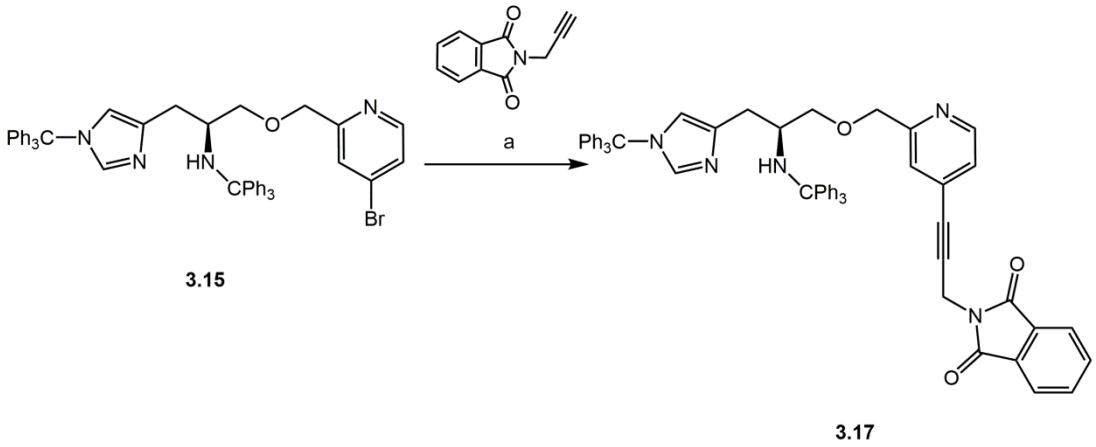

Figure 141. Formation of N-methyltriphenyl-[(2-([2-amino-3-(1-methyltriphenyl-imidazol-4-yl)propoxy]methyl)pyridin-4-yl) pro-2-yn-1-yl)-2-(2-oxohexahydro-1H-isoindole-1,3(2H)-dione ***3.17*** *from* ***3.15*** *and* ***3.16*** *(a) N_2 atm., Dry THF:Et_3N (1:1), Pd$(PPh_3)_2(Cl)_2$,CuI, Δ*

Despite the successful synthesis of **3.17**, it was in low yield and the major product formed from the reaction was instead of **3.17**, the homocoupled N-propargylphthalimide product **3.20** shown in Figure 142. Within the literature it has been demonstrated by Ho *et al.*[262] that the concentration of both CuI and O_2 has an effect on homocoupling yield. Thus the cross-coupling reaction was optimised by lowering the amount of catalytic CuI added to the solution, in an effort to increase the yield of the desired product, **3.15**. The conditions which gave the highest yield over a 12 hour reaction time was 1 mol% of CuI, giving a pure isolated yield of 79 %.

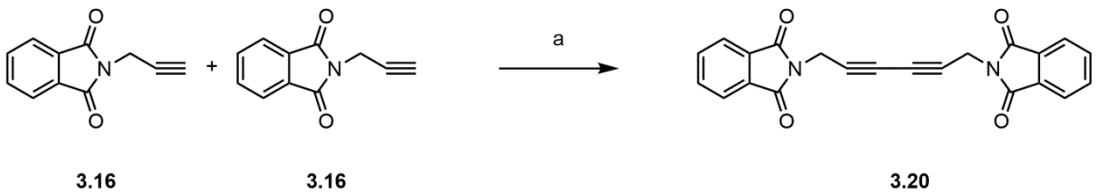

Figure 142. The competing homocoupling reaction to form 2,2'-hexa-2,4-diyne-1,6-diylbis(1H-isoindole-1,3(2H)-dione) (a) N_2 atm., Dry THF:Et_3N (1:1), Pd$(PPh_3)_2(Cl)_2$,CuI, Δ

The deprotection of the Phth group in **3.17** was carried out to give **3.18** shown in Figure 143. Compound **3.17** was dissolved in a minimum amount of DCM:EtOH mixture, hydrazine monohydrate was added and the reaction was heated at reflux for 12 hours. The reaction mixture was cooled and the major by-product, phthalhydrazide, was removed by filtration. The filtrate was washed with 1M NaOH solution to remove any residual phthalhydrazide to give compound **3.18** as an off white solid in 90 % yield.

This was then characterised using ^{1}H and ^{13}C NMR spectroscopy, infrared spectroscopy and ESI mass spectrometry. The formation of **3.18** is supported by ^{1}H NMR spectroscopy in which the two doublets of doublets with resonances at 7.90 and 7.75 ppm (J =3, 5 Hz) corresponding to the phthalimide group have been lost, but the singlet resonance corresponding to the protons adjacent to the alkyne is still present at 4.31 ppm and has shifted upfield from 4.66 in **3.17**. In addition, the ESI-MS analysis showed a molecular ion peak $[M+H]^{+}$ for **3.18** at *m/z* 770.3874, which is consistent with a compound of formula $C_{53}H_{48}N_5O$, the expected molecular formula of compound **3.18**.

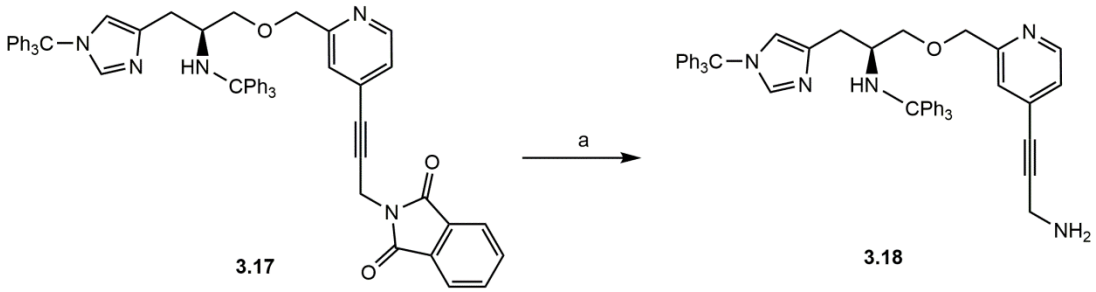

*Figure 143. Deprotection of compound **3.17** to give N-methyltriphenyl-[(2-([2-amino-3-(1-methyltriphenyl-imidazol-4-yl)propoxy]methyl)pyridin-4-yl) pro-2-yn-1-amine **3.18**. (a) N_2H_4, EtOH, DCM, Δ*

The leaving group chosen to facilitate the amide coupling between biotin and compound **3.18** was pentaflurophenyl ester(PFP) which has been shown to efficiently facilitate the formation of a biotin amide bond with the literature.[222-223, 229]

Due to the high cost of biotin-pentaflurophenyl ester, **3.8**, (£528 per gram)[263] this compound was synthesised in house following a literature procedure developed by Rizzacasa *et al.*[264], shown in Figure 144. Compound **3.8** was obtained as a white crystalline solid in 75% yield and characterised by ^{1}H NMR spectroscopy and ESI MS. The formation of **3.8** was supported by the loss of the carbonyl proton at 11.90 ppm and the peaks in the ^{1}H NMR spectrum match those given in the literature.[264]

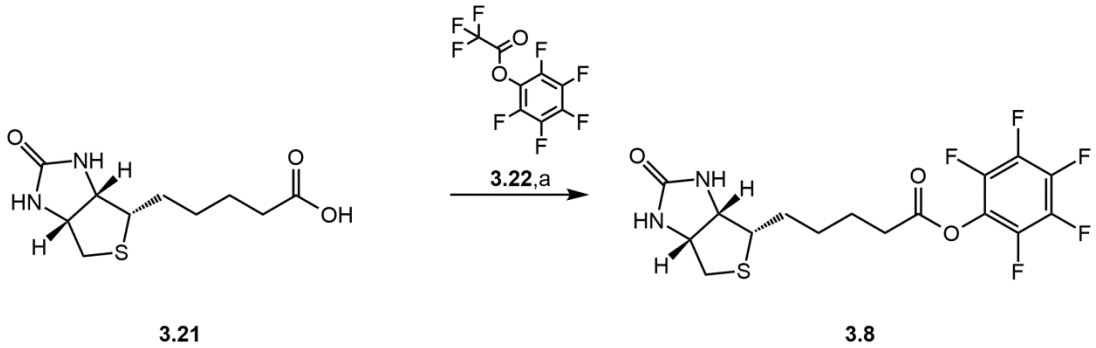

*Figure 144. Formation of biotin-pentaflurophenyl-ester **3.8** (a) pentafluorophenyl trifluoroacetate **3.22**, DMF, Et_3N*

As both compounds **3.18** and **3.8** had been successfully synthesised, they were used in the synthesis of compound **3.19**, shown in Figure 145. Compound **3.18** was dissolved in DMF and **3.8** and Et_3N were added to the solution, which was stirred for 12 hours. The reaction mixture was purified *via* flash column chromatography to give **3.19** as a brown oil, which was triturated with diethyl ether to give a white powder in 85% yield. The compound was characterised using ^{1}H and ^{13}C NMR spectroscopy, infrared spectroscopy and ESI mass spectrometry. The formation of **3.19** was supported by the ^{13}C NMR in which the resonance corresponding to the carbonyl of the new amide bond has shifted upfield after the reaction has been completed from 170.53 to 164.35 ppm. In addition, the ESI-MS analysis showed a molecular ion peak $[M+H]^+$ for **3.19** at *m/z* 996.4651 and a $[M+Na]^+$ peak at *m/z* 1018.4479, consistent with compounds of formula $C_{63}H_{62}N_7O_3S$ and $C_{63}H_{61}N_7O_3SNa$, respectively, which is the expected molecular formula of compound **3.19**. The ^{1}F NMR is featureless indicating the loss of the pentaflurophenol leaving group.

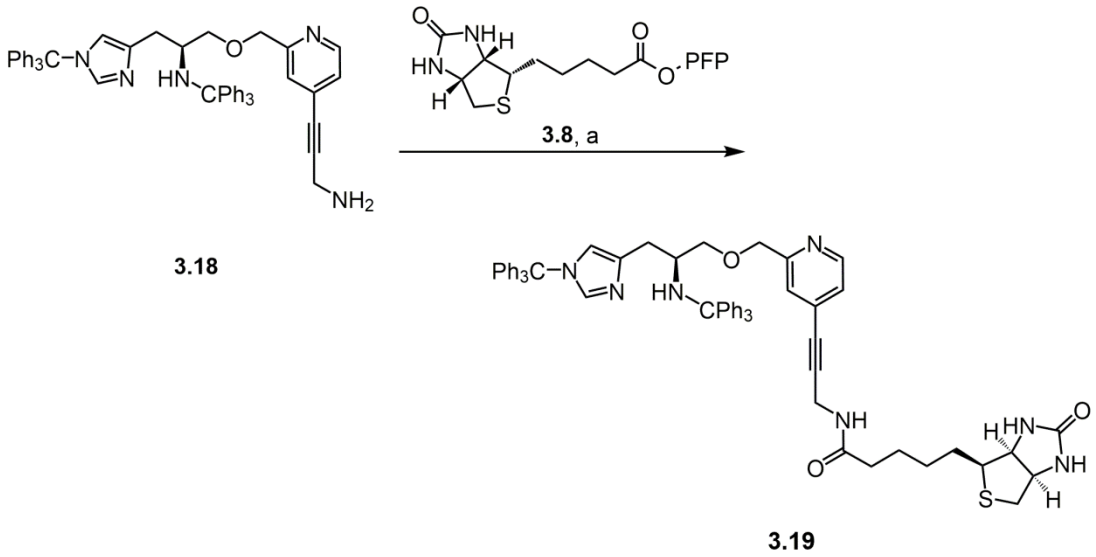

*Figure 145. Biotinylation of compound **3.18** to form N- methyltriphenyl-[(2-([2-amino-3-(1-methyltriphenyl-imidazol-4-yl)propoxy]methyl)pyridin-4-yl) pro-2-yn-1-yl)-2-(2-oxohexahydro-1H-thieno[3,4-d]imidazole-4-yl)pentamide, **3.19**. (a) Biotin-pentaflurophenyl-ester, Et_3N, DMF*

The deprotection of the trityl groups present in compound **3.19** to give compound **3.12** is shown in Figure 146. Initially, the same methodology used to form **2.3** was used, but this was shown to cause significant degradation. As such a new methodology was developed. Compound **3.19** was heated for 10 minutes in 3 M HCl and the reaction mixture was evaporated at low temperature to give **3.12** in 90% yield. This compound was characterised using ^{1}H and ^{13}C NMR spectroscopy, infrared spectroscopy and ESI mass spectrometry. The formation of **3.12** was supported by ^{1}H NMR spectroscopy in which the resonances corresponding to the trityl groups had disappeared. In addition, the ESI-MS analysis showed a molecular ion peak $[M+H]^+$ for **3.12** at *m/z* 512.2385, which is consistent with a compound of formula $C_{25}H_{34}N_7O_3S$ respectively which is the expected molecular formula of compound **3.12**.

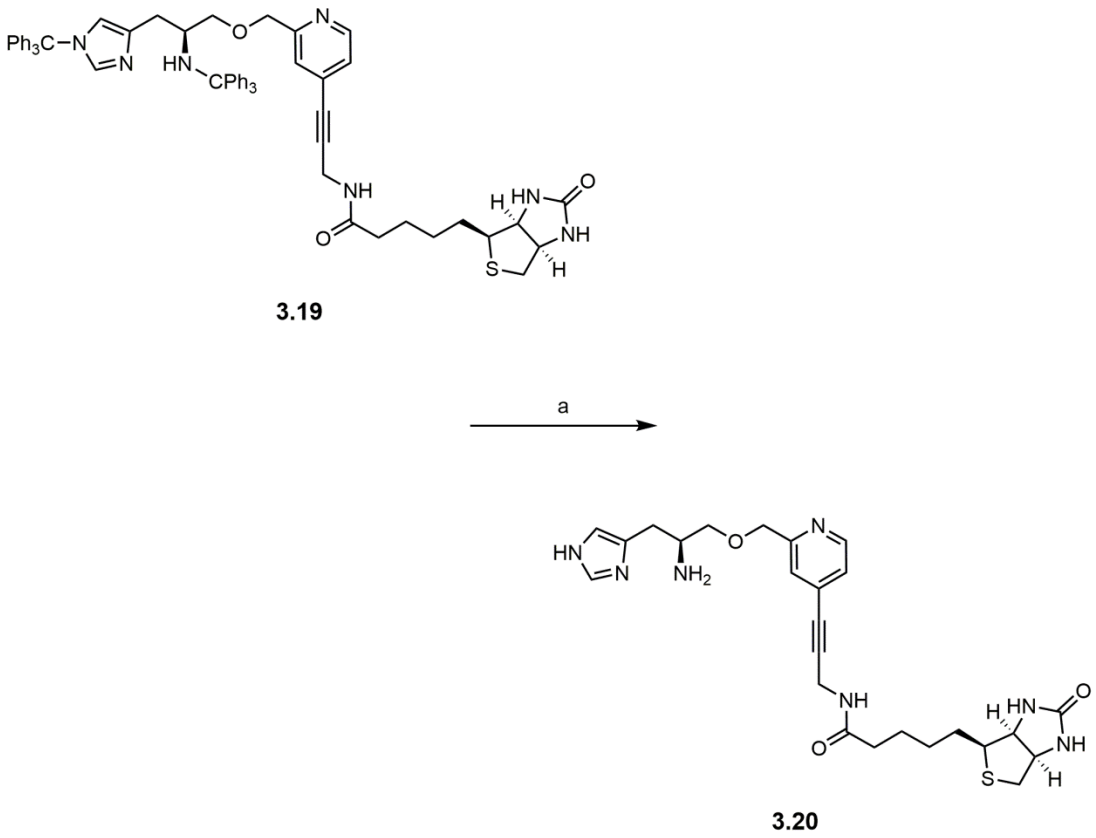

*Figure 146. Deprotection of **3.19** to form N-[(2-([2-amino-3-(1H-imidazol-4-yl)propoxy]methyl)pyridin-4-yl) pro-2-yn-1-yl)-2-(2-oxohexahydro-1H-thieno[3,4-d]imidazole-4-yl)pentamide **3.12** (a) THF, 3M HCl, Δ*

Having previously shown in **Section 2.3.2** that either the HCl salt or free base can successfully be used to synthesise the compound **Cu(2.3)X_2** and due to the small amount of compound **3.12.3HCl** available (35 mg), it was deemed that an anion exchange column would be problematic and as such the compound was left as the HCl salt.

The successful synthesis of compound **3.12.3HCl** allows for the reaction with copper salts to form their respective Cu complexes, hereafter **Cu(3.12)**. Elemental analysis was used to confirm the purity of the compound. The elemental analysis of **3.12.3HCl** gave %C, 48.37, %H, 5.85; %N, 15.82, which is consistent with a compound with the molecular formula of $C_{25}H_{36}N_7O_3SCl_3$ (Calculated %C, 48.35; %H, 5.84; %N, 15.79). The purity of the compound is reflected in the sharp melting point of 172-174 °C.

3.3 Copper Complexes

3.3.1 Synthesis of [2- -3-(1-*H* -imidazol-4-yl) propoxy]methyl)pyridin-4-yl)pro-2-yn-1-yl)-2-(2-oxohexahydro-1H-thieno[3,4-d]imidazole-4-yl) pentamide copper complexes, **Cu(3.12)X_2**

Having successfully synthesised the biotin-linked ligand, compound **3.12.2HCl**, the corresponding copper(II) complex **Cu(3.12)X_2** (X = NO_3, Cl) was synthesised in the presence of 3 equivalents of base as shown in Figure 147. This reaction was carried out in a MeOH:H_2O (8:2) solution and on addition of base the solution turned from pale blue to emerald green. Addition of diethyl ether resulted in the formation of an emerald green precipitate that was isolated *via* filtration yielding compound **Cu(3.12)X_2** in 67% and 56% yield for Cl_2 and NO_3 respectively.

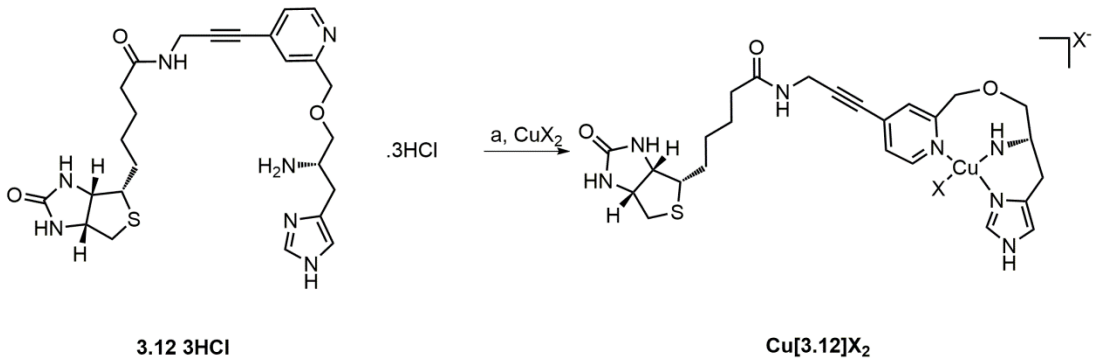

Figure 147. Synthetic scheme for the formation of Cu(2.3)X_2 (a) CuX_2, MeOH:H_2O, Et_3N, X = Cl, NO_3

It should be noted that for both **Cu(3.12)Cl_2** and **Cu(3.12)NO_3** were very hygroscopic and as such it was not possible to obtain elemental analysis of either of these compounds despite many attempts. And as such purity of these compounds could not be assessed using elemental analysis. The EPR analysis, section **3.3.2**, of the two compounds was found to exhibit a single species giving some confidence in the purity of the sample.

3.3.2 Characterisation of (1-*H* -imidazol-4-yl) propoxy]methyl)pyridin-4-yl)pro-2-yn-1-yl)-2-(2-oxohexahydro-1H-thieno[3,4-d]imidazole-4-yl) pentamide copper complexes, **Cu(3.12)X$_2$**

As expected for a d^9 Cu^{2+} system, the ^{1}H NMR spectrum of **Cu(3.12)Cl$_2$** was featureless due to the paramagnetism of the Cu ion. The ESI-MS showed the presence of the singly charged ion with the charge derived from the metal centre for compound **Cu(3.12)Cl$_2$** at *m/z* 574.1660, in agreement with the molecular formula $C_{25}H_{33}CuN_7O_3S^+$ which is expected for **Cu(3.12)$^+$.** There was no presence of a peak corresponding to the doubly charged $[M]^{2+}$ ion expected to occur at *m/z* 287.0828. Furthermore, no peak was found at the predicted *m/z* for **Cu(3.12)$_2^+$**, *m/z* 1085.4016 for the singularly charged ion or at *m/z* 542.7008 for the doubly charged ion. As previously discussed in **Section 2.3.2** the appearance of the singly charged ion is likely due to reduction in electron capture of the electrospray ionization source.[202] Therefore, the expected chemical structure for **Cu(3.12)$^+$** is shown in Figure 40.

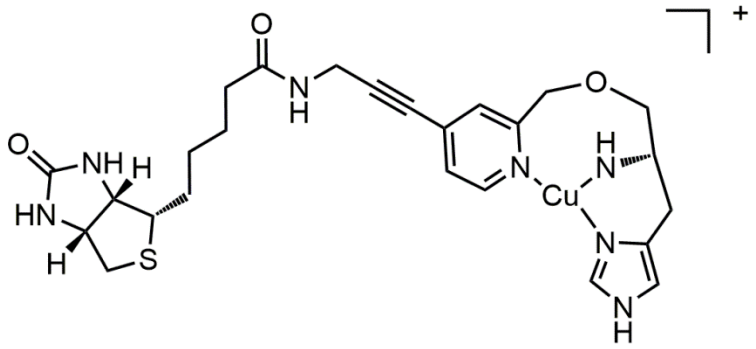

[Cu(3.12)]$^+$

*Figure 148. Proposed structure for the molecular ion peak of observed in the ESI-MS spectrum of compound **Cu(3.12)$^+$***

As in compound **Cu(2.3)**, there is the potential problem of the formation of the bis-coordinated ligand, compound **Cu(3.12)$_2$**. However, as the complex is going to be incorporated into an artificial enzyme this binding mode will be disfavoured as the vestibule is sterically crowded and the strength of biotin binding is much higher than the binding of the complex, thus favouring the monomeric binding site. This coupled with the insoluble nature of **Cu(3.12)Cl$_2$** in MeOH prevented the use of the Job's analysis carried out on **Cu(2.3)Cl$_2$** as the like the UV spectrum of **2.3** the UV spectrum of **Cu(3.12)Cl$_2$**, shown in Figure 149, is broad and generally featureless with a shoulder at ~ 545 nm which is likely a

low intensity *d-d* transition. The lack of an obvious an intense feature makes performing Jobs analysis difficult. This similarity of the UV spectra means that both the electronic and the structural environments are unchanged by the incorporation of the alkyne linker.

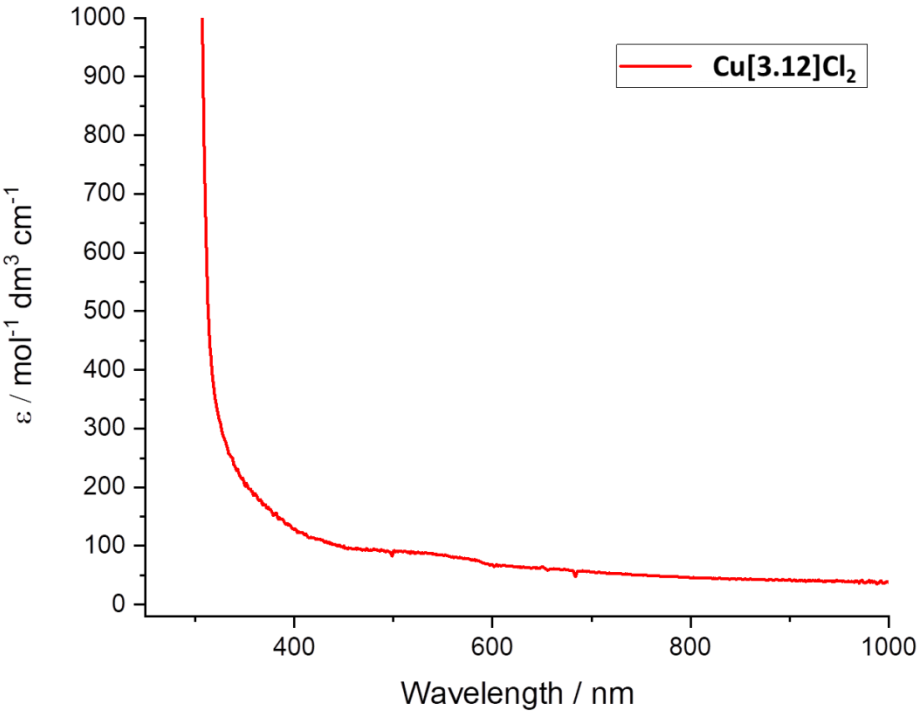

Figure 149. UV spectrum of ***Cu(3.12)Cl$_2$*** *in MES buffer (pH 6, 50 mM)*

The EPR spectrum of **Cu(3.12)Cl$_2$** in water is identical to that of **Cu(2.3)Cl$_2$**, as shown in Figure 150, spin Hamiltonian parameters are shown in Table 12 As the EPR spectrum of a particular molecule is indicative the geometry of the coordination environment and the *d*-orbital manifold of the Cu ion. These data indicate that the coordination geometry and electronic structure of the Cu is unchanged by the incorporation of both the alkyne linker and biotin moiety. Consequently, any spectroscopic changes seen on incorporation of **Cu(3.12)Cl$_2$** into the Sav host are due to a change caused by the new protein environment as opposed to an effect of the linker.

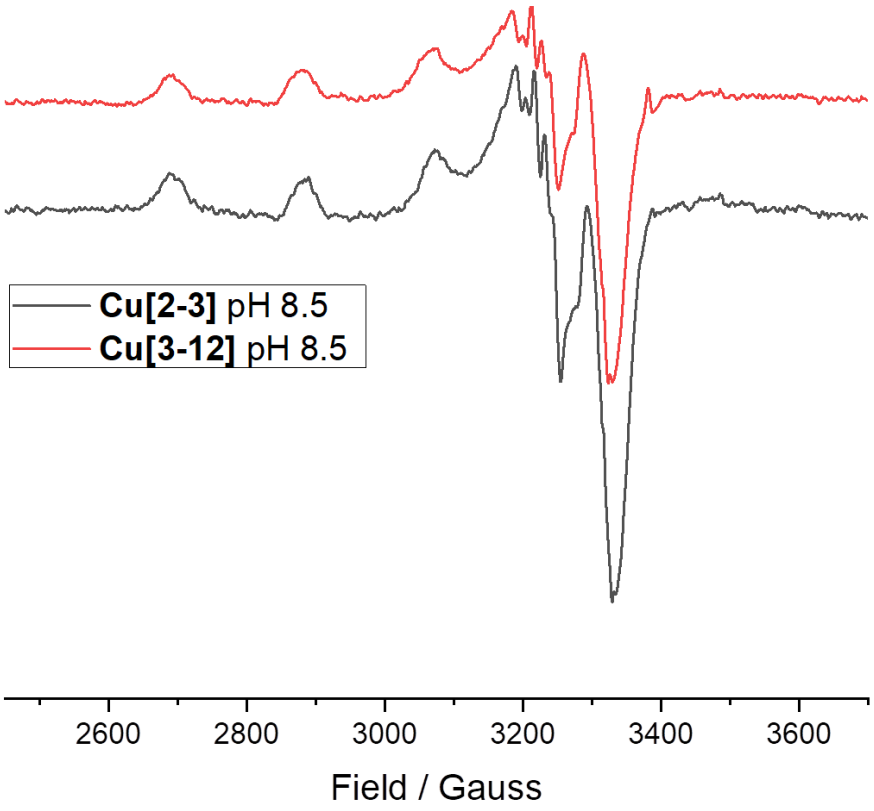

Figure 150. X- Band EPR spectra of ***Cu(2.3)Cl$_2$*** *and* ***Cu(3.12)Cl$_2$*** *pH 8.5 HEPES Buffer*

Table 12. Spin Hamiltonian parameters of ***Cu(2.3)Cl$_2$*** *and* ***Cu(3.12)Cl$_2$****. Linewidth: Gaussian = 0.3 gauss Lorentzian = 0.3 gauss*

	g			A_{Cu} / MHz			A_N
pH	g_z	g_y	g_x	A_3	A_2	A_3	
Cu(2.3)Cl$_2$	2.230	2.065	2.037	55	58	570	32, 31, 18
Cu(3.12)Cl$_2$	2.230	2.065	2.037	55	58	570	32, 31, 18

Many attempts were made to crystallise **Cu(3.12)Cl$_2$** and **Cu(3.12)(NO$_3$)$_2$** however this was severely hindered by the solubility of the complexes and remained unsuccessful, preventing full structural characterisation of the complex.

3.4 Formation and Characterisation of ArMs using **Cu(3.12)Cl_2**

3.4.1 Nomenclature of Artificial enzymes

Artificial metalloenzyme are identified by the metal complex, **M(X.Y)Z**, incorporated into the Sav host, indicated by ⊂. Any point mutation is indicated using standard nomenclature of the original amino acid code followed by the position in the amino acid sequence and terminated with the new amino acid code. For example,

M(X.Y) Z ⊂ Sav A123B

The K121A/E101Q-Sav variant used as the protein host will be referred to as Sav 2XM herein. This mutant was used in place of the wild type as it increases the space inside the vestibule for the ligand and is commonly used within the literature.[222, 229, 242]

3.4.2 Formation and Characterisation of **Cu(3.12)Cl_2⊂Sav2XM**

3.4.2.1 Formation of **Cu(3.12)Cl_2⊂Sav2XM**

Following its successful synthesis and characterisation, **Cu(3.12)Cl_2** could be incorporated into Sav. As Sav is tetrameric, the protein was treated with 4.1 eqv. of **Cu(3.12)Cl_2** in DMF and incubated for 5 minutes, at which point excess **Cu(3.12)Cl_2** was removed *via* filtration using a 10 KDa filter.

3.4.2.2 UV/Visible Spectroscopy of **Cu(3.12)Cl_2⊂Sav2XM**

The UV/Visible spectrum of **Cu(3.12)Cl_2⊂Sav** is shown in Figure 152. The incorporation of **Cu(3.12)Cl_2** into Sav2XM results in the appearance of 2 new bands (488 and 360 nm) and the shifting of the band at 543 nm. The broad band at 682 nm can be assigned as a *d-d* transition due to its low intensity ($\varepsilon \sim 100$ $M^{-1}cm^{-1}$). This is because *d-d* transitions are forbidden by the Laporte (parity) selection rule and as a result such bands have low intensity. The band at 360 nm can be assigned as a charge transfer band as it is significantly more intense than the *d-d* transition ($\varepsilon = 436$ $M^{-1}cm^{-1}$). This increase in intensity is due to the fact that charge transfer transitions are both spin and Laporte allowed resulting in a more intense transition. However, this transition is weaker than a normal charge transfer band which would be expected to have an extinction coefficient of >1000 $M^{-1}cm^{-1}$. As the intensity of a given absorption band is also dependent on the overlap of the metal and

ligand orbitals as well as the selection rules discussed above, the lower extinction coefficient could be due to the poor overlap of a streptavidin based orbital with the Cu centre resulting in a LMCT band with a low extinction coefficient. It is difficult to confidently assign the band at 488 nm as it has low intensity (ε = 150 $M^{-1}cm^{-1}$) similar to a *d-d* transition but is higher in energy than a typical *d-d* transition (CuCl = 510 nm). The appearance of these new bands is caused by the incorporation of the of the metal complex into the protein as they are not present in either the **SAV2XM** or **Cu(3.12)Cl$_2$** spectra indicating that the secondary coordination sphere provided by the protein is affecting the electronic structure of the metal complex

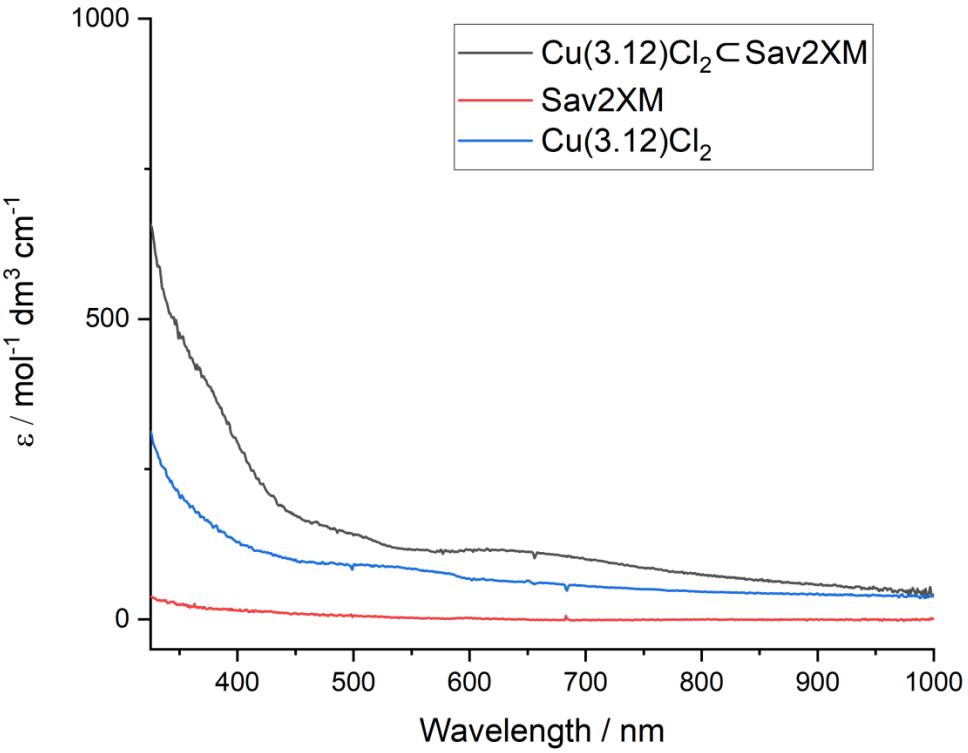

*Figure 151. UV/Visible spectrum of **Cu(3.12)Cl$_2$⊂Sav2XM**, **SAV2XM** and **Cu(3.12)Cl$_2$***

A HABA (4-hydroxyazobenzene-2-carboxylic acid) titration was used to assess the binding stoichiometry of **Cu(3.12)Cl$_2$** complexes into Sav. This methodology relies on the fact that HABA binds Sav in the biotin binding pocket with a 1:1 ratio per subunit and has a significantly lower binding constant to Sav (K_a~10^4 M^1) than biotin (K_a~ 10^{13} M^{-1}), and hence HABA is displaced on biotin binding.[265] The formation of a HABA⊂Sav complex results in an intense absorption band in the UV/visible spectrum, shown in Figure 152. The binding of biotin can be observed by the decrease in intensity of the absorption band corresponding to the HABA⊂Sav complex (λ= 506 nm)[223] as a function of increasing the concentration of **Cu(3.12)Cl$_2$**.The titrations use a large excess of HABA (150 eqv.) to ensure

complete formation of HABA⊂Sav and it is assumed that biotin quantitatively displaces HABA.

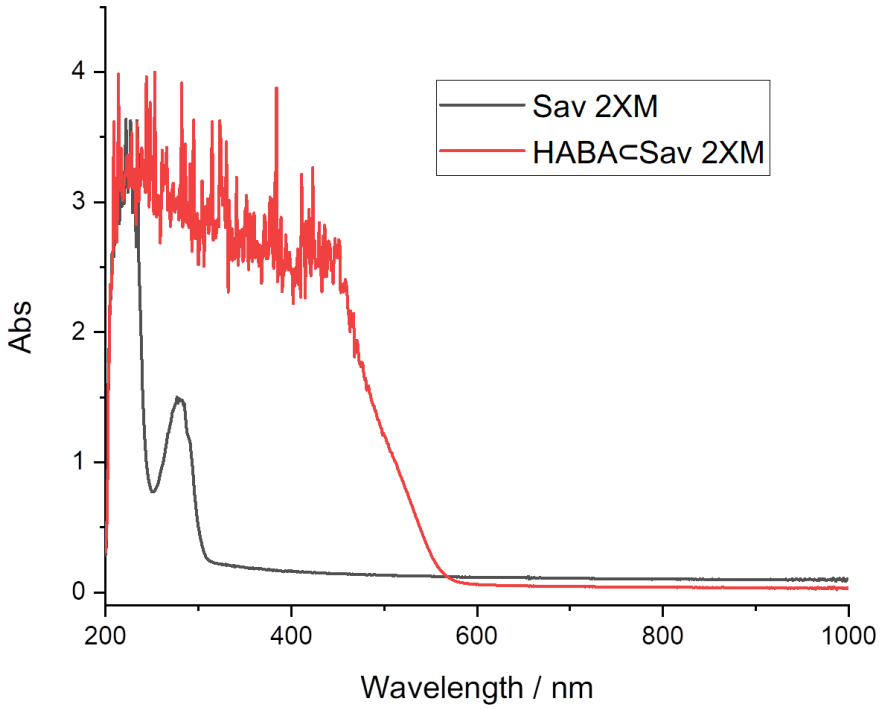

Figure 152.The UV/Vis spectrum of Sav 2XM (15 µM) before and after addition of 150 eqv. HABA at pH 7 (200mM phosphate buffer)

The intensity of the 506 nm band on addition of **Cu(3.12)Cl_2** is shown in Figure 153. The intensity of the 506 nm band shows a linear decrease until 4 equivalents of **Cu(3.12)Cl_2** have been added, at which point there is an increase in absorption. This indicates that full occupancy within Sav has been reached at a 4:1 ratio as predicted by the tetrameric structure. The increase in intensity after this point is due to the native absorption of the complex at 506 nm, as shown in Figure 152.

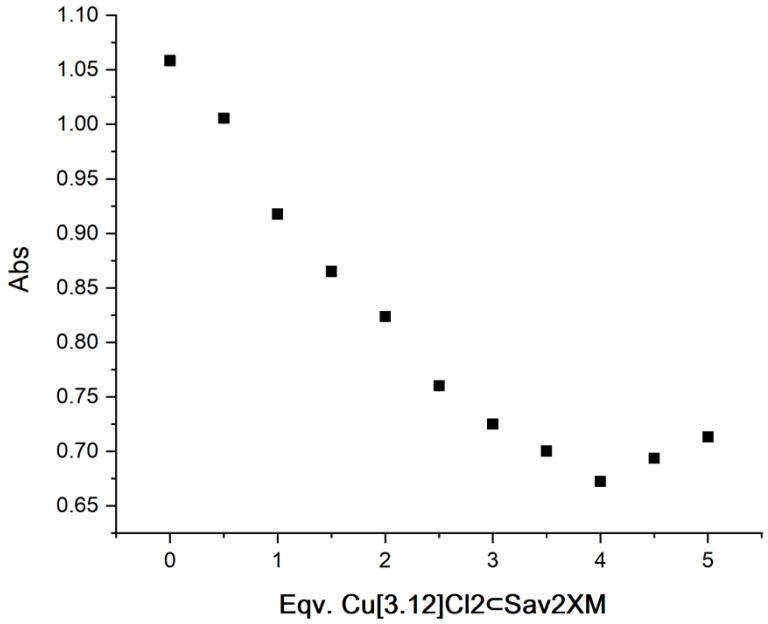

Figure 153. HABA titration of **Cu(3.12)Cl_2⊂Sav2XM**. (Streptavadin 8 µM, , HABA 10 mM, 150 equivalents) **Cu(3.12)Cl_2** in DMF (1 mM, 1 µL, 0.5 equivalents increments) at pH 7 (200 mM sodium phosphate). Titration monitored at λ_{max} = 506 nm

3.4.2.3 EPR Spectroscopy of **Cu(3.12)Cl_2⊂Sav2XM**

The EPR spectrum of **Cu(3.12)Cl_2⊂Sav2XM** and **Cu(3.12)Cl_2** at pH 8.5 is shown in Figure 154. Initial inspection of these spectra indicate the presence of more than one Cu species in the sample, corroborated by the presence of shoulders at the side of each visible hyperfine peak in the g_z region of the spectrum. It can also be noticed that the hyperfine parameters for both of these species are different to that of **Cu(3.12)Cl_2** indicating that incorporation of the complex into the protein host has changed the electronic structure of the Cu.

In order to understand the effect of the incorporation of **Cu(3.12)Cl_2** into Sav, simulations of the EPR spectra are required to extract the *g* and A values. However, the simulation of mixed spectra are difficult due to the number of overlapping parameters. This results in uncertainty in the *g* and A values hindering interpretation. Therefore, each species must be individually assigned before undergoing analysis. As previously shown for **Cu(2.3)Cl_2** in section **2.2.2.3**, the speciation of the complex was affected by the pH of the solution. Hence, a pH titration was carried out for **Cu(3.12)Cl_2⊂Sav2XM**, shown in Figure 155

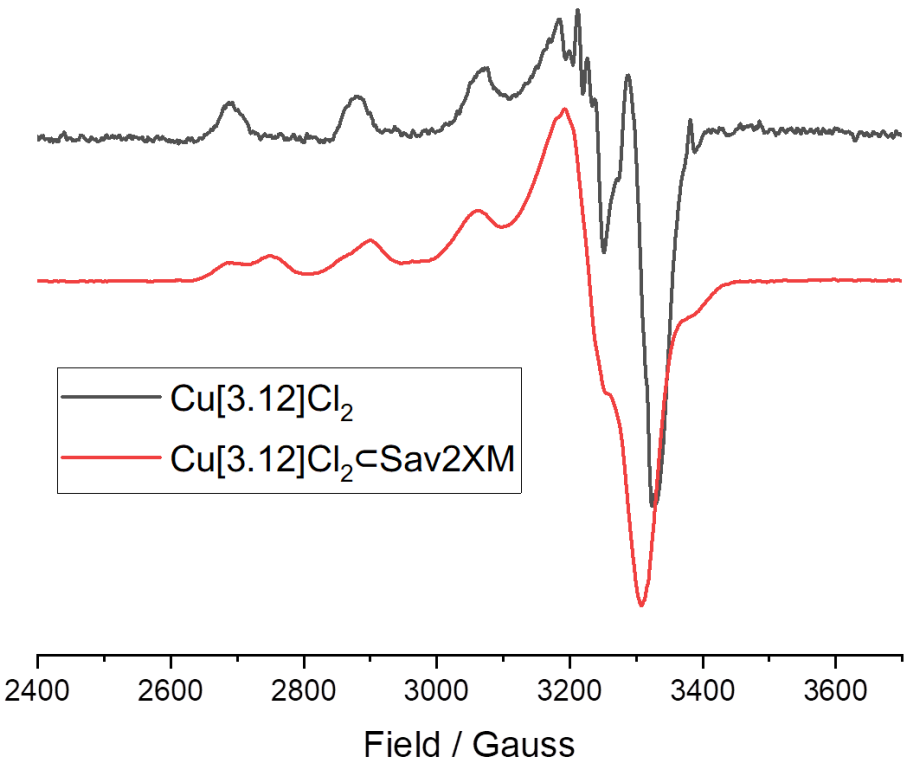

*Figure 154. The X-Band EPR spectrum of **Cu(3.12)Cl_2⊂Sav2XM** pH 8.5 MES buffer*

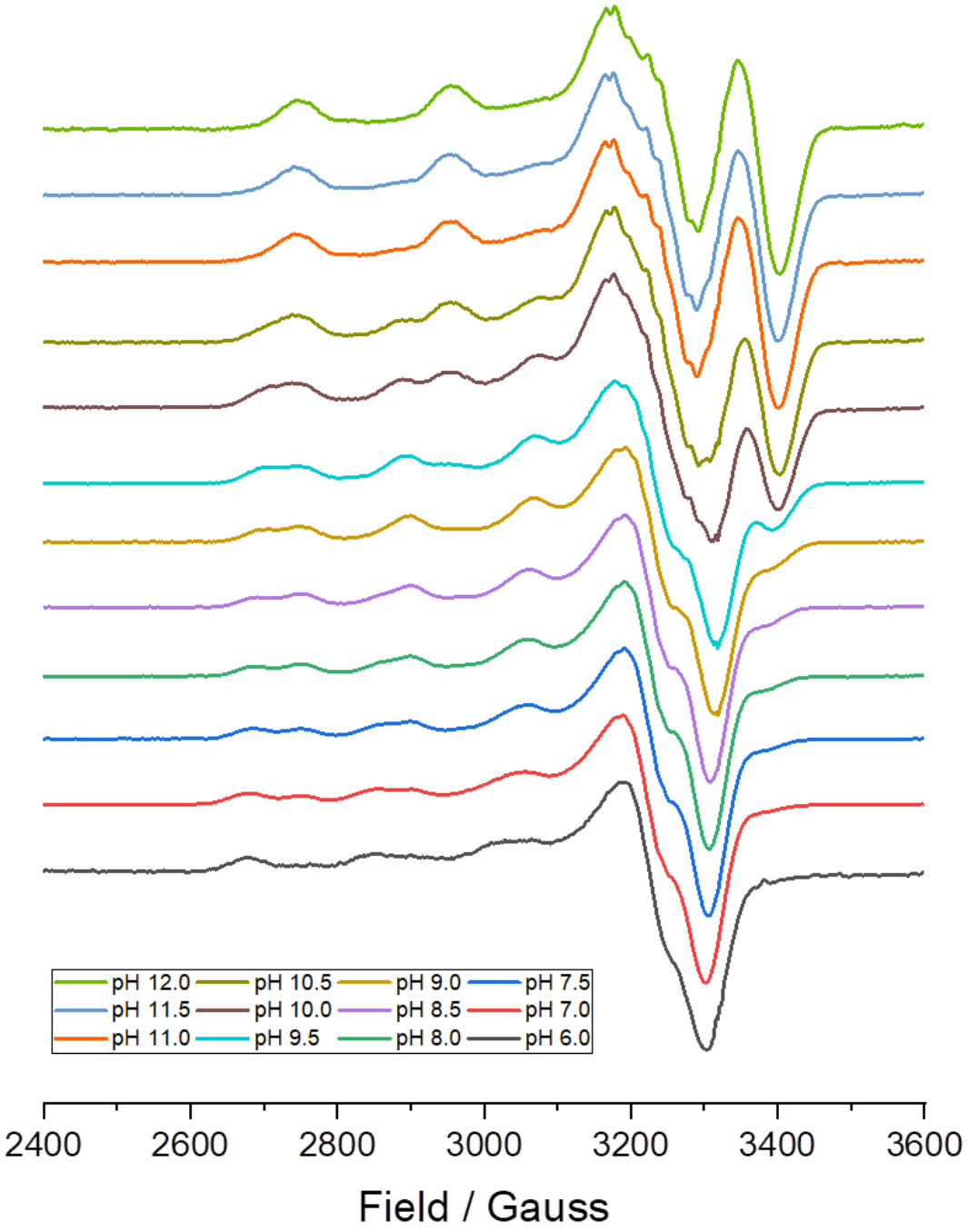

Figure 155. X-Band EPR spectra of ***Cu(3.12)Cl$_2$⊂Sav2XM*** *at varying pH in mixed buffer solution (5 mM MES, 5 mM HEPES, 5 mM CHES, 5 mM Sodium phosphate)*

Observation of the g_z region of the pH titration data it reveals that a minimum of three species are interconverting as the pH becomes more basic. This indicates that once **Cu(3.12)Cl$_2$** is incorporated into Sav the protein facilitates additional enviroments or protonation states than observed for **Cu(2.3)Cl$_2$** for which only two species are present across this pH range. **Cu(3.12)Cl$_2$⊂Sav2XM** was not stable at high enough concentration below pH 6 to record sutible EPR spectra so these spectra are ommitted.

The nature of the species can be assigned using the resulting EPR parameters. In order to extract the contribution from each of the species, subtraction spectra were used to identify the EPR parameters. As a general procedure, the spectrum containing a mix of species A and B was subtracted from the spectrum of either A or B (depending which of the two components is the lowest in intensity and/or which spectra of the pure species were available), using the g_z region as a reference to determine the "amount" of species to subtract, i.e. subtraction proceeds until the peaks corresponding to the minor species are removed in the g_z region. Once all of the parameters for each spectrum were identified simultaneous simulations were used to identify the weighting of each species present in the spectrum, as decribed in section **2.2.2.4**

As the EPR spectra of **Cu(3.12)Cl_2⊂Sav2XM** above pH 11 could be identified as a single species and as such was simulated initially. The EPR spectrum of **Cu(3.12)Cl_2⊂Sav2XM** is shown in Figure 156, observation of the g_z region of the spectrum shows the presence of only two resonances present. This is a consequence of the low g_z and high A_z values (2.172 and 620 MHz) resulting in the g_z region of the spectrum overlapping with the g_{xy} region. The low g_z and high A_z results in the appearance of the overshoot feature observed at 3375 G. The phenomenological explanation of the overshoot feature is that it is caused by an off axis turning point which arises when the hyperfine pattern (A value) expands faster than the decrease in *g*, during the molecular orbital transition. As such the highest resonance 'overshoots' the lowest *g* value and as such appears as an additional resonance.[266]

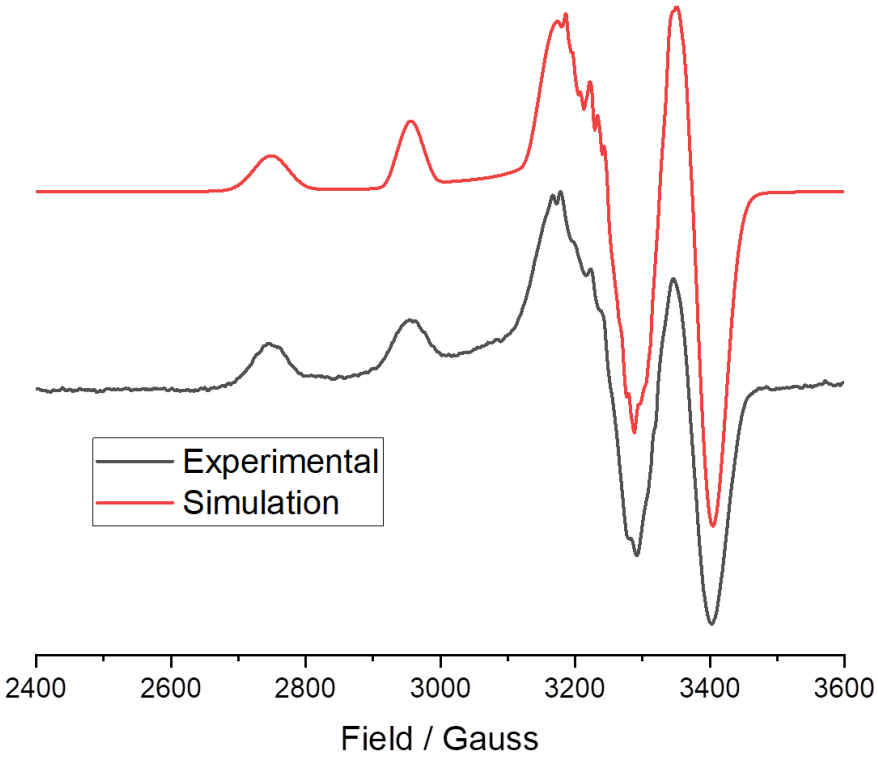

Figure 156. X-Band EPR spectrum of ***Cu(3.12)Cl$_2$⊂Sav2XM (S1)*** *pH 12 in a mixed buffer solution (5mM MES, 5 mM HEPES, 5 mM CHES, 5 mM Sodium phosphate)*

The spectra of Cu(3.12)Cl_2-Sav2XM at pH 11 was fully simulated (Figure 156) to obtain the full set of spin Hamiltonian parameters of **Cu(3.12)Cl_2⊂Sav2XM** at pH 11, referred to as **S1**. The simulations were performed using the same methodology detailed in section **2.2.2.2.** The simulated spectrum and full set of spin Hamiltonian parameters are shown in Figure 156 and Table 13.

Table 13. Spin Hamiltonian parameters for ***Cu(3.12)Cl$_2$⊂Sav2XM*** *at varying pH. N.B for* ***S2*** *and* ***S3*** *g_{xy} A^N are unreliable due to the nature of the subtraction procedure. G = Gaussian L = Lorentzian*

	g			A_{Cu} / MHz			A^N	Line Width / Gauss	
Species	g_z	g_y	g_x	A_z	A_y	A_x		G	L
S1	2.172	2.053	2.02	620	45	97	32, 41, 13	0.3	0.3
S2	2.23	2.076	2.04	565	47	16	35, 31, 18	0.3	0.3
S3	2.236	2.069	2.036	455	65	40	35, 30	0.5	0.5
S4	2.246	2.077	2.048	530	40	20	37, 30	2	2

The EPR spectrum of **Cu(3.12)Cl_2⊂Sav2XM** at pH 10 is shown in Figure 157. From initial inspection of the g_z region of the spectra it can be seen that there are five resonances present within the sample. This clearly indicates that within the solution there are multiple Cu environments present within the sample as the maximum expected for a Cu signal is four (2nI+1). Two of these resonances occur at the same field in **S1**, (2739 and 2950 G) indicating that one component of the mixture is **S1**.

As **S1** can be identified within the sample it is now possible to conduct a subtraction from the pH 10 spectrum in order to facilitate simulations of the second species. The subtraction was carried out using the loss of the features at 2739, 2950 and 3390 G to determine what percentage of the **S1** was removed as these features clearly belong to **S1** present in the sample. The resulting subtraction spectrum is shown Figure 157.

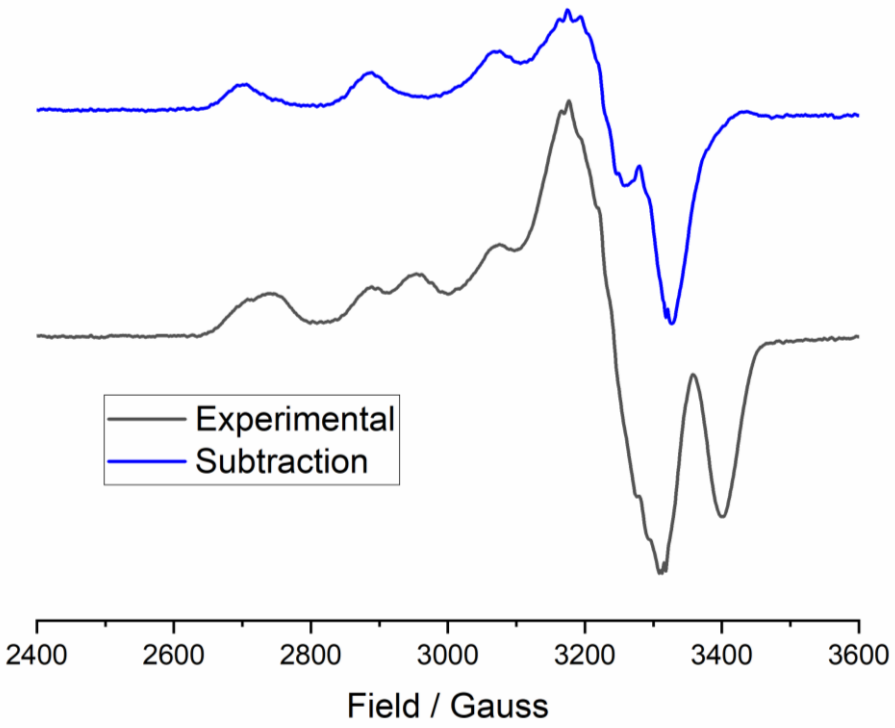

*Figure 157. X-Band EPR spectrum of **Cu(3.12)Cl_2⊂Sav2XM** pH 10 in a mixed buffer solution, black, and after subtraction of 31% of high pH species, blue. (5 mM TRIS, 5mM MES, 5 mM HEPES, 5 mM CHES, 5 mM sodium acetate)*

The g_z region of the subtraction spectrum shown in Figure 157 features three evenly spaced hyperfine peaks due to the nuclear splitting provided by the Cu (A_z = 570 MHz), whilst the fourth overlaps with the g_{xy} region of the spectrum. From this, it can be assumed

that this is a single Cu environment present in the sample; this environment is hereby identified as **S2**.

The subtraction spectrum can be simulated to give the full spin Hamiltonian parameters of the second species, shown in Figure 50 and Table 1. The simulation of this spectrum proved particularly challenging, in particular for the feature at 3275 G. However, this peak may be an artefact from the subtraction process as its intensity is dependent on the percentage of S1 species removed. This means that the precise g_{xy} vales are unreliable including super hyperfine coupling parameters.

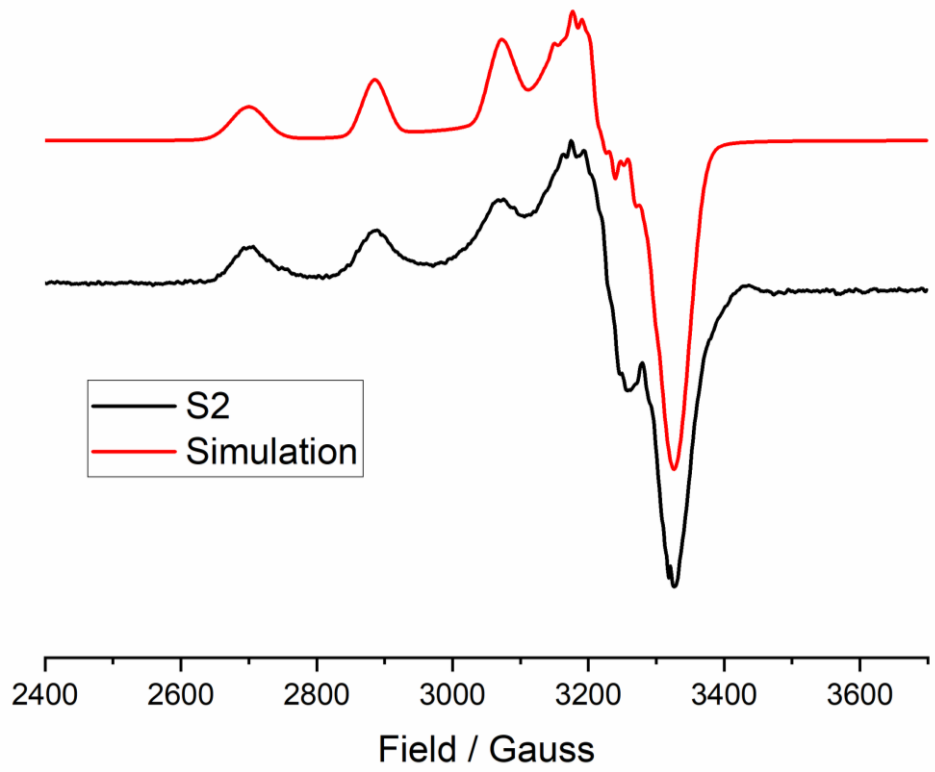

Figure 158. Simulation of the subtraction spectrum of ***Cu(3.12)Cl$_2$⊂Sav2XM*** *pH 10,* ***S2***

In order to confirm both the identity of **S2** and to probe the nature of the peak at 3275 G, a second subtraction was carried out on the EPR spectrum of **Cu(3.12)Cl$_2$⊂Sav2XM** at pH 9.5, shown in Table 13, using the same methodology previously. The subtraction spectrum revealed one of the hyperfine features in the z region of the spectrum showed a clear shoulder, with a new resonance occurring at a higher field (2760 G) to either **S1** or **S2** where the lowest field peak occurs at 2740 and 2702 G respectively. This indicates there is a third Cu environment present in solution with the other resonances masked by those corresponding to **S2**. Therefore, a further subtraction can be carried out by removing a

percentage of **S2** previously identified to reveals the EPR spectrum of the 3rd species, **S3**, present in the sample.

This resulting spectrum has been simulated to obtain an estimate of the spin Hamiltonian parameters. Due to the low intensity and manipulations carried out on the data, the spectrum, shown in Figure 159, is noisy and thus contains several artefacts. The resulting simulation of **S3** is shown in Figure 160 and reported in Table 13. As with **S2** due to the inherent noise present in this spectrum only the g_z and A_z region of the spectra can be reported with a high degree of certainty.

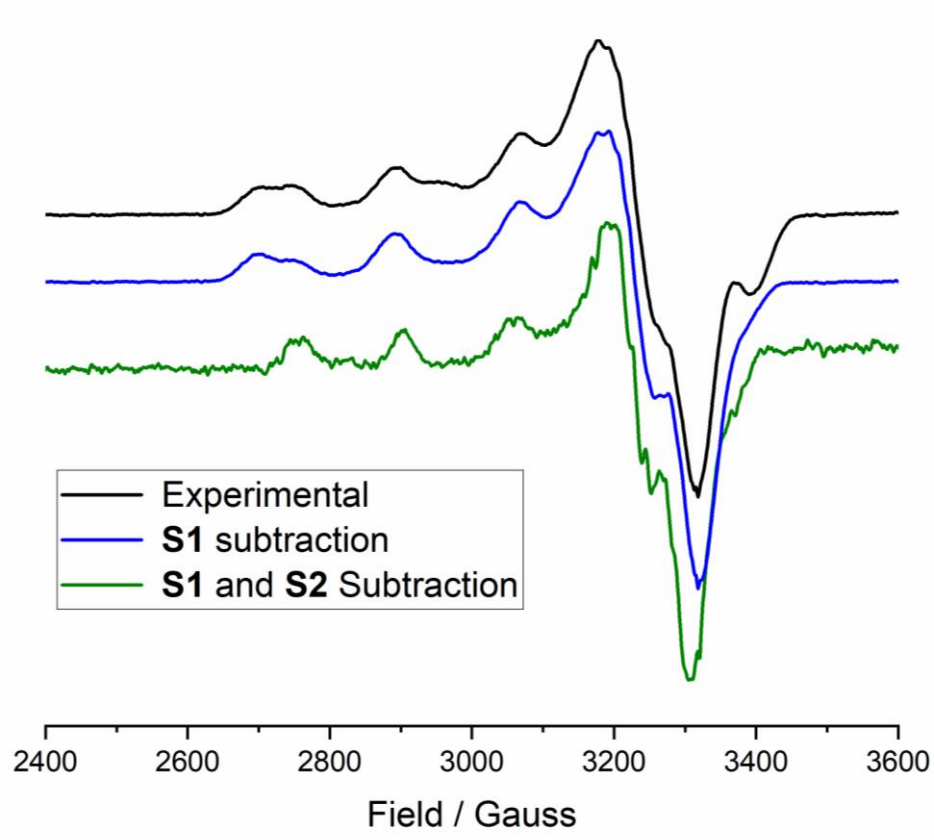

Figure 159. ***Cu(3.12)Cl$_2$⊂Sav2XM*** *at pH 9.5 in a mixed buffer solution and subtraction spectra after removal of 10% of* ***S1*** *species and after further removal of 50%* ***S2*** *(buffer: 5 mM TRIS, 5mM MES, 5 mM HEPES, 5 mM CHES, 5 mM sodium acetate)*

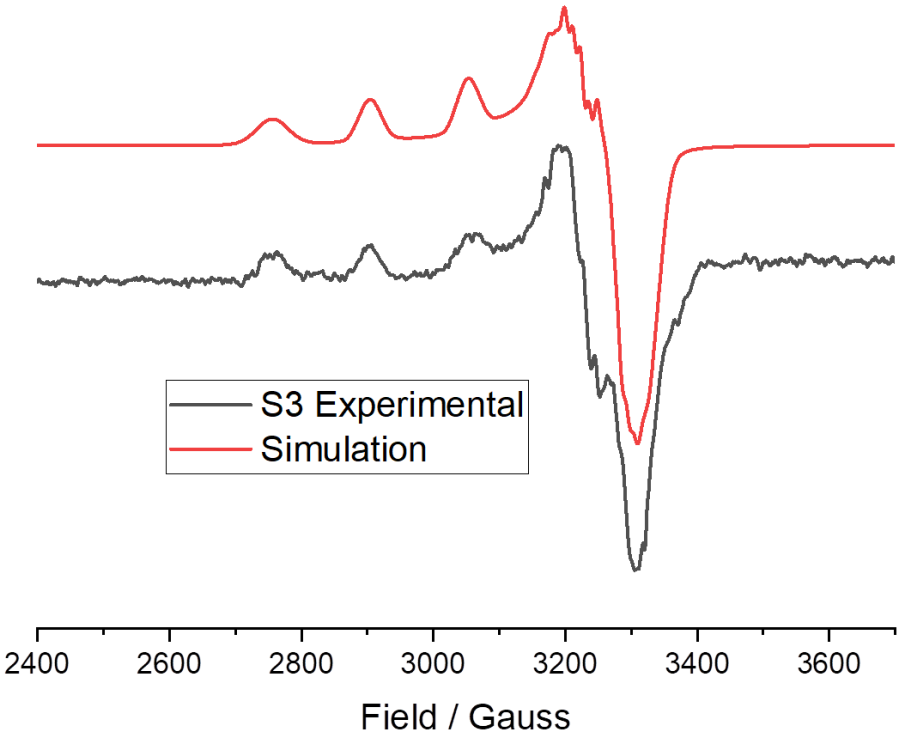

*Figure 160. Simulation of the subtraction spectrum of **Cu(3.12)Cl$_2$⊂Sav2XM** pH 9.5 after subtraction of **S1** and **S2**, in a mixed buffer solution. (5 mM TRIS, 5mM MES, 5 mM HEPES, 5 mM CHES, 5 mM Sodium acetate)*

Observation of all spectra across the varying pH of **Cu(3.12)Cl$_2$⊂Sav2XM** (Figure 155) indicates that a fourth species, **S4**, is present in the sample. The percentage of **S4** present in the sample appears to increase as the pH decreases, as highlighted by the increase in intensity of the low field resonance (~2670 G).

S4 is the predominant species present in the EPR spectra at pH 6, Figure 161. From observation of the data there are shoulders present on the resonances in the g_z region of the spectrum indicating that there is a second species present in the sample. Therefore, a subtraction spectrum was used to remove any **S3** present in the spectrum to allow for **S4** to be simulated fully, shown in Figure 162. Following this, **S4** was simulated to obtain the spin Hamiltonian parameters. Due to the uncertainty of the g_{xy} region of the spectra present in **S3** the g_{xy} parameters in **S4** will also be uncertain. As such a large line width (2.0 Gauss) was used during the simulations and hence A_N coupling is not reported.

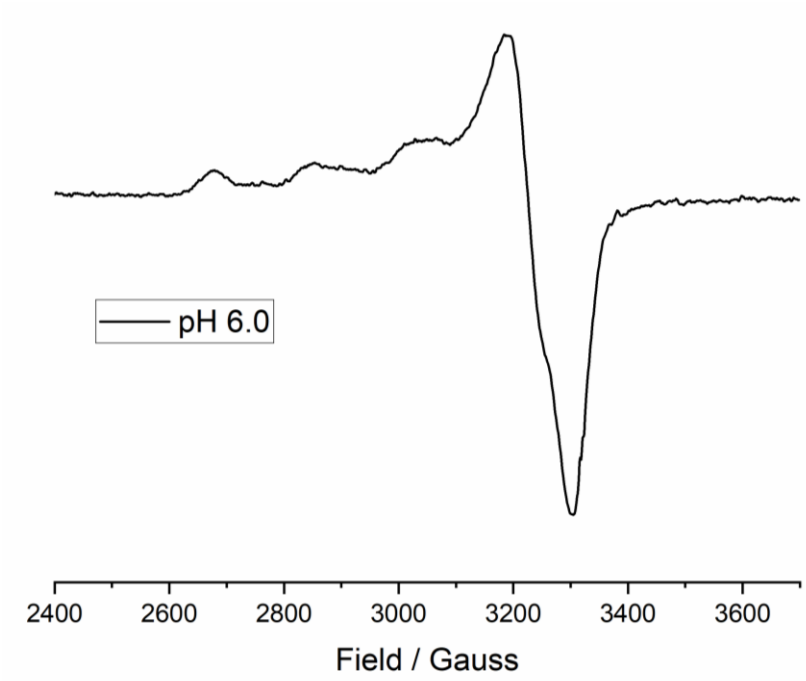

Figure 161.The EPR spectrum of ***Cu(3.12)Cl$_2$⊂Sav2XM*** *at pH 6.0*

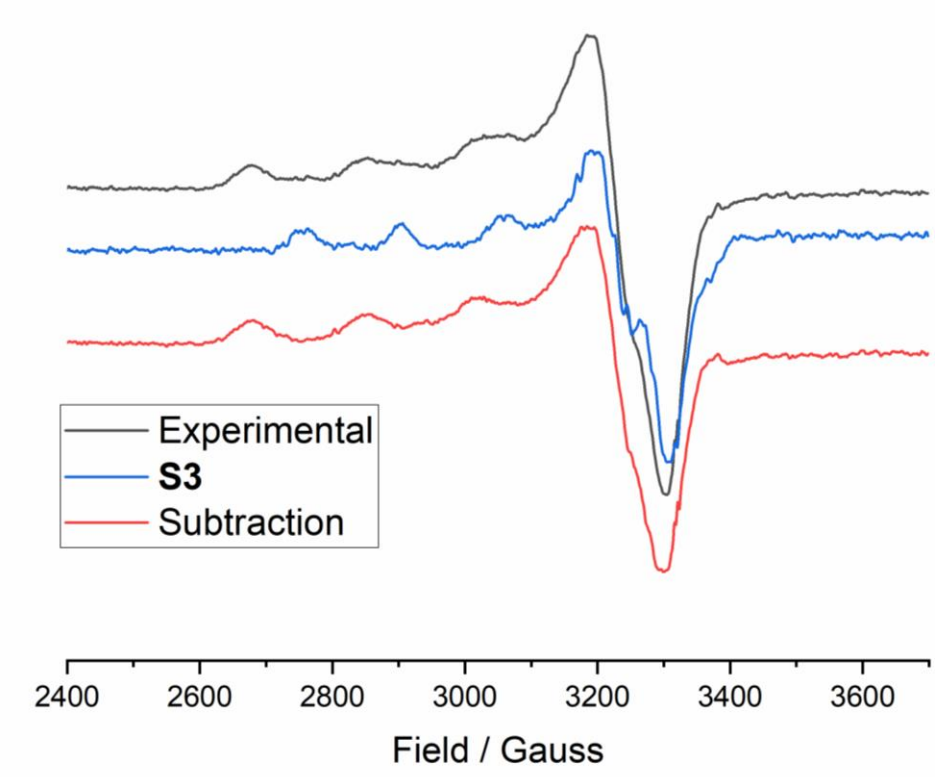

Figure 162. ***Cu(3.12)Cl$_2$⊂Sav2XM*** *at pH 6 in a mixed buffer solution and subtraction spectra after removal of 5% of* ***S3*** *(buffer: 5 mM TRIS, 5mM MES, 5 mM HEPES, 5 mM CHES, 5 mM sodium acetate)*

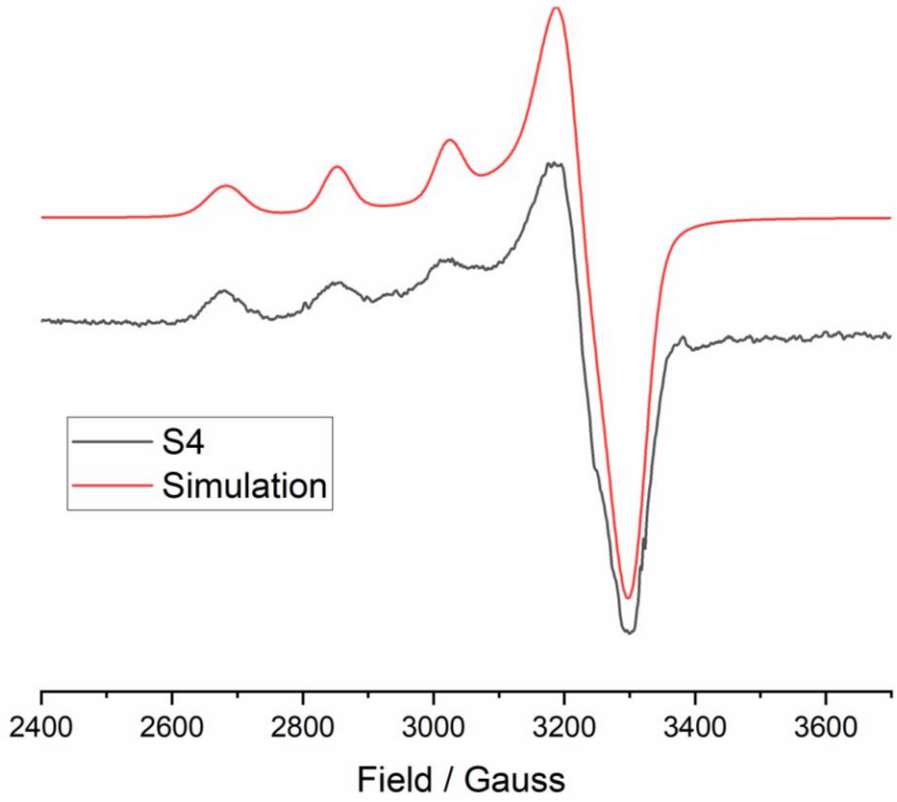

Figure 163. Simulation of the subtraction spectrum of ***Cu(3.12)Cl$_2$⊂Sav2XMat*** *pH 6,* ***S4****, after subtraction of* ***S3*** *in a mixed buffer solution. (5 mM TRIS, 5mM MES, 5 mM HEPES, 5 mM CHES, 5 mM Sodium acetate)*

Having obtained the spin Hamiltonian parameters for the g_z region of the four species present in the sample (**S1, S2, S3, S4**) it is possible to estimate the amount of each species present at a given pH by addition of a weighting factor in to the simulations. Following that, it is then possible to estimate a pK_a for each of the processes. The amount of each species present in each spectrum is shown in Table 14 and is plotted as a function of pH in Figure 164. However, there are many combinations of the variables at low pH where 3 overlapping species are present and intensities of these spectra are chosen by hand, there is potential for a large degree of human error introduced into these simulations. Due to the number of combinations which produce an adequate simulation the variation in speciation is represented by the error bars, shown in Figure 164.

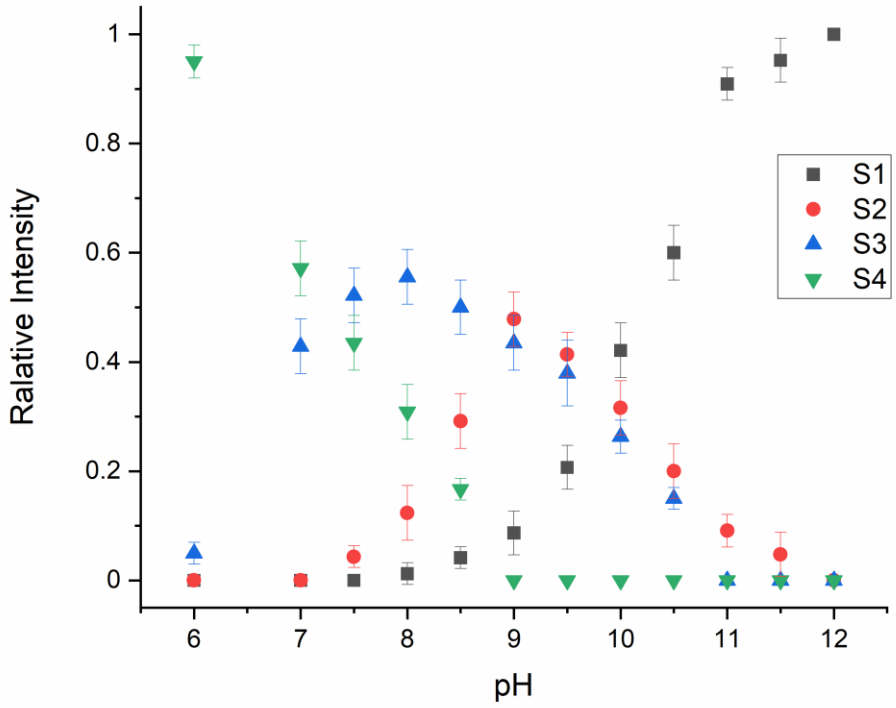

*Figure 164. Speciation plot of **S1**, **S2**, **S3** and **S4** of **Cu(3.12)Cl_2⊂Sav2XM** at various pH values*

*Table 14. Speciation of **Cu(3.12)Cl_2⊂Sav2XM** at varying pH used in Figure 164*

pH	S1	±S1 Variation	S2	±S2 Variation	S3	±S3 Variation	S4	±S4 Variation
6.0	0.00	0.00	0.00	0.00	0.05	0.02	0.95	0.03
7.0	0.00	0.00	0.00	0.00	0.43	0.05	0.57	0.05
7.5	0.00	0.00	0.04	0.02	0.52	0.05	0.43	0.05
8.0	0.01	0.02	0.12	0.05	0.56	0.05	0.31	0.05
8.5	0.04	0.02	0.29	0.05	0.50	0.05	0.17	0.02
9.0	0.09	0.04	0.48	0.05	0.43	0.05	0.00	0.00
9.5	0.21	0.04	0.41	0.04	0.38	0.06	0.00	0.00
10.0	0.42	0.05	0.32	0.05	0.26	0.03	0.00	0.00
10.5	0.60	0.05	0.20	0.05	0.15	0.02	0.00	0.00
11.0	0.91	0.03	0.09	0.03	0.00	0.00	0.00	0.00
11.5	0.95	0.04	0.05	0.04	0.00	0.00	0.00	0.00
12.0	1.00	0.00	0.00	0.00	0.00	0.00	0.00	0.00

Using the Henderson-Hasselbalch equation discussed in **Section 2.2.2.3** it is possible to obtain estimates of the pK_a of each. The intensities reveal that below pH 7 and above pH 11.5 there is a single Cu species present within the sample, **S4** and **S1** respectively. Assuming that each interconversion step is a protonation/deprotonation event as opposed to changes in coordination the formation of **S1** has an apparent pK_a of 10.5; formation of **S2** has an apparent pK_a of 8.5 and formation of **S3** has an apparent pK_a of 6.5. However, it should be noted that a coordination change unrelated to the pH may be occurring.

The pK_a of **S2** is similar to that observed in **Cu(2.3) (section 2.2.2.3)**, which could indicate that the same process is occurring. This process is likely the deprotonation of the exogenous ligand, H_2O, to form a hydroxide, OH^-. The pK_a of this processes is commensurate with the experimentally observed pK_a value for the deprotonation of $[Cu(H_2O)_6]^{2+}$ which has been found to be 8.[267] On comparison of the spin Hamiltonian parameters of **S2** and the **Cu(2.3)Cl_2** pH 9 species (Table 15) it the parameters are similar, supporting the assignment.

*Table 15. Selected spin Hamiltonian Parameters of **S2** and **Cu(2.3)Cl_2** at pH 9. Line widths: Gaussian = 0.3 Gauss Lorentzian = 0.3 Gauss*

		g			A_{Cu} / MHz	
Species	g_z	g_y	g_x	A_z	A_y	A_x
S2	2.230	2.076	2.040	565	47	16
Cu(2.3)Cl_2 pH 9	2.230	2.065	2.037	570	58	55

The species defined as **S1** is of particular interest, as not only does it possess significantly different *g* and A values to all other species observed for **Cu(3.12)Cl_2⊂Sav2XM**, but also because at high pH, specific LPMOs, *e.g. Bl*AA10*,* exhibits similar spin Hamiltonian parameters to **S1**, shown in Figure 165. Understanding what coordinative or conformational change results in the formation of **S1** may provide experimental insight to the changes observed in LPMOs.

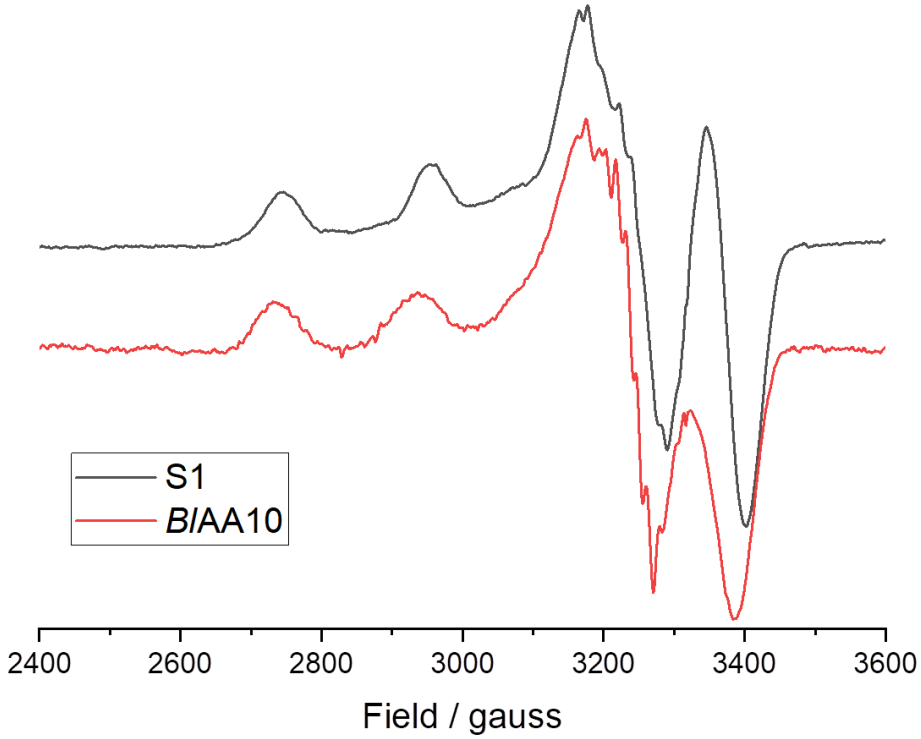

*Figure 165 A comparison of the X-Band EPR spectrum of **BlAA10** at pH 12 and **S1**. BlAA10 EPR spectrum provided by Peter J Lindley*

S1 is not observed at high pH in the same pH titration experiment seen for **Cu(2.3)** described in **Chapter 2**. This implies that the observed change in coordination environment is induced or facilitated by the nearby protein environment.

The potential causes for the change in spin Hamilton parameters upon formation of **S1** are examined**.** For the formation of **S1,** there are two possibilities, shown in Figure 166, the formation of **S1** from **S2** exclusively or from both **S2** and **S3** simultaneously. In both cases the formation of **S4** results in large changes to both g_z and A_z values from 2.240 and 455 MHz in **S3** and 2.236 and 455 MHz in **S2** respectively to 2.172 and 620 MHz in **S1**. In both cases there is a significant reduction in g_z and a significant increase in A_z. However, as **S2** has been assigned as the **[Cu(2.3)(OH)]**$^+$ it is likely that the formation of **S1** occurs exclusively from **S2**.

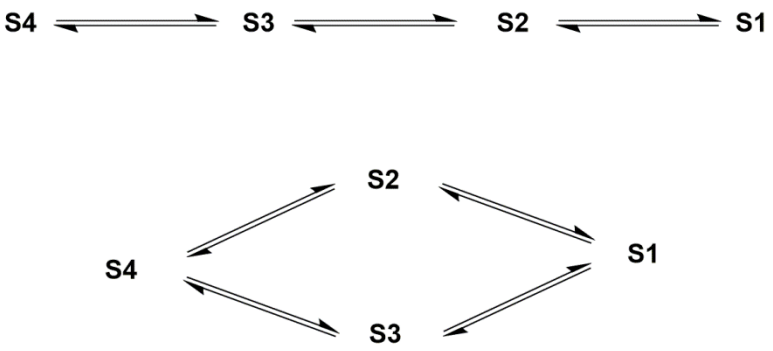

*Figure 166. Possible routes for the formation of **S4***

The pK_a of ~10.5 for **S1** allows for the prediction of the (potential) candidate for the amino acid which is responsible for the change in Cu *g* and A values. This change could be induced *via* either direct coordination to the Cu centre by a new ligand or the induction of a change in the hydrogen bonding network present in the vestibule on deprotonation. The amino acids with a side chain pK_a of 10-11 are tyrosine and lysine and thus are potential candidates.[268] Inspection of the amino acid sequence and crystal structure of **SavWT** reveals a lysine residue nearby the estimated location of the active site, K121, (Figure 167).However, this residue is not present in **Sav2XM** in which the K121A mutation is made. Therefore this hypothesis can be discounted.

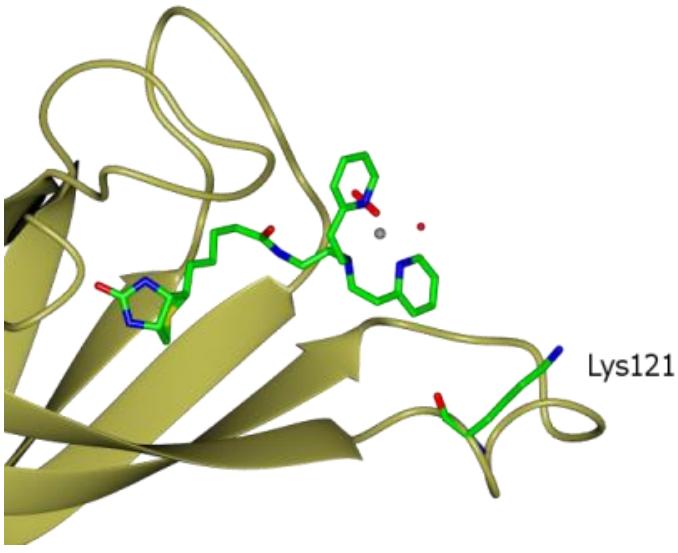

Figure 167. A streptavidin artificial enzyme [Cu(biot-et-dpea)(H_2O)($H_2O_2^-$)]$_2^+$ ⊂ Sav WT (PDB 6ANX) indicating the lysine close to the Cu site

To aid in the identification of the potential cause of this change, all of the species identified by the pH titration were compared to complexes and proteins found within the literature. This comparison was carried out using Peisach-Blumberg plots which use the values of g_z and A_z to gain insight in to the nature of the ligands and the charge present on the Cu ion based on previously characterised proteins and model complexes.[168]

Assuming that the coordination geometry remains unchanged, so that Cu is coordinated by 3 nitrogen atoms and one oxygen atom (3N1O), the following Peisach-Blumberg plot can be plotted, shown in Figure 168. Initial inspection of this plot shows that **S1** is both the highest and left most point. This indicates that that **S1** is either an anion or dianion as it lies significantly left and above a negatively charged triglycine complex, TRG^-; this supports the assignment of the complex as having a formal -2 charge. However, it should be noted that the inclusion of LPMOs onto the plot highlights the potential problem with using a Peisach-Blumberg plot to assign charge. LPMOs are clustered in what has been assigned a singular positive charge whereas they have a formal +2 charge. This highlights the effect of weakly coordinating axial ligands on the location within the Peisach-Blumberg plot and as such these insights must be used cautiously.

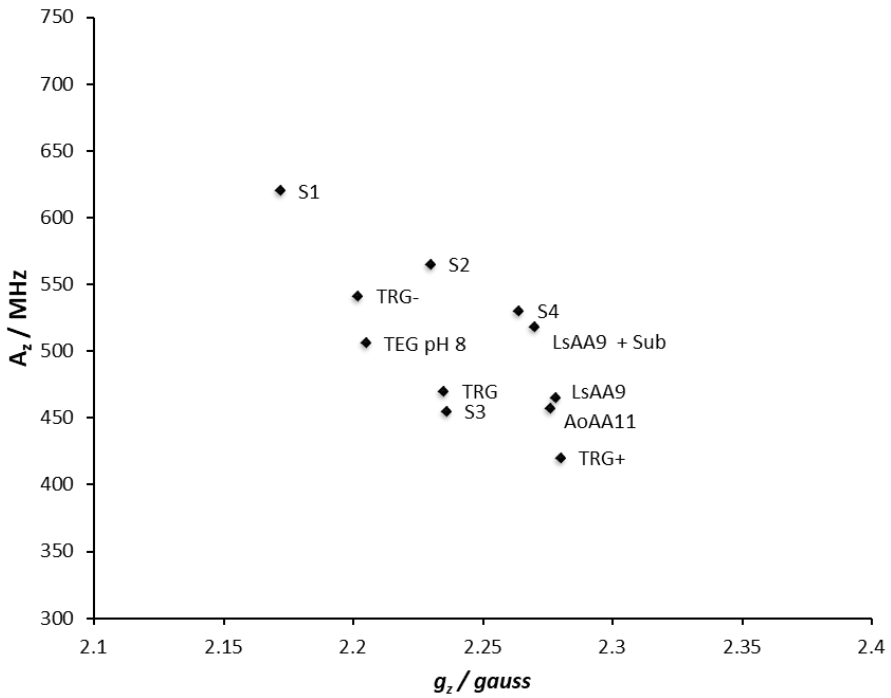

Figure 168. ***S1-4*** *plotted on Peisach-Blumberg plot of Cu(II) proteins with primary coordination spheres consisting of 3 nitrogen atoms and 1 oxygen atom (3N1O) adapted from Arch. Biochem. Biophys.* ***1974,*** *165 (2), 691-708*

Table 16. Table of g_z and $|A_z|$ of various 3N1O Cu(II) sites, used in Figure 168

Species	Abbreviation	g_z	A_z	Reference
$Cu(3.12)Cl_2 \subset Sav2XM$	**S1**	2.172	620	This work
$Cu(3.12)Cl_2 \subset Sav2XM$	**S2**	2.230	565	This work
$Cu(3.12)Cl_2 \subset Sav2XM$	**S3**	2.236	455	This work
$Cu(3.12)Cl_2 \subset Sav2XM$	**S4**	2.264	530	This work
$[Cu(Glycly)_2Glycine]^+$	**TRG+**	2.280	420	*Crawford et al.* [269]
$[Cu(Glycly)_2Glycine]$	**TRG**	2.235	470	*Crawford et al.* [269]
$[Cu(Glycly)_2Glycine]^-$	**TRG-**	2.202	541	*Crawford et al.* [269]
*Ls*AA9	**LsAA9**	2.278	465	*Frandsen et al.*[109]
*Ls*AA9	**LsAA9 + Sub**	2.270	518	*Frandsen et al.*[109]
$[Cu(Glycly)_3Glycine]^+$	**TEG pH 8**	2.205	506	*Vanngard et al.*[270]
*Ao*AA11	**AoAA11**	2.276	457	*Hemsworth et al*[101]

Using the equations discussed in section **2.2.2.2** it is possible to calculate the covalency of the ground state α_{GS}^2 and the various contributions to the A values, A^{Fermi}, A^{SD} and A^{SO} for all of the possible values of A_{iso}. As the value of A_{iso} value is dependent on the signs of the A values and as it is not possible to calculate the signs of the A values from a CW EPR experiment all possible A_{iso} values were calculated and used in subsequent calculations shown in Table 18. The general trend shows that the ground state covalency, α_{GS}^2, either remains approximately the same or becomes significantly more ionic. As the position of **S1** on the Peisach-Blumberg plot indicates that the overall charge of the complex has decreased it would be commensurate with the α_{GS}^2 value increasing due to the negative charges now on the ligand. Therefore, the two possible values for A_{iso} are -159 or -189 MHz.

Assuming that **S2** can be defined as a **$[Cu(3.12)(OH^-]^+Cl^-$** species, a positively charged complex, if a dianonic complex has been formed the ligand must have undergone three further deprotonations or two further deprotonations for a negatively charged complex. Compound **3.12** has two potential sites for deprotonation the non-coordinated N atom of the imidazole ring or the primary amine, which have a pK_a of ~18 and 20-30 respectively.[271] Therefore, it is not possible for **3.12** to provide enough negatively charged ligands for a dinegative Cu complex to be formed within this coordination environment hence **S1** is not well described by a 3N1O coordination geometry. This suggests that there has been a change to the coordination environment as this species is not formed in the model complex outside of streptavidin and this is likely to have been induced by the protein. As nearby

amino acid side chains have been previously ruled out this suggests that coordination from the protein backbone may be responsible.

In a Peisach-Blumberg plot with 4N type *c*oordination, Figure 169, **S1** is more central and clusters with a compounds that have no net charge. This would be commensurate with two deprotonations assuming that the negatively charged hydroxide atom would be lost on the coordination of a fourth N containing ligand. Assuming that the new ligand is negatively charged, **3.12** would be able to support a single deprotonation and hence this coordination geometry is much more feasible. The new nitrogen containing ligand could be provided by the amide backbone of the protein. This assignment could be supported by the literature in which tryglycine copper complexes are shown to coordinate to the Cu *via* deprotonated amides. These deprotonations occur at similar pHs to the formation of **S1**.[270]

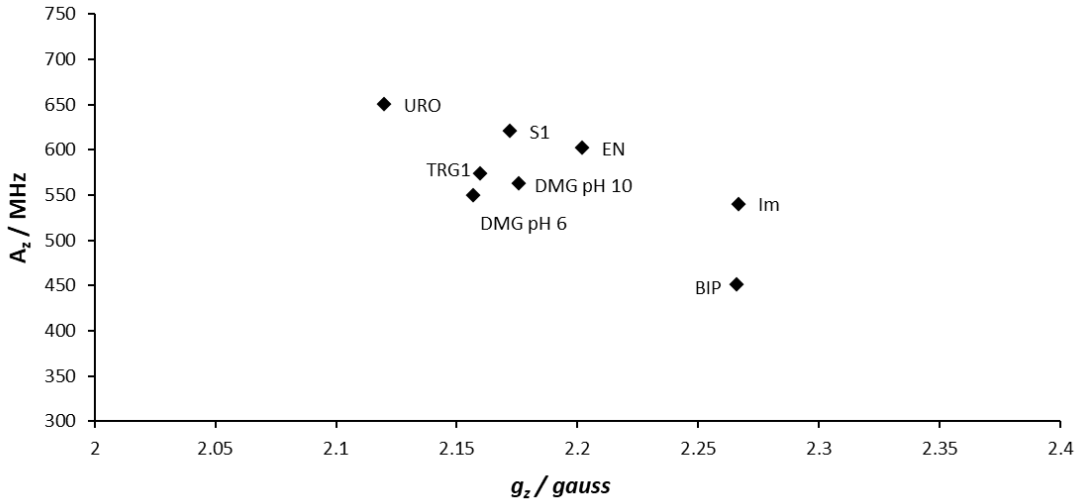

Figure 169. ***S1*** *plotted on a Peisach-Blumberg plot of Cu(II) proteins with primary coordination spheres consisting of 3 nitrogen atoms and 1 oxygen atom (3N1O) adapted from Arch. Biochem. Biophys.* ***1974,*** *165 (2), 691-708*

Table 17. Table of g_z and $|A_z|$ of various 4N Cu(II) sites, used in Figure 169

Species	Abreviation	g_z	$\|A_z\|$	Reference
Cu(3.12)Cl2⊂Sav2XM pH10.5	**S1**	2.172	620	This work
$[Cu(Uroporphyrin)]^{2-}$	**URO**	2.120	650	*Blumberg et al.*[128]
$[Cu(Glycly)_2\ Glycine]^{2-}$	**TRG2-**	2.160	574	*Vanngard et al.*[270]
[Cu(Dimethylglyoxime)] pH 6	**DMG pH 6**	2.157	549	*Vanngard et al.*[272]
[Cu(Dimethylglyoxime)] pH 10	**DMG pH 10**	2.176	563	*Vanngard et al.*[272]
$[Cu(Imidazole)_4]^{2+}$	**Im**	2.267	540	*Malmström et al.*[273]
$[Cu(Bipyridyl)_2]^{2+}$	**BIP**	2.266	451	*McCormick et al.*[274]
$[Cu(Ethylenediamine)(OTf)_2]$	**EN**	2.202	602	*Ward et al.*[275]

Currently there is not enough data to confidently identify the changes to coordination on the formation of **S1**. The α^2_{GS} value for **S1** significantly increases, indicating that the bonding around the Cu center has become more ionic. This indicates that a deprotonation on the ligand or the binding of a new negatively charged ligand has occurred.

The use of Peisach-Blumberg plots suggest that if the coordination geometry remains constant at 3N1O then there must be more than one deprotonation on the ligand which would be unfeasible. When **S1** is plotted on a *Peisach-Blumberg plot* with a 4N coordinating ligands its position suggests only a single deprotonation on the ligand would be required. However, this analysis does not provide enough evidence for the change in coordination as coupling to four nitrogen atoms is not observed in the simulations. Therefore, to gain certainty on the coordination geometry of **S1** additional evidence is required. To probe these potential conformational changes, ENDOR EPR could be used. This technique would allow for all of the nitrogen couplings to the Cu center to be identified and thus allow for a confident assessment to be made. Further evidence, could be provided by a high pH crystal structure; however there are no methods within the literature to crystalize streptavidin above pH 8.

Table 18.The Parameters used to calculate α_{GS}^2 of the species observed in the pH titration

A_{ISO}	A^{Fermi}				A^{SD}				A^{SOz}				α_{GS}^2			
	S4	S3	S2	S1	S4	S3	S2	S1	S4	S3	S2	S1	S4	S3	S2	S1
AISO (Ax +ve/Ay +ve)	-307	-248	-301	-253	-564	-510	-563	-587	348	303	298	220	0.84	0.77	0.85	0.91
AISO (Ax-ve/Ay-ve)	-347	-318	-343	-348	-524	-440	-521	-492	348	303	298	220	0.78	0.66	0.79	0.76
AISO (Ax -ve /Ay +ve)	-321	-275	-311	-318	-551	-483	-552	-522	348	303	298	220	0.82	0.73	0.83	0.81
AISO (Ax +ve /Ay -ve)	-334	-291	-332	-283	-537	-466	-531	-557	348	303	298	220	0.80	0.70	0.80	0.86

3.4.3 Crystal Structure of **Cu(3.12)Cl_2⊂Sav2XM**

3.4.3.1 Crystallisation of *apo* **Sav2XM**

Sav2XM was tested for crystallisation using an established method for crystallisation of streptavidin, in which ammonium sulphate was employed as a precipitant. These were each set up in a 48 well sitting drop plate, ammonium sulphate screens were carried out at pH 4 using 0.1 M sodium acetate and screened between 1.0 – 0.4 M ammonium sulphate. **Sav2XM** was quick to crystallise (crystals formed in two days) using ammonium sulfate, mostly forming square blocks.

3.4.3.2 Soaking of **Sav2XM** with **Cu(3.12)Cl_2**

Due to the ease in which streptavidin crystallises the most common methodology within the literature to incorporate a biotinylated metal complex is *via* a soaking methodology.[240] To do this a 10 mM **Cu(3.12)Cl_2** solution was prepared, and 1 μL of this solution was added to a 9 μL drop of the mother liquor . Suitable crystals were transferred to the soaking drop and incubated at 27 °C for 4-24 hours, at which point the crystals had assumed a yellow green colour, shown in Figure 170.

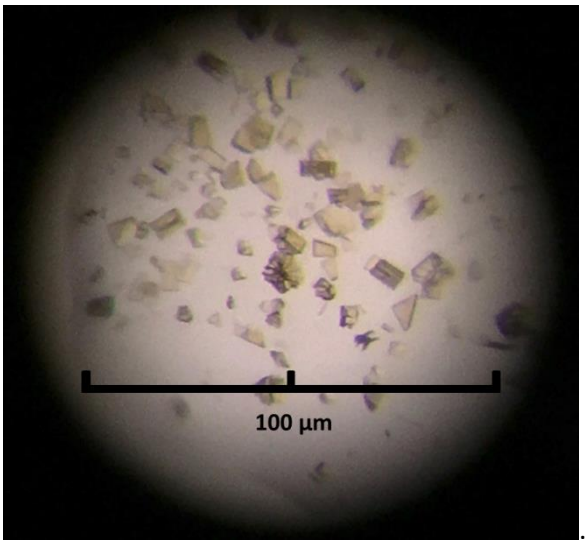

*Figure 170. **Sav2XM** crystals after 24 hours incubating with Cu(3.12)Cl_2*

3.4.3.2 Data collection and structure of Cu(3.12)Cl_2⊂Sav2XM

Cu(3.12)Cl_2⊂Sav2XM crystals were initially tested in house in order to assess the quality of X–ray diffraction. A crystal suspended within the loop and a example diffraction image from testing is shown in Figure 171. These crystals were strongly diffracting and showed clear

diffraction spots during in house collection, shown in Figure 171. Complete data sets used to solve the structure of **Cu(3.12)Cl_2⊂Sav2XM** were collected at Diamond Light Source, using beamline I24: Microfocus MX.

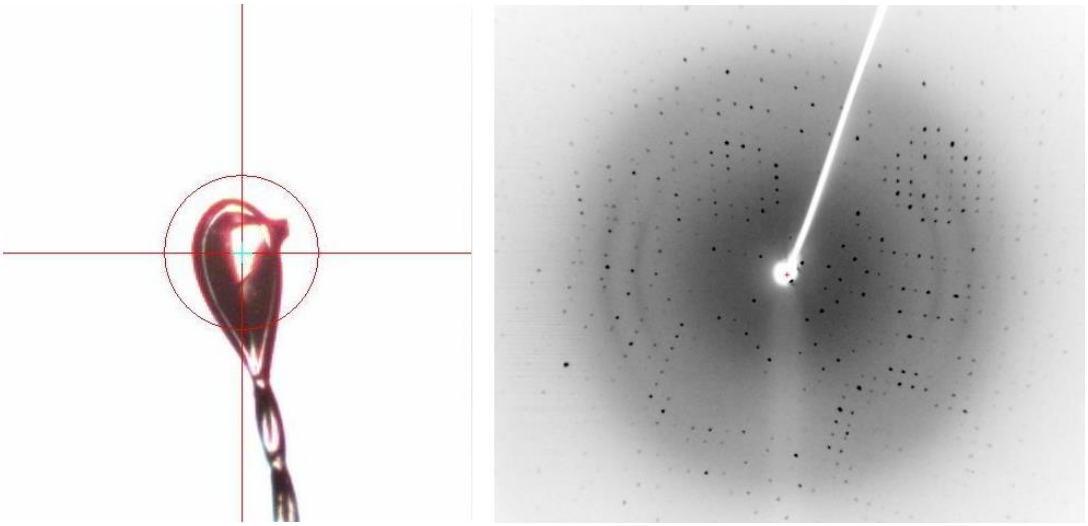

Figure 171. Left. Crystal held in loop and photographed after in house testing. Right. Test Sav2XM crystal x-ray diffraction pattern showing strong spots

The **Cu(3.12)Cl_2⊂Sav2XM** structures were solved by molecular replacement using MOLREP[276] with the 'apo' structure of **Sav2XM (PDB 6AUC)**[242] as the search model. Refinement cycles involving REFMAC and manual alteration in COOT[277] were applied before the R_{cryst} and R_{free} remained constant. The overall folding of secondary structure of the protein remained unchanged on soaking as expected. As the soaking time of the crystals increased the amount of density found in the biotin binding domain of the pocket increased. As such I will be discussing the best data set, **Sav2XM-Optimal** in the section below which was solved to a resolution of 1.47 Å with a R_{free} of 0.191.

After fitting the electron density of biotin there is clearly more density present within the vestibule, indicating that the ligand has been successfully anchored within the protein, shown in Figure 172. Therefore a model of the **3.12** was built and fitted to this density, however this density is poorly defined indicating that the ligand is likely very flexible and as such results in some disorder within the vestibule.

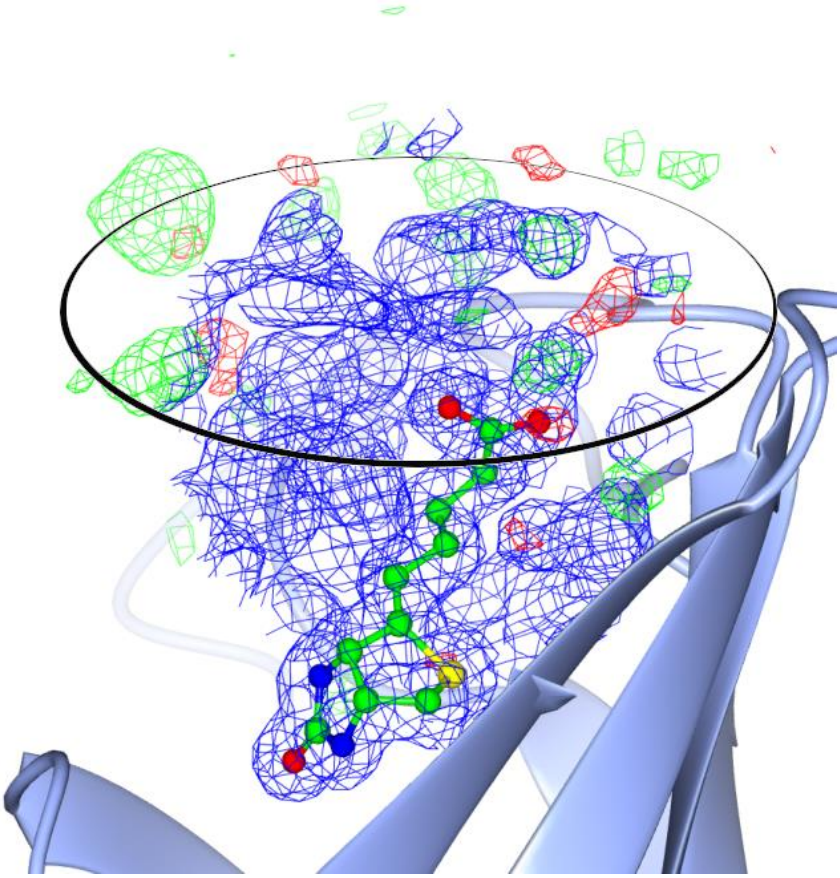

Figure 172. ***Sav2XM-Optimal*** *with a biotin ligand fit within the binding pocket. The black oval highlights the additional unfit electron density within the streptavidin vestibule.* F_0 *mas shown at 0.5 σ.* mF_0-DF_c *map at 1.5 σ*

Despite having the density present within the vestibule compatible to **3.12**, significant problems were found when the metal ion was included. Firstly, the residual density is too low to allow for the placing of a Cu ion at full occupancy. As such an anomalous density map was used in an attempt to locate a possible partially occupied site. The anomalous density map of **Sav2XM-Optimal** (Figure 173) clearly shows the anomalous scattering caused by the S atom found in the biotin portion of **3.12** but reveals no anomalous scattering for a Cu ion. The incorporation of the ligand but loss of the copper could imply precipitation of the Cu ion has occurred during the soaking process. It should be noted that these crystals were prepared at pH 4.5 and it is was demonstrated that it was not possible to obtain an EPR spectrum of **Cu(3.12)Cl_2⊂Sav2XM** below pH 6 (Section **3.4.2.3)**. Thus the acidic crystallisation conditions could be responsible for the precipitation of the Cu ion.

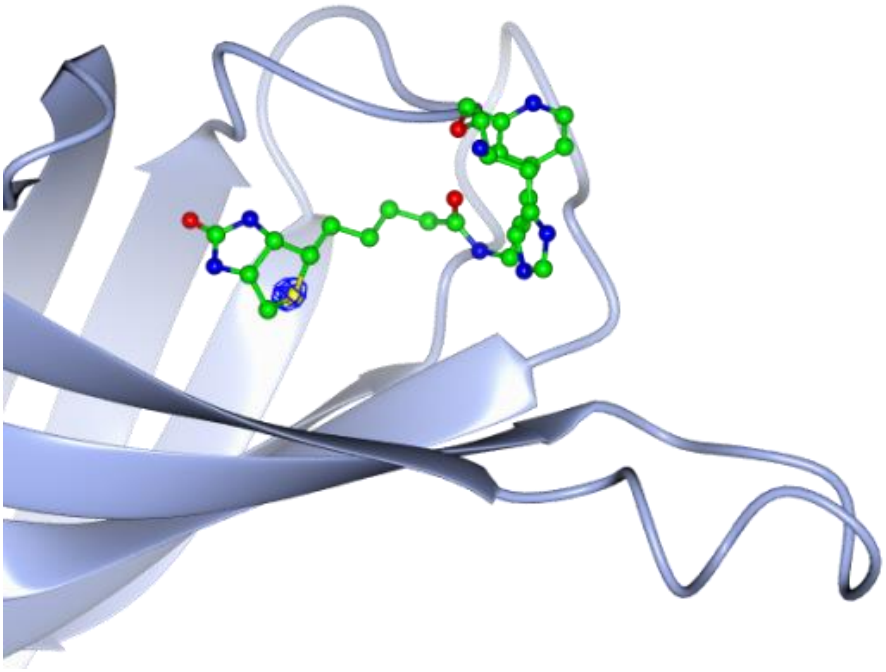

*Figure 173. Anomalous Density Scattering map of **Sav2XM-Best-** shown at 4.5 σ*

The model of **3.12** can be fitted into the density found in the vestibule, shown in Figure 174. However, there is a second pocket of density also found within the vestibule. This implies that there is a lot of disorder present within the vestibule. The cause of this disorder is likely to be due to the long linker length present in **3.12**, compared to other streptavidin artificial enzymes (Section **3.2.2**). The longer linker length present within **3.12** results in a larger degree of flexibility and therefore allows for a large number of conformations within the vestibule. The large number of conformations may explain the lack of an anomalous signal for the Cu ion as it is smeared over the whole vestibule.

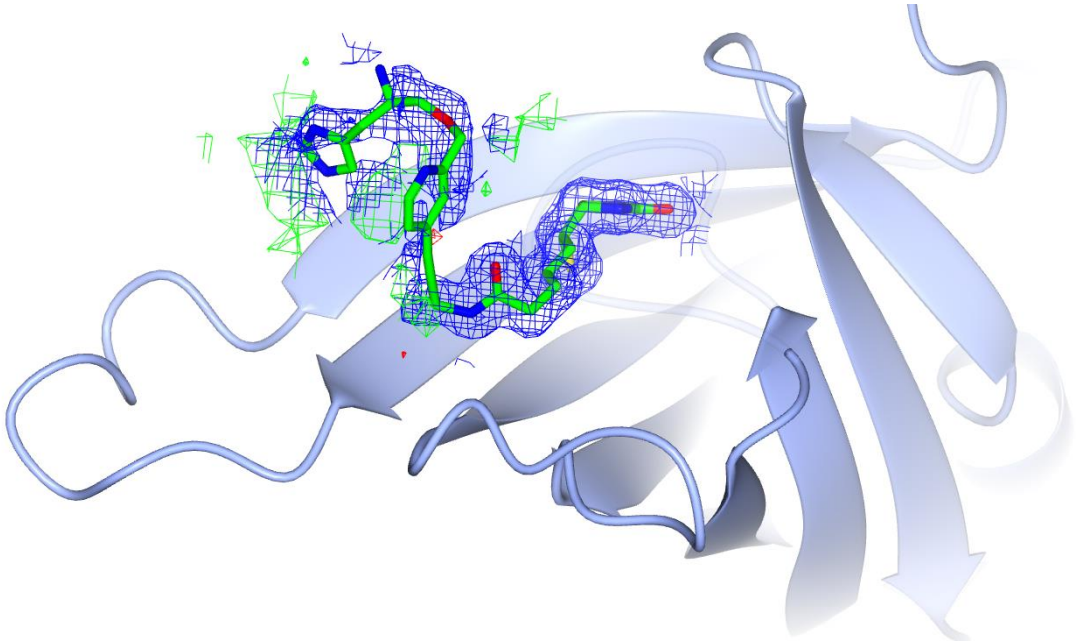

*Figure 174. The structure of **Sav2XM-Best** when **3.12** is used as a ligand. .F_0-F_c map at 1.5 σ, electron density maps shown at 0.5 σ*

While the structure shown in Figure 174 attempts to fit the residual density within the vestibule there is still a lot of unaccounted density within the vestibule. Therefore, it is currently not possible to solve the structure while including the ligand to a high degree of certainty. This observation, coupled with the lack of a Cu ion within the structure, means that this solid state structure is not a good representation of **Cu(3.12)Cl_2⊂Sav2XM** in solution. As such full analysis of the bond lengths and angles will not occur.

3.4.3.1 Further attempts for the Crystallisation of *apo* **Sav2XM**

As the acidic conditions were thought to be causing precipitation of Cu ion during soaking methods the following conditions were used in an attempt to grow crystals of *apo* **Sav2XM** at a neutral pH. For these two alternative precipitants were used 4K polyethylene glycol (PEG) and methylpentane-2,4-diol (MPG) as these have been previously shown to afford streptavidin crystals at pH 6 and pH 7 respectively.[278] The crystal screens were carried out as follows, PEG screens were carried out at pH 7 using between 12% to 20% PEG 4000 using 0.1 M HEPES. Finally MPG screens were carried out at pH 7 using 46% MPG using 0.1 M HEPES at pH 6. Unfortunately neither of these methods afforded crystals suitable for use in ligand soaking experiments. Therefore, the hypothesis that the low pH (due to the crystallisation conditions) was causing the precipitation of Cu could not be examined further.

3.5 Conclusions

The goal of this chapter was to modify **2.3** to use it in an artificial metalloenzyme construct. The streptavidin-biotin methodology was selected: incorporation of **2.3** into the protein scaffold using biotin as an anchor allows for the coordination geometry of **2.3** to remain unchanged and opens to the possibility of mutagenic studies on streptavidin.

The attachment of the biotin anchor was carried out synthetically using a combination of Sonogashira cross-coupling and amide synthesis. A linker was incorporated onto **2.3** *via a* Sonogashira coupling reaction, the formation of **3.17** was confirmed by the appearance of a new resonance at 4.66 ppm in the ^{1}H NMR spectrum with a relative intensity of 2 corresponding to the formation of the alkyne. The primary amine within the linker was then revealed and used in an amide coupling with biotin-pentaflurophenol to form **3.12**, confirmed by the ^{13}C NMR in which the resonance corresponding to the carbonyl of the new amide bond has shifted upfield after the reaction. The ^{1}F NMR is featureless indicating the loss of the pentaflurophenol leaving group, and is supported by MS analysis which matches the expected *m/z* for **3.12**.

The addition of the biotin anchor was shown not to affect the coordination geometry of the Cu ion. The EPR spectrum of both **Cu(2.3)Cl$_2$** and **Cu(3.12)Cl$_2$** are identical. As such any changes to the electronic structure can be attributed to the environment created by anchoring **Cu(3.12)Cl$_2$** within the protein.

The uptake of **Cu(3.12)Cl$_2$** by streptavidin was confirmed by a HABA titration, in which HABA was displaced from the biotin binding site of streptavidin by **Cu(3.12)Cl$_2$** in the expected 4:1 (ligand : streptavidin) ratio. Uptake by streptavidin also caused a change in the Cu environment of the protein, with the spin Hamiltonian parameters of **Cu(3.12)Cl$_2$⊂Sav2XM** differing at all pH compared to **Cu(2.3)Cl$_2$.** The protein also stabilised a highly covalent species at high pH (> pH10) identified by both its low g_z value (2.172) and significantly higher A_z value (610 MHz) which is not accessible by the free ligand. This behaviour is also observed in some LPMOs indicating that they form a similar environment at a high pH. The calculation of the α_{GS}^2 value for **S1** increased suggesting that the coordination environment has become more ionic which is supported by the use of Peisach-Blumberg plots. The Peisach-Blumberg plots suggest a change in the coordination environment has occurred but there is not enough evidence to assign this change.

Crystallographic studies of **Cu(3.12)Cl_2⊂Sav2XM** ultimately proved problematic. While it was shown to be possible to incorporate **3.12** into protein crystals of **Sav2XM**, the anomalous density map could not locate any copper ions within the structure. This result, coupled with a large amount of disordered density found within the vestibule of streptavidin, prevents further examination of the exact coordination and ligand geometries within the vestibule of **SAV2XM**.

Chapter 4. Reactivity Studies of Cu(2.3), Cu(3.12) and Cu(3.12) ⊂ Sav

The goal of the work described in this chapter was to design, synthesise and characterise small molecule compounds which are able to mimic the spectroscopy and reactivity observed for LPMOs. In previous chapters these complexes where synthesised and characterised by NMR spectroscopy, mass spectrometry and EPR spectroscopy, herein the reactivity of **Cu(2.3) Cu(3.12)** and **Cu(3.12)⊂Sav** is reported (Figure 175).

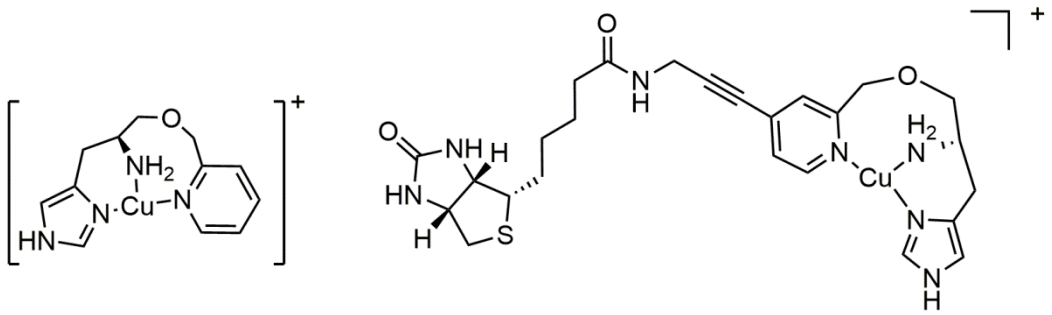

*Figure 175. Schematic scheme of **Cu(3.12)** and **Cu(3.12)** respectively*

4.1 Observation of Reactive Oxygen Species

The observation of ROS is difficult due to their transient nature. As such they are not observable by conventional UV/Visible methods due to their low lifetimes (milliseconds) hence they time resolved techniques to be detected, isolated and studied.

4.1.1 Stopped flow Spectroscopy

The stopped flow method was initially developed by B. Chance to study the kinetics of the H_2O_2 reaction with peroxidase.[279] The stopped flow experiment allows for the monitoring of the kinetics of a reaction using minimal amounts of reactants over a short timescale. This is facilitated by rapid mixing of solutions of two or more compounds (1-2 ms), which would not be possible in a conventional UV/Vis experiment. Following the mixing, the solution is transferred into an observation chamber at which point the flow of reagents is stopped and the species formed during a single reaction can be monitored overtime. A basic schematic of a stopped flow instrument is shown in Figure 176.[280]

The evolution of the reaction can be monitored *via* various techniques which commonly include UV/Visible spectroscopy and fluorescence spectroscopy; however, circular dichroism (CD) and NMR spectroscopies have also been used in conjunction with stopped flow experiments to study protein folding.[281] For the systems considered in this investigation, as the formation of ROS would create an intense charge transfer band between the oxygen atom and copper, a UV/Visible setup is ideal.

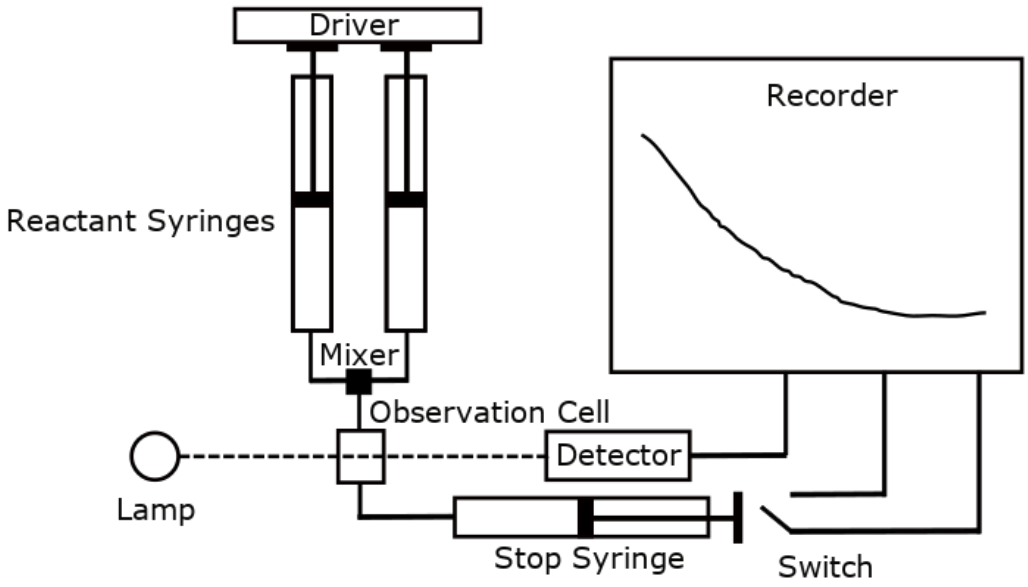

Figure 176. Schematic diagram of the key components of a UV/Vis Stopped flow spectrometer adapted from C. R Bagshaw.[280]

4.1.2 Generation of Reactive Oxygen species

The active species which performs HAA on the substrate in the catalytic cycle of LPMOs is believed to be the **Cu(II)-O$^{-\bullet}$** as discussed in **Section 1.2.3**. The mechanism for the formation of this species and the subsequent reaction with substrate is shown in Figure 177. When oxygen is used as the co-substrate in order to form a **Cu(II)-O$^{-\bullet}$** intermediate the reaction must proceed *via* two further PCET steps, following the initial reaction of Cu(I)-LPMO with O_2. As such, the inefficiency of these two steps may prevent any reactive intermediate from forming in a high enough concentration to be observable in a typical stopped flow experiment. Furthermore the concentration of O_2 in water is limited by its solubility. Therefore, in order to form such a species in an observable quantity, alternative means of accessing the oxyl species must be employed.

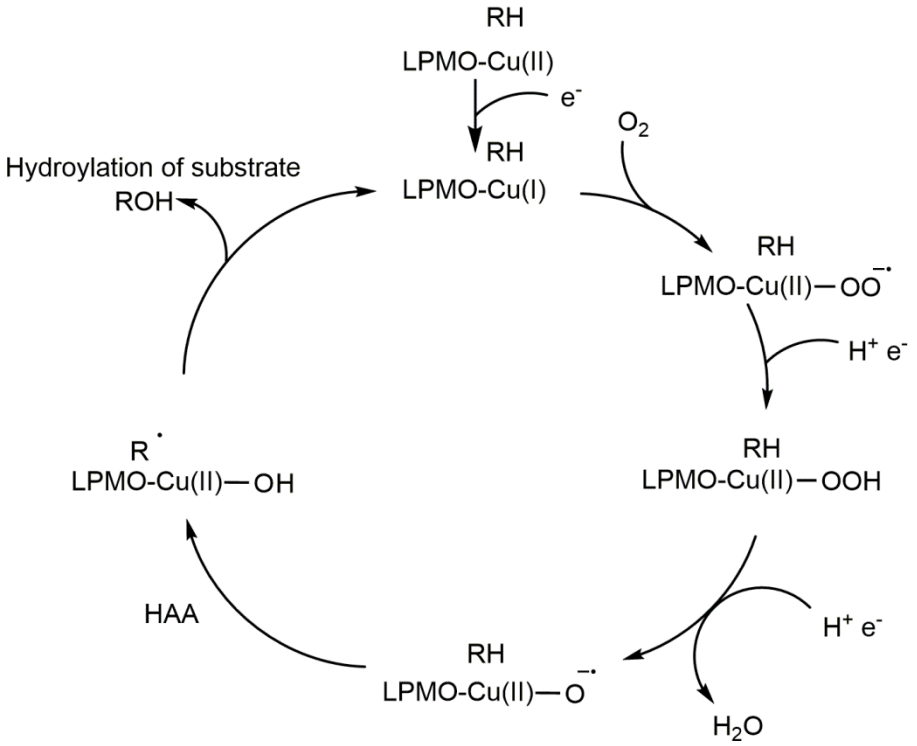

Figure 177. The proposed catalytic cycle of LPMOs on reaction with O_2[123]

An alternative source of oxidants which are commonly used to generate ROS are peroxides. The use of peroxides is commonly known as a "peroxide-shunt" experiment. In this experiment the metal-oxyl ($M(^{N})$-$O^{\bullet}$) or metal-oxo ($M(^{N+1})$=O) is formed directly *via* a reaction of the metal with the peroxide and the subsequent loss of a water which allows the reaction to be driven in the absence of other oxidants and redox partners. Within the literature the most common use of the peroxide shunt methodology is in the study of P450 enzymes, where a peroxide shunt experiment is used to generate compound I, an iron(IV) oxo $(Fe(IV)=O)^{+\bullet}$ compound, shown in Figure 178.[282]

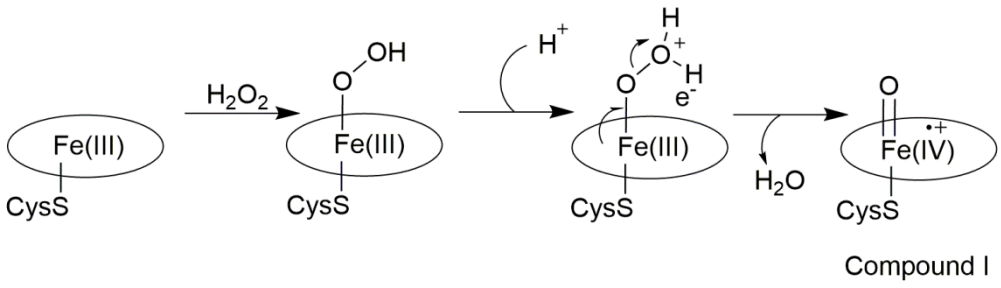

Figure 178 .A H_2O_2 peroxide shunt for the formation of Compound I in P450. Adapted from Shoji et al.[283]

Meta-chloroperoxybenzoic acid (*m*CPBA), shown in Figure 179, is widely used as an oxidant in a peroxide shunt experiment, for example in the formation of Compound I in Cytochrome P450 and in small molecule mimics of P450.[282, 284-286] *m*CPBA has been shown to generate Compound I efficiently (70% yield) where H_2O_2 have been known to cause significant oxidative damage to the heme group.[286] Similar oxidative damage has been observed when LPMOs have undergone reactions with H_2O_2 which deactivate the enzyme.[118] As such, *m*CPBA is a promising candidate to use in an attempt to observe a Cu oxygen species within the LPMO reaction mechanism, therefore it will be used with **Cu(2.3)** in an attempt to generate ROS.

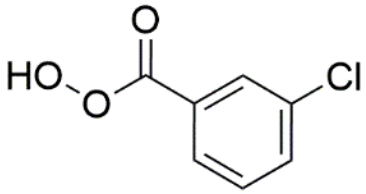

Figure 179. The schematic structure of meta-*chloroperoxybenzoic acid (mCPBA)*

4.1.3 Previously Reported Stopped Flow Experiments with LPMOs

The earliest report of the use of stopped flow experiments to study LPMOs is by Kjaergaard *et al.*[125] who determined the rate of reoxidation of Cu(I) in *Ta*AA9 by following the appearance of *d-d* band corresponding to the presence of Cu(II). The rate of reoxidation was found to be > 0.15 s^{-1}, suggesting that the reoxidation of Cu(I) occurred *via* an inner sphere electron transfer mechanism in which a **Cu(II)-OO$^-$** intermediate was formed. As using the redox potential for the reduction of one-electron reduction of O_2 to O_2^- (-165 mV *vs* SHE) and reported redox potentials for AA9 LPMOs (~ 275 mV *vs* SHE) the rate of an outersphere electron transfer was calculated using Marcus theory $\sim 4.5 \times 10^{-4}$ s^{-1} which is significantly slower ($\sim 10^3$) than the experimentally observed rate. However, the copper superoxide was not observed directly.

Further work by Jones *et al.*[287] examined the difference of reoxidation of *Hj*AA9 on reactions with O_2, H_2O_2, peracetic acid and tert-butyl hydroperoxide. The reoxidation by O_2 was found to occur at a significantly slower rate than that previously observed in other studies (50 M^{-1} s^{-1}), and similarly to the *Ta*AA9 case no intermediates were observed. On reoxidation by H_2O_2 two new UV/Visible bands at 420 nm and 520 nm were formed, identified as tryptophanyl and tyrosyl radicals, respectively. The identity of the tryptophanyl radical was supported by the appearance of an organic radical in the EPR

spectrum of the protien.[287] The organic hydroperoxides dramatically reduced the rate of rate constants deduced for the reoxidation intermediate ($K_{Trp} = H_2O_2 = 7.9 \times 10^3\ M^{-1}\ s^{-1}$ *vs* AcOOH =1.5 $M^{-1}\ s^{-1}$ vs tBuOOH =0.49 $M^{-1}\ s^{-1}$, $K_{Tyr} = H_2O_2 = 4.9 \times 10^3\ M^{-1}\ s^{-1}$ *vs* AcOOH =1.2 $M^{-1}\ s^{-1}$ vs tBuOOH =0.27 $M^{-1}\ s^{-1}$) which is commensurate with the decrease in bond dissociation enthalpies of these peroxides (51 kcal/mol H_2O_2, 47 kcal/mol AcOOH, 41 kcal/mol ^{t}BuOOH). The ratio of the two bands did not change indicating that the formation of the two new bands was not dependent on the alkoxyl formed on reaction.

4.1.4 Reactions of **Cu(2.3), Cu(3.12)** and **Cu(3.12) ⊂ Sav2XM** with *m*CPBA

The general procedure for the stopped flow experiments is as follows. Under a N_2 atmosphere and in deoxygenated H_2O or buffer solutions two syringes were prepared. The first contained *m*CPBA at any given concentration and the second contained the appropriate copper complex. The stopped flow instrument was purged with deoxygenated buffer or water prior to use to remove any residual O_2 in the system. These syringes were then transferred to the stopped flow instrument under a liquid-liquid seal.

In order to react with *m*CPBA, **Cu(2.3)(SO_4)** must be reduced to the Cu(I) state; therefore, **Cu(2.3)(SO_4)** was incubated with one equivalent of ascorbic acid for 30 minutes. The complete reduction of **Cu(2.3)(SO_4)** was confirmed by EPR spectroscopy in which no signal was observed. Furthermore, in the UV/Vis spectrum the *d-d* band at 625 nm characteristic of the Cu(II) complex was seen to be supressed, shown in Figure 180. These data indicate that full reduction to Cu(I) had occurred.

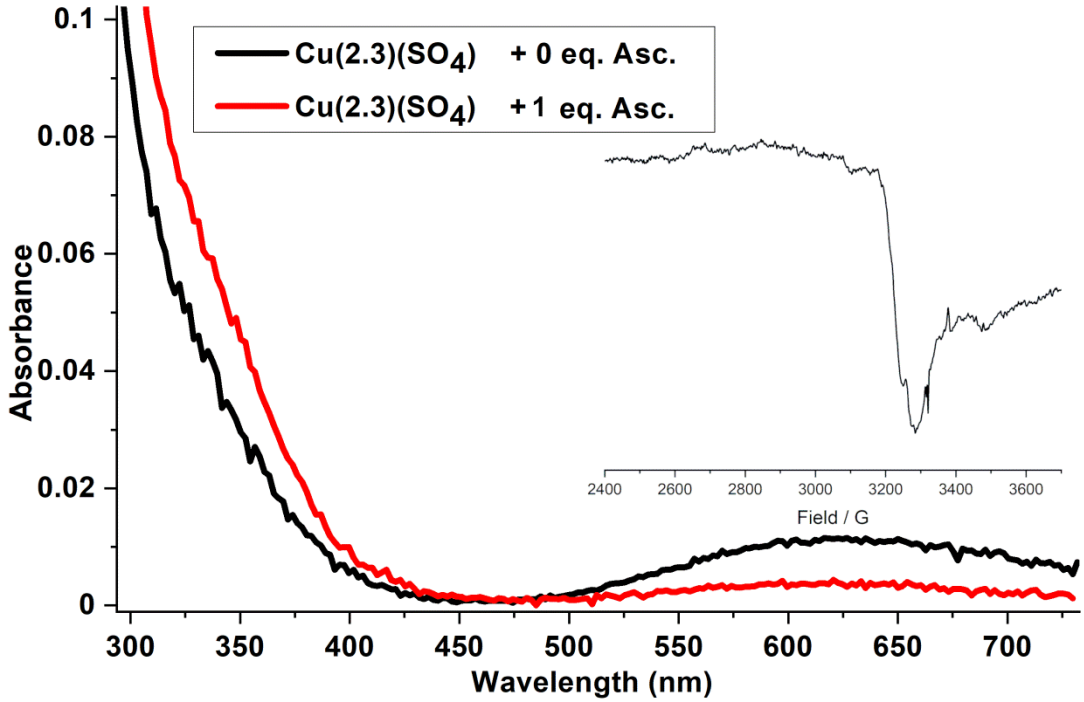

Figure 180. UV/Visible spectrum of ***Cu(2.3)(SO$_4$)*** *in the presence and absence of ascorbic acid. Conditions: HEPES 50 mM pH 8.0,* ***Cu(2.3)(SO$_4$)*** *0.35 mM, Asc 0.35 mM. Inset. EPR spectrum of* ***Cu(2.3)(SO$_4$)*** *following ascorbate addition*

The reaction of **Cu(2.3)(SO$_4$)** with mCPBA was monitored *via* UV/Vis stopped flow and is shown in Figure 181. In a 10 millisecond timeframe a new band appears at 352 nm and the Cu *d-d* band at 625 nm reappears indicating that the Cu(I) has been reoxidised to Cu(II). This appears to be occurring over the same timeframe as the band at 352 nm appearing indicating that these two bands may be coupled to one another. Initial control experiments at pH 6 indicated that the band is dependent on both the presence of **Cu(2.3)(SO$_4$)** in the Cu(I) form and *m*CPBA as no band was observed for reactions with *m*CPBA and ascorbate, **Cu(II)(2.3)(SO$_4$)** and *m*CPBA, or **Cu(II)(2.3)(SO$_4$)** and ascorbate. The band at 352 nm could be tentatively assigned as a LMCT band from potentially a ROS, this can be deduced from its extinction coefficient assuming that 70% conversion occurs (maximum conversion observed in P450) the $\varepsilon = 400\ M^{-1}\ cm^{-1}$. However, this requires further investigation in order to determine the validity of these claims.

This finding is of particularly interest as recent unpublished data obtained by Dr. Daniel Diaz in the Walton group has found that LPMOs undergo a reaction with *m*CPBA under similar conditions, resulting in a band appearing at 354 nm within a similar timescale, shown in Figure 182. This indicated that the small molecule complex was replicating the reactivity observed in LPMOs.

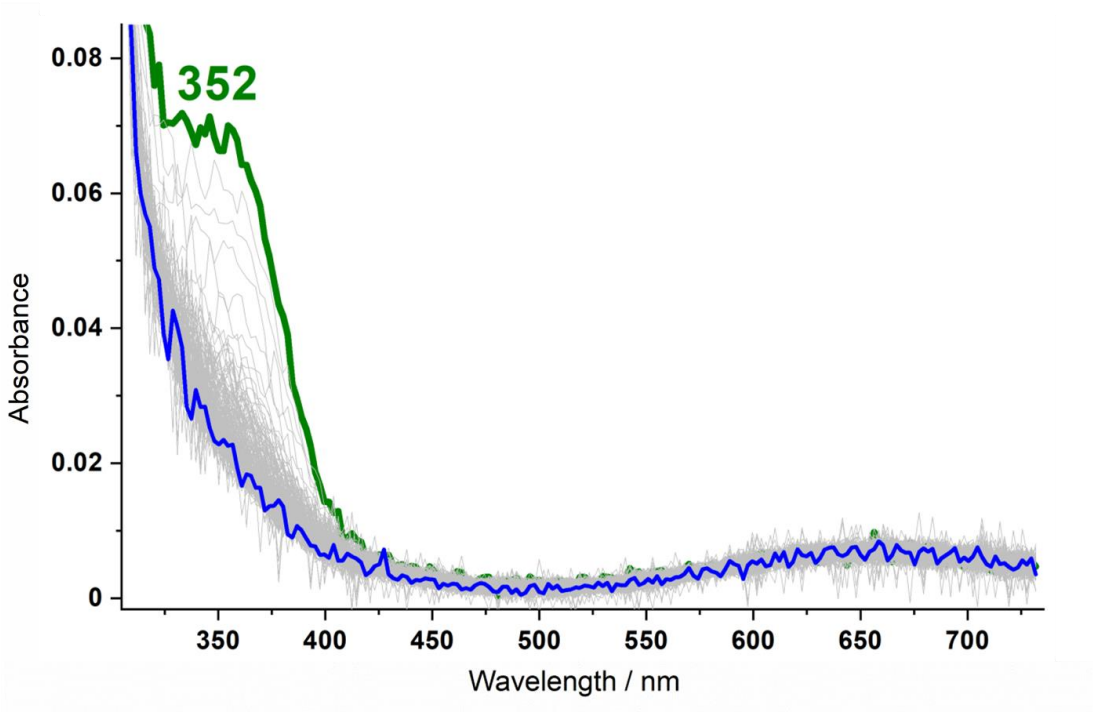

Figure 181. The stopped flow UV/Vis spectra of the reaction of ***Cu(2.3)(SO$_4$)*** *(0.25 mM) with mCPBA (1 mM) in Milli-Q H_2O over a 500 millisecond timescale. Blue spectrum is UV/Vis spectrum at 30 ms and green UV/Vis spectrum is at 2 ms*

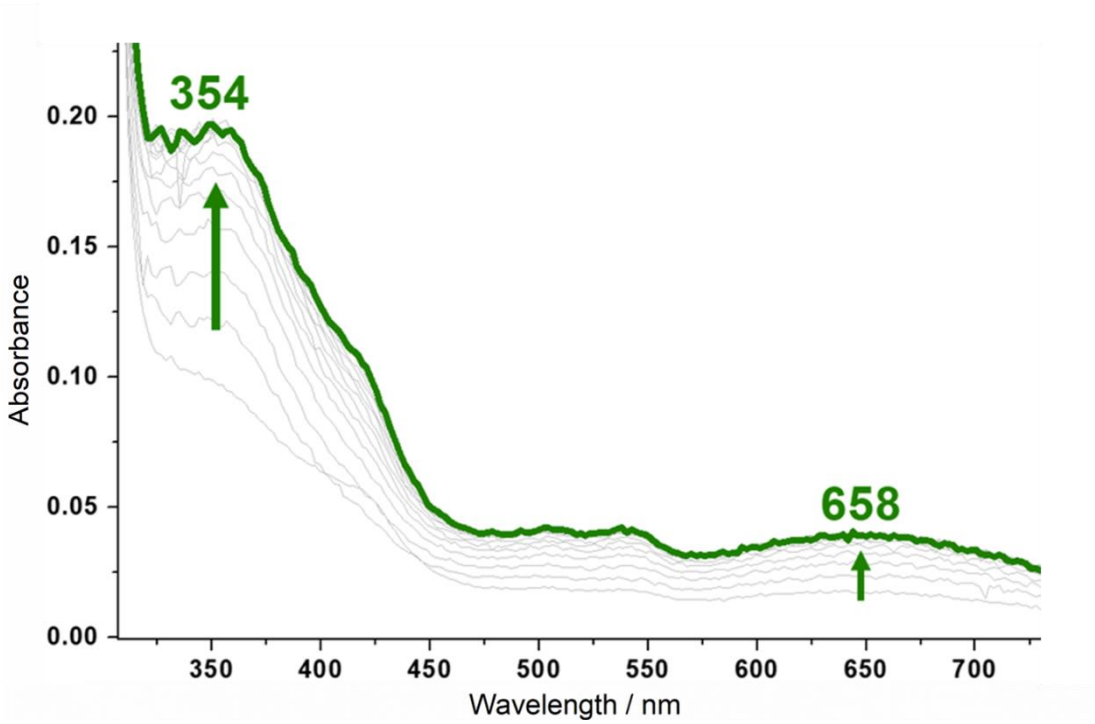

Figure 182. The stopped flow UV/Vis spectra of the reaction of CvAA9 with 5 eq of mCPBA over a 500 millisecond timescale. (pH 8 HEPES 50 mM). Used with permission of Dr. Daniel Diaz

It should be noted that over a longer time scale another band appears in the spectrum at 408 nm, shown in Figure 183, this band is long lived (minutes). This band at 408 nm occurs both in the presence or absence of *m*CPBA. The long lived lifetime and the fact that this species is formed in the absence of *m*CPBA and is therefore not formed as a result of the peroxide shunt experiment and therefore not explored further.

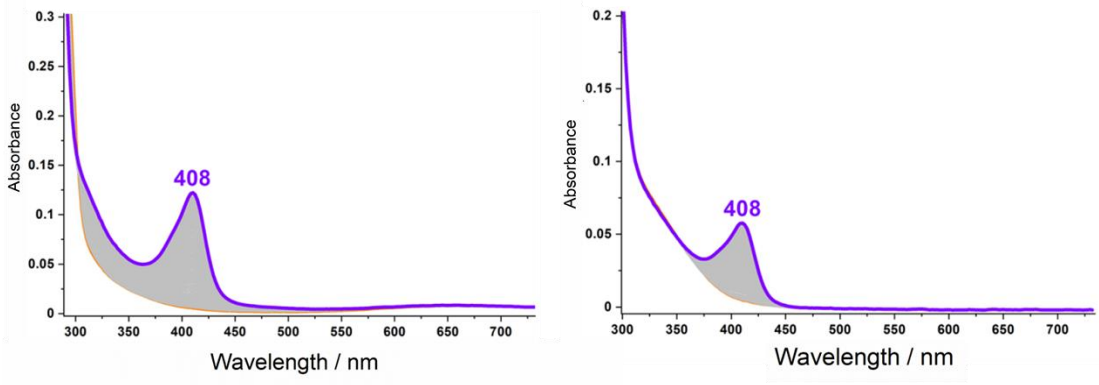

Figure 183. The stopped flow UV/Vis spectra of the reaction of ***Cu(2.3)(SO$_4$)*** *(0.25 mM) in the presence (Left) and absence (Right) of mCPBA (1 mM) over a 500 second timescale.(pH 6 MES buffer 50 mM)*

It has been shown in **chapter 2** that the electronic environment of **Cu(2.3)Cl$_2$** exhibits a pH dependence, this same dependence is observed in **Cu(2.3)(SO$_4$)** hence the pH dependence on the reaction was explored. These experiments showed a general trend where the intensity of the band at 352 nm increased with pH, shown in Figure 184. The intensity of the 352 band increases between pH 9 and 10 which would not be expected if the change was due to the speciation as the high pH species of **Cu(2.3)(SO$_4$)** is fully formed at pH 9. Hence, the intensity of the band is likely dependent on proton concentration, as opposed to speciation of **Cu(2.3)(SO$_4$)**. This is not unexpected as in the Cu(I) form of **Cu(2.3)(SO$_4$)** it would be expected that no exogenous ligand would be present on the complex, as Cu(I) favours the three coordinate T-shaped geometry over square planar favoured by Cu(II). Therefore the exogenous ligand would be lost on reduction. As it was found that the exogenous ligand was responsible for the change in speciation (**chapter 2**) no change should occur between these pHs in the Cu(I) form**.**

As the band at 352 nm is formed very quickly, reaching maximum intensity in <5 ms, a study to determine the rate law based on the initial rates of formation was not possible as the first measurement is taken at 2 ms at which some samples have already begun to decay, Figure 184. From this data it can be seen that at higher pH the formation of this band occurs significantly more slowly, reaching a maximum intensity at ~10 ms and has higher intensity therefore future experiments were carried out at higher pHs.

As pH influences species formation, this was the first variable to be investigated. The rate of decay of the 352 nm band is shown in Figure 184. From these data it can be observed that two different processes are present: below pH 8 the species undergoes what appears to be an exponential decay over an extremely short timeframe. However, it was not possible to model the decay of the higher pH species as a single exponential indicating that multiple decay pathways are occurring. Hence, further experiments were carried out at pH 8 in order to maximise species formation but to maintain a single exponential decay.

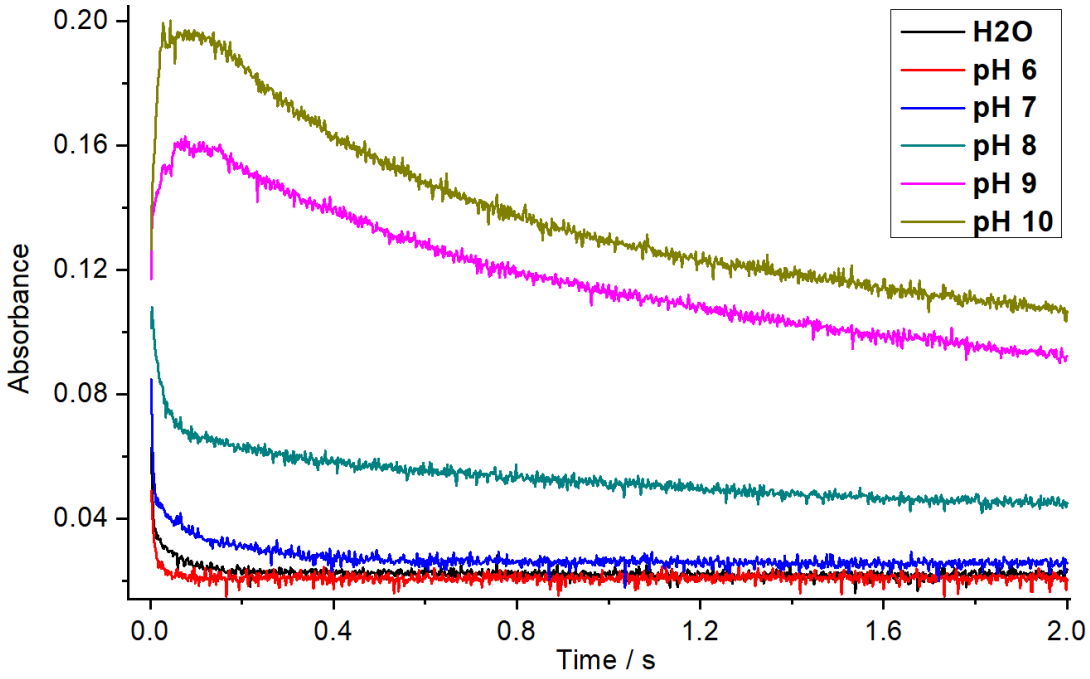

Figure 184. Decay of the 352 nm band formed on the reaction of ***Cu(2.3)(SO$_4$)*** *(0.31 mM) with mCPBA (1.0 mM) on varying the pH over a 2 second timescale (pH 6: MES 50 mM, pH 7-8 HEPES 50 mM, pH 9 CHES, pH 10 CAPS 50 mM)*

In order to calculate the observed rate of decay of the 352 nm band, the data at each pH were fitted using the equation for a single exponential decay or two exponential decays. For an illustration on how initial rates of decay were calculated, the following procedure

using a single exponential decay is described. First, the experimental decay was modelled using a single exponential as,

$$y = A_1 e^{-\frac{x}{t_1}} + y0$$

using Origin Lab fitting software. Thus the equation for the rate of decay was obtained by finding the differential of the equation,

$$\frac{dy}{dx} = A_1 \frac{1}{t_1} e^{--\frac{x}{t_1}}$$

At time 0 as,

$$e^0 = 1$$

Therefore, the initial rate (where $x = 0$) can be calculated as,

$$initial\ rate = A_1 \frac{1}{t_1}$$

Following the calculation of the initial rate of decay, this rate of decay can be plotted against the [H^+] (Figure 185).These data reveals a linear dependence and hence the rate of decay is first order to [H^+] concentration.

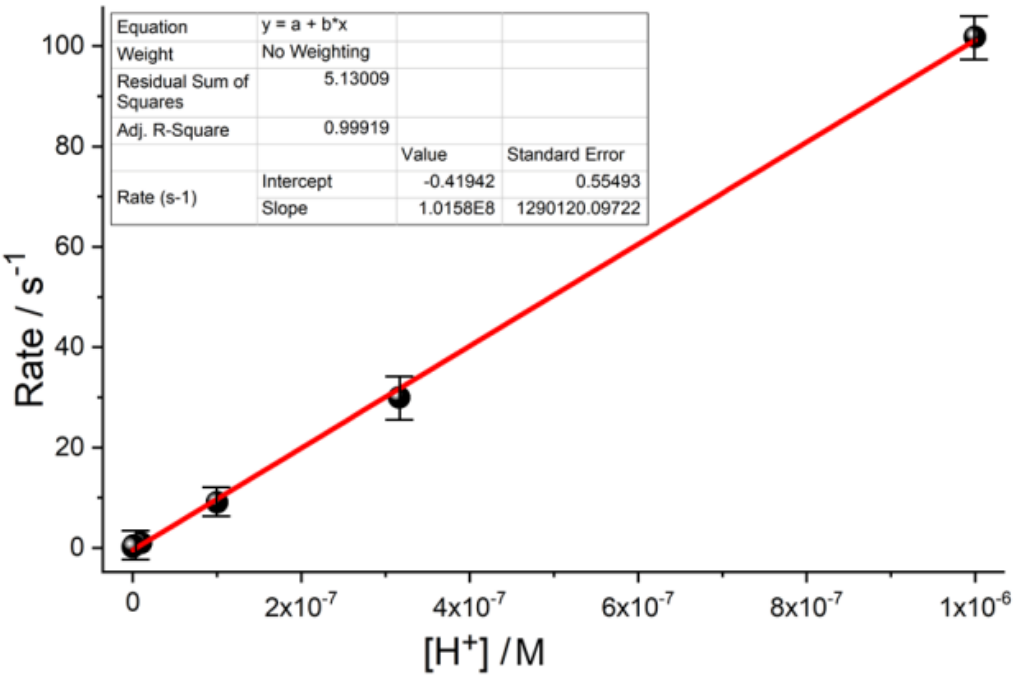

Figure 185. Rate of decay of the 352 band plotted against proton concentration (4 °C, pH 6: MES 50 mM, pH 7-8 HEPES 50 mM, pH 9 CHES, pH 10 CAPS 50 mM) Error bars represent standard deviation of three independent repeats

Further experiments were carried out to determine the effect of both *m*CPBA concentration (Figure 186) and **Cu(2.3)** concentration (Figure 187). The dependence of the rate of decay on *m*CPBA is non-linear. This indicates that *m*CPBA plays a more complex role in the decay of the 352 nm band which is currently not understood. On modification to the concentration of **Cu(2.3)** it was found that the rate of decay is first order with respect to the concentration of **Cu(2.3)** . Therefore, the rate of decay of the band could be described as,

$$Rate = K_{obs}[H^+][Cu(2.3)]$$

This behaviour could be consistent with the formation and decay of a reactive oxygen species, and to test the validity of this hypothesis further control experiments were carried out.

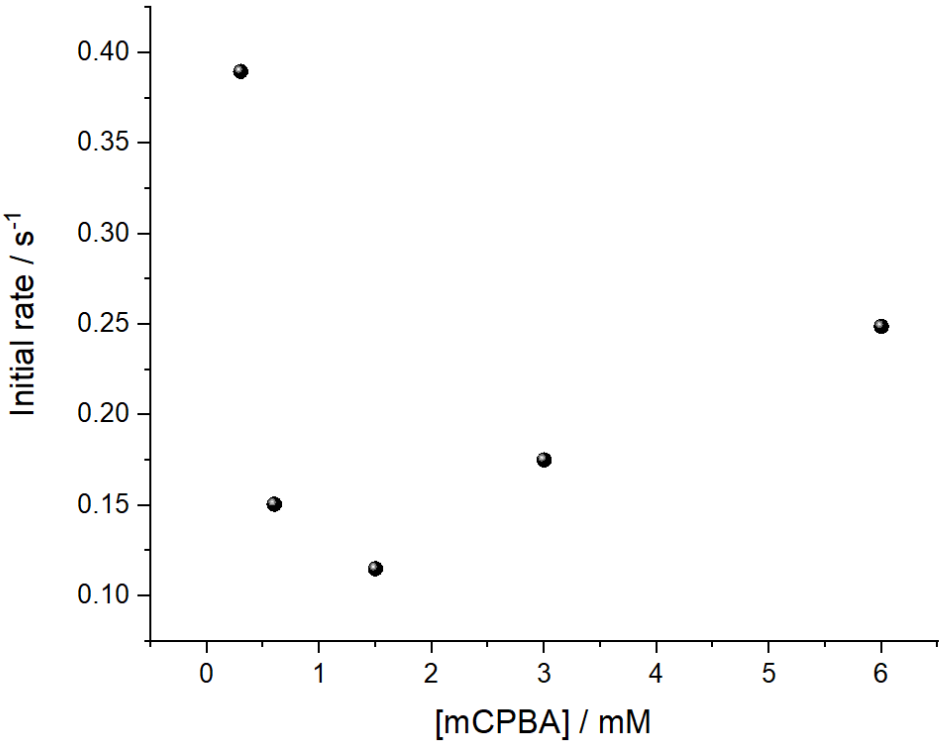

Figure 186 Initial rate of decay of the 352 band plotted against mCPBA concentration (HEPES 50 mM pH 8, 4 °C)

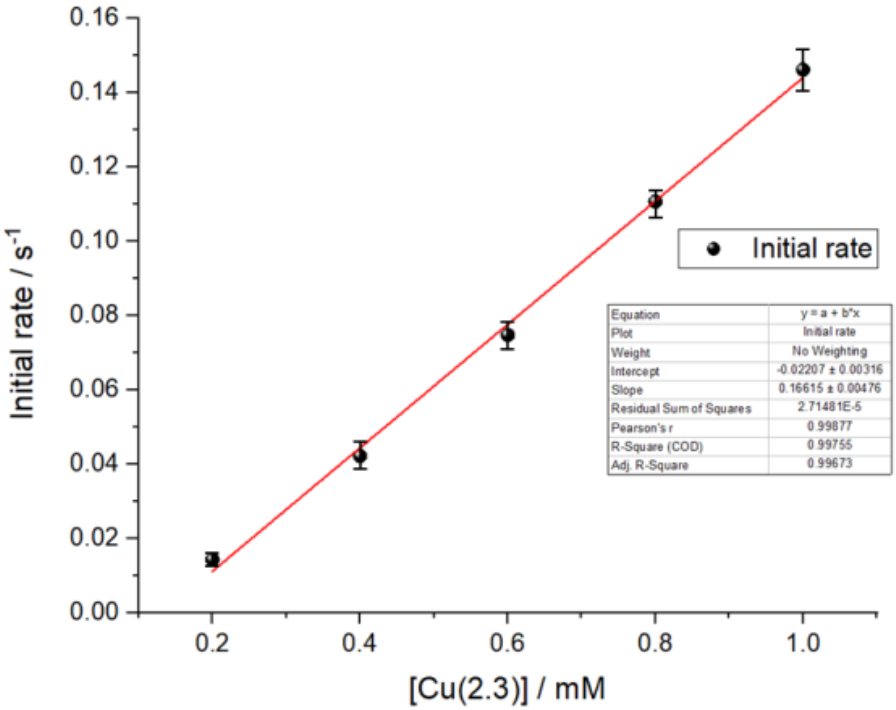

Figure 187. Initial rate of decay of the 352 band plotted against ***[Cu(2.3)]***$^{+}$ *concentration (HEPES 50 mM pH 8, 4 °C) Error bars represent standard deviation of three independent repeats*

It has to be noted that, as it is not possible to separate the ascorbic acid from the reaction mixture, following reduction of the Cu centre the oxidised ascorbic acid remains in solution, therefore, the effect of ascorbic acid on the 352 nm band must also be investigated. The intensity of the 352 nm band was found to be dependent on the concentration of ascorbic acid present in solution (Figure 188), however, the intensity of the 625 nm band corresponding to the *d-d* transition did not increase. This indicates that the bands are not coupled to one another and as such are two different processes occurring on a similar timescale.

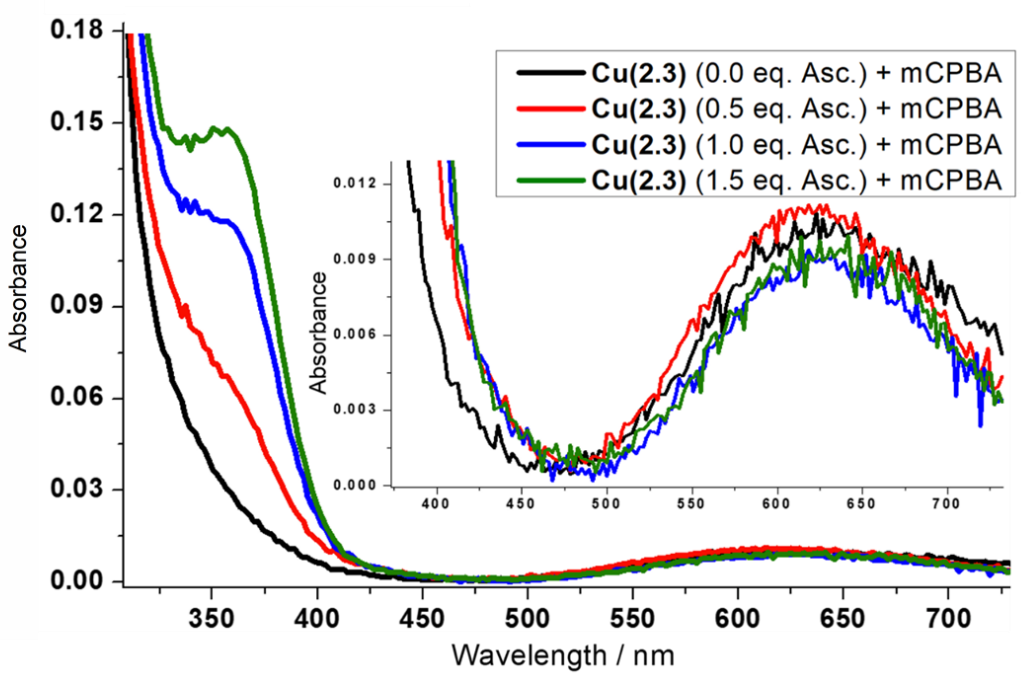

Figure 188. Intensity of the band at 352 nm formed on the reaction of ***Cu(2.3)(SO$_4$)*** *(0.31 mM) with mCPBA (1.0 mM) on varying the ascorbic acid concentration (pH 8, HEPES 50 mM). Inset graph: zoomed region focusing on the 652 nm band*

The assignment of these two bands as independent to one another can be assessed by the use of singular value decomposition (SVD, Section **2.2.4.4**),

$$\mathbf{A} = \mathbf{U\Sigma V^T}$$

Where, A is an $m \times m$ matrix constructed from the multiplication of the array of stopped flow spectra with its transpose. The A matrix can then be decomposed into its principal components. From this decomposition data two principle components, σ values, are obtained:

$$91 \; and \; 2.5$$

On inspection of the right singular vectors of the σ values below, could be interpreted as spectra noise and hence were discarded. This indicates that two independent processes are occurring. The rows of V^T matrix correspond to the principal components contribution to a given wavelength intensity separated from the time component (Figure 189). On inspection of these data, it is revealed that the first principal component (**P1**) likely corresponds to the band at 352 nm while the second principal component (**P2**) corresponds to the 652 nm band. These data clearly demonstrates that the formation of the 352 nm band is a separate occurrence from the reoxidation of Cu(I) to Cu(II).

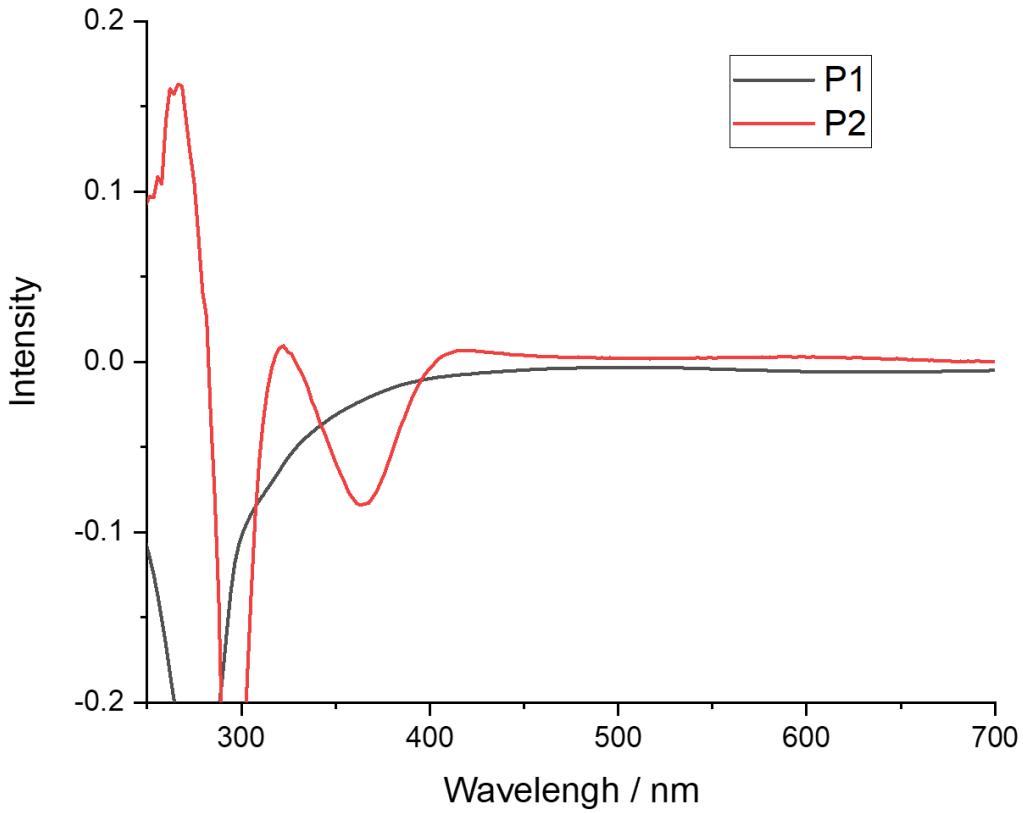

Figure 189. The right singular vectors spectra of the first and second singular values from the principles component analysis of the reaction of ***Cu(2.3)*** *and mCPBA*

As the ascorbic acid was shown to affect the intensity of the 352 nm band at pH 8, control experiments were carried out at higher concentrations of ascorbate and Cu. It was found that the presence of $Cu(SO_4)$ results in the appearance of a band similar to that observed in **Cu(2.3)(SO_4)**, only at a reduced intensity (Figure 190). This indicates that, while the formation of the species is improved by the presence of the ligand, it just requires a Cu ion.

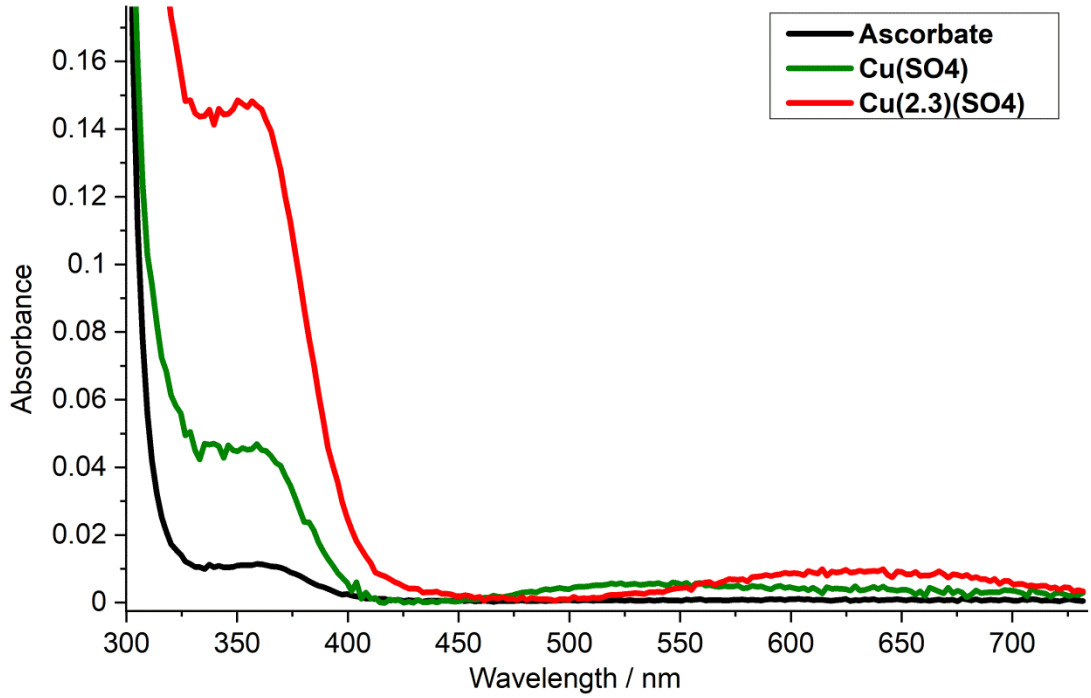

Figure 190. Intensity of the band at 352 nm formed on the reaction of ***Cu(2.3)(SO$_4$)*** *(0.35 mM) and* ***Cu(SO$_4$)$_2$*** *with mCPBA (1.0 mM), Ascorbic acid(0.35 mM)((pH 8, HEPES 50 mM)*

The combination of these two experiments strongly indicates that the band forming at 352 nm is not a Cu-based ROS, as the changes in intensity of the 352 nm band were not coupled with those of the Cu *d-d* band. These data are not consistent with a Cu-bound ROS, which would be expected for a Cu-OO^- or Cu-$O^{-\bullet}$ species.

To evaluate whether different complexes could exhibit a different behaviour, and to further test the conclusions about the role of ascorbate, **Cu(3.12)** and **Cu(3.12)⊂Sav2XM** were also reacted with *m*CPBA under the same conditions. The incorporation of **Cu(3.12)** into the artificial enzyme allows for removal of ascorbic acid after reduction *via* membrane filtration as the high molecular weight of the protein (MW **SAV2XM** ~50 K Da) allows for centrifugal filtration to be used. It was observed that the reaction of **Cu(3.12)** results in the same reactivity as that observed for **Cu(2.3)** (Figure 191). However, on incorporation of **Cu(3.12)** into **SAV2XM** this same reactivity was not observed (Figure 192), supporting once again the evidence that the 355 nm band is connected to the presence of ascorbic acid in solution.

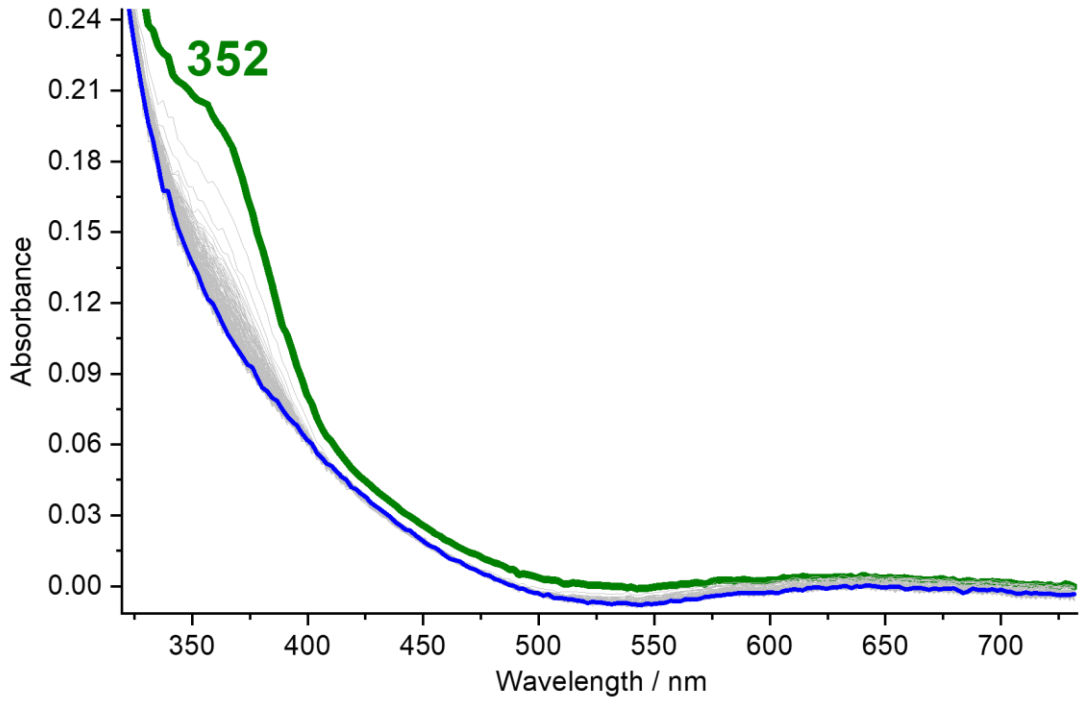

Figure 191. The stopped flow UV/Vis spectra of the reaction of ***Cu(3.12)Cl$_2$*** *(0.25 mM) with mCPBA (1 mM) in over a 500 millisecond timescale.(pH 8 HEPES 50 mM)*

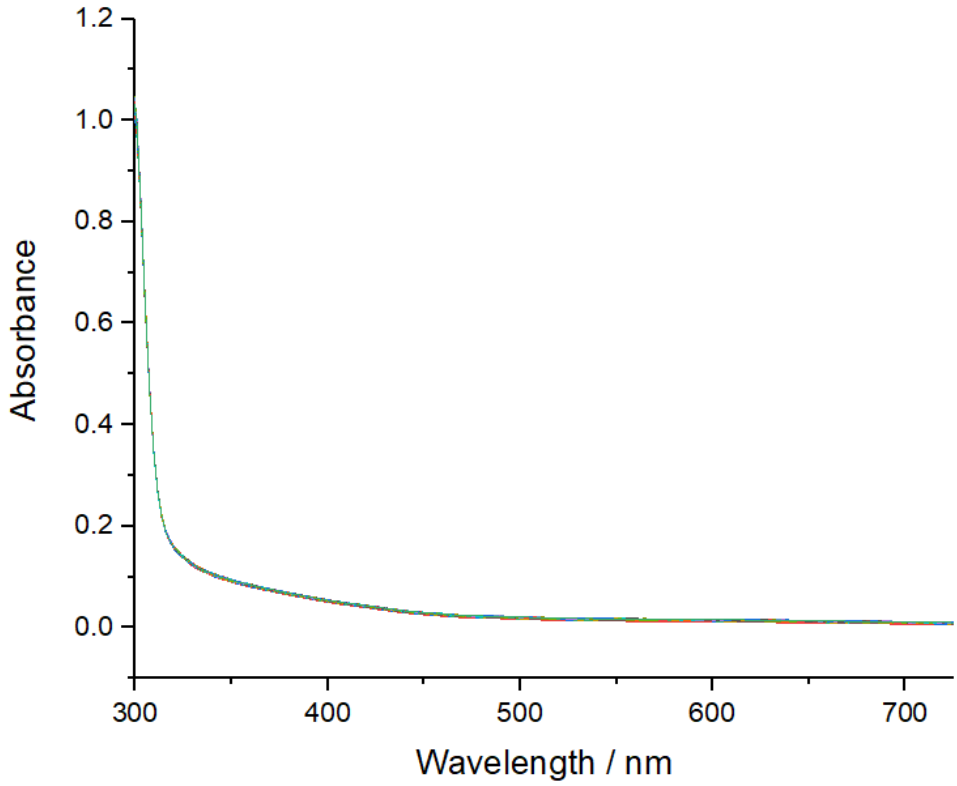

Figure 192. The stopped flow UV/Vis spectra of the reaction of ***Cu(3.12)(Cl)$_2$⊂Sav2XM*** *(0.25 mM) with mCPBA (1 mM) in at pH 8 over a 600 millisecond timescale.(pH 8 HEPES 50 mM)*

This species is likely a transient organic species formed *via* the reaction of ascorbic acid with a species generated from the reaction of *m*CPBA with Cu. Within the literature the formation of dehydroascorbic acid the oxidised form of ascorbic acid has been reported by Moeslinger *et al.*[288] which was found to have an absorption maximum of 345 nm. The authors also demonstrated the intensity of the band corresponding to dehydroascorbic acid increased with pH. As such this is the most likely candidate for the identity of this band.

To definitively exclude the presence of any organic radical species (e.g. an ascorbate or a ligand based radical), rapid freeze quench experiments were performed. Freeze quench is a technique used to trap intermediates in which the reaction mixture is sprayed into an isopentane bath at − 140 °C. The frozen powder can then be packed into an EPR tube and subjected to a typical CW EPR experiment.[289] On performing these experiments no signal for any organic radical could be observed in the spectrum (Figure 193). On returning the sample to room temperature, the expected EPR spectrum for **Cu(2.3)** was obtained indicating that the ligand is not being modified by this reaction in a way that affects the electronics of the Cu ion. This experiment shows that at least over a short time period no oxidative damage is occurring to the ligand. Furthermore, the use of alternative reducing agents was attempted but the complete reduction of **Cu(2.3)** to Cu(I) could not be observed. Hence, no further reactivity testing with *m*CPBA was carried out.

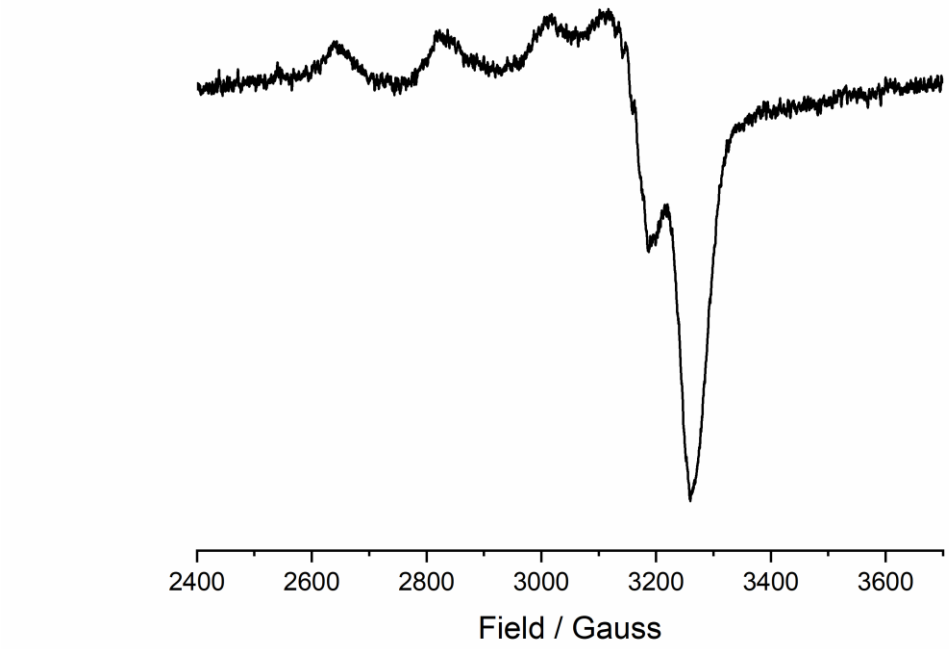

*Figure 193.The freeze quench EPR of **Cu(2.3)** (0.5 mM) (10 ms) following the reaction with mCPBA (5 equivalents) .(pH 8 HEPES 50 mM)*

Thus the definitive identity of the band at 352 nm could not be fully elucidated, but can tentatively be attributed to the rapid formation and then decay of dehydroascorbic acid due to its similar absorption wavelength and pH dependence. However, it has clearly been demonstrated that it is not a Cu oxygen reactive species, or the same species as was previously observed for LPMOs. Further experiments and kinetic studies could be carried out in an attempt to further understand the nature of this intermediate, however, these are not within the scope of this work.

4.2 Monitoring Catalytic Oxidation

4.2.1 Monitoring the Oxidation of Polysaccharides

LPMOs have been shown to be active on a range of polysaccharide substrates in the presence of a reducing agent, such as ascorbic acid, and a suitable oxidant, such as molecular oxygen or hydrogen peroxide. Enzymatic activity is commonly determined experimentally *via* the use of matrix assisted laser desorption ionisation-time of flight mass spectrometry (MALDI-TOF-MS), where the attack of the C1 or C4 carbon of the glycosidic bond by the LPMO produces identifiable oxidised products, aldonic acids in the case of C1 attack and ketoaldoses in the case of C4 attack, as discussed in **Section 1.2.4.1.** An example MALDI-TOF-MS spectrum which shows the breakdown products off cellulose following LPMO activity is shown in Figure 194.

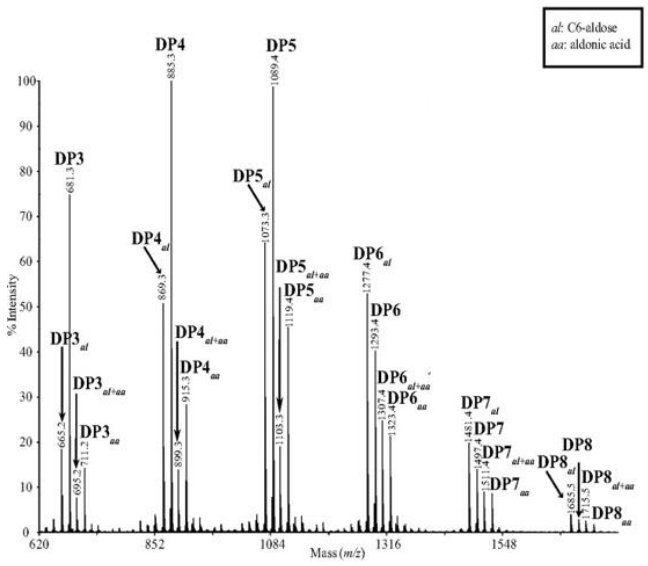

Figure 194. An example of a MALDI-TOF-MS analysis of an activity assay of TaAA9 on PASC, the degree of polymerisation (DP) of the polysaccharide is indicated on the spectrum. (Gallic acid 3 mM, 25 mM triethylammonium acetate pH 5.4, 5 g/L PASC). Adapted from Quinlan et al.[45] o2

While MALDI-TOF-MS can indicate the presence or absence of activity, this methodology is not quantitative for product formation, and hence other quantitative methodologies have been developed to monitor enzymatic activity, ranging from inexpensive colorimetric assays[164, 290-292] to expensive high-performance chromatographic methods.[293] These methods will be discussed in detail in the following sections.

High performance chromatographic (HPAEC) methods can detect carbohydrates directly using electrochemical methods. This method converts the sugars to oxyanions which are able to bind a column (stationary phase). These can then be eluted from the column using an appropriate mobile phase. The movement of the sugars is dependent on several factors such as size, structure and conformation, allowing the separation of extremely similar sugars. After separation the sugars are detected by pulsed amperometric electrochemistry in which the sugar is oxidised by a gold electrode. The current is then measured which is integrated over a time delay to yield the charge. Following this detection the electrode is cleaned by fully oxidising the surface at a higher potential to remove the sugar, followed a lower potential to remove any gold oxide formed. This is known as the waveform and is what is responsible for preventing poisoning of the electrode.[294-295]

However, this quantification can only be carried out on the soluble fraction produced by any given activity assay, any oxidation that has occurred on the insoluble fraction is not observed. This restricts these assays to sugars with low polymerisation numbers (1-6) as these are soluble in aqueous medium, thus this may not give a complete picture of the oxidation carried out by the enzyme. HPAEC has shown not to be very effective in the detection of C4- oxidised sugars, so may not be useful for LPMOs which are C4 specific or other non-specific catalysts.[296]

Colorimetric assays are commonly performed to indirectly quantify oxidation carried out by a catalyst or enzyme using UV/Visible spectroscopy. These methods rely on the use of an organic molecule that upon oxidation forms a coloured or florescent product, which can then be quantified via the Beer-Lambert Law, shown below,

$$A = \varepsilon C l$$

Where A is the absorbance, ε is the molar absorbance coefficient of the compound, *C* is the concentration and *l* is the path length of the cell. Using a combination of calibration curves and/or the ε of the oxidised product it is possible to calculate the concentration at any given time. From these data it is then possible to calculate the rates of reaction.

4.2.2 Amplex Red/Horseradish Peroxidase Assay

4.2.2.1 Introduction

The Amplex red assay/Horseradish peroxidase assay was developed to allow for the quantification of H_2O_2 production by an enzyme or complex using an indirect method.[291-292] This can be used as an approximate method to predict the oxidative ability of the enzyme or catalyst.[290] This assay measures peroxide concentration indirectly via the conversion of Amplex red to resorufin, shown in Figure 195, in the presence of horseradish peroxidase (HRP). HRP reacts with H_2O_2 to form Compound I which then oxidises Amplex red to form Compound II and an Amplex red radical. The subsequent reaction of Compound II with the Amplex red radical forms resorufin and regenerate the HRP resting state. The formation of resorufin allows for the extremely sensitive detection of H_2O_2 (picomolar) as the non-florescent substrate is converted to the strongly florescent resorufin with a stoichiometry of 1 in relation to H_2O_2. The reaction of horseradish peroxidase is extremely fast ($k = 2.1 \cdot \times 10^9\ M^{-1}s^{-1}$) and hence H_2O_2 is immediately consumed and does not result in oxidative damage to the enzyme.

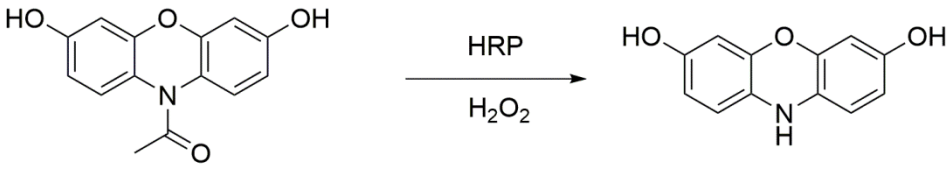

Figure 195. The reaction of Amplex red to form resorufin via the reaction of H_2O_2 in the presence of Horseradish Peroxidase

This methodology requires Amplex red to be in a large excess in order to prevent resorufin from becoming further oxidised to resazurin, which is non-florescent.[291] Furthermore, HRP activity must be maintained through the assay and thus if the rate of H_2O_2 exceeds the rate of HRP inactivation of HRP can occur due to a build-up of H_2O_2 causing oxidative damage to the enzyme thus the assay will detect no or reduced activity resulting in a misleading result.[297]

In the presence of reducing agent and absence of substrate it has been shown that LPMOs generate H_2O_2.[125] This is thought to occur via the following reaction, Cu(I) reacts with O_2 to generate a Cu(II) superoxide species, which then undergoes two hydrogen atom abstractions to form **Cu(I)-H_2O_2** species from which H_2O_2 can dissociate from the Cu centre (Figure 196). The Cu(II) ion can then be reduced to Cu(I) and re-enter the reaction cycle.

Therefore, the rate of production of H_2O_2 could be used as an indirect measurement of the activity of the complex.

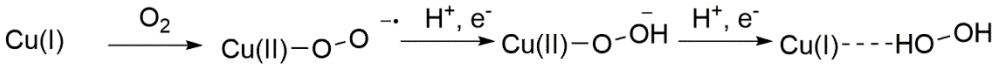

Figure 196. The formation of H_2O_2 from a reaction of Cu(I) and O_2

4.2.2.2 Results and Analysis

This assay was carried out as follows, a solution of **Cu(2.3)(Cl)$_2$, Cu(3.12)Cl$_2$** or **Cu(3.12)Cl$_2$⊂Sav2XM** (50 µM) in a sodium phosphate buffer (pH 6, 0.1 M) was prepared. In tandem, a solution of ascorbic acid (asc) (30 µM), Amplex red (50 µM) and horseradish peroxidase (HRP) (~ 30 µg/mL) was prepared. These two solutions were combined in a 5:45 (Cu solution: Amplex solution) ratio to give the final concentrations of (Cu, 5 µM, asc 27 µM, Amplex red 45 µM, HRP 27 µg/mL). This assay was assessed *via* the florescence of the band at 450 and 500 nm and the concentration of H_2O_2 production was assessed *via* the use of a calibration curve, shown in Figure 197, in which fixed concentrations of H_2O_2 were reacted with the horseradish peroxidase solution over the same timeframe.

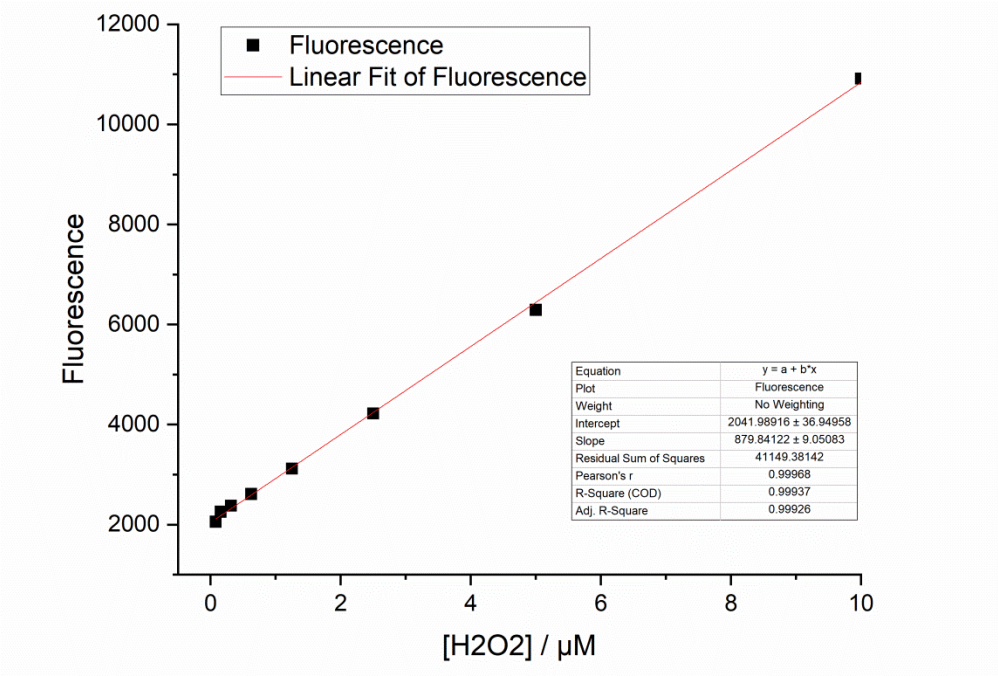

Figure 197. Calibration curve used to determine H_2O_2 production for the Amplex red assay (sodium phosphate buffer, pH 6, 0.1 M)

The rate of H_2O_2 produced by **Cu(2.3)Cl_2** , **Cu(3.12)Cl_2** and **Cu(3.12)Cl_2⊂Sav2XM** is shown in Figure 198. This reveals that the reactivity of **Cu(2.3)Cl_2** is unaffected by the addition of a linker and subsequent biotinylation which is commensurate with the EPR spectroscopy which showed that the Cu environment of **Cu(2.3)Cl_2** and **Cu(3.12)Cl_2** are the same (Section **3.4.3.2)**. Incorporation of **Cu(3.12)Cl_2** into SAV2XM reduces H_2O_2 production from 3.278 ± 0.181 µM min^{-1} to 2.367 ± 0.353 µM min^{-1} at 5 µM of Cu. Below 0.3 µM Cu the reaction proceeds at a rate lower than 0.4 µM min^{-1} which is the expected rate for the background reaction for the formation of resorufin and therefore these data are omitted.[291]

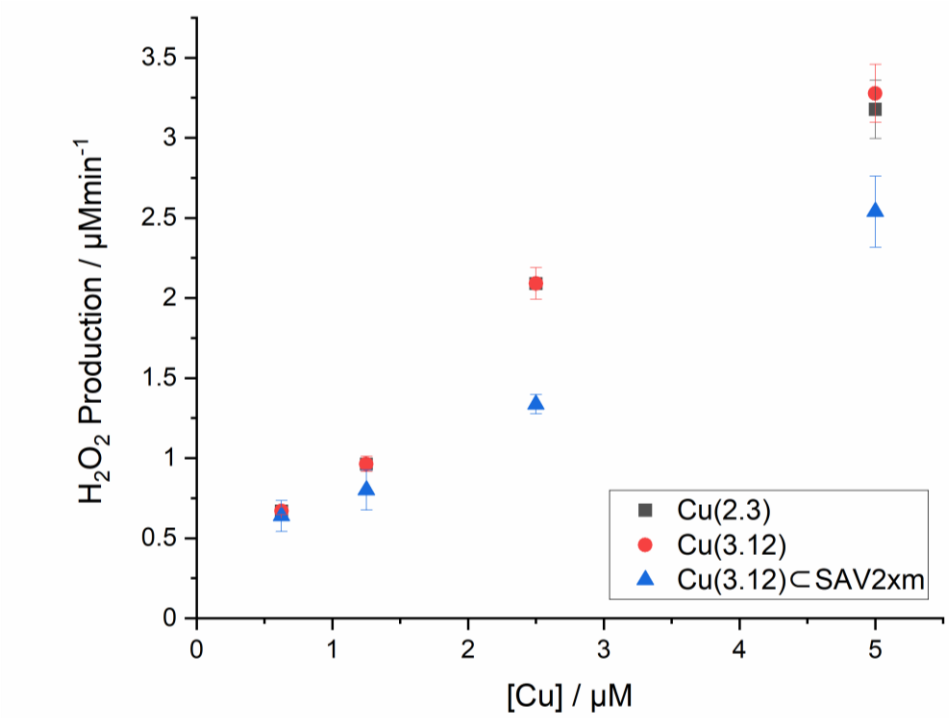

Figure 198. Hydrogen peroxide production by ***Cu(2.3)Cl_2*** *and* ***Cu(3.12)Cl_2*** *and* ***Cu(3.12)Cl_2⊂Sav2*** *(sodium phosphate buffer, pH 6, 0.1 M). Error bars represent standard deviation of three independent repeats*

Within the literature, H_2O_2 has been shown to react with Cu centres anchored to streptavidin and form a stable **Cu-OOH^-** species on the reaction with H_2O_2.[222] The generated H_2O_2 could immediately react with the Cu complex to form the 'relatively' stable Cu-OOH^- species. This would be in equilibrium with the free peroxide in solution and hence would result in a reduction in reaction rates. Thus the stability of this putative **Cu-OOH^-** is inversely correlated to the rate of H_2O_2 production. If this hypothesis is true the modification of nearby amino acid residues close to the active site should affect the rate of H_2O_2 production.

Thus in order to probe this hypothesis various streptavidin mutants (S112H, K121Y and K121A/S112E) were used to probe the rate of formation for H_2O_2 (Figure 199) and thus probe if residues within the vestibule could affect the stability of any reactive intermediate formed. The rate of H_2O_2 production of these mutants is shown in Table 19, from this data it can be seen that the residues at position 112 and 121 in the amino acid sequence has an effect on H_2O_2 production for the artificial enzyme as each of the mutants produces a different amount of H_2O_2.The EPR spectra of each of these enzymes are the same(Figure 200) and therefore the cause for this reactivity could be interpreted as due to the secondary coordination sphere provided by the protein.

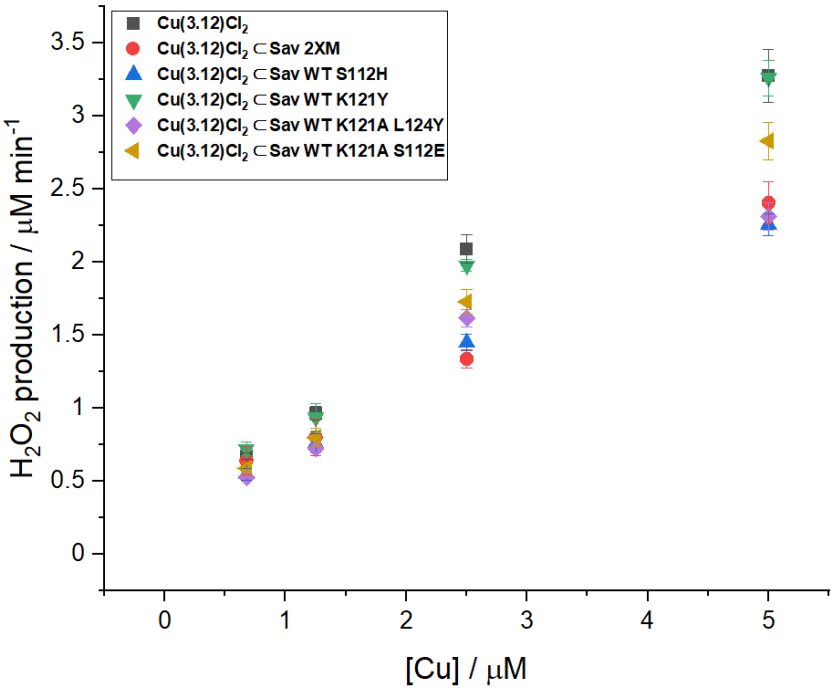

Figure 199. Hydrogen peroxide production by ***Cu(3.12)Cl$_2$, Cu(3.12)Cl$_2$⊂Sav2XM, Cu(3.12)Cl$_2$⊂SavWT S112H, Cu(3.12)Cl$_2$⊂SavWT K121Y*** *and* ***Cu(3.12)Cl$_2$⊂SavWT K121A/S112E*** *(sodium phosphate buffer, pH 6, 0.1 M). Data shown in Table 19. Error bars represent standard deviation of three independent repeats*

Table 19. Data from the Amplex red assy by ***Cu(3.12)Cl$_2$, Cu(3.12)Cl$_2$⊂Sav2XM, Cu(3.12)Cl$_2$⊂SavWT S112H, Cu(3.12)Cl$_2$⊂SavWT K121Y, Cu(3.12)Cl$_2$⊂SavWT K121A/L124Y Cu(3.12)Cl$_2$⊂Sav2XM K121A/S112E*** *plotted in Figure 199*

Species	[Cu] / uM			
	5	2.5	1.25	0.675
Cu(3.12)Cl$_2$	3.27	2.09	0.96	0.67
Error	0.18	0.10	0.05	0.02
Cu(3.12)Cl$_2$⊂Sav2XM	2.41	1.34	0.80	0.64
Error	0.14	0.06	0.13	0.10
Cu(3.12)Cl$_2$⊂SavWT S112H	2.26	1.45	0.76	0.55
Error	0.08	0.06	0.07	0.04
Cu(3.12)Cl$_2$⊂SavWT K121Y	3.26	1.98	0.93	0.72
Error	0.12	0.04	0.09	0.05
Cu(3.12)Cl$_2$⊂SavWT K121A/L124Y	2.31	1.62	0.72	0.52
Error	0.09	0.06	0.03	0.03
Cu(3.12)Cl$_2$⊂SavWT K121A/S112E	2.83	1.73	0.80	0.59
Error	0.13	0.08	0.06	0.04

While none of the mutants result in an increase to the rate of H_2O_2 production compared to the unincorporated complex, **Cu(3.12)Cl$_2$⊂ SAVWT K121Y** restores activity to the same level as the unincorporated complex (At 5 μM. **Cu(3.12)Cl$_2$** $= 3.20 \pm 0.13$ μM min^{-1}, **Cu(3.12)Cl$_2$⊂ SAVWT K121Y** $= 3.26 \pm 0.12$ μM min^{-1}). This indicates that if the stabilisation hypothesises is correct the point mutation of Lysine 121 to tyrosine induces a significant change to the hydrogen bonding network which results in no stabilisation of the Cu peroxide complex.

The **SAVWT K121A L124Y** mutant result do not appear to affect the rate H_2O_2 production, on comparison of the rates of H_2O_2 production with **SAV2XM** they are found to be within error of one another (At 5 μM **Cu(3.12)Cl$_2$⊂Sav2XM** $= 2.41 \pm 0.14$ μM min^{-1}, and **Cu(3.12)Cl$_2$⊂ SAVWT K121A L124Y** 2.31 ± 0.09 μM min^{-1}). Assuming that the stabilisation hypothesis is true, this indicates that the amino acid residue at the **124** position does not meaningfully affect any intermediate within the vestibule as H_2O_2 remains constant. Thus the 124 position does not affect the H-bonding network within the vestibule.

Two mutants effect the 112 position **SavWT S112H** and **SavWT K121A/S112E.** The **SavWT K121A/S112E** mutant increases H_2O_2 production compared to **SAV2XM (** 2.83 ± 0.13 μM min^{-1} *vs* 2.41 ± 0.14 μM min^{-1}). The increase in H_2O_2 production observed for **SavWT K121A/S112E** could be attributed to a decrease in pK_A from 13 to 4.3 from serine to glutamic acid by assuming that the hydrogen bond is stabilising the copper peroxide

intermediate this data would imply that the 112 residue is acting as a hydrogen bonding acceptor. As the pK_A of a hydrogen bonding acceptor decreases the worse of a hydrogen bond acceptor it becomes and hence results in the destabilisation the intermediate.[298] The other mutant, **SavWT S112H**, decreases H_2O_2 production compared to **SAV2XM** (2.26 ± 0.08 µM min^{-1} *vs* 2.41 ± 0.14 µM min^{-1}). This is an unexpected result as following the previous argument it would be expected that a similar increase in H_2O_2 production for **SavWT S112H** (pK_A of histidine = 6 vs pK_A *of* serine = 10) would occur. However, unlike **SAV2XM** and **K121A/S112E** the 121 position is not an alanine so the change in H_2O_2 production cannot be attributed to the histidine as the 121 residue has previously been shown to be key for the rate of H_2O_2 production by the **SAVWT K121Y** mutant. To examine this hypothesis the **SavWT S112H/K121A** mutant would be required.

However, without a crystal structure of **Cu(3.12)Cl_2⊂Sav** it is not possible to examine the precise role of these residues. These findings demonstrate that the complex hydrogen bonding network present within the streptavidin vestibule affects the reactivity of **Cu(3.12)Cl_2** when it is incorporated within the artificial enzyme.

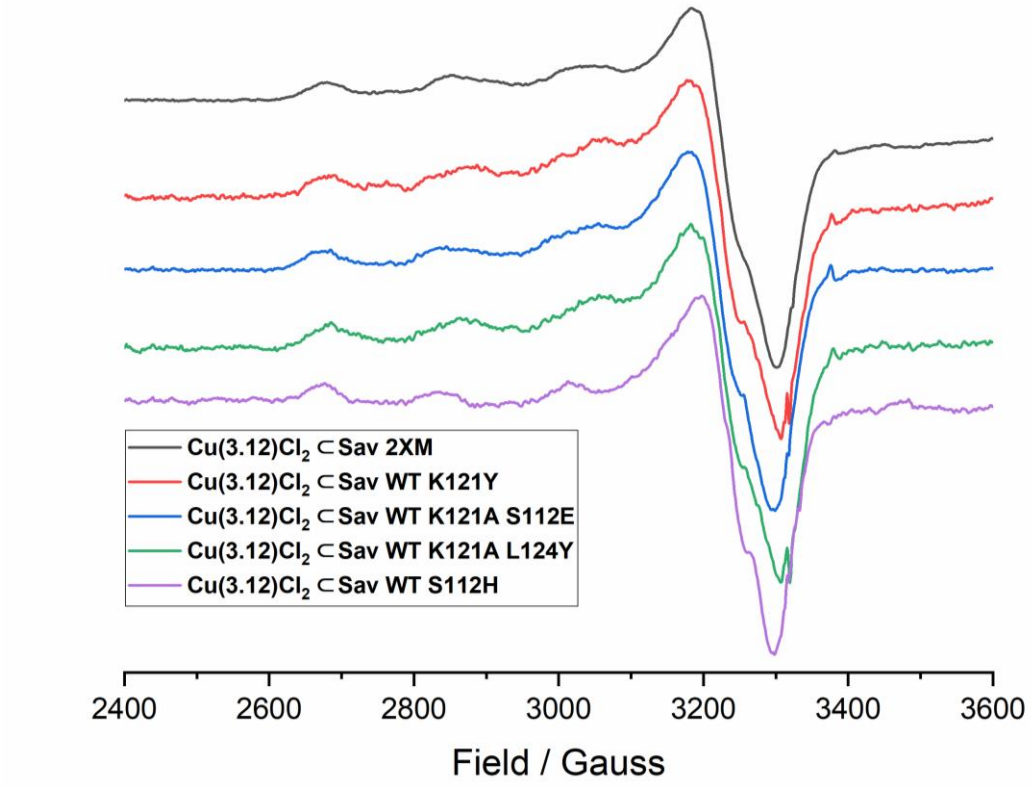

Figure 200. Continuous wave X-Band EPR spectrum of ***Cu(3.12)Cl_2****,* ***Cu(3.12)Cl_2⊂Sav2XM,*** ***Cu(3.12)Cl_2⊂SavWT S112H****,* ***Cu(3.12)Cl_2⊂SavWT K121Y*** *and* ***Cu(3.12)Cl_2⊂SavWT K121A/S112E*** *(sodium phosphate buffer, pH 6, 0.1 M).150 K*

4.2.3 Reactivity against Cellulose

The goal of this project was to design a small molecule mimic which was able to reproduce both the spectroscopic and reactive properties of LPMOs. The electronic characteristics of the complexes have been explored in Chapter 2 and 3, whilst the activity against polysaccharide substrates is reported herein. For these activity tests three different polysaccharides were selected: Avicel (crystalline cellulose), β-chitin (squid pen chitin) and phosphoric acid-swollen cellulose (PASC). These substrates are commonly used within LPMO activity testing and they represent a range of polysaccharide bond strengths and crystallinity.

As the Cu environment of **Cu(2.3)Cl_2** and **Cu(3.12)Cl_2⊂Sav2XM** has been shown to vary dependent on pH (section **2.2.2.3** and **3.4.2.3,** respectively), two pH values were chosen for testing **Cu(2.3)Cl_2** (pH 5.8 and pH 8.5), while for **Cu(3.12)Cl_2⊂Sav2XM** three pH values were chosen (5.8, 8.5 and 12).

The complexes were incubated with the various polysaccharides in the presence of a reducing agent (1 mM ascorbic acid) and O_2 for 24 hours. LPMOs known to be active on these substrates (*Cv*AA9, cellulose, and *Ba*AA10, chitin), were used as a positive control to determine the effectiveness of the assay. The reaction was run for 4 hours at 35 °C and then was analysed by MALDI-TOF mass spectrometry.

Analysis of the reaction mixture by MALDI-TOF mass spectrometry did not reveal the presence of any products under these conditions, the spectra of the samples containing the complexes did not differ from the negative controls, shown in Figure 201. The positive controls showed the presence of peaks corresponding to soluble polysaccharides indicating that the assay was working well and that the lack of activity is due to the copper complexes being unable to oxidise the polysaccharides.

The lack of degradation observed by **Cu(2.3)Cl_2 , Cu(3.12)** and **Cu(3.12)Cl_2⊂Sav2X** is unsurprising as it was shown that these complexes were unable to generate any observable ROS intermediates as discussed in Section **4.2.2**. Furthermore, the complexes do not have a way to locate themselves close to the polysaccharides, unlike LPMOs which possess a binding face. This may hinder reactivity as potential reactive species generated may be released into solution at which point they may disproportionate.

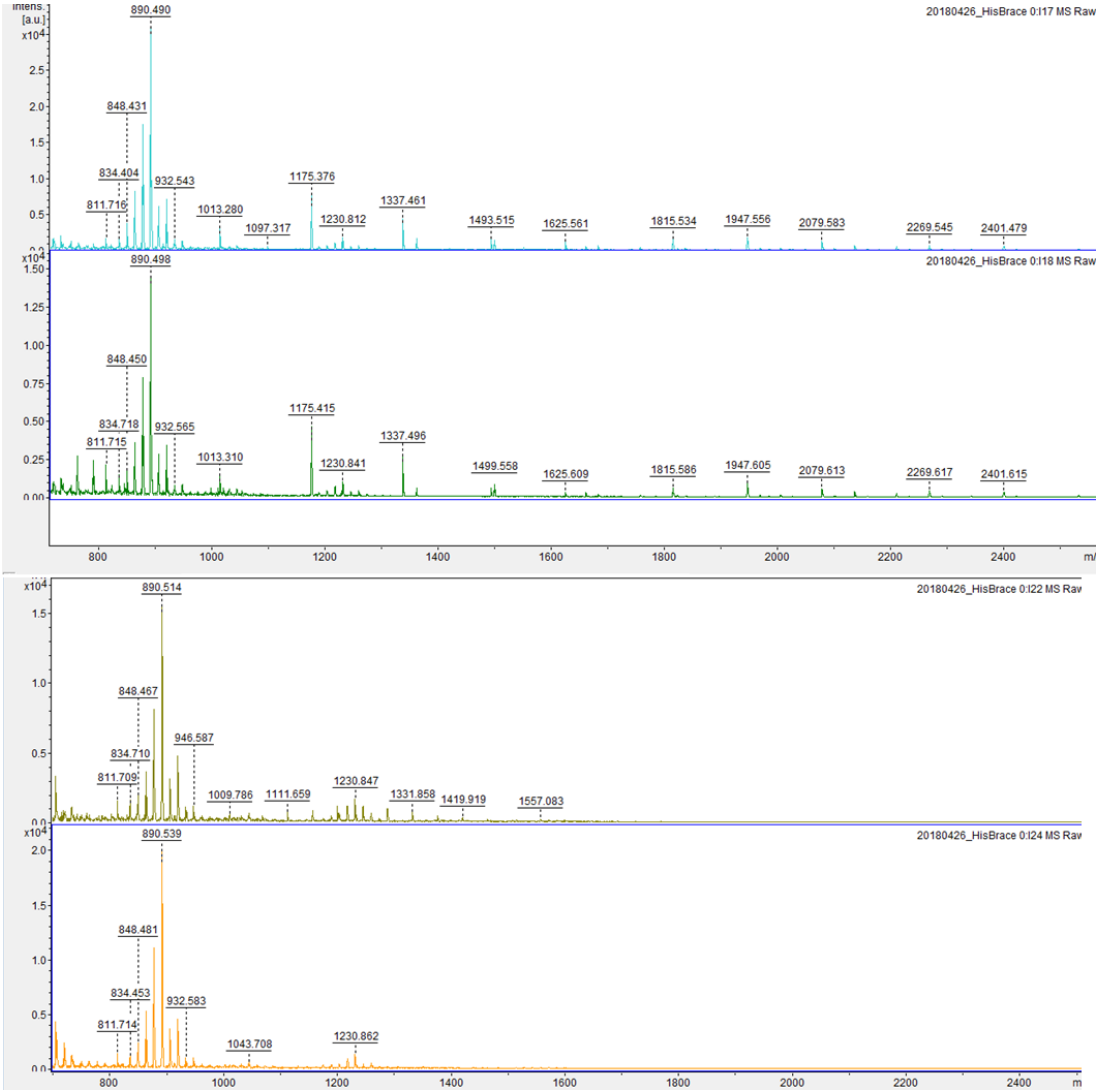

Figure 201. Results of MALDI-TOF analysis of the polysaccharide degredation assay. ***Blue.*** *chitin and ascorbic acid (1 mM).* ***Green.*** *Chitin and ascorbic acid (1 mmol). and model complex, $Cu(L_{NH2})Cl_2$ (0.01 mmol).* ***Brown.*** *Avicel and ascorbic acid (1 mmol).* ***Yellow.*** *Avicel and ascorbic acid (1 mmol). and model complex, $Cu(L_{NH2})Cl_2$ (0.01 mmol).*

From these experiments it is clear that **$Cu(2.3)Cl_2$, Cu(3.12)** and **$Cu(3.12)Cl_2$⊂Sav2X** are unable to break down the strong bonds found within polysaccharides. As such alternative assays were used to assess the oxidative competence of these compounds.

4.3.3 Further Activity Assays

Two further assays were planned to test the activity of the complexes, the *p*-nitrophenyl-β-D-glucopyranoside and 2,6-dimethoxyphenol (DMP) Assays (discussed below). However, due to the COVID19 global pandemic and a personal injury these were not carried out. Following the results of the Amplex red assay it would be expected that these activity assays would follow a similar trend where incorporation of **Cu(3.12)Cl_2** into streptavidin would result in a decrease in reactivity due to the stabilisation of any Cu peroxide intermediates formed and that point mutations made to streptavidin could either further reduce reactivity or restore it to the level of the unincorporated complex.

4.4 Conclusions

In this chapter the reactivity of **Cu(2.3)**, **Cu(3.12)** and **Cu(3.12) ⊂ Sav** with oxidants were examined. Initially the reaction of **Cu(2.3)** with *m*CPBA was believed to result in the formation of a Cu-oxygen reactive species, due to the appearance of a band at 352 nm which was similar in intensity, energy and lifetime to that of LPMOs undergoing the same reaction. By studying the rates of decay it was found that the lifetime of this species was dependent on the ascorbic acid concentration, pH and concentration of **Cu(2.3)** present in solution.

The concentration of ascorbic acid was shown to increase the intensity of the 352 nm band while the d-d band at 652 nm did not increase. Hence, the whole data set was examined by SVD, which revealed the presence of two independent processes occurring (two significant non-zero σ values of 91and 2.5 were obtained). On plotting the right singular vectors of these values, it was found that the first principle component corresponded to the formation of the 352 nm band and the second corresponded to the formation of the 652 nm band indicating that these two processes are independent. This indicates that the formation of the 352 nm band does not correspond to a Cu-oxygen reactive species. Freeze quench EPR spectroscopy, ruled out the presence of any organic radicals corresponding to this band. Hence, the most likely candidate for this band is the formation of dehyroascorbic acid which has an absorption maximum of 345 nm and pH dependence similar to what is observed for observe **Cu(2.3)**.[288]

The ability of both the complexes and corresponding artificial enzymes to produce H_2O_2 was tested *via* an Amplex red assay. It was found that the small molecule complexes **Cu(2.3)** and **Cu(3.12)** produced the same amount of H_2O_2 indicating that the addition of the biotin linker did not affect the chemistry of the complex, which is commensurate with the EPR data (Section **2.2.2.2**). However it was demonstrated that the incorporation of **Cu(3.12)** into SAV2XM resulted in a significant reduction to H_2O_2 production (~3.3 μM versus 2.8 μM). Point mutations made to the streptavidin vestibule were shown to have an effect on this reactivity where the mutant **K121Y** restored activity to the same level as before incorporation, indicating that this amino acid residue is important for the activity of the artificial enzyme with respect to the Amplex red assay.

The reactivity of these complexes with O_2 and H_2O_2 was tested against common polysaccharide substrates, and it was found that they were unable to catalyse the oxidative cleavage of the 1,4 glycosidic bond.

Chapter 5 Conclusions and Future Work

5.1 Final Conclusions

The goal of this work was to design, synthesise and characterise a new ligand capable of modelling the active site of LPMOs. The active site of LPMOs consists of a Cu(II) ion which is coordinated by three nitrogen atoms (two imidazole ligands *trans* to one another and a primary amine *trans* to an exogenous solvent) in a Jahn-Teller distorted octahedral geometry. Therefore, a novel ligand **2.3** has been designed and successfully synthesised which incorporates the primary amine into the coordination sphere by linking *L*-histidinol and 2-chloromethylpyridine *via* a Williamson ether synthesis. This compound was synthesised and characterised by mass spectrometry, NMR and IR spectroscopy and the purity was determined by CHN analysis. The overall yield was found to be 32% over a five step synthesis.

The corresponding Cu complex of **2.3** was shown to bind Cu in a 1:1 ratio and found to have similar EPR parameters to LPMOs in the presence of substrate (g_z = 2.271 vs g_z = 2.271, A_z = 523 MHz Vs A_z = 518 MHz).[1-2] The compound was found to have a pH dependence in water where the exogenous ligand H_2O would deprotonate to an OH^- with a pK_a of 7.8. This is similar behaviour to that observed in LPMOs and suggested that **2.3** possesses a vacant coordination site which would be required for reactivity.[3]

During the course of this work, the importance of the secondary coordination sphere for LPMO activity had been demonstrated using mutagenic studies.[4] Therefore, in order to allow for a secondary coordination sphere to be incorporated into **2.3**, an artificial enzyme approach was used. To anchor **2.3** into a protein host a biotin streptavidin approach was selected. The modification of **2.3** to allow for the attachment of biotin to the complex has been carried out as follows: a linker was attached to **2.3** in the 4 position of the pyridine ring using a Sonogashira cross-coupling. Following this, the primary amine present in the linker was deprotected and subsequently biotinylated. This led to the successful synthesis of the biotinylated compound **3.12** in seven steps with an overall yield of 22%. This compound was characterised by mass spectrometry, NMR and IR spectroscopy and the purity was determined by CHN analysis.

The corresponding Cu complex of **3.12** was demonstrated to be the same as **2.3** through the use of EPR and UV/Vis spectroscopy, demonstrating the addition of the biotin and linker to **2.3** did not affect the electronic environment of the Cu center. The incorporation of **Cu(3.12)** into streptavidin induces changes to the Cu environment which were observed both in the EPR (g_z = 2.236 to g_z = 2.271 and A_z = 523 MHz to A_z = 455 MHz at pH 6) and UV/Visible spectrum (appearance of a band at 360 nm ε = 436 $M^{-1}cm^{-1}$). Furthermore, the artificial enzyme is able to stabilise a new high pH species, **S1**, which is extremely similar to the species formed in *Bl*AA10 LPMO at a similar pH. Analysis of the spin Hamiltonian parameters of this species indicates that a change to either the coordinating atoms, provided by the protein, or a significant change to the coordination geometry occurs on the formation of this species.

Efforts to crystallise **Cu(3.12)Cl_2⊂Sav** using a soaking methodology was ultimately unsuccessful as despite density which corresponded to **3.12** being observed within the vestibule, no anomalous density corresponding to a Cu ion could be observed. This is likely due to the acidic crystallization and soaking conditions causing the precipitation of Cu. This theory is commensurate with the spectroscopic data as it had been demonstrated using EPR spectroscopy that **Cu(3.12)Cl_2⊂Sav** is unstable at low pH, as no spectrum could be recorded below pH 6**.** Streptavidin crystals at higher pH could not be grown despite using literature methodology and hence this hypothesis could not be probed further.

The reactivity of **Cu(2.3), Cu(3.12)** and **Cu(3.12)Cl_2⊂Sav** were tested with *m*CPBA in an attempt to observe a reactive oxygen intermediate. This work initially appeared promising with a band at 352 nm appearing for both **Cu(2.3)** and **Cu(3.12)** on reactions with *m*CPBA in the UV/visible stopped flow spectrum. This band appears at a similar wavelength to that of a band observed in LPMOs (354 nm) under the same reaction conditions. However, on further study it could be demonstrated through the use of careful control experiments that this reactivity is most likely due to the oxidation of ascorbate to dehyroascorbic acid instead of the formation of a Cu based ROS.

The reactivity of **Cu(2.3), Cu(3.12)** and **Cu(3.12)Cl_2⊂Sav** were tested against polysaccharide substrates and were found to be inactive. The reactivity of these complexes were assessed by an Amplex red assay which found that **Cu(2.3)** and **Cu(3.12)** were equally reactive while a significant reduction in reactivity occurs on the incorporation of **Cu(3.12)** into the artificial enzyme (3.278 ± 0.18 $\mu Mmin^{-1}$ to 2.367 ± 0.12 $\mu Mmin^{-1}$). However, this reactivity could be

restored on the point mutation of streptavidin to form the **K121Y** mutant demonstrating that the secondary coordination sphere provided by **SAV** affects the reactivity of **Cu(3.12).**

To conclude, these complexes and corresponding artificial enzymes are promising complexes for the modeling of LPMOs and their reactivity. However, further characterisation of **Cu(3.12)Cl_2⊂Sav** is required in order to understand the effects of point mutations within the vestibule on **Cu(3.12)** reactivity.

5.2 Future Work

5.2.1 Chapter 2

The crystallisation of **Cu(2.3)** proved problematic mostly due to the limited solubility of the complexes. Thus the ligand could be modified to improve solubility; this could be carried out *via* the addition of steric bulk to the imidazole ring. This could be accomplished by using two different protecting groups during the synthesis of **2.3** which would allow for the protecting group on the amine to be selectively removed. The remaining protecting group could be left attached to the ligand and thus aid in the solubilisation of the resultant complex in non-polar organic solvents. Furthermore, this would allow for the formation of the Cu(I) species directly *via* the reaction of a modified ligand with a Cu(I) salt which was not possible with **2.3** due to problems with solubility of the appropriate Cu(I) salt.

In the absence of a crystal structure, the number of nitrogen atoms directly coordinating to the Cu centre by **2.3** could be unambiguously elucidated *via* the use of ENDOR EPR experiments. These experiments would allow for the couplings to all of the nitrogen atoms directly coordinating to the Cu ion to be defined by their SHF. Further characterisation of the **Cu(2.3)** using electrochemistry could be carried out in order to obtain the redox potential of the copper centre which would allow for comparisons to LPMOs and other Cu complexes within the literature.

The ligand **2.3** could also be modified to allow for a Hammet type analysis to be carried out on the complex. This could be carried out by modifying the pyridine ring to include electron withdrawing or electron donating groups. This would allow for the electronics of the Cu centre to be controlled and the effect of these modifications on the oxidative ability of the subsequent complex to be assessed.

In the absence of a crystal structure of **Cu(2.3)** computational methods such as density functional theory (DFT) could be used to assess the coordination geometry and EPR spectroscopy of the complex.

5.2.2 Chapter 3

The crystal structure of **Cu(3.12)Cl_2⊂Sav2XM** was not obtained. This is believed to be due to the low pH used to crystallise '*apo*' **Sav2XM** and during subsequent soaking experiments. In order to probe this hypothesis, additional crystal screens could be carried out using PEG or MPTG at a more neutral pH (6-8), this could facilitate soaking experiments in which **Cu(3.12)Cl_2** does not precipitate as demonstrated by EPR spectroscopy. If this proves unsuccessful, it has been recently shown by Olshansky *et al.*[5] that it is possible to sequentially alter the pH of the crystals and soaking conditions of **Sav2XM** crystals grown in the ammonium sulfate conditions. Hence, a similar study could be carried out using **Cu(3.12)Cl_2**.

The long linker length may also be effecting the position of **Cu(3.12)Cl_2** within the streptavidin vestibule, this linker could be shortened *via* a direct modification of **3.12**.This could be carried out by the use of 5-bromo-2-choromethyl pyridine which would result in a shortening of the linker length from seven to five atoms.

Further characterisation of **Cu(2.3)** could be carried out *via* the use of electrochemistry in order to obtain the redox potential of the copper centre. This would allow us to determine the effect, if any, of incorporation of **Cu(3.12)** into streptavidin on the redox potential of the complex.

5.2.3 Chapter 4

Further analysis could be used to determine the identity of the 408 nm band formed on the reaction of Cu with *m*CPBA and ascorbic acid. Further experiments can be carried out at higher pH where the species was found to be more stable. These experiments could include further EPR freeze quench experiments, mass spectrometry and additional stopped flow experiments. Furthermore, these experiments could be carried out on a preparative scale and the products of this reaction could be separated from the reaction mixture and analysed *via* traditional organic techniques such as ^{1}H NMR spectroscopy. The identity of these products could then be used to determine potential intermediates for their formation.

The oxidative ability of **Cu(2.3), Cu(3.12)** and the corresponding artificial enzymes can be further tested. The two best candidates for this are the 2,6-dimethoxyphenol and *p*-nitrophenyl-β-D-glucopyranoside assays.[164, 290] These assays would allow for reactivity comparisons with literature data both for small molecule Cu complexes and LPMOs using the PPNG or DMP assay, respectively.

These assays use peroxide to generate the active species assuming that the complexes behave similarly to that previously observed for the amplex red assay. It would be expected that **Cu(2.3)** and **Cu(3.12)** would exhibit the same activity. Assuming that the reduction in activity for the amplex red assay is due to the stabilisation of a Cu-Hyperperoxo complex, a similar suppression in activity would be expected for the corresponding WT artificial enzyme. This reactivity could be modulated by the use of streptavidin mutants as seen in the Amplex red study.

Chapter 6 Experimental

6.1 General considerations for experimental procedures

NMR spectra were acquired on either a Jeol ECS400 or ECX400 (Operating frequencies; $_1$H 399.78 MHz, ^{13}C 100.53 MHz, ^{19}F 376.17 MHz, ^{31}P 162 MHz). Chemical shifts (δ) are quoted in parts per million referenced to residual proton signal of the solvent; *J* values are quoted in Hz and are referred to ^{1}H - ^{1}H couplings, unless otherwise stated. All ^{13}C NMR spectra were recorded with ^{1}H decoupling. Assignments were completed with the aid of COSY, DEPT, NOESY, HSQC, HMBC experiments. Mass spectrometry measurements were performed on a either a Bruker micrOTOF MS (ESI) or a Waters GCT Premier Acceleration TOF MS (LIFDI) instrument. Elemental analyses were performed using an Exeter Analytical Inc. CE-440 analyser. Melting points were measured on a Stuart Scientific SMP3 apparatus. Diffraction data for small molecule X-ray crystallography was collected using an Oxford Diffraction SuperNova system with EOS CCD camera at 110 K. The UV/Visible absorption spectra were acquired on a Shimadzu UV-1800 spectrometer or on a Perkin Elmer Lambda 465 diode array spectrophotometer.Crystal structures were solved with Olex2[300] using Superflip[299] structure solution program and refined with ShelXL.[300]

Continuous wave (CW) X-band frozen solution EPR spectra were acquired on a Bruker EMX spectrometer operating at ~9.30 GHz, with modulation amplitude of 4 G, modulation frequency 100 kHz and microwave power of 10.02 mW (3 scans) at 155 K. Q-band spectra were acquired on a Jeol JES-X320 spectrometer operating at ~34.7GHz, with modulation width 1 mT and microwave power of 0.75-1 mW at 77 K.

6.2 Synthesis and characterisation of (2S)-1-(1H-imidazol-4-yl)-3-[(pyridin-2-yl)methoxy]propan-2-amine, **2.3**

6.2.1 Synthesis of dityrityl-L-histidine methyl ester, 2.6

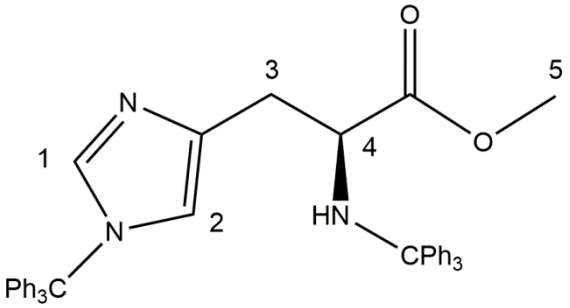

L-histidine methyl ester hydrochloride (1.000 g, 42 mM) was stirred with Et_3N (21.0 g, 208 mM, 5 eq) and acetonitrile (50 mL) for 0.5 h. Triphenylmethyl chloride (29.0 g, 104 mM, 2.5 eq) was dissolved in acetonitrile (900 mL) and added in small portions at 0 °C. The mixture was allowed to warm to room temperature and stirred overnight. The solvent was evaporated and the residual solid was stirred with water (200 mL) for 0.5 h. A light yellow solid material was filtered, washed with water, and then dried 12 hours in a vacuum oven. The compound was used in the synthesis of Dityrityl-L-histidinol with no further purification.

Yield: 2.712 g (30.8 mM, 74%)

^{1}H NMR ($CDCl_3$, 400 MHz) δ: 7.10-7.40 (m, > 31H, phenyl-H, H_1) 6.63 (s, 1H, H_2),3.68 (m, 1H, H_4) 3.05 (s, 3H, H_5), 2.97 (dd, 1H, H_{3A}, J = 3, 14 Hz) 2.80 (dd, 1H, H_{3B}, J = 14, 6 Hz)

^{13}C NMR (DMSO, 100.51 MHz) δ: 173.958 (**C**=O), 147.591 (Ph_3), 145.712(Ph_3), 142.079 ($\mathbf{C_{imd\text{-}Q}}$), 136.453 ($\mathbf{C_1}$), 129.034 ($Ph_3$), 128.0136 ($Ph_3$), 127.604 ($Ph_3$), 127.3747 ($Ph_3$), 126.488 ($Ph_3$), 126.1064 ($Ph_3$), 119.241 ($\mathbf{C_2}$), 80.391 (N**C**-$Ph_3$), 70.2159 ($NH_2$**C**-$Ph_3$), 56.284 ($\mathbf{C_4}$), 50.848 ($\mathbf{C_5}$), 33.436 ($\mathbf{C_3}$)

ESI-Mass spectrometry: [M-H]+ at 654.3138 ([M-H]+ calc. for $C_{45}H_{40}N_3O_2$: 654.3138, error – 2.3 mDa)

MP: 76-78 °C

6.2.2 Synthesis of dityrityl-L-histidinol, 2.8

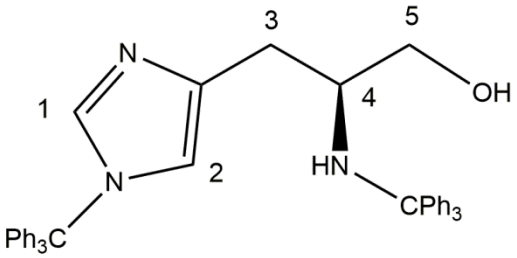

Under a nitrogen atmosphere using dry solvents, $LiAlH_4$ (0.040 g, 1.046 mM, 3.4 eq) was dissolved in THF (5 mL). Dityrityl-L-histidine methyl ester (0.271 g, 0.308 mM, 1 eq) was dissolved in THF (2.5 mL). The $LiAlH_4$ solution was cooled to 0 °C and the dityrityl-L-histidine methyl ester solution was added dropwise to this solution. The reaction mixture was allowed to warm up to room temperature and then stirred for 30 minutes. A solution of NaOH (0.012 g, 0.308 mM, 3 eq) in H_2O (5 mL) was added to the reaction mixture, which was then stirred for an additional 15 minutes. The reaction mixture was filtered and the solvents were removed *in vacuo*. The crude was purified on a silica chromatography column using 1:1 ethyl acetate: chloroform as the mobile phase. RF: 0.6. On purification dityrityl-L-histidinol was obtained as a white foam.

Yield: 0.152 g (0.234 mM, 78 % yield)

^{1}H NMR ($CDCl_3$, 399.78 MHz) δ: 7.08-7.50 (m, >31H, phenyl-H, H_1), 6.30 (s, 1H, H_2), 3.55 (dd, 1H, H_{5a}, J = 3, 11 Hz), 2.99 (dd, 1H, H_{5b}, J = 6, 11 Hz), 2.92 (m, 1H H_4), 2.44 (dd, 1H, H_{3a}, J = 3, 14 Hz), 1.95 (dd, 1H, H_{3b}, J = 6, 14 Hz).

^{13}C NMR ($CDCl_3$, 100.5 MHz) δ: 147.104 (Ph_3), 142.2501 (Ph_3), 138.036 (**$C_{imd\text{-}Q}$**), 137.530 (**C_1**), 129.673 (Ph_3), 128.681 (Ph_3), 128.071(Ph_3), 127.775(Ph_3), 126.221 (Ph_3), 120.4617 (**C_2**), 75.205 (**C**-Ph_3), 70.981 (**C_4**), 65.688 (**C_5**), 52.434 (**C_3**)

ESI-Mass spectrometry: [M-H]+ at 626.3179 ([M-H]+ calc. for $C_{44}H_{40}N_3O$: 626.3166, error – 2.1 mDa)

IR (ATIR): 3319, 3054, 3024, 1492, 1447, 1326, 1212, 1189, 1153, 1129, 1038, 904, 825, 702, 743, 637, 619, 531, 489

MP: 85-86 °C

6.2.3 Synthesis of (2S)-N-triphenyl-methyl-1-(1-H- triphenyl-methyl-1H imidazol-4-yl)-3-[(pyridin-2-yl)methoxy]propan-2-amine, 2.13

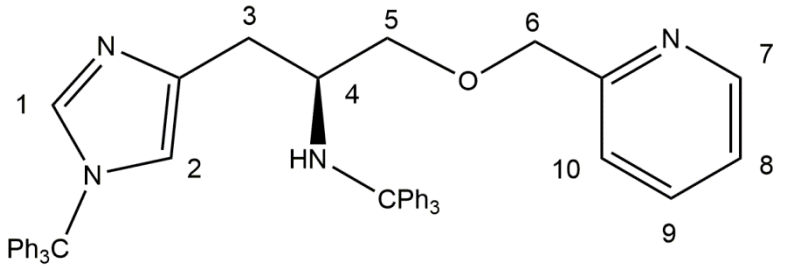

Under a nitrogen atmosphere, NaH (0.466 g, 20 mM, 10 eq) was suspended in THF (15 mL) and stirred for 1 hour. Ditrityl-L-histidinol (1.26 g, 2.02 mM, 1 eq) was added to the mixture and stirred for an additional hour. To this solution, 2-(chloromethyl)pyridine (0.331 g, 2.02 mM, 1 eq) was added along with NaI (10 mg) and the reaction was stirred for 12 hours at room temperature. To the reaction mixture H_2O (25 mL) was added and stirred for an additional hour. The reaction was dried in vacuo, extracted with DCM (3 x 35 mL). The organic layers were combined, dried with $MgSO_4$ filtered, and dried *en vacuo*. This was then purified on a silica chromatography column with 1:3:0.01 ethyl acetate, DCM, ammonia solution.

Yield: 0.885 g, 61%

1H NMR (CDCl3, 399.78 MHz) δ:8.527 (d, 1H, J = 5 Hz, H_7), 7.630-7.105 (m, > 36H, Aromatic H), 6.398 (s, 1H, H_2) 3.269 (dd, 1H, J = 4, 9 Hz, H_5), 3.020 (m, 1H, H_4) 2.869 (dd, 1H, J = 3, 9 Hz, H_5), 2.717 (dd, 1H, J = 4, 14 Hz, H_3), 2.293 (dd, 1H, J = 7, 14 Hz, H_3) 2.093 (s, 2H, H_6),

^{13}C NMR ($CDCl_3$, 100.5 MHz) δ: 149.679 ($C_{Pyr\text{-}Q}$), 147.113 (C_7), 133.581 (C_1), 138.1678 (Ph_3), 129.767 (Ph_3), 128.861 ($C_{Imd\text{-}Q}$), 128.126 ($C_{10/8}$), 126.324 ($C_{10/8}$), 125.533 (C_2), 72.970 (**C**-Ph_3), 72.598 (C_6), 71.130 (C_5), 52.220 (C_4), 25.710 (C_3)

ESI-Mass spectrometry: [M-H]+ at 717.3588 ([M-H]+ calc. for $C_{45}H_{37}N_3O$: 717.3593, error -2.7 mDa)

IR (ATIR): 3291, 3058, 3032, 2920, 2860, 1589, 1444, 1359, 1233, 1199, 1184, 1159, 1126, 1084, 1031, 990, 905, 868, 824, 743, 698, 659, 640, 620, 533, 507, 490

MP: 81 -84 °C.

6.2.4 Synthesis of (2S)-1-(1H-imidazol-4-yl)-3-[(pyridin-2-yl)methoxy]propan-2-amine, 2.3

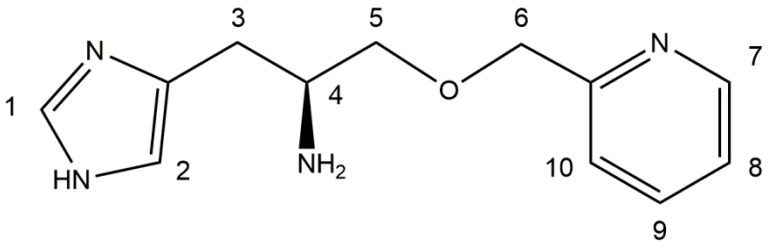

($(Ph_3C)_2$ $L_{2\text{-}NH2}$) (0.885 g, 0.409 mM) was dissolved in THF (12 mL), and 3 M HCl (10 mL) aqueous solution were added. The mixture was stirred at 90 °C for 4 hours. The solvents were evaporated, and the solid was washed with DCM (3 x 30 mL). The aqueous phase was evaporated, giving the (2S)-1-(1H-imidazol-4-yl)-3-[(pyridin-2-yl)methoxy]propan-2-amine ·tris HCl salt. This compound was then run through a strong anion exchange resin (Dowex®, MSA-1) and eluted with H_2O as the free base, (2S)-1-(1H-imidazol-4-yl)-3-[(pyridin-2-yl)methoxy]propan-2-amine.

Yield: 0.139 g, 92%

^{1}H NMR (CD_3OD, 399.78 MHz) δ: 8.972 (s, 1H, H_1), 8.915 (d, 1H J = 6 MHz, H_7), 8.587 (apparent t, 1H, J =4 Hz, H_9), 8.175 (d, 1H, J = 4 Hz, H_{10}) 8.105 (apparent t, 1H, J = 6Hz, H_8), 7.65 (s, 1H, H_2) 5.126 (bs, 2H, H_6) 4.106 (apparent d, 1H, J = 9 Hz, H_5) 3.734 (m, 2H, $H_{5/4}$) 3.150 (m, 2H,H_3)

^{13}C NMR (CD_3OD, 100.52 MHz) 153.467($C_{Pyr\text{-}Q}$), 148.328 (C_7), 142.378 (C_9), 135.905 (C_1), 129.173 ($C_{Imd\text{-}Q}$), 127.657 (C_8), 126.828 (C_{10}), 119.743 (C_2), 70.917 (C_6), 69.534 (C_5), 51.800 (C_4), 25.713 (C_3)

ESI-Mass spectrometry: $[M\text{-}H]^+$ at 233.1394 ($[M\text{-}H]^+$ calc. for $C_{12}H_{17}N_4O$: 233.1324, error 0.3 mDa)

IR (ATIR): 3370, 2867, 2057, 1618, 1525, 1470, 1365, 1293, 1125, 1078, 980, 942, 764, 627, 408

MP: 73-74 °C

Elemental Analysis: Found %C, 62.03, %H, 6.92; %N, 24.10 ($C_{12}H_{16}N_4O$ Calculated - %C, 62.05; %H, 6.94; %N, 24.12.).

6.3 Synthesis and characterisation of (1-*H* -imidazol-4-yl) propoxy]methyl)pyridin-4-yl)pro-2-yn-1-yl)-2-(2-oxohexahydro-1H-thieno[3,4-d]imidazole-4-yl) pentamide, **3.12**

6.3.1 Synthesis of 4-bromo-(2-chloromethyl)-pyridine, 3.14

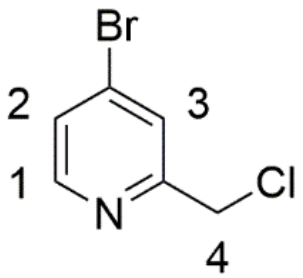

Procedure:

Procedure adapted from Deng *et al*.[301]

4-Bromo-2-pyridylmethanol (0.257 g, 1.37 mM) was dissolved in DCM (10ml) and the solution was cooled to 0 ^{O}C. To this solution thionyl chloride (1ml, 17.7 mM, 10 eq) was added dropwise. The solution was warmed to room temperature and stirred for 45 minutes. The solution was washed with sat. $NaHCO_3$ (1 X 20 ml), H_2O (1 X 20 ml), and sat. brine solution(1 X 20 ml). The organic layer was dried *en vacuo* to give the pure product as a brown oil which was used with no further purification.

Yield: 0.188 g (67%)

1H NMR ($CDCl_3$, 399.78 MHz) δ: 8.375 (d, 1H, J = 5 Hz, H_1) 7.665 (d, 1H, J = 1.8 Hz, H_2) 7.405 (dd, 1H, J= 1.8, 5 Hz, H_3) 4.625 (s, 2H, H_4)

13C NMR ($CDCl_3$, 100.5 MHz) 158.02 ($_{Pyr\text{-}Q}$), 150.13 (C_1), 133.38 (C_2), 126.52 (C_3), 126.30 (**C**-Br), 45.93 (C_4

ESI-Mass spectrometry: $[M\text{-}H]^+$ at 205.9358 ($[M\text{-}H]^+$ calc. for C_6H_6NBrCl: 205.9367, error 0.9 mDa)

6.3.2 Synthesis of 1-[(4-bromopyridin-2-yl)methoxy]-N-methyltriphenyl-3-(1-methyltriphenyl-1H-imidazol-4-yl)propan-2-amine, 3.15

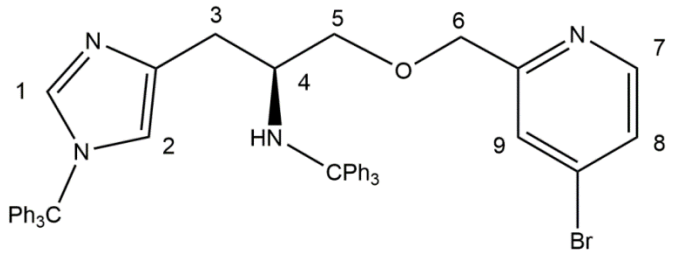

Procedure:

Under a nitrogen atmosphere, NaH (0.084 g, 3.8 mM, 5 eq) was suspended in THF (15 mL). Ditrityl-*L*-histidinol (0.4177 g, 0.69 mM, 1 eq) was added to the suspension and stirred for an hour. To this solution, 4-bromo-(2-chloromethyl)pyridine (0.1499 g, 0.74 mmol, 1.1 eq) was added along with NaI (5 mg) and the reaction was stirred for 12 hours at room temperature. On completion of the reaction, as monitored by the loss of the TLC spot corresponding to Ditrityl-*L*-histidinol, H_2O (5 mL) was added to the reaction mixture and stirred for an additional hour. The reaction mixture was then dried *in vacuo.* The reaction mixture was redissolved in DCM (10 ml) washed with H_2O (3 X 10 ml) and brine (1 X 10 ml). extracted with DCM (3 x 35 mL). The organic layers were combined, dried with $MgSO_4$ filtered, and dried *en vacuo*. This was then purified on a silica chromatography column with 1:3:0.01 ethyl acetate, DCM, ammonia solution to give an off white foam. RF: 0.45

Yield: 0.5206 g (97%)

1H NMR ($CDCl_3$, 399.78 MHz) δ 8.265 (d, 1H, J = 5 Hz, H_7) 7.54-7.05 (m, >42H, Ph_3, $H_{1,8,9}$) 6.34 (s, 1H, H_2) 4.28 (q, 2H, J = 13, 2 Hz, H_6) 3.225 (dd, 1H J = 9, 4 Hz, H_{5a}) 2.97 (m, H_4) 2.87(dd, 1H, J = 8, 6 Hz, H_{5b}) 2.63 (dd, 1H J = 14, 5 Hz, H_{3a}) 2.19 (dd, 1H, J =14, 7 Hz,H_{3b})

13C NMR ($CDCl_3$, 100.51 MHz) δ 149.678 ($C_{Pyr\text{-}Q}$), 147.113 (C_7), 138.168 ((C_1), (**C**Ph_3), Ph_3), 133.581(Ph_3), 129.766 (Ph3), 128.861 (Ph_3), 128.126 ($C_{Imd\text{-}Q}$), 127.879 (Ph_3), 126.324 (C_8), 125.533 (C_9), 124.465 (**C**-Br), 120.097 (C_2), 72.970 (C_6), 72.598 (**C**-Ph_3), 71.130 (C_5) , 52.220 (C_4), 25.710 (C_3)

ESI-Mass spectrometry: $[M\text{-}H]^+$ at 795.2674 ($[M\text{-}H]^+$ calc. for $C_{50}H_{44}N_4BrO$: 795.2693, error 1.9 mDa)

IR (ATIR): 3660, 2983, 1776, 1719, 1594,1573, 1555, 1492, 1448, 1418, 1390, 1345, 1160, 1128, 1090, 1035, 941, 905, 747, 701, 660, 640, 624, 530

MP: 82-84 °C.

6.3.3 Synthesis of N-methyltriphenyl-[(2-([2-amino-3-(1-methyltriphenyl-imidazol-4-yl)propoxy]methyl)pyridin-4-yl) pro-2-yn-1-yl)-2-(2-oxohexahydro-1H-isoindole-1,3(2H)-dione, 3.17

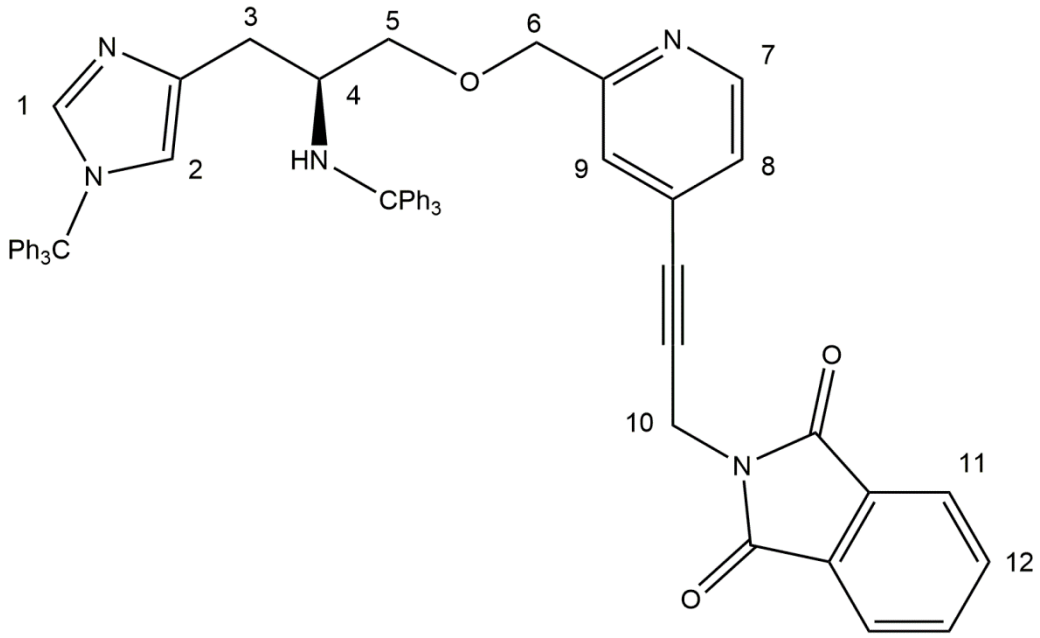

Procedure:

Under a nitrogen atmosphere, **3.15** (0.5206 g, 0.65 mM), N-propargylphthalimide (0.2428 g, 1.30 mM, 2 eq.) and, $PdCl2(PPh_3)_2$ (0.046 g, 10 mol%) were dissolved in a 1:1 Dry THF:Et_3N solution. The solution was stirred for 30 minutes after this period CuI (0.1 mg ,1 mol%) was added to the reaction mixture which was then heated at 80 °C 12 hours. At which point the solution is filtered, washed with THF and dried *en vacuo*. The reaction mixture was redissolved in DCM (10 ml) washed with H_2O (3 X 10 ml) and brine (1 X 10 ml). The organic layer was dried with $MgSO_4$, filtered and dried *en vacuo.* This was then purified *via* silica chromatography column with 1:3:0.01 ethyl acetate, DCM, ammonia solution to give an off-white foam. RF 0.25.

Yield 0.4654 g (79%)

1H NMR (CDCl3, 399.78 MHz) δ 8.40 (d, 1H, J = 5 Hz, H_7) 7.895 (dd, 2H, J = 5, 3 Hz, H_{11}) 7.755 (dd, 2H, J = 5 , 3 Hz, H_{12}) 7.55-7.05 (m, >36H, CPh_3, $H_{1,8,9}$) 6.35 (s, 1H H_2) 4.66 (s, 2H, H_{10}) 4.28 (dd, 2H, J = 13, 2 Hz, H_6) 3.225 (dd, 1H J = 9, 4 Hz, H_{5a}) 2.97 (m, H_4) 2.87(dd, 1H, J = 8, 6 Hz, H_{5b}) 2.63 (dd, 1H J = 14, 5 Hz, H_{3a}) 2.19 (dd, 1H, J =14, 7 Hz,H_{3b})

13C NMR ($CDCl_3$, 100.51 MHz) δ 167.274 (**C**=O), 163.136 (**C**=O), 155.383 ($C_{Pyr\text{-}Q}$), 144.932 (PH_3), 143.340 ($C_{Imd\text{-}Q}$), 138.677 (C_1), 137.4715 (C_2), 134.767 (C_{12}), 130.467 ($C_{Pth\text{-}Q}$), 128.159 (Ph_3), 127.100 (Ph_3), 125.889 (Ph_3), 124.993 (Ph_3), 124.163 (Ph_3), 123.944 (Ph_3), 122.361 (Ph_3), 120.473 (PH_3), 119.815 (Pyr**C**-C≡C), 119.300 (C_8), 116.153 (C_2), 83.418 (Pyr-**C**≡C), 77.000 (C_6), 71.145 (**C**-Ph_3), 69.372 (C_5), 56.565 (C_4), 48.336 (C_{10}), 27.005 (C_3)

ESI-Mass spectrometry: $[M\text{-}H]^+$ at 900.3902 ($[M\text{-}H]^+$ calc. for $C_{61}H_{50}N_5O_3$: 900.3908, error 0.7 mDa)

IR (ATIR): 2948, 1775, 1717, 1598, 1545, 1491, 1448, 1442, 1392, 1348, 1283, 1240, 1160, 1119, 1085, 1035, 998, 936, 900, 842, 749, 702, 660, 527

MP: 101-102 °C.

6.3.4 Synthesis of N-methyltriphenyl-[(2-([2-amino-3-(1-methyltriphenyl-imidazol-4-yl)propoxy]methyl)pyridin-4-yl) pro-2-yn-1-amine, 3.18

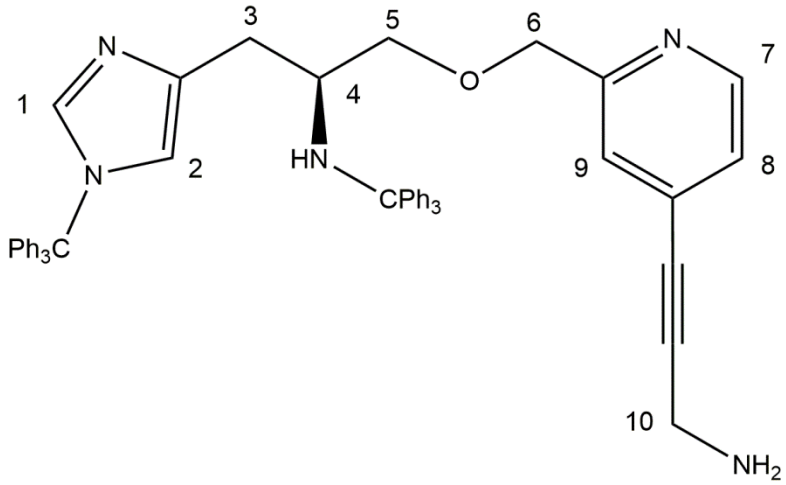

Procedure:

Under a nitrogen atmosphere, **3.17** (0.1789 g, 0.2 mM) was dissolved in a mixture of DCM (3 mL) and ethanol (1 mL). To this solution, hydrazine monohydrate (50 µL, 1 mM, 5 eq) was added dropwise. The reaction mixture was then heated to 80 °C 12 hours. The reaction mixture was allowed to cool and was filtered to remove phthalhydrazine and dried *en vacuo.* The resulting solid was redissolved in DCM (15 mL) and was washed with 1M NaOH (2 X 15 mL) to remove residual phthalhydrazine. The organic layer was dried with $MgSO_4$ filtered, and dried *en vacuo.* A white foam was obtained which was used in further steps with no further purification.

Yield: 0.0895 g (58 %)

1H NMR (CDCl3, 399.78 MHz) δ 8.401 (d, 1H, J = 8 Hz, H_7), 7.56-7.03 (m, >36H, CPh_3, $H_{1,8,9}$), 6.366 (s, 1H, H_2), 4.305 (s, 2H H_{10}), 3.562 (s, 2H, H_6), 3.2362 (dd, 1H, J = 6, 9 Hz, H_{5a}), 2.984 (m, 1H, H_4), 2.904 (dd, 1H, J = 6, 9 Hz, H_{5b}), 2.631 (dd, 1H, J = 5, 14 Hz, H_{3a}), 2.517 (br d, 1H, NH2), 2.227 (dd, 1H, J = 7, 14 Hz, H_{3b})

13C NMR ($CDCl_3$, 100.51 MHz) δ 159.360 (C_{Pyr-q}) 148.870 (Ph_3) 147.259 (Ph_3) 147.358 (Ph_3) 142.605 (C_7) 138.810 (Ph_3), 131.992 (Ph_3), 129.799 (Ph_3), 127.0731 (Ph_3), 127.873 (C_9), 126.280 (C_8), 123.0287 (Pyr**C**- C≡C),, 119.996 (C_2), 95.031 (Pyr**C**≡C), 80.557 (PyrC≡**C**), 75.0451 (C_5), 73.243(**C_q**-Ph_3), 72.423 (C_3), 71.174 (**C**-Ph_3), 52.331 (C_4), 32.220 (C_{10}), 31.0664 (C_6)

ESI-Mass spectrometry: $[M-H]^+$ at 770.3874 ($[M-H]^+$ calc. for $C_{53}H_{48}N_5O$: 770.3853, error -2.1 mDa)

IR (ATIR): 3282, 3060, 2972, 2928, 1700, 1661, 1600, 1544, 1495, 1448, 1285, 1235, 1209, 1159, 1131, 1092, 989, 952, 907, 872, 817, 746, 706, 638

MP: 117-119°C

6.3.5 Synthesis of Biotin pentaflurophenyl ester, **3.8**

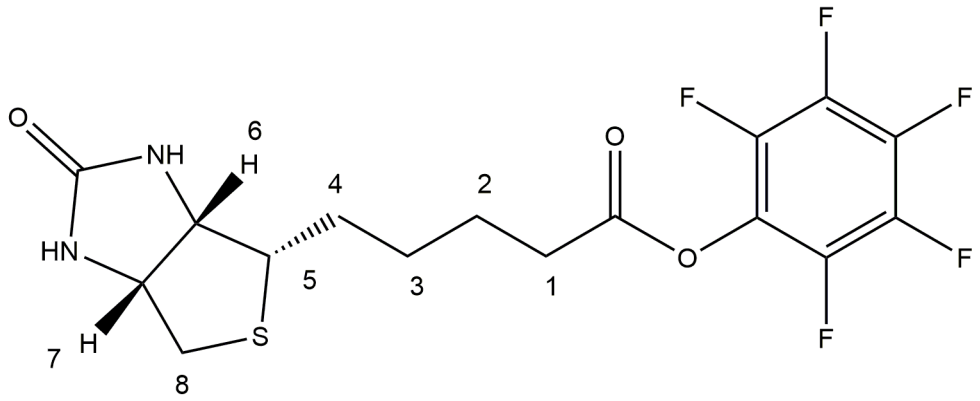

Procedure: Adapted: Rizzacasa *et al.*[264], Biotin (1.00 g, 4.093 mM) was dissolved in 20 mL DMF at 70 ºC and allowed to cool to room temperature. To this solution Et_3N (0.73g, 1.00 mL, 7.175 mM) was added, followed by pentaflurophenyl trifluoroacetate (1.63 g, 1.00 mL, 5.820 mM). The reaction was allowed to stir for 30 and became pink. Solvent was removed *en vacuo* and the reaction mixture was purified *via* flash column chromatography using 1:10 MeOH:DCM (RF: 0.8) as a solvent system to give Biotin pentaflurophenyl ester as a white crystalline solid.

Yield: 1.351 g (3.30 mM, 80%)

1H NMR (DMSO D_6, 399.74 MHz) 6.416 (bs, 1H, $H_{6/7}$) 6.337 (bs, 1H, $H_{6/7}$) 4.283 – 4.251 (m, 1H, H_{8a}), 4.1241-4.090 (m, 1H, H_{8b}) 1.687 – 1.588 (m, 4H, $H_{2/4}$) 1.486 -1.3756 (m, 2H, H_3)

ESI-Mass spectrometry: $[M-H]^+$ at 411.0792 ($[M-H]^+$ calc. for $C_{16}H_{16}N_2O_3SF_6$: 411.0796, error 0.4 mDa), $[M-Na]^+$ at 433.0605 ($[M-Na]^+$ calc. for $C_{16}H_{15}N_2O_3SF_6Na$: 433.0616, error 1.14 mDa)

MP: 187-190 °C.

6.3.6 Synthesis of N- methyltriphenyl-[(2-([2-amino-3-(1-methyltriphenyl-imidazol-4-yl)propoxy]methyl)pyridin-4-yl) pro-2-yn-1-yl)-2-(2-oxohexahydro-1H-thieno[3,4-d]imidazole-4-yl)pentamide, 3.19

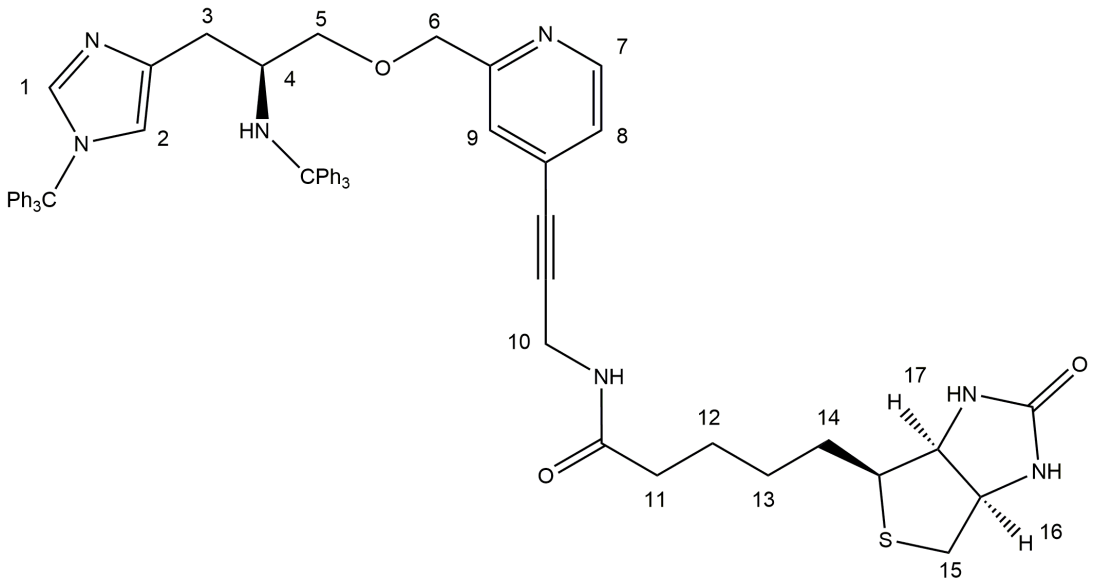

Procedure:

Under a nitrogen atmosphere **3.18** (0.045 g, 0.12 mM) and biotin-pentofluroester (0.045, 0.11 mM, 0.95 eq) was dissolved in DMF (10 mL) to this Et_3N (50 μL) was added and the reaction mixture was stirred 12 hours. The DMF was removed *en vacuo* and to give a brown oil. The oil was triturated with diethyl ether over as 48 hour period to remove residual DMF until a free flowing white solid was formed The filtrate was removed to give the pure product as a white solid.

Yield: 0.0982 g (0.0986 mM, 85 %)

1H NMR ($CDCl_3$, 399.74 MHz) δ 8.3735 (d, 1H, J = 8, H_7), 7.475 – 6.9975 (m, >36H, $H_{8,9}$,CPh_3), 6.3399 (s, 1H, H_2),4.365 –4.214 (m, 5H, J = 5, 40 Hz, $H_{17/18/10/4}$) 3.169 (dd, 1H, J = 3, 8Hz, H_{5a}) 3.0414-2.9933 (m, 1H, H_{15}) 2.942 – 2.836 (m, 4H, $H_{16/5b/3b}$), 2.735 (dd, 1H, J = 8,12 Hz, H_{3b}) 2.616 – 2.565 (m, 2H, H_6) 2.243 (t, 2H, J = 7Hz, H_{11}) 1.696 – 1.542 (m, 4H, $H_{12/14}$) 1.409 – 1.316 (m, 2H, H_{13})

13C NMR ($CDCl_3$, 100.51 MHz) (175.250 N_{amide}**C**=O), 164.354 (N**C**=ON), 162.6563, ($C_{Pyr\text{-}Q}$) 159.204 (Ph_3), 148.877 (Ph_3), 147.094 (Ph_3), 142.287 (C_7), 138.082 (Ph_3), 131.559 (Ph_3), 129.725 (Ph_3), 128.813(Ph_3), 128.136(Ph_3), 127.888(Ph_3), 126.343(Ph_3), 124.255(Ph_3), 123.139 (Pyr**C**-**C**≡C), 120.135 (C_9), 90.650 (Pyr**C**≡C), 80.6372 (PyrC≡**C**), 72.417 (**C**-Ph_3), 71.129 (C_6), 65.951 (**C**-Ph_3), 61.746 (C_5) , 55.767 (C_{18}), ,52.163 ((C_{17}), 40.586 (C_{15}), 36.590 (C_4), 35.665 (C_{16}), 31.527 (C_{11}), 30.945 (C_{10}), 29.667 (C_3), 28.227 (C_{13}), 28.094 (C_{14}), 25.633 (C_{12})

ESI-Mass spectrometry: $[M\text{-}H]^+$ at 996.465 ($[M\text{-}H]^+$ calc. for $C_{63}H_{62}N_7O_3S$: 996.4651, error -2.2 mDa), $[M\text{-}Na]^+$ at 1018.4479 ($[M\text{-}Na]^+$ calc. for $C_{63}H_{61}N_7O_3S$ Na: 1018.4449, error -3.0 mDa)

IR (ATIR): 3263, 3058, 3055, 2929, 2850, 1699, 1660, 1595, 1540, 1494, 1444, 1353, 1323, 1237, 1202, 1198, 1160, 1125, 1091,989, 909, 851 702

MP: 165-168 °C.

6.3.7 Synthesis of (1-H -imidazol-4-yl) propoxy]methyl)pyridin-4-yl)pro-2-yn-1-yl)-2-(2-oxohexahydro-1H-thieno[3,4-d]imidazole-4-yl) pentamide , 3.12

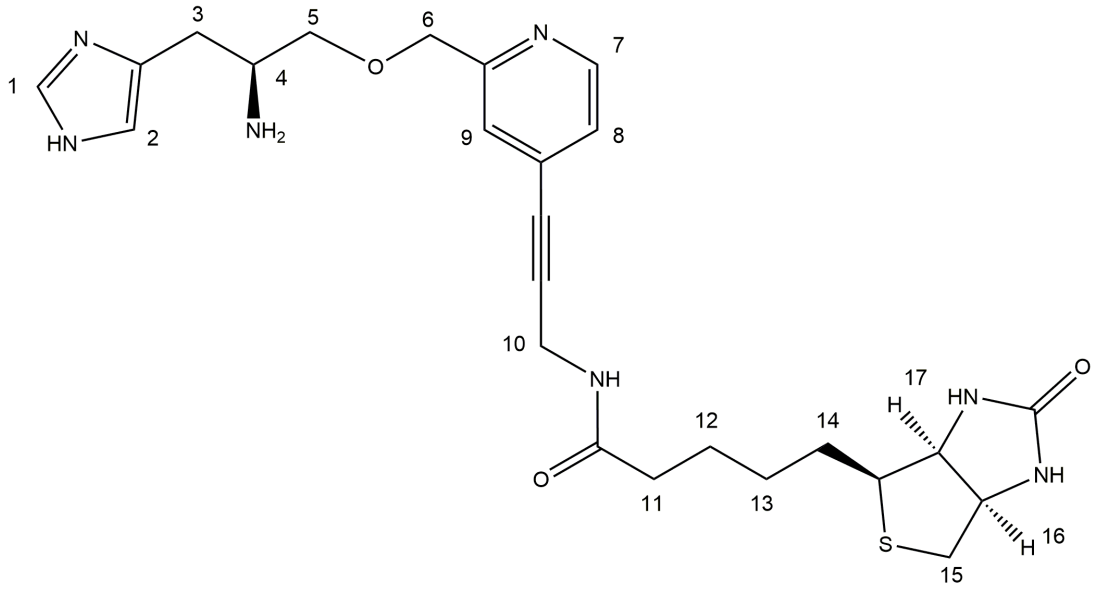

Procedure:

Under a nitrogen atmosphere, **3.19** was dissolved in a mixture of THF:DCM (2 mL: 1 mL) to this 3M HCl was added dropwise to the solution and the reaction mixture was stirred at room temperature for 48 hours while being monitored using ESI mass spectrometry. After the disappearance of both the *M/Z* for both the single and doubly protected starting materials the reaction mixture was dried *en vacuo* and to give a brown oil. This was washed with diethyl ether (20 mL X 3) to remove the trityl group the aqueous layer was dried and triturated with ether over a period of 48 hours to remove residual solvent until an off white powder was obtained.

1H NMR (D_2O, 399.74 MHz) δ 8.598 – 8.5752 (m, 2H,$H_{7/1}$), 7.888 – 7.7481 (m, 2H, $H_{9/8}$) 7.3460 (s, 1H, H_2), 4.507 -4.413 (m, 1H, H_{16a}) 4.327-4.240 (m, 1H, H_{16b}) 4.1909 (t, 2H, H_{12}), 3.901- 3.830 (m, 2H, H_6) 3.780 – 3.724 (m, 1H, H_{5a}) 3.233 – 3.159 (m, 3H, $H_{5b/3a}$) 2.8975 – 2.806 (m, 1H, H_{3b}) 2.2972 – 2.196 (m, 2H, H_{10}), 1.419 – 1.404 (m, 4H, $H_{11/14}$) 1.364 – 1.2490 (m, 2H, H_{13})

13C NMR (D_2O, 100.51 MHz) δ 77.0819, (N_{amide}**C**=O), 165.096 (N**C**=ON), 155.245 ($C_{Pyr\text{-}Q}$), 141.523 (C7) 134.190, (C_1) 128.376 (C_2), 128.288 ($C_{Imd\text{-}Q}$), 126.7906 (C_7), 126.667 (C_8), 123.139 (Pyr**C**-**C**≡C), 99.738 (Pyr**C**≡C), 78.168, (PyrC≡**C**), 67.917, (C_6), 61.891, 55.272 (C_5)

50.059 (C_{18}), 47.491 (C_{17}), 39.739 (C_{15}), 35.229 (C_4), 33.522 (C_{16}), 29.593 (C_{11}), 27.582 (C_{10}), 25.025 (C_{14}), 24.215 (C_{12})

ESI-Mass spectrometry: $[M-H]^+$ at 512.2439 ($[M-H]^+$ calc. for $C_{25}H_{34}N_7O_3S$: 512.2438, error – 0.1 mDa)

IR (ATIR): 3246, 3053, 2925, 2857, 1700, 1663, 1595, 1535, 1493, 1444, 1352, 1322, 1288, 1238, 1205, 1159, 1130, 1091, 994, 909, 868, 846, 732, 701, 658, 644, 535

MP: 172-174 °C.

Elemental Analysis: Found - %C, 48.37, %H, 5.85; %N, 15.82 ($C_{25}H_{33}N_7O_3Cl_3S$ calculated %C, 48.35; %H, 5.84; %N, 15.79)

6.4 Synthesis and Characterisation of Additional Compounds

6.4.1 Synthesis of (2S)-1-bromo-*N*-*tert*-phenyl-3-(1-*tert*-phenyl-1*H*-imidazol-4-yl)propan-2-amine, **2.18**

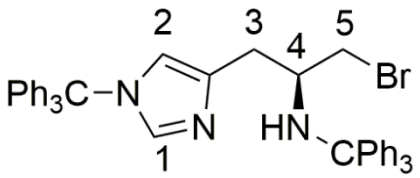

Procedure:

Under a nitrogen atmosphere using dry solvents, Carbon tetrabromide (0.128 g, 0.38 mM) and triphenylphosphine (0.100g, 0.38 mM) were dissolved in chloroform (10 mL) and cooled to 0 °C. To this a solution dityrityl-L-histidinol (0.2187 g, 0.35 mM) in chloroform (5 mL) was added dropwise. After the addition was complete the reaction mixture was warmed to room temperature and stirred for 12 hours. When the reaction was judged to have gone to completion *via* TLC the solvent was removed *in vacuo.* The reaction mixture was purified using flash column chromatography using a 1:1 ethyl acetate:DCM solvent system with a RF of 0.7.The solvent was removed to give (2S)-1-bromo-N-tert-phenyl-3-(1-tert-phenyl-1H-imidazol-4-yl)propan-2-amine as a pale brown foam.

Yield: 0.1405 g (0.20 mM, 52 % yield)

1H NMR ($CDCl_3$, 399.78 MHz) δ: 7.482 – 7.069 (m, m, >31H, phenyl-H, H_1), 6.5883 (s, 1H, H_2) 4.5504 (m, 1H, H_4), 3.1654 (d, 2H, H_5 J = 7 Hz) 2.5725 (dd, 1H, J = 4, 13 Hz, H_{3a}), 2.5583 (dd, 1H, J = 7, 13 Hz, H_{3b})

ESI-Mass spectrometry: [M-H]+ at 688.2337 ([M-H]+ calc. for $C_{45}H_{39}NBr$: 688.2322, error -- 1.6 mDa)

6.4.2 Synthesis of α-(1-methyl-1-nitroethyl)-2-pyridinemethanol, 3.5

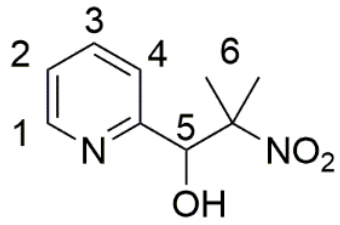

Procedure:

Procedure adapted from *J. G. Verkade et al.*[244]

Under a N_2 atmosphere 2-nitropropane (1 mL, 11 mM) were stirred with magnesium sulfate (0.53 g, 0.44 mM) for 5 minutes until a slurry had formed. 2-pyridine carboxaldehyde (0.2 mL, 2 mM) was added and the reaction was stirred for 5 minutes. Then P(*i*-PrNCH$_2$CH$_2$)$_3$N (0.06 g, 0.001 mM) in of 2-nitropropane (1 mL, 11 mM) was added and the reaction mixture was stirred 12 hours. The solution was taken up in 10 mL of DCM, the $MgSO_4$ was filtered off and the reaction mixture was extracted with H_2O (3 x 20 mL). The organic layer was then dried with $MgSO_4$, filtered again and the solvent evaporated, giving a brown solid.

Yield: 0.3281 g (85%.1.7 mM)

^{1}H NMR ($CDCl_3$, 399.78 MHz) δ: 8.716 (d, 1H, J = 10 Hz, H_1), 7.711 (dd, 1H, J = 8, 2 Hz, H_3), 7.300 (dd, 1H, J = 2 ,7 Hz, H_4), 7.21 (d, 1H, J =8 Hz, H_2), 5.262 (s, 1H, H_5), 5.014 (bs, O**H**), 1.589 (s, 3H, H_6), 1.421 (s, 3H, H_6)

ESI-Mass spectrometry: $[M-H]^+$ at 197.0920 ($[M-H]^+$ calc. for $C_9H_{12}N_2O_3$: 197.0926, error 0.1 mDa)

6.4.3 2 Synthesis of 2-dimethyl-2-nitro-1(2-pyridyl)-1-propan-*p*-toluenesulfonate, **3.15-OTs**

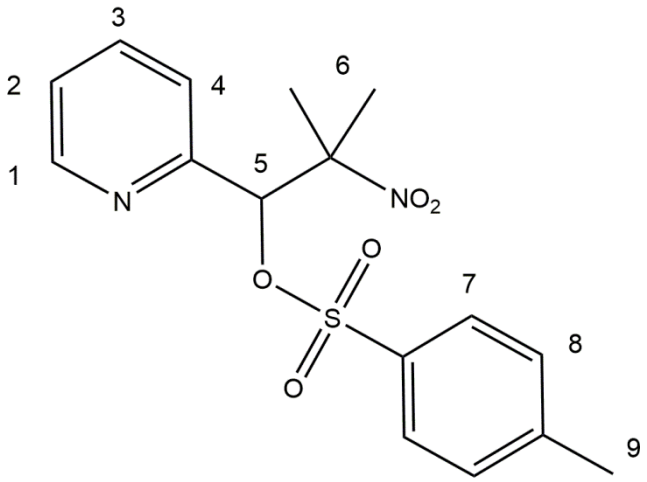

2, 2-dimethyl-2-nitro-1(2-pyridyl)-1-propanol (0.2302 g, 1.17 mM) and 4-Toluenesulfonyl chloride (0.246 g, 1.29 mM) were dissolved in DCM (5mL). To this solution Et_3N (0.53 mL, 3.91 mM) and 4-dimethylaminopyridine (0.050 g, 0.01 mM) were. The reaction was stirred for 12 hours and the solvent was removed *in vacuo*. The reaction was purified *via* silica column chromatography with the solvent system being 1:1 ethyl acetate: DCM. RF: 0.8. Obtaining 2, 2-dimethyl-2-nitro-1(2-pyridyl)-1-propan-*p*-toluenesulfonate as an off white solid.

Yield: 0.131 g 22%

^{1}H NMR ($CDCl_3$, 399.78 MHz) δ: 8.553 (ddd, 1H, J = 5, 2, 1 Hz, H_1), 7.698 (m, 3H, $H_{3/7}$), 7.425 (dd, 1H, J = 8, H_2), 7.292 (m, 3H, $H_{4/8}$), 6.047 (s, 1H, H_5), 2.436 (s, 3H, H_9), 1.629 (s, 3H, H_{6a}), 1.491 (s, 3H, H_{6b})

ESI-Mass spectrometry: $[M-H]^+$ 351.1009 ($[M-H]^+$ calc. for $C_{16}H_{19}N_2O_5S$:, 351.1009 error 0.0 mDa), $[M-Na]^+$ 373.0834 ($[M-Na]^+$ calc. for $C_{16}H_{19}N_2O_5SNa$:, 351.1009 error -0.8 mDa)

6.4.4 Synthesis of 2(2-Bromoethyl) pyridine HBr, 2.15.HBr

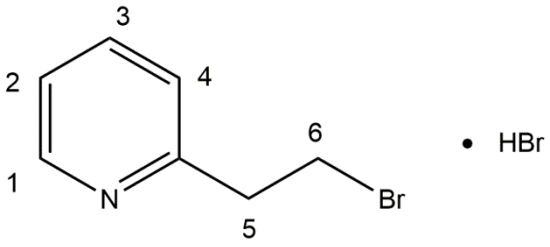

Procedure:

Procedure adapted from adapted from *Hejchman et al..*[196]

2-(2hydroxyethyl)pyridine (0.1094 g,0.8690 mmol) was added to hydrobromic acid (10 ml, 48% *w/w*) this solution was heated to reflux for 3 hours. The hyrdobromic acid and residual water was removed *en vacuo*. To give 2(2-Bromoethyl) pyridine HBr as a brown solid.

Yield : 0.9157 (0.8555 mM, 98%)

^{1}H NMR ($CDCl_3$, 399.78 MHz)δ: 8.47 (d, 1H, H_1, J = 5 Hz), 8.42 (dd, 1H, H_3, J = 5, 11 Hz), 7.91 (ad, 1H, H_2, J = 5 Hz), 7.85 (d, 1H,H_4, J = 11 Hz), 4.00 (t, 2H, H_5 , J = 6 Hz), 3.90 (t ,2H, H_6 , J = 6 Hz).

6.5 Synthesis and characterisation of Cu Complexes

5.5.1 General procedure for the formation of Cu complexes

A CuX_2 (where X is the relevant counter ion) solution was prepared in MeOH (0.08 $Moldm^{-3}$). To this a solution of the relevant ligand (0.08 $Moldm^{-3}$) was added to the solution dropwise over 10 minutes. The reaction mixture was then stirred for 1 hour following this the complex was precipitated by the addition of excess diethyl ether (ca. 25 mL). The complex was then extracted by filtration washed with diethyl ether (3 X 10 mL).

6.5.2 Characterisation of Cu(2.3)X_2

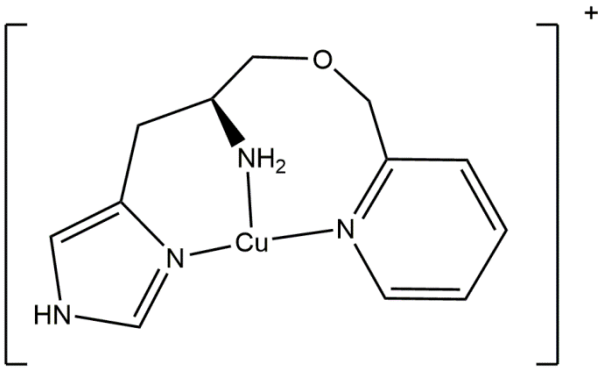

ESI-Mass spectrometry: $[M-H]^+$ 295.0605 ($[M-H]^+$ calc. for $C_{12}H_{16}N_4OCu$: 295.0615 error 1.0 mDa)

EPR Spectroscopy:

Linewidths used for simulation: Gaussian = 0.4 Gauss, Lorentzian = 0.4 Gauss

Solvent	*g*			A_{Cu} / MHz			A^N	A^{Cl}
	g_z	g_y	g_x	A_x	A_y	A_z		
H_2O pH 6	2.245	2.079	2.041	30	38	550	33, 38, 18	
H_2O pH 9	2.230	2.065	2.037	55	58	570	32, 31, 18	
MeOH	2.271	2.079	2.051	30	40	523	35,39,21	

Elemental Anlaysis: Found - %C, 29.23, %H, 5.14; %N, 17.07 (Calculated %C, 29.22; %H, 5.12; %N, 17.05.) $C_{12}H_{16}N_6O_{11}Cu + 2H_2O$

5.5.2 Characterisation of **Cu(3.12)Cl$_2$**

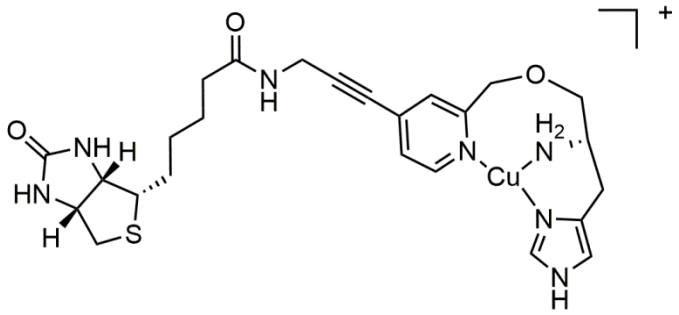

ESI-Mass spectrometry: $[M-H]^+$ 574.1660 ($[M-H]^+$ calc. for $C_{25}H_{33}CuN_7O_3S$: 574.1662 error 0.2 mDa)

EPR Spectroscopy:

Linewidths used for simulation: Gaussian = 0.3 Gauss, Lorentzian = 0.3 Gauss

Solvent	*g*			A_{Cu} / MHz			A^N
	g_z	g_y	g_x	A_x	A_y	A_z	
H_2O pH 6	2.245	2.079	2.041	30	38	550	33, 38, 18
H_2O pH 9	2.230	2.065	2.037	55	58	570	32, 31, 18

6.6 Preparation and Characterisation of **Cu(3.12)Cl_2⊂Sav**

6.6.1 General Preparation of **Cu(3.12)Cl_2⊂Sav**

A solution of the appropriate streptavidin mutant was prepared at 350 µL at 150 µM. To this solution **Cu(3.12)Cl_2** was added (25 µL 10 mM in DMF). This solution was incubated for 10 minutes to ensure uptake of **Cu(3.12)Cl_2**. At which point the protein was washed *via* centrifuge filtration (3 X 500 µL). At which point the concentration of streptavidin was measured using UV/Vis spectroscopy (ε = 41326 $M^{-1}cm^{-1}$(at 280nm)).

6.6.2 Procedure for HABA titration

A 100 µL cuvette, was charged with 240 µL of *apo*-streptavidin solution (8 µM, in 200 mM phosphate buffer pH 7), to this solution 4'-hydroxyazobenzene-2-carboxylic acid (28.8 µl, 10 mM, 150 equivalents) was added to ensure saturation and was incubated for 10 minutes. To this a solution of **Cu(3.12)Cl_2** in DMF (1 mM, 1 µL, 0.5 equivalents) were added until 5 equivalents had been added to solution. The titration was monitored by UV/visible spectroscopy at λ_{max} = 506 nm.

6.6.3 Electron Paramagnetic Resonance Spectroscopy

6.6.3.1 pH Titration Procedure

An EPR sample of **Cu(3.12)Cl_2⊂Sav** (0.4 mM) as prepared in a mixed buffer solution (5mM MES, 5 mM HEPES, 5 mM CHES, 5 mM Sodium phosphate). After each spectrum the solution was defrosted removed from the and the pH was measured using a Fisherbrand™ accumet™ AE150 Benchtop pH Meter (microelectrode) and the pH was adjusted using 0.1 mM HCl or NaOH respectively.

6.6.3.2 Spin Hamiltonian Parameters

	g			A_{Cu} / MHz			A^N	Line Width	
Species	g_z	g_y	g_x	A_z	A_y	A_x		G	L
S1	2.172	2.053	2.02	620	45	97	32, 41, 13	0.3	0.3
S2	2.23	2.076	2.04	565	47	16	35, 31, 18	0.3	0.3
S3	2.236	2.069	2.036	455	65	40	35, 30	0.5	0.5
S4	2.246	2.077	2.048	530	40	20	37, 30	2	2

6.6.4 Crystallisation of Cu(3.12)Cl2⊂Sav

6.6.4.1 Crystallisation of Apo-Sav

Apo-Sav protein crystals were obtained at 20 °C within two d by a sitting-drop vapor diffusion technique mixing 1.5 µL crystallization buffer (2.0 M ammonium sulfate, 0.1 M sodium acetate, pH 4.0) and 3.5 µL protein solution (26 mg/mL lyophilized protein in water). The droplet was equilibrated against a reservoir solution of 100 µL crystallization buffer.

6.6.4.2 Soaking experiments

Subsequently, single crystals of Sav were soaked for 4-24 hours day at 27 °C in a soaking buffer, which was prepared by mixing 1 µL of a 10 mM stock solution of **Cu(3.12)Cl_2** (in water with 100 mM $CuCl_2$), 9 µL crystallization buffer, and 0.5 µL of the original protein solution. A range of soaking conditions were tested and the best crystals (those with the most ligand density in the vestibule) were obtained after a 24 hour soaking period. Shorter soaking periods resulted in no density present in the biotin binding pocket. The results of these soaking periods are shown in Table 20Efforts to increase the concentration of **Cu(3.12)Cl_2** resulted in precipitation of the crystallisation buffer. Following the soaking procedure the crystals were shock frozen in liquid nitrogen.

*Table 20. The correlation between **Cu(3.12.)$_2$** soaking time and ligand incorporation into **SAV2XM***

Pin num.	Resolution / Å	Soaking time / Hours	Biotin Density
HA00AX0872	1.24	4	None
HA00BA5498	1.45	12	Biotin
HA00AW8355	1.66	24	Biotin + Extra density
HA00AQ4638	1.47	24	Biotin + Extra density

Of these datasets HA00AQ4638 was selected as **Sav2XM-Optimal**

6.6.4.3 Diffraction Data Processing

X-ray diffraction data were collected at Diamond Light Source, using beamline I03: Microfocus MX. The **Cu(3.12)Cl_2⊂Sav2XM** structures were solved by molecular replacement using MOLREP,[276] with the 'apo' structure of **Sav2XM (PDB 6AUC)**[242] (where both the ligand and water molecules had been removed) as the search model. Refinement cycles involving REFMAC and manual alteration in COOT were applied before the R_{cryst} and R_{free} remained constant.

6.6.4.4 Refinement data of **Sav2XM-Optimal**

Data Collection	Space Group	I 41 2 2
	a, b, c	57.612, 57.612, 183.857
	(°)	90.000, 90.000, 90.000
	Resolution / Å	1.47Å
	CC(1/2)	0
	I / I	14.2
	Completeness / %	99.9
Refinement	Resolution / Å	1.47
	No. reflections all/free	26918 / 1375
	R-factor/R-free	0.171 / 0.191
No. Atoms	Protein	1739
	Ligand	31
	Water	89
B-factors (Å^2)	Protein	23.6
	Ligand	24.8
	Water	35
RMS Deviations	Bonds / Å	0.0143
	Angles / °	1.923
Ramachandran plot	Favoured / %	94.26
	Allowed / %	4.92

6.7 Activity Assays

6.7.1 Polysaccharide Activity Assay

Avicel (crystalline cellulose), β-chitin (squid pen chitin) and phosphoric acid-swollen cellulose (PASC) were used as substrates at 1 mg/mL. Reactions were carried out in 100 µL solutions. 1 mM ascorbic acid, 1 µM of the relevant copper complex, artificial enzyme or LPMO, in 5 mM buffer solution (MES at pH 5.8, HEPES at pH 8 and CHES at pH 12). The reaction mixtures were incubated at 37 °C for 4 hours. Following this the soluble fraction was removed following centrifugation to remove the insoluble polysaccharides.

Soluble fractions activity reactions were analysed using MALDI-TOF (ultraflex III) mass spectrometry. Samples were mixed with the 2,5-dihydroxybenzoic acid matrix (20 mg mL^{-1} concentration, in 50% acetonitrile, 0.1% trifluoroacetic acid) in either a 1:1 or 1:5 sample to matrix ratio. Sample-matrix mixtures were spotted (1 µL) onto the sample plate and left to dry. A pre-made calibration solution (containing a set number of protein standards) was mixed with the matrix and spotted onto the plate, making sure that all samples were within 1 spot of the calibration spot. The spots were analysised using a Bruker Ultraflex III matrix-assisted laser desorption ionization–time of of flight (MALDI-TOF/TOF) instrument. The instrument was controlled using the Bruker FlexControl software. Using the spot imaging, the laser (100 Hz laser frequency, laser power of 40 mW) was manually moved around the spot to prevent damage to the sample. Depending on the sample concentration, data collection (standard run set at 800 shots) was repeated (sometimes at different laser intensities) and spectra added together in a cumulative manner to improve signal definition. Spectra were processed and analysed using the related Bruker flexAnalysis software.

6.7.1 Amplex Red Activity Assay

This assay is carried out using the procedure developed by Kittl *et al.*[302]

Solution Preparation: Two stock solutions were prepared, the first the Amplex reagent which consists of 30 µM Ascorbatic acid, 50 µM Amplex red and 30 µg/mL Horseradish peroxidase in sodium phosphate buffer (1 mL, 100 mM, pH 6). The second, the working solution, which consists of the appropriate copper complex or artificial enzyme at 50 µM in a sodium phosphate buffer pH 6, 100 mM.

Calibration curve: To 384-well plate a series of dilutions of 20 mM H_2O_2 (5 µL) covering a range off 0.1 to 10 µM solutions in sodium phosphate buffer (1X) To this 45 µL of Amplex reagent is added to the solution which is then incubated for 5 minutes at RT The florescence of resurofin is recorded at 450 and 500 nm using a BMG Labtech POLARstar OPTIMA. The florescence measurement is then plotted against peroxide concentration to obtain a calibration cureveR^2 should be >0.99.

Sample measurement: To 384-well plate a series of dilutions between of working solution (5 µL) between 0.5 and 50 µM were prepared in sodium phosphate buffer (1X). To this 45 µL of Amplex reagent is added to the solution and the florescence of the sample at 450/500 nm was monitored using a BMG Labtech POLARstar OPTIMA for 15 minutes.

Data Processing: Before further processing the data was examined for when it deviates from linearity any data after this point is discarded. The Florescence over time curve is then plotted and the slop of the graph is calculated. From the slope of the peroxide calibration curve the rates of H_2O_2 production can then be calculated.

Appendix

Small Molecule X-ray crystallography Data

Name	$Cu(Histamine)Cl_2$
Identification code	phw1704
Empirical formula	$C_5H_9Cl_2CuN_3$
Formula weight	245.59
Temperature/K	110.00(10)
Crystal system	monoclinic
Space group	$P2_1/m$
a/Å, b/Å, c/Å	8.7403(5), 5.9883(4), 8.9647(5)
α/° , β/°, γ/°	90, 109.715(7), 90
Volume/$Å^3$	441.70(5)
Z	2
$\rho_{calc}g/cm^3$	1.847
μ/mm^{-1}	8.569
F(000)	246.0
Crystal size/mm^3	0.127 × 0.062 × 0.036
Radiation	CuKα (λ = 1.54184)
2Θ range for data collection/°	10.482 to 133.982
Index ranges	$-9 \leq h \leq 10$, $-6 \leq k \leq 7$, $-9 \leq l \leq 10$
Reflections collected	1537
Independent reflections	874 [R_{int} = 0.0214, R_{sigma} = 0.0282]
Data/restraints/parameters	874/24/79
Goodness-of-fit on F^2	1.115
Final R indexes [I>=2σ (I)]	R_1 = 0.0537, wR_2 = 0.1446
Final R indexes [all data]	R_1 = 0.0615, wR_2 = 0.1498
Largest diff. peak/hole / e $Å^{-3}$	1.40/-1.45

Name	$Cu(Histamine)_2(PF_6)_2$
Empirical formula	$C_{10}H_{18}CuF_{12}N_6P_2$
Formula weight	575.78
Temperature/K	110.00(10)
Crystal system	monoclinic
Space group	$P2_1/c$
a/Å , b/Å, c/Å	7.8296(5) , 16.0361(11), 7.6801(6)
α/° , β/°, γ/°	90, 107.468(8), 90
Volume/$Å^3$	919.81(12)
Z	2
$\rho_{calc}g/cm^3$	2.079
μ/mm^{-1}	4.6
F(000)	574
Crystal size/mm^3	0.205 × 0.115 × 0.006
Radiation	CuKα (λ = 1.54184)
2Θ range for data collection/°	11.034 to 134.066
Index ranges	$-9 \le h \le 6$, $-19 \le k \le 15$, $-7 \le l \le 9$
Reflections collected	3223
Independent reflections	1633 [R_{int} = 0.0300, R_{sigma} = 0.0405]
Data/restraints/parameters	1633/0/154
Goodness-of-fit on F^2	1.046
Final R indexes [I>=2σ (I)]	R_1 = 0.0309, wR_2 = 0.0698
Final R indexes [all data]	R_1 = 0.0405, wR_2 = 0.0749
Largest diff. peak/hole / e $Å^{-3}$	0.31/-0.42

Name	$Cu(2.3)_2(SO_4)_2$
Empirical formula	$C_{50}H_{72}Cu_2N_{16}O_{14}S_2$
Formula weight	1312.43
Temperature/K	110.00(10)
Crystal system	monoclinic
Space group	$P2_1$
a/Å , b/Å, c/Å	14.0034(3), 12.8855(2), 16.3517(3)
α/° , β/°, γ/°	90 , 96.788(2), 90
Volume/$Å^3$	2929.81(10)
Z	2
$\rho_{calc}g/cm^3$	1.488
μ/mm^{-1}	0.875
F(000)	1372.0
Crystal size/mm^3	0.44 × 0.296 × 0.221
Radiation	MoKα (λ = 0.71073)
2Θ range for data collection/°	6.804 to 64.328
Index ranges	-10 ≤ h ≤ 20, -18 ≤ k ≤ 16, -22 ≤ l ≤ 24
Reflections collected	21015
Independent reflections	16267 [R_{int} = 0.0253, R_{sigma} = 0.0603]
Data/restraints/parameters	16267/2/769
Goodness-of-fit on F^2	1.023
Final R indexes [I>=2σ (I)]	R_1 = 0.0444, wR_2 = 0.0921
Final R indexes [all data]	R_1 = 0.0575, wR_2 = 0.1006
Largest diff. peak/hole / e $Å^{-3}$	0.78/-0.59

Name	$Cu(Histamine)_2(NO_3)_2$
Identification code	phw1705
Empirical formula	$C_{10}H_{18}CuN_8O_6$
Formula weight	409.86
Temperature/K	110.00(10)
Crystal system	monoclinic
Space group	$P2_1/c$
a/Å, b/Å, c/Å	8.9210(2), 6.52413(18), 14.3120(4)
α/° , β/°, γ/°	90, 104.754(3), 90
Volume/$Å^3$	805.52(4)
Z	2
$\rho_{calc}g/cm^3$	1.690
μ/mm^{-1}	2.381
F(000)	422.0
Crystal size/mm^3	0.225 × 0.115 × 0.031
Radiation	CuKα (λ = 1.54184)
2Θ range for data collection/°	10.254 to 133.94
Index ranges	$-9 \le h \le 10$, $-6 \le k \le 7$, $-17 \le l \le 12$
Reflections collected	2717
Independent reflections	1438 [R_{int} = 0.0156, R_{sigma} = 0.0223]
Data/restraints/parameters	1438/0/127
Goodness-of-fit on F^2	1.082
Final R indexes [I>=2σ (I)]	R_1 = 0.0233, wR_2 = 0.0620
Final R indexes [all data]	R_1 = 0.0263, wR_2 = 0.0640
Largest diff. peak/hole / e $Å^{-3}$	0.28/-0.32

Abbreviations List

LPMO	Lytic polysaccharide monooxygenases
AA	Auxiliary Activities
His-brace	Histidine brace
CDH	Cellobiose dehydrogenase
CBM	carbohydrate binding module
GH	glycoside hydrolases
HAA	Hydrogen atom abstraction
Cu(II)-OO^{-}).	Copper(II)-Superoxide species
Cu(II)-$O^{-\bullet}$	Copper(II)-Oxyl
Cu(I)-H_2O_2	Copper(I) hydrogen peroxide
Cu(II)-OH	Copper(II) hydroxide
Cu(II)-OOH^{-}	Copper(II)-hydroperoxo
ROS	Reactive oxygen species
O_2	Dioxygen
H_2O_2.	Hydrogen Peroxide
PCET	Proton coupled electron transfer
Bpy	Bipyridine
NHC	N-heterocyclic carbene
Trpy	2,2‘:6‘,2‘ ‘-terpyridine
Cu(III)OH	Cu(III) hydroxide
MeCN	Acetonitrile
THF	Tetrahydrofuran
DCM	Dichloromethane
NaOH	Sodium Hydroxide
EtOAc	Ethyl acetate
NaH	Sodium hydride
ESI MS	Electrospray ionization *mass spectrometry*
NMR	Nuclear magnetic resonance
EPR	*Electron Paramagnetic Resonance*
CLG	Carbon leaving group
HCl	Hydrochloric Acid

HBr	Hydrobromic acid
HSQC	Heteronuclear Single Quantum Correlation
HMBC	Heteronuclear Multiple Bond Correlation
COSy	correlation spectroscopy
OTs	*P*-toluenesulfonyl groups
Fmoc	Fluorenylmethoxycarbonyl
BOC	*Tert*-butyl carbamates
Phth	Phthalimides
EtOH	Ethanol
SAV	Streptavidin
HABA	4-hydroxyazobenzene-2-carboxylic acid
TON	Turnover number
Mg	micrograms
µL	microlitres
mL	milliliters
M	Molar
mM	millimolar
µM	micromolar
µmol	micromoles
δ	chemical shift
J	Coupling constant
nm	nanometers
°	degrees
°C	degrees Celsius
K	Kelvin
^{13}C	carbon
^{1}H	proton
Br	broad
d	doublet
dd	doublet of doublets
t	triplet
Å	Angstroms

mDa	milliDalton
m/z	mass/charge
Vis	visible
Ph	Phenyl
cm^{-1}	wavenumber
DMSO	dimethylsulfoxide
DMF	Dimethylformamide
His	histidine
Met	Methionine (met),
Cys	cysteine
Gly	Glycine
Ser	Serine
Asp	Aspartic acid
MHz	Megahertz
CeuO	Cuprous oxidase
T1	type 1 copper centre
T2	type 2 copper centre
T3	type 3 copper centre
PDB	Protien Data Bank
TNC	Trinuclear cluster
GO	Galactose oxidase
TPQ	trihydroxyphenylalanine quinone
CAZy	carbohydrate active enzyme
MMO	methane monooxygenases
sMMO	soluble Methane monooxygenases
pMMO	particulate Methane monooxygenases
NCBMs	non-coupled binuclear copper monooxygenases
PHM	peptidylglycine α-hydroxylating monooxygenase
DβM	dopamine β-monooxygenase
TβM	tyramine β-monooxygenase
MOX	monooxygenase X
CO	carbon monoxide

MPa	megapascal
QM/MM	quantum mechanics/molecular mechanics
DFT	density functional theory
S	Spin
PB plot	Peisach–Blumberg plot
Pyr	Pyridine
Imd	Imidaole
q	quaternary
m	*meta*
o	*ortho*
p	*para*
ΔE	energy gap
h	Planck's constant
v	frequency
β	Bohr magneton
g_e	spectroscopic g-factor
SHC	super hyperfine coupling
A^{Fermi}	Fermi contact term
A^{SD}	spin-dipolar term
A^{SO}	spin–orbit term
SOMO	singly occupied molecular orbital
HOMO	Highest occupied molecular orbital
OMs	mesylate
S_N	Nucleophilic substitution
E	Elimination
DEAD	diethyl azodicarboxalate
Δ	Heat
N_2	Nitrogen
ε	Extinction coefficient
DELFT	density functional theory informed Ligand field theory
Biot	Bioin
Et	ethyl

Prop	Propyl
But	Butyl
Biotin PFP	pentafluorophenyl ester
G	Gauss
Lys	Lyscine
UV	Ultraviolet
asc	Ascorbic acid
LMCT	Ligand to metal charge transfer
*m*CPBA	*Meta-*chloroperoxybenzoic acid
P450	Cytochrome P450

References

1. Festa, R. A.; Thiele, D. J., Copper: An essential metal in biology. *Current Biology* **2011,** *21* (21), R877-R883.
2. Sykes, A. G., Active-Site Properties Of The Blue Copper Proteins. In *Adv. Inorg. Chem.*, Sykes, A. G., Ed. Academic Press: 1991; Vol. 36, pp 377-408.
3. Holm, R. H.; Kennepohl, P.; Solomon, E. I., Structural and Functional Aspects of Metal Sites in Biology. *Chem. Rev.* **1996,** *96* (7), 2239-2314.
4. Shibata, N.; Inoue, T.; Nagano, C.; Nishio, N.; Kohzuma, T.; Onodera, K.; Yoshizaki, F.; Sugimura, Y.; Kai, Y., Novel Insight into the Copper-Ligand Geometry in the Crystal Structure of Ulva pertusa Plastocyanin at 1.6-Å Resolution: Structural Basus for Regulationof the Copper Site by Residue 88. *J. Biol. Chem.* **1999,** *274* (7), 4225-4230.
5. Baker, E. N., Structure of azurin from Alcaligenes denitrificans refinement at 1·8 Å resolution and comparison of the two crystallographically independent molecules. *J. Mol. Biol.* **1988,** *203* (4), 1071-1095.
6. Inoue, T.; Kai, Y.; Harada, S.; Kasai, N.; Ohshiro, Y.; Suzuki, S.; Kohzuma, T.; Tobari, J., Refined crystal structure of pseudoazurin from Methylobacterium extorquens AM1 at 1.5 A resolution. *Acta Crystallogr D Biol Crystallogr* **1994,** *50* (3), 317-328.
7. Hart, P. J.; Nersissian, A. M.; Herrmann, R. G.; Nalbandyan, R. M.; Valentine, J. S.; Eisenberg, D., A missing link in cupredoxins: crystal structure of cucumber stellacyanin at 1.6 A resolution. *Protein Sci.* **1996,** *5* (11), 2175-2183.
8. Guss, J. M.; Harrowell, P. R.; Murata, M.; Norris, V. A.; Freeman, H. C., Crystal structure analyses of reduced (CuI) poplar plastocyanin at six pH values. *J. Mol. Biol.* **1986,** *192* (2), 361-387.
9. Lowery, M. D.; Solomon, E. I., Axial ligand bonding in blue copper proteins. *Inorg. Chim. Acta* **1992,** *198-200*, 233-243.
10. Nersissian, A. M.; Immoos, C.; Hill, M. G.; Hart, P. J.; Williams, G.; Herrmann, R. G.; Valentine, J. S., Uclacyanins, stellacyanins, and plantacyanins are distinct subfamilies of phytocyanins: plant-specific mononuclear blue copper proteins. *Protein Sci.* **1998,** *7* (9), 1915-1929.
11. Koch, M.; Velarde, M.; Harrison, M. D.; Echt, S.; Fischer, M.; Messerschmidt, A.; Dennison, C., Crystal Structures of Oxidized and Reduced Stellacyanin from Horseradish Roots. *J. Am. Chem. Soc.* **2005,** *127* (1), 158-166.
12. McGuirl, M. A. D., D.M., Copper Proteins with Type 2 Sites. In *Encyclopedia of Inorganic and Bioinorganic Chemistry, R.A. Scott (Ed.).* 2011.
13. Wilmot, C. M.; Hajdu, J.; McPherson, M. J.; Knowles, P. F.; Phillips, S. E. V., Visualization of Dioxygen Bound to Copper During Enzyme Catalysis. *Science* **1999,** *286* (5445), 1724.
14. Decker, H., *Copper Proteins with Dinuclear Active Sites*. Encyclopedia of Inorganic and Bioinorganic Chemistry, R.A. Scott (Ed.). ed.; 2011.
15. Solem, E.; Tuczek, F.; Decker, H., Tyrosinase versus Catechol Oxidase: One Asparagine Makes the Difference. *Angew. Chem. Int. Ed* **2016,** *55* (8), 2884-2888.
16. Decker, H.; Tuczek, F., Tyrosinase/catecholoxidase activity of hemocyanins: structural basis and molecular mechanism. *Trends Biochem. Sci* **2000,** *25* (8), 392-397.
17. Tamilarasan, R.; McMillin, D. R., Spectroscopic studies of the type 2 and type 3 copper centres in the mercury derivative of laccase. *Biochem. J.* **1989,** *263* (2), 425-429.
18. Walton, P. H.; Steward, M.; Lindley, P.; Paradisi, A.; Davies, G. J., Copper oxygenases. In *Comprehensive Coordination Chemistry III*, Que, L.; Lu, Y., Eds. ELSEVIER ACADEMIC PRESS INC: 2020; pp 1-24.

19. Severns, J. C.; McMillin, D. R., Temperature and anation studies of the type 2 site in Rhus vernicifera laccase. *Biochemistry* **1990,** *29* (37), 8592-8597.
20. Morie-Bebel, M. M.; Morris, M. C.; Menzie, J. L.; McMillin, D. R., A mixed-metal derivative of laccase containing mercury(II) in the type 1 binding site. *J. Am. Chem. Soc.* **1984,** *106* (12), 3677-3678.
21. Dayan, J.; Dawson, C. R., Substrate specificity of ascorbate oxidase. *Biochem. Biophys. Res. Commun.* **1976,** *73* (2), 451-458.
22. Mano, N., Features and applications of bilirubin oxidases. *Appl. Microbiol. Biotechnol.* **2012,** *96* (2), 301-307.
23. Le Roes-Hill, M.; Goodwin, C.; Burton, S., Phenoxazinone synthase: what's in a name? *Trends Biotechnol.* **2009,** *27* (4), 248-258.
24. Rensing, C.; Grass, G., Escherichia coli mechanisms of copper homeostasis in a changing environment. *FEMS Microbiol. Rev.* **2003,** *27* (2-3), 197-213.
25. Askwith, C.; Eide, D.; Van Ho, A.; Bernard, P. S.; Li, L.; Davis-Kaplan, S.; Sipe, D. M.; Kaplan, J., The FET3 gene of S. cerevisiae encodes a multicopper oxidase required for ferrous iron uptake. *Cell* **1994,** *76* (2), 403-410.
26. Heppner, D. E.; Kjaergaard, C. H.; Solomon, E. I., Mechanism of the Reduction of the Native Intermediate in the Multicopper Oxidases: Insights into Rapid Intramolecular Electron Transfer in Turnover. *J. Am. Chem. Soc.* **2014,** *136* (51), 17788-17801.
27. Babcock, G. T.; Wikström, M., Oxygen activation and the conservation of energy in cell respiration. *Nature* **1992,** *356* (6367), 301-309.
28. Tsukihara, T.; Shimokata, K.; Katayama, Y.; Shimada, H.; Muramoto, K.; Aoyama, H.; Mochizuki, M.; Shinzawa-Itoh, K.; Yamashita, E.; Yao, M.; Ishimura, Y.; Yoshikawa, S., The low-spin heme of cytochrome c oxidase as the driving element of the proton-pumping process. *Proc. Natl. Acad. Sci. U. S. A..* **2003,** *100* (26), 15304-15309.
29. Hartley, A. M.; Lukoyanova, N.; Zhang, Y.; Cabrera-Orefice, A.; Arnold, S.; Meunier, B.; Pinotsis, N.; Maréchal, A., Structure of yeast cytochrome c oxidase in a supercomplex with cytochrome bc1. *Nat. Struct. Mol. Biol.* **2019,** *26* (1), 78-83.
30. Abramson, J.; Riistama, S.; Larsson, G.; Jasaitis, A.; Svensson-Ek, M.; Laakkonen, L.; Puustinen, A.; Iwata, S.; Wikström, M., The structure of the ubiquinol oxidase from Escherichia coli and its ubiquinone binding site. *Nat. Struct. Biol.* **2000,** *7* (10), 910-917.
31. Solomon, E. I.; Heppner, D. E.; Johnston, E. M.; Ginsbach, J. W.; Cirera, J.; Qayyum, M.; Kieber-Emmons, M. T.; Kjaergaard, C. H.; Hadt, R. G.; Tian, L., Copper Active Sites in Biology. *Chem. Rev.* **2014,** *114* (7), 3659-3853.
32. Avigad, G.; Amaral, D.; Asensio, C.; Horecker, B. L., The d-Galactose Oxidase of Polyporus circinatus. *J. Biol. Chem.* **1962,** *237* (9), 2736-2743.
33. Yin, D.; Urresti, S.; Lafond, M.; Johnston, E. M.; Derikvand, F.; Ciano, L.; Berrin, J.-G.; Henrissat, B.; Walton, P. H.; Davies, G. J.; Brumer, H., Structure–function characterization reveals new catalytic diversity in the galactose oxidase and glyoxal oxidase family. *Nat. Commun.* **2015,** *6*, 10197.
34. Luo, Y.-R., *Comprehensive handbook of chemical bond energies*. CRC press: 2007.
35. Thomas, F., Ten years of a biomimetic approach to the copper(II) radical site of galactose oxidase. *Eur. J. Inorg. Chem.* **2007,** (17), 2379-2404.
36. Matoba, Y.; Bando, N.; Oda, K.; Noda, M.; Higashikawa, F.; Kumagai, T.; Sugiyama, M., A Molecular Mechanism for Copper Transportation to Tyrosinase That Is Assisted by a Metallochaperone, Caddie Protein. *J. Biol. Chem.* **2011,** *286* (34), 30219-30231.
37. Kampatsikas, I.; Bijelic, A.; Pretzler, M.; Rompel, A., A Peptide-Induced Self-Cleavage Reaction Initiates the Activation of Tyrosinase. *Angew. Chem. Int. Ed.* **2019,** *58* (22), 7475-7479.

38. Matoba, Y.; Kumagai, T.; Yamamoto, A.; Yoshitsu, H.; Sugiyama, M., Crystallographic Evidence That the Dinuclear Copper Center of Tyrosinase Is Flexible during Catalysis. *J. Biol. Chem.* **2006,** *281* (13), 8981-8990.
39. Nagakubo, T.; Kumano, T.; Ohta, T.; Hashimoto, Y.; Kobayashi, M., Copper amine oxidases catalyze the oxidative deamination and hydrolysis of cyclic imines. *Nat. Commun.* **2019,** *10* (1), 413.
40. Agostinelli, E.; Belli, F.; Dalla Vedova, L.; Longu, S.; Mura, A.; Floris, G., Catalytic Properties and the Role of Copper in Bovine and Lentil Seedling Copper/Quinone-Containing Amine Oxidases: Controversial Opinions. *Eur. J. Inorg. Chem.* **2005,** *2005* (9), 1635-1641.
41. Mure, M.; Mills, S. A.; Klinman, J. P., Catalytic Mechanism of the Topa Quinone Containing Copper Amine Oxidases. *Biochemistry* **2002,** *41* (30), 9269-9278.
42. Adelson, C. N.; Johnston, E. M.; Hilmer, K. M.; Watts, H.; Dey, S. G.; Brown, D. E.; Broderick, J. B.; Shepard, E. M.; Dooley, D. M.; Solomon, E. I., Characterization of the Preprocessed Copper Site Equilibrium in Amine Oxidase and Assignment of the Reactive Copper Site in Topaquinone Biogenesis. *J. Am. Chem. Soc.* **2019,** *141* (22), 8877-8890.
43. Wilce, M. C. J.; Dooley, D. M.; Freeman, H. C.; Guss, J. M.; Matsunami, H.; McIntire, W. S.; Ruggiero, C. E.; Tanizawa, K.; Yamaguchi, H., Crystal Structures of the Copper-Containing Amine Oxidase from Arthrobacter globiformis in the Holo and Apo Forms: Implications for the Biogenesis of Topaquinone. *Biochemistry* **1997,** *36* (51), 16116-16133.
44. Phillips, C. M.; Beeson, W. T.; Cate, J. H.; Marletta, M. A., Cellobiose Dehydrogenase and a Copper-Dependent Polysaccharide Monooxygenase Potentiate Cellulose Degradation by Neurospora crassa. *ACS Chem. Biol.* **2011,** *6* (12), 1399-1406.
45. Quinlan, R. J.; Sweeney, M. D.; Lo Leggio, L.; Otten, H.; Poulsen, J. C. N.; Johansen, K. S.; Krogh, K. B. R. M.; Jorgensen, C. I.; Tovborg, M.; Anthonsen, A.; Tryfona, T.; Walter, C. P.; Dupree, P.; Xu, F.; Davies, G. J.; Walton, P. H., Insights into the oxidative degradation of cellulose by a copper metalloenzyme that exploits biomass components. *Proc. Natl. Acad. Sci. U. S. A.* **2011,** *108* (37), 15079-15084.
46. Vaaje-Kolstad, G.; Westereng, B.; Horn, S. J.; Liu, Z.; Zhai, H.; Sorlie, M.; Eijsink, V. G. H., An Oxidative Enzyme Boosting the Enzymatic Conversion of Recalcitrant Polysaccharides. *Science* **2010,** *330* (6001), 219-222.
47. Bissaro, B.; Røhr, Å. K.; Müller, G.; Chylenski, P.; Skaugen, M.; Forsberg, Z.; Horn, S. J.; Vaaje-Kolstad, G.; Eijsink, V. G. H., Oxidative cleavage of polysaccharides by monocopper enzymes depends on H2O2. *Nat. Chem. Biol.* **2017,** *13* (10), 1123-1128.
48. Cantarel, B. L.; Coutinho, P. M.; Rancurel, C.; Bernard, T.; Lombard, V.; Henrissat, B., The Carbohydrate-Active EnZymes database (CAZy): an expert resource for Glycogenomics. *Nucleic Acids Res.* **2009,** *37* (Database), D233-D238.
49. Lo Leggio, L.; Simmons, T. J.; Poulsen, J. C. N.; Frandsen, K. E. H.; Hemsworth, G. R.; Stringer, M. A.; Von Freiesleben, P.; Tovborg, M.; Johansen, K. S.; De Maria, L.; Harris, P. V.; Soong, C. L.; Dupree, P.; Tryfona, T.; Lenfant, N.; Henrissat, B.; Davies, G. J.; Walton, P. H., Structure and boosting activity of a starch-degrading lytic polysaccharide monooxygenase. *Nat. Commun.* **2015,** *6*, 5961.
50. Vu, V. V.; Beeson, W. T.; Span, E. A.; Farquhar, E. R.; Marletta, M. A., A family of starch-active polysaccharide monooxygenases. *Proc. Natl. Acad. Sci. U. S. A.* **2014,** *111* (38), 13822-13827.
51. Couturier, M.; Ladevèze, S.; Sulzenbacher, G.; Ciano, L.; Fanuel, M.; Moreau, C.; Villares, A.; Cathala, B.; Chaspoul, F.; Frandsen, K. E.; Labourel, A.; Herpoël-Gimbert, I.; Grisel, S.; Haon, M.; Lenfant, N.; Rogniaux, H.; Ropartz, D.; Davies, G. J.; Rosso, M.-N.; Walton, P. H.; Henrissat, B.; Berrin, J.-G., Lytic xylan oxidases from wood-decay fungi unlock biomass degradation. *Nat. Chem. Bio.* **2018,** *14* (3), 306-310.

52. Sabbadin, F.; Hemsworth, G. R.; Ciano, L.; Henrissat, B.; Dupree, P.; Tryfona, T.; Marques, R. D. S.; Sweeney, S. T.; Besser, K.; Elias, L.; Pesante, G.; Li, Y.; Dowle, A. A.; Bates, R.; Gomez, L. D.; Simister, R.; Davies, G. J.; Walton, P. H.; Bruce, N. C.; McQueen-Mason, S. J., An ancient family of lytic polysaccharide monooxygenases with roles in arthropod development and biomass digestion. *Nat. Commun.* **2018,** *1723*, 0-38.
53. Filiatrault-Chastel, C.; Navarro, D.; Haon, M.; Grisel, S.; Herpoël-Gimbert, I.; Chevret, D.; Fanuel, M.; Henrissat, B.; Heiss-Blanquet, S.; Margeot, A.; Berrin, J.-G., AA16, a new lytic polysaccharide monooxygenase family identified in fungal secretomes. *Biotechnol. Biofuels* **2019,** *12* (1), 55-55.
54. Ross, M. O.; Rosenzweig, A. C., A tale of two methane monooxygenases. *J. Biol. Inorg. Chem.* **2017,** *22*, 307-319.
55. Banerjee, R.; Jones, J. C.; Lipscomb, J. D., Soluble Methane Monooxygenase. *Annu. Rev. Biochem.* **2019,** *88* (1), 409-431.
56. Lieberman, R. L.; Rosenzweig, A. C., Crystal structure of a membrane-bound metalloenzyme that catalyses the biological oxidation of methane. *Nature* **2005,** *434* (7030), 177-182.
57. Sirajuddin, S.; Barupala, D.; Helling, S.; Marcus, K.; Stemmler, T. L.; Rosenzweig, A. C., Effects of zinc on particulate methane monooxygenase activity and structure. *J. Biol. Chem.* **2014,** *289* (31), 21782-21794.
58. Balasubramanian, R.; Rosenzweig, A. C., Structural and mechanistic insights into methane oxidation by particulate methane monooxygenase. *Acc. Chem. Res.* **2007,** *40* (7), 573-580.
59. Balasubramanian, R.; Smith, S. M.; Rawat, S.; Yatsunyk, L. A.; Stemmler, T. L.; Rosenzweig, A. C., Oxidation of methane by a biological dicopper centre. *Nature* **2010,** *465* (7294), 115-119.
60. Smith, S. M.; Rawat, S.; Telser, J.; Hoffman, B. M.; Stemmler, T. L.; Rosenzweig, A. C., Crystal structure and characterization of particulate methane monooxygenase from Methylocystis species strain M. *Biochemistry* **2011,** *50* (47), 10231-10240.
61. Cao, L.; Caldararu, O.; Rosenzweig, A. C.; Ryde, U., Quantum refinement does not support dinuclear copper sites in crystal structures of particulate methane monooxygenase. *Angew. Chem. Int. Ed.* **2017,** *57* (1), 162-166.
62. Ross, M. O.; MacMillan, F.; Wang, J.; Nisthal, A.; Lawton, T. J.; Olafson, B. D.; Mayo, S. L.; Rosenzweig, A. C.; Hoffman, B. M., Particulate methane monooxygenase contains only mononuclear copper centers. *Science* **2019,** *364* (6440), 566-570.
63. Cutsail, G. E.; Ross, M. O.; Rosenzweig, A. C.; DeBeer, S., Towards a unified understanding of the copper sites in particulate methane monooxygenase: an X-ray absorption spectroscopic investigation. *Chem. Sci.* **2021,** *12* (17), 6194-6209.
64. Klinman, J. P., The Copper-Enzyme Family of Dopamine β-Monooxygenase and Peptidylglycine α-Hydroxylating Monooxygenase: Resolving the Chemical Pathway for Substrate Hydroxylation. *J. Biol. Chem.* **2006,** *281* (6), 3013-3016.
65. Hess, C. R.; McGuirl, M. M.; Klinman, J. P., Mechanism of the Insect Enzyme, Tyramine β-Monooxygenase, Reveals Differences from the Mammalian Enzyme, Dopamine β-Monooxygenase. *J. Biol. Chem.* **2008,** *283* (6), 3042-3049.
66. Xin, X.; Mains, R. E.; Eipper, B. A., Monooxygenase X, a Member of the Copper-dependent Monooxygenase Family Localized to the Endoplasmic Reticulum. *J. Biol. Chem.* **2004,** *279* (46), 48159-48167.
67. Klinman, J. P., Mechanisms Whereby Mononuclear Copper Proteins Functionalize Organic Substrates. *Chem. Rev.* **1996,** *96* (7), 2541-2562.
68. Prigge, S. T.; Eipper, B. A.; Mains, R. E.; Amzel, L. M., Dioxygen Binds End-On to Mononuclear Copper in a Precatalytic Enzyme Complex. *Science* **2004,** *304* (5672), 864.

69. Chufán, E. E.; Prigge, S. T.; Siebert, X.; Eipper, B. A.; Mains, R. E.; Amzel, L. M., Differential Reactivity between Two Copper Sites in Peptidylglycine α-Hydroxylating Monooxygenase. *J. Am. Chem. Soc.* **2010,** *132* (44), 15565-15572.
70. Prigge, S. T.; Kolhekar, A. S.; Eipper, B. A.; Mains, R. E.; Amzel, L. M., Substrate-mediated electron transfer in peptidylglycine α-hydroxylating monooxygenase. *Nat. Struct. Biol.* **1999,** *6* (10), 976-983.
71. Chen, P.; Bell, J.; Eipper, B. A.; Solomon, E. I., Oxygen Activation by the Noncoupled Binuclear Copper Site in Peptidylglycine α-Hydroxylating Monooxygenase. Spectroscopic Definition of the Resting Sites and the Putative CuIIM−OOH Intermediate. *Biochemistry* **2004,** *43* (19), 5735-5747.
72. Vendelboe, T. V.; Harris, P.; Zhao, Y.; Walter, T. S.; Harlos, K.; El Omari, K.; Christensen, H. E. M., The crystal structure of human dopamine β-hydroxylase at 2.9 Å resolution. *Sci. Adv.* **2016,** *2* (4), e1500980.
73. Penttinen, L.; Rutanen, C.; Jänis, J.; Rouvinen, J.; Hakulinen, N., Unraveling Substrate Specificity and Catalytic Promiscuity of Aspergillus oryzae Catechol Oxidase. *ChemBioChem* **2018,** *19* (22), 2348-2352.
74. Matoba, Y.; Kihara, S.; Bando, N.; Yoshitsu, H.; Sakaguchi, M.; Kayama, K. e.; Yanagisawa, S.; Ogura, T.; Sugiyama, M., Catalytic mechanism of the tyrosinase reaction toward the Tyr98 residue in the caddie protein. *PLoS Biol.* **2019,** *16* (12), e3000077.
75. Miarzlou, D. A.; Leisinger, F.; Joss, D.; Häussinger, D.; Seebeck, F. P., Structure of formylglycine-generating enzyme in complex with copper and a substrate reveals an acidic pocket for binding and activation of molecular oxygen. *Chemical Science* **2019,** *10* (29), 7049-7058.
76. Appel, M. J.; Meier, K. K.; Lafrance-Vanasse, J.; Lim, H.; Tsai, C.-L.; Hedman, B.; Hodgson, K. O.; Tainer, J. A.; Solomon, E. I.; Bertozzi, C. R., Formylglycine-generating enzyme binds substrate directly at a mononuclear Cu(I) center to initiate O2 activation. *Proc. Natl. Acad. Sci. U.S.A.* **2019,** *116* (12), 5370-5375.
77. Oka, T.; Simpson, F. J.; Child, J. J.; Mills, S. C., Degradation of rutin by Aspergillus flavus. Purification of the dioxygenase, quercetinase. *Can. J. Microbiol.* **1971,** *17* (1), 111-118.
78. Simpson, F. J.; Talbot, G.; Westlake, D. W. S., Production of carbon monoxide in the enzymatic degradation of rutin. *Biochem. Biophys. Res. Commun.* **1960,** *2* (1), 15-18.
79. Steiner, R. A.; Kalk, K. H.; Dijkstra, B. W., Anaerobic enzyme·substrate structures provide insight into the reaction mechanism of the copper-dependent quercetin 2,3-dioxygenase. *Proc. Natl. Acad. Sci. U. S. A.* **2002,** *99* (26), 16625-16630.
80. Fusetti, F.; Schröter, K. H.; Steiner, R. A.; van Noort, P. I.; Pijning, T.; Rozeboom, H. J.; Kalk, K. H.; Egmond, M. R.; Dijkstra, B. W., Crystal Structure of the Copper-Containing Quercetin 2,3-Dioxygenase from Aspergillus japonicus. *Structure* **2002,** *10* (2), 259-268.
81. Kooter, I. M.; Steiner, R. A.; Dijkstra, B. W.; van Noort, P. I.; Egmond, M. R.; Huber, M., EPR characterization of the mononuclear Cu-containing Aspergillus japonicus quercetin 2,3-dioxygenase reveals dramatic changes upon anaerobic binding of substrates. *Eur. J. Biochem.* **2002,** *269* (12), 2971-2979.
82. Ciano, L.; Davies, G. J.; Tolman, W. B.; Walton, P. H., Bracing copper for the catalytic oxidation of C–H bonds. *Nat. Catal.* **2018,** *1* (8), 571-577.
83. Tandrup, T.; Frandsen, K. E. H.; Johansen, K. S.; Berrin, J.-G.; Lo Leggio, L., Recent insights into lytic polysaccharide monooxygenases (LPMOs). *Biochem. Soc. Trans.* **2018,** *46* (6), 1431-1447.
84. Hangasky, J. A.; Iavarone, A. T.; Marletta, M. A., Reactivity of O2 versus H2O2 with polysaccharide monooxygenases. *Proc Natl Acad Sci USA* **2018,** *115* (19), 4915.
85. Zoghlami, A.; Paës, G., Lignocellulosic Biomass: Understanding Recalcitrance and Predicting Hydrolysis. *Front. Chem.* **2019,** *7*, 874-885.

86. Hemsworth, G. R.; Johnston, E. M.; Davies, G. J.; Walton, P. H., Lytic Polysaccharide Monooxygenases in Biomass Conversion. *Trends Biotechnol.* **2015,** *33* (12), 747-761.
87. Brown, T. R., A techno-economic review of thermochemical cellulosic biofuel pathways. *Bioresour. Technol.* **2015,** *178*, 166-176.
88. Robak, K.; Balcerek, M., Review of Second Generation Bioethanol Production from Residual Biomass. *Food Technol. Biotechnol.* **2018,** *56* (2), 174-187.
89. Payne, C. M.; Knott, B. C.; Mayes, H. B.; Hansson, H.; Himmel, M. E.; Sandgren, M.; Ståhlberg, J.; Beckham, G. T., Fungal Cellulases. *Chem. Rev.* **2015,** *115* (3), 1308-1448.
90. Reese, E. T.; Siu, R. G. H.; Levinson, H. S., The Biological Degradation of Soluble Cellulose Derivatives and its Relationship to the Mechanism of Cellulose Hydrolysis. *J. Bacteriol. Res.* **1950,** *59* (4), 485-497.
91. Eriksson, K.-E.; Pettersson, B.; Westermark, U., Oxidation: An important enzyme reaction in fungal degradation of cellulose. *FEBS Lett.* **1974,** *49* (2), 282-285.
92. Vaaje-Kolstad, G.; Westereng, B.; Horn, S. J.; Liu, Z.; Zhai, H.; Sørlie, M.; Eijsink, V. G. H., An Oxidative Enzyme Boosting the Enzymatic Conversion of Recalcitrant Polysaccharides. *Science* **2010,** *330* (6001), 219-222.
93. Quinlan, R. J.; Sweeney, M. D.; Lo Leggio, L.; Otten, H.; Poulsen, J.-C. N.; Johansen, K. S.; Krogh, K. B. R. M.; Jørgensen, C. I.; Tovborg, M.; Anthonsen, A.; Tryfona, T.; Walter, C. P.; Dupree, P.; Xu, F.; Davies, G. J.; Walton, P. H., Insights into the Oxidative Degradation of Cellulose by a Copper Metalloenzyme That Exploits Biomass Components. *Proc. Natl. Acad. Sci. U. S. A.* **2011,** *108*.
94. Harris, P. V.; Welner, D.; McFarland, K. C.; Re, E.; Navarro Poulsen, J. C.; Brown, K.; Salbo, R.; Ding, H.; Vlasenko, E.; Merino, S.; Xu, F.; Cherry, J.; Larsen, S.; Lo Leggio, L., Stimulation of lignocellulosic biomass hydrolysis by proteins of glycoside hydrolase family 61: structure and function of a large, enigmatic family. *Biochemistry* **2010,** *49* (15), 3305-16.
95. Karkehabadi, S.; Hansson, H.; Kim, S.; Piens, K.; Mitchinson, C.; Sandgren, M., The first structure of a glycoside hydrolase family 61 member, Cel61B from Hypocrea jecorina, at 1.6 A resolution. *J. Mol. Biol.* **2008,** *383* (1), 144-154.
96. Bennati-Granier, C.; Garajova, S.; Champion, C.; Grisel, S.; Haon, M.; Zhou, S.; Fanuel, M.; Ropartz, D.; Rogniaux, H.; Gimbert, I.; Record, E.; Berrin, J.-G., Substrate specificity and regioselectivity of fungal AA9 lytic polysaccharide monooxygenases secreted by Podospora anserina. *Biotechnol. Biofuels* **2015,** *8* (1), 1-14.
97. Vaaje-Kolstad, G.; Westereng, B.; Horn, S. J.; Liu, Z. L.; Zhai, H.; Sørlie, M.; Eijsink, V. G. H., An oxidative enzyme boosting the enzymatic conversion of recalcitrant polysaccharides. *Science* **2010,** *330*, 219-222.
98. Frandsen, K. E. H.; Simmons, T. J.; Dupree, P.; Poulsen, J.-C. N.; Hemsworth, G. R.; Ciano, L.; Johnston, E. M.; Tovborg, M.; Johansen, K. S.; von Freiesleben, P.; Marmuse, L.; Fort, S.; Cottaz, S.; Driguez, H.; Henrissat, B.; Lenfant, N.; Tuna, F.; Baldansuren, A.; Davies, G. J.; Lo Leggio, L.; Walton, P. H., The molecular basis of polysaccharide cleavage by lytic polysaccharide monooxygenases. *Nat Chem Biol* **2016,** *12* (4), 298-303.
99. Frommhagen, M.; Sforza, S.; Westphal, A. H.; Visser, J.; Hinz, S. W. A.; Koetsier, M. J.; van Berkel, W. J. H.; Gruppen, H.; Kabel, M. A., Discovery of the combined oxidative cleavage of plant xylan and cellulose by a new fungal polysaccharide monooxygenase. *Biotechnol. Biofuels* **2015,** *8* (1), 101.
100. Vaaje-Kolstad, G.; Bøhle, L. A.; Gåseidnes, S.; Dalhus, B.; Bjørås, M.; Mathiesen, G.; Eijsink, V. G. H., Characterization of the Chitinolytic Machinery of Enterococcus faecalis V583 and High-Resolution Structure of Its Oxidative CBM33 Enzyme. *J. Mol. Biol.* **2012,** *416* (2), 239-254.
101. Hemsworth, G. R.; Henrissat, B.; Davies, G. J.; Walton, P. H., Discovery and characterization of a new family of lytic polysaccharide monooxygenases. *Nat. Chem. Bio.* **2014,** *10* (2), 122-126.

102. Jalak, J.; Kurašin, M.; Teugjas, H.; Väljamäe, P., Endo-exo Synergism in Cellulose Hydrolysis Revisited*. *J. Biol. Chem.* **2012,** *287* (34), 28802-28815.
103. White, A.; Rose, D. R., Mechanism of catalysis by retaining beta-glycosyl hydrolases. *Curr Opin Struct Biol* **1997,** *7* (5), 645-51.
104. Zechel, D. L.; Withers, S. G., Glycosidase Mechanisms: Anatomy of a Finely Tuned Catalyst. *Acc. Chem. Res.* **2000,** *33* (1), 11-18.
105. Ciano, L.; Paradisi, A.; Hemsworth, G. R.; Tovborg, M.; Davies, G. J.; Walton, P. H., Insights from semi-oriented EPR spectroscopy studies into the interaction of lytic polysaccharide monooxygenases with cellulose. *Dalton Trans.* **2020,** *49* (11), 3413-3422.
106. Eibinger, M.; Ganner, T.; Bubner, P.; Rošker, S.; Kracher, D.; Haltrich, D.; Ludwig, R.; Plank, H.; Nidetzky, B., Cellulose surface degradation by a lytic polysaccharide monooxygenase and its effect on cellulase hydrolytic efficiency. *J. Biol. Chem.* **2014,** *289* (52), 35929-35938.
107. Müller, G.; Várnai, A.; Johansen, K. S.; Eijsink, V. G. H.; Horn, S. J., Harnessing the potential of LPMO-containing cellulase cocktails poses new demands on processing conditions. *Biotechnol. Biofuels* **2015,** *8* (1), 187.
108. van Wyk, N.; Drancourt, M.; Henrissat, B.; Kremer, L., Current perspectives on the families of glycoside hydrolases of Mycobacterium tuberculosis: their importance and prospects for assigning function to unknowns. *J. Glycobiol.* **2017,** *27* (2), 112-122.
109. Frandsen, K. E. H.; Simmons, T. J.; Dupree, P.; Poulsen, J.-c. N.; Hemsworth, G. R.; Ciano, L.; Johnston, E. M.; Tovborg, M.; Johansen, K. S.; von Freiesleben, P.; Marmuse, L.; Fort, S.; Cottaz, S.; Driguez, H.; Henrissat, B.; Lenfant, N.; Tuna, F.; Baldansuren, A.; Davies, G. J.; Lo Leggio, L.; Walton, P. H., The molecular basis of polysaccharide cleavage by lytic polysaccharide monooxygenases. *Nat. Chem. Bio.* **2016,** *12* (4), 298-303.
110. Vu, V. V.; Hangasky, J. A.; Detomasi, T. C.; Henry, S. J. W.; Ngo, S. T.; Span, E. A.; Marletta, M. A., Substrate selectivity in starch polysaccharide monooxygenases. *J. Biol. Chem.* **2019,** *294* (32), 12157-12166.
111. Lenfant, N.; Hainaut, M.; Terrapon, N.; Drula, E.; Lombard, V.; Henrissat, B., A bioinformatics analysis of 3400 lytic polysaccharide oxidases from family AA9. *Carbohydr. Res.* **2017,** *448*, 166-174.
112. Bey, M.; Zhou, S.; Poidevin, L.; Henrissat, B.; Coutinho, P. M.; Berrin, J.-G.; Sigoillot, J.-C., Cello-oligosaccharide oxidation reveals differences between two lytic polysaccharide monooxygenases (family GH61) from Podospora anserina. *Appl. Environ. Microbiol.* **2013,** *79* (2), 488-496.
113. Wu, M.; Beckham, G. T.; Larsson, A. M.; Ishida, T.; Kim, S.; Payne, C. M.; Himmel, M. E.; Crowley, M. F.; Horn, S. J.; Westereng, B.; Igarashi, K.; Samejima, M.; Ståhlberg, J.; Eijsink, V. G. H.; Sandgren, M., Crystal structure and computational characterization of the lytic polysaccharide monooxygenase GH61D from the Basidiomycota fungus Phanerochaete chrysosporium. *J. Biol. Chem.* **2013,** *288* (18), 12828-12839.
114. Petrović, D. M.; Bissaro, B.; Chylenski, P.; Skaugen, M.; Sørlie, M.; Jensen, M. S.; Aachmann, F. L.; Courtade, G.; Várnai, A.; Eijsink, V. G. H., Methylation of the N-terminal histidine protects a lytic polysaccharide monooxygenase from auto-oxidative inactivation. *Protein Sci.* **2018,** *27* (9), 1636-1650.
115. Gudmundsson, M.; Kim, S.; Wu, M.; Ishida, T.; Momeni, M. H.; Vaaje-Kolstad, G.; Lundberg, D.; Royant, A.; Ståhlberg, J.; Eijsink, V. G. H.; Beckham, G. T.; Sandgren, M., Structural and electronic snapshots during the transition from a Cu(II) to Cu(I) metal center of a lytic polysaccharide onooxygenase by x-ray photoreduction. *J. Biol. Chem.* **2014,** *289* (27), 18782-18792.
116. Gregory, R. C.; Hemsworth, G. R.; Turkenburg, J. P.; Hart, S. J.; Walton, P. H.; Davies, G. J., Activity, stability and 3-D structure of the Cu(ii) form of a chitin-active lytic

polysaccharide monooxygenase from Bacillus amyloliquefaciens. *Dalton Trans.* **2016,** *45* (42), 16904-16912.
117. Hemsworth, G. R.; Ciano, L.; Davies, G. J.; Walton, P. H., Production and spectroscopic characterization of lytic polysaccharide monooxygenases. *Methods Enzymol.* **2018,** *613*, 63-90.
118. Paradisi, A.; Johnston, E. M.; Tovborg, M.; Nicoll, C. R.; Ciano, L.; Dowle, A.; McMaster, J.; Hancock, Y.; Davies, G. J.; Walton, P. H., Formation of a Copper(II)–Tyrosyl Complex at the Active Site of Lytic Polysaccharide Monooxygenases Following Oxidation by H2O2. *J. Am. Chem. Soc.* **2019,** *141* (46), 18585-18599.
119. Wang, B.; Johnston, E. M.; Li, P.; Shaik, S.; Davies, G. J.; Walton, P. H.; Rovira, C., QM/MM Studies into the H2O2-Dependent Activity of Lytic Polysaccharide Monooxygenases: Evidence for the Formation of a Caged Hydroxyl Radical Intermediate. *ACS Catal.* **2018,** *8* (2), 1346-1351.
120. Span, E.; Suess, D.; Deller, M.; Britt, R.; Marletta, M., The Role of the Secondary Coordination Sphere in a Fungal Polysaccharide Monooxygenase. *ACS Chem. Biol.* **2017,** *12(4)*, 1095-1103.
121. Kim, S.; Ståhlberg, J.; Sandgren, M.; Paton, R. S.; Beckham, G. T., Quantum mechanical calculations suggest that lytic polysaccharide monooxygenases use a copper-oxyl, oxygen-rebound mechanism. *Proc. Natl. Acad. Sci. U.S.A.* **2014,** *111* (1), 149.
122. Li, X.; Beeson, William T. I. V.; Phillips, Christopher M.; Marletta, Michael A.; Cate, Jamie H. D., Structural Basis for Substrate Targeting and Catalysis by Fungal Polysaccharide Monooxygenases. *Structure* **2012,** *20* (6), 1051-1061.
123. Wang, B.; Walton, P. H.; Rovira, C., Molecular Mechanisms of Oxygen Activation and Hydrogen Peroxide Formation in Lytic Polysaccharide Monooxygenases. *ACS Catal.* **2019,** *9* (6), 4958-4969.
124. Bertini, L.; Breglia, R.; Lambrughi, M.; Fantucci, P.; De Gioia, L.; Borsari, M.; Sola, M.; Bortolotti, C. A.; Bruschi, M., Catalytic Mechanism of Fungal Lytic Polysaccharide Monooxygenases Investigated by First-Principles Calculations. *Inorg. Chem.* **2018,** *57* (1), 86-97.
125. Kjaergaard, C. H.; Qayyum, M. F.; Wong, S. D.; Xu, F.; Hemsworth, G. R.; Walton, D. J.; Young, N. A.; Davies, G. J.; Walton, P. H.; Johansen, K. S.; Hodgson, K. O.; Hedman, B.; Solomon, E. I., Spectroscopic and computational insight into the activation of O2 by the mononuclear Cu center in polysaccharide monooxygenases. *Proc. Natl. Acad. Sci. U.S.A.* **2014,** *111* (24), 8797-8802.
126. O'Dell, W. B.; Agarwal, P. K.; Meilleur, F., Oxygen Activation at the Active Site of a Fungal Lytic Polysaccharide Monooxygenase. *Angew. Chem. Int. Ed* **2017,** *56* (3), 767-770.
127. Bissaro, B.; Streit, B.; Isaksen, I.; Eijsink, V. G. H.; Beckham, G. T.; DuBois, J. L.; Røhr, Å. K., Molecular mechanism of the chitinolytic peroxygenase reaction. *Proc. Natl. Acad. Sci. U. S. A.* **2020,** *117* (3), 1504-1513.
128. Blumberg, W. E.; Peisach, J., An Electron Spin Resonance Study of Copper Uroporphyrin III and Other Touraco Feather Components. *J. Biol. Chem* **1965,** *240* (2), 870-876.
129. Courtade, G.; Ciano, L.; Paradisi, A.; Lindley, P. J.; Forsberg, Z.; Sørlie, M.; Wimmer, R.; Davies, G. J.; Eijsink, V. G. H.; Walton, P. H.; Aachmann, F. L., Mechanistic basis of substrate–O2coupling within a chitin-active lytic polysaccharide monooxygenase: An integrated NMR/EPR study. *Proc. Natl. Acad. Sci. U.S.A.* **2020,** *117* (32), 19178.
130. Span, E.; Suess, D.; Deller, M.; Britt, R.; Marletta, M., The Role of the Secondary Coordination Sphere in a Fungal Polysaccharide Monooxygenase. *ACS Chem. Biol.* **2017,** *12*.
131. Simmons, T. J.; Frandsen, K. E. H.; Ciano, L.; Tryfona, T.; Lenfant, N.; Poulsen, J. C.; Wilson, L. F. L.; Tandrup, T.; Tovborg, M.; Schnorr, K.; Johansen, K. S.; Henrissat, B.; Walton, P. H.; Lo Leggio, L.; Dupree, P., Structural and electronic determinants of lytic

polysaccharide monooxygenase reactivity on polysaccharide substrates. *Nat. Commun.* **2017,** *8* (1), 1064.
132. Hansson, H.; Karkehabadi, S.; Mikkelsen, N.; Douglas, N. R.; Kim, S.; Lam, A.; Kaper, T.; Kelemen, B.; Meier, K. K.; Jones, S. M.; Solomon, E. I.; Sandgren, M., High-resolution structure of a lytic polysaccharide monooxygenase from Hypocrea jecorina reveals a predicted linker as an integral part of the catalytic domain. *J. Biol. Chem.* **2017,** *292* (46), 19099-19109.
133. Chaplin, A. K.; Wilson, M. T.; Hough, M. A.; Svistunenko, D. A.; Hemsworth, G. R.; Walton, P. H.; Vijgenboom, E.; Worrall, J. A. R., Heterogeneity in the Histidine-brace Copper Coordination Sphere in Auxiliary Activity Family 10 (AA10) Lytic Polysaccharide Monooxygenases. *J. Biol. Chem.* **2016,** *291* (24), 12838-12850.
134. Forsberg, Z.; Røhr, A. K.; Mekasha, S.; Andersson, K. K.; Eijsink, V. G.; Vaaje-Kolstad, G.; Sørlie, M., Comparative study of two chitin-active and two cellulose-active AA10-type lytic polysaccharide monooxygenases. *Biochemistry* **2014,** *53* (10), 1647-56.
135. Leggio, L. L.; Simmons, T. J.; Poulsen, J. C. N.; Frandsen, K. E. H.; Hemsworth, G. R.; Stringer, M. A., Structure and boosting activity of a starch-degrading lytic polysaccharide monooxygenase. *Nat Commun* **2015**.
136. Borisova, A. S.; Isaksen, T.; Dimarogona, M.; Kognole, A. A.; Mathiesen, G.; Várnai, A.; Røhr, Å. K.; Payne, C. M.; Sørlie, M.; Sandgren, M.; Eijsink, V. G. H., Structural and Functional Characterization of a Lytic Polysaccharide Monooxygenase with Broad Substrate Specificity*. *J. Biol. Chem.* **2015,** *290* (38), 22955-22969.
137. Bissaro, B.; Isaksen, I.; Vaaje-Kolstad, G.; Eijsink, V. G. H.; Røhr, Å. K., How a Lytic Polysaccharide Monooxygenase Binds Crystalline Chitin. *Biochemistry* **2018,** *57* (12), 1893-1906.
138. Vu, V. V.; Ngo, S. T., Copper active site in polysaccharide monooxygenases. *Coord. Chem. Rev.* **2018,** *368*, 134-157.
139. Hansson, H.; Karkehabadi, S.; Mikkelsen, N.; Douglas, N. R.; Kim, S.; Lam, A.; Kaper, T.; Kelemen, B.; Meier, K. K.; Jones, S. M.; Solomon, E. I.; Sandgren, M., High-resolution structure of a lytic polysaccharide monooxygenase from Hypocrea jecorina reveals a predicted linker as an integral part of the catalytic domain. *J. Biol. Chem.* **2017,** *292* (46), 19099-19109.
140. Mirica, L. M.; Ottenwaelder, X.; Stack, T. D. P., Structure and Spectroscopy of Copper−Dioxygen Complexes. *Chem. Rev.* **2004,** *104* (2), 1013-1046.
141. Elwell, C. E.; Gagnon, N. L.; Neisen, B. D.; Dhar, D.; Spaeth, A. D.; Yee, G. M.; Tolman, W. B., Copper–Oxygen Complexes Revisited: Structures, Spectroscopy, and Reactivity. *Chem. Rev.* **2017,** *117* (3), 2059-2107.
142. Hatcher, L. Q.; Karlin, K. D., Oxidant types in copper–dioxygen chemistry: the ligand coordination defines the Cun-O2 structure and subsequent reactivity. *J. Biol. Inorg. Chem.* **2004,** *9* (6), 669-683.
143. Osako, T.; Terada, S.; Tosha, T.; Nagatomo, S.; Furutachi, H.; Fujinami, S.; Kitagawa, T.; Suzuki, M.; Itoh, S., Structure and dioxygen-reactivity of copper(i) complexes supported by bis(6-methylpyridin-2-ylmethyl)amine tridentate ligands. *Dalton Trans.* **2005,** (21), 3514-3521.
144. Zhang, C. X.; Liang, H.-C.; Kim, E.-i.; Shearer, J.; Helton, M. E.; Kim, E.; Kaderli, S.; Incarvito, C. D.; Zuberbühler, A. D.; Rheingold, A. L.; Karlin, K. D., Tuning Copper−Dioxygen Reactivity and Exogenous Substrate Oxidations via Alterations in Ligand Electronics. *J. Am. Chem. Soc.* **2003,** *125* (3), 634-635.
145. Kunishita, A.; Ishimaru, H.; Nakashima, S.; Ogura, T.; Itoh, S., Reactivity of Mononuclear Alkylperoxo Copper(II) Complex. O−O Bond Cleavage and C−H Bond Activation. *J. Am. Chem. Soc.* **2008,** *130* (13), 4244-4245.

146. Kunishita, A.; Teraoka, J.; Scanlon, J. D.; Matsumoto, T.; Suzuki, M.; Cramer, C. J.; Itoh, S., Aromatic Hydroxylation Reactivity of a Mononuclear Cu(II)−Alkylperoxo Complex. *J. Am. Chem. Soc.* **2007,** *129* (23), 7248-7249.
147. Castillo, I.; Neira, A. C.; Nordlander, E.; Zeglio, E., Bis(benzimidazolyl)amine copper complexes with a synthetic 'histidine brace' structural motif relevant to polysaccharide monooxygenases. *Inorg. Chim. Acta* **2014,** *422*, 152-157.
148. Neira, A. C.; Martínez-Alanis, P. R.; Aullón, G.; Flores-Alamo, M.; Zerón, P.; Company, A.; Chen, J.; Kasper, J. B.; Browne, W. R.; Nordlander, E.; Castillo, I., Oxidative Cleavage of Cellobiose by Lytic Polysaccharide Monooxygenase (LPMO)-Inspired Copper Complexes. *ACS Omega* **2019,** *4* (6), 10729-10740.
149. Abe, T.; Morimoto, Y.; Tano, T.; Mieda, K.; Sugimoto, H.; Fujieda, N.; Ogura, T.; Itoh, S., Geometric Control of Nuclearity in Copper(I)/Dioxygen Chemistry. *Inorg. Chem.* **2014,** *53* (16), 8786-8794.
150. Hatcher, L. Q.; Vance, M. A.; Narducci Sarjeant, A. A.; Solomon, E. I.; Karlin, K. D., Copper−Dioxygen Adducts and the Side-on Peroxo Dicopper(II)/Bis(μ-oxo) Dicopper(III) Equilibrium: Significant Ligand Electronic Effects. *Inorg.* **2006,** *45* (7), 3004-3013.
151. Liang, H.-C.; Henson, M. J.; Hatcher, L. Q.; Vance, M. A.; Zhang, C. X.; Lahti, D.; Kaderli, S.; Sommer, R. D.; Rheingold, A. L.; Zuberbühler, A. D.; Solomon, E. I.; Karlin, K. D., Solvent Effects on the Conversion of Dicopper(II) μ-η2:η2-Peroxo to Bis-μ-oxo Dicopper(III) Complexes: Direct Probing of the Solvent Interaction. *Inorg.* **2004,** *43* (14), 4115-4117.
152. Mandal, S.; De, A.; Mukherjee, R., Formation of {Cu(μ-O)2}2+ Core Due to Dioxygen Reactivity of a Copper(I) Complex Supported by a New Hybrid Tridentate Ligand: Reaction with Exogenous Substrates. *Chem. Biodivers.* **2008,** *5* (8), 1594-1608.
153. Kunishita, A.; Kubo, M.; Sugimoto, H.; Ogura, T.; Sato, K.; Takui, T.; Itoh, S., Mononuclear Copper(II)−Superoxo Complexes that Mimic the Structure and Reactivity of the Active Centers of PHM and DβM. *J. Am. Chem. Soc.* **2009,** *131* (8), 2788-2789.
154. Yang, L.; Powell, D. R.; Houser, R. P., Structural variation in copper(i) complexes with pyridylmethylamide ligands: structural analysis with a new four-coordinate geometry index, τ4. *Dalton Trans.* **2007,** (9), 955-964.
155. Hatcher, L. Q.; Vance, M. A.; Narducci Sarjeant, A. A.; Solomon, E. I.; Karlin, K. D., Copper−Dioxygen Adducts and the Side-on Peroxo Dicopper(II)/Bis(μ-oxo) Dicopper(III) Equilibrium: Significant Ligand Electronic Effects. *Inorg. Chem.* **2006,** *45* (7), 3004-3013.
156. Mahadevan, V.; Hou, Z.; Cole, A. P.; Root, D. E.; Lal, T. K.; Solomon, E. I.; Stack, T. D. P., Irreversible Reduction of Dioxygen by Simple Peralkylated Diamine−Copper(I) Complexes: Characterization and Thermal Stability of a [Cu2(μ-O)2]2+ Core. *J. Am. Chem. Soc.* **1997,** *119* (49), 11996-11997.
157. Donoghue, P. J.; Tehranchi, J.; Cramer, C. J.; Sarangi, R.; Solomon, E. I.; Tolman, W. B., Rapid C–H Bond Activation by a Monocopper(III)–Hydroxide Complex. *J. Am. Chem. Soc.* **2011,** *133* (44), 17602-17605.
158. Dhar, D.; Tolman, W. B., Hydrogen Atom Abstraction from Hydrocarbons by a Copper(III)-Hydroxide Complex. *J. Am. Chem. Soc.* **2015,** *137* (3), 1322-1329.
159. Dhar, D.; Yee, G. M.; Spaeth, A. D.; Boyce, D. W.; Zhang, H.; Dereli, B.; Cramer, C. J.; Tolman, W. B., Perturbing the Copper(III)–Hydroxide Unit through Ligand Structural Variation. *J. Am. Chem. Soc.* **2016,** *138* (1), 356-368.
160. Donoghue, P. J.; Gupta, A. K.; Boyce, D. W.; Cramer, C. J.; Tolman, W. B., An Anionic, Tetragonal Copper(II) Superoxide Complex. *J. Am. Chem. Soc.* **2010,** *132* (45), 15869-15871.
161. Pirovano, P.; Magherusan, A. M.; McGlynn, C.; Ure, A.; Lynes, A.; McDonald, A. R., Nucleophilic Reactivity of a Copper(II)–Superoxide Complex. *Angew. Chem. Int. Ed.* **2014,** *53* (23), 5946-5950.

162. Bailey, W. D.; Gagnon, N. L.; Elwell, C. E.; Cramblitt, A. C.; Bouchey, C. J.; Tolman, W. B., Revisiting the Synthesis and Nucleophilic Reactivity of an Anionic Copper Superoxide Complex. *Inorg. Chem.* **2019,** *58* (8), 4706-4711.
163. Bacik, J. P.; Mekasha, S.; Forsberg, Z.; Kovalevsky, A. Y.; Vaaje-Kolstad, G.; Eijsink, V. G. H.; Nix, J. C.; Coates, L.; Cuneo, M. J.; Unkefer, C. J.; Chen, J. C. H., Neutron and Atomic Resolution X-ray Structures of a Lytic Polysaccharide Monooxygenase Reveal Copper-Mediated Dioxygen Binding and Evidence for N-Terminal Deprotonation. *Biochemistry* **2017,** *56* (20), 2529-2532.
164. Concia, A. L.; Beccia, M. R.; Orio, M.; Ferre, F. T.; Scarpellini, M.; Biaso, F.; Guigliarelli, B.; Réglier, M.; Simaan, A. J., Copper Complexes as Bioinspired Models for Lytic Polysaccharide Monooxygenases. *Inorg. Chem.* **2017,** *56* (3), 1023-1026.
165. Scarpellini, M.; Neves, A.; Hörner, R.; Bortoluzzi, A. J.; Szpoganics, B.; Zucco, C.; Nome Silva, R. A.; Drago, V.; Mangrich, A. S.; Ortiz, W. A.; Passos, W. A. C.; de Oliveira, M. C. B.; Terenzi, H., Phosphate Diester Hydrolysis and DNA Damage Promoted by New cis-Aqua/Hydroxy Copper(II) Complexes Containing Tridentate Imidazole-rich Ligands. *Inorg. Chem.* **2003,** *42* (25), 8353-8365.
166. Fukatsu, A.; Morimoto, Y.; Sugimoto, H.; Itoh, S., Modelling a 'histidine brace' motif in mononuclear copper monooxygenases. *Chem. Commun.* **2020,** *56* (38), 5123-5126.
167. Place, C.; Zimmermann, J.-L.; Mulliez, E.; Guillot, G.; Bois, C.; Chottard, J.-C., Crystallographic, Electrochemical, and Pulsed EPR Study of Copper(II) Polyimidazole Complexes Relevant to the Metal Sites of Copper Proteins. *Inorg. Chem.* **1998,** *37* (16), 4030-4039.
168. Peisach, J.; Blumberg, W. E., Structural implications derived from the analysis of electron paramagnetic resonance spectra of natural and artificial copper proteins. *Arch. Biochem. Biophys.* **1974,** *165* (2), 691-708.
169. Shimoyama, Y.; Kojima, T., Metal–Oxyl Species and Their Possible Roles in Chemical Oxidations. *Inorg. Chem.* **2019,** *58* (15), 9517-9542.
170. Siegbahn, P. E. M., O-O Bond Formation in the S4 State of the Oxygen-Evolving Complex in Photosystem II. *Chem. Eur.* **2006,** *12* (36), 9217-9227.
171. Shimoyama, Y.; Ishizuka, T.; Kotani, H.; Shiota, Y.; Yoshizawa, K.; Mieda, K.; Ogura, T.; Okajima, T.; Nozawa, S.; Kojima, T., A Ruthenium(III)–Oxyl Complex Bearing Strong Radical Character. *Angew. Chem. Int. Ed.* **2016,** *55* (45), 14041-14045.
172. Kobayashi, K.; Ohtsu, H.; Wada, T.; Kato, T.; Tanaka, K., Characterization of a Stable Ruthenium Complex with an Oxyl Radical. *J. Am. Chem. Soc.* **2003,** *125* (22), 6729-6739.
173. Mabbs, F. E.; Collison, D., *Electron Paramagnetic Resonance of D Transition Metal Compounds*. Elsevier: 1992.
174. Deschamps, P.; Kulkarni, P. P.; Gautam-Basak, M.; Sarkar, B., The saga of copper(II)–l-histidine. *Coord. Chem. Rev.* **2005,** *249* (9), 895-909.
175. Casella, L.; Gullotti, M., Coordination modes of histidine: 4. Coordination structures in the copper(II)-L-histidine (1:2) system. *J. Inorg. Biochem.* **1983,** *18* (1), 19-31.
176. Sigel, H.; McCormick, D. B., Structure of the copper(II)-L-histidine 1:2 complex in solution. *J. Am. Chem. Soc.* **1971,** *93* (8), 2041-2044.
177. Perrin, D. D.; Sharma, V. S., Histidine complexes with some bivalent cations. *J. Chem. Soc.* **1967,** (0), 724-728.
178. Kruck, T. P. A.; Sarkar, B., Structure of the Species in the Copper (II)–L-Histidine System. *Can. J. Chem.* **1973,** *51* (21), 3563-3571.
179. Deschamps, P.; Kulkarni, P. P.; Sarkar, B., X-ray Structure of Physiological Copper(II)−Bis(l-histidinato) Complex. *Inorg. Chem.* **2004,** *43* (11), 3338-3340.
180. Mandal, S.; Mandal, S.; Ghosh, S. K.; Sar, P.; Ghosh, A.; Saha, R.; Saha, B., A review on the advancement of ether synthesis from organic solvent to water. *RSC Adv.* **2016,** *6* (73), 69605-69614.

181. Williamson, A., Ueber die Theorie der Aetherbildung. *Justus Liebigs Ann. Chem.* **1851,** *77* (1), 37-49.
182. Mao, D.; Yang, W.; Xia, J.; Zhang, B.; Song, Q.; Chen, Q., Highly effective hybrid catalyst for the direct synthesis of dimethyl ether from syngas with magnesium oxide-modified HZSM-5 as a dehydration component. *J. Catal.* **2005,** *230* (1), 140-149.
183. Fossum, Z. Y. L.-S. T. E., Aryl ether synthesis via low-cost Ullmann coupling systems. *Arrkivoc* **2009,** *XIV* (14), 255-265.
184. Lepore, S. D.; He, Y., Use of Sonication for the Coupling of Sterically Hindered Substrates in the Phenolic Mitsunobu Reaction. *J. Org. Chem.* **2003,** *68* (21), 8261-8263.
185. Wang, Z., Williamson Ether Synthesis. In *Comprehensive Organic Name Reactions and Reagents*, Wang, Z., Ed. 2010; pp 3026-3030.
186. Cowdrey, W. A.; Hughes, E. D.; Ingold, C. K.; Masterman, S.; Scott, A. D., 257. Reaction kinetics and the Walden inversion. Part VI. Relation of steric orientation to mechanism in substitutions involving halogen atoms and simple or substituted hydroxyl groups. *J. Chem. Soc.* **1937,** (0), 1252-1271.
187. Ma, D.; Cai, Q., Copper/Amino Acid Catalyzed Cross-Couplings of Aryl and Vinyl Halides with Nucleophiles. *Acc. Chem. Res.* **2008,** *41* (11), 1450-1460.
188. Zhang, Q.; Wang, D.; Wang, X.; Ding, K., (2-Pyridyl)acetone-Promoted Cu-Catalyzed O-Arylation of Phenols with Aryl Iodides, Bromides, and Chlorides. *J. Org. Chem.* **2009,** *74* (18), 7187-7190.
189. Isidro-Llobet, A.; Álvarez, M.; Albericio, F., Amino Acid-Protecting Groups. *Chem. Rev.* **2009,** *109* (6), 2455-2504.
190. Himes, R. A.; Park, G. Y.; Barry, A. N.; Blackburn, N. J.; Karlin, K. D., Synthesis and X-ray Absorption Spectroscopy Structural Studies of Cu(I) Complexes of HistidylHistidine Peptides: The Predominance of Linear 2-Coordinate Geometry. *J. Am. Chem. Soc.* **2007,** *129* (17), 5352-5353.
191. Nelli, Y.-R.; Douat-Casassus, C.; Claudon, P.; Kauffmann, B.; Didierjean, C.; Guichard, G., An activated building block for the introduction of the histidine side chain in aliphatic oligourea foldamers. *Tetrahedron* **2012,** *68* (23), 4492-4500.
192. 026180 - 2-Chloromethyl-pyridine hydrochloride. http://www.fluorochem.co.uk/Products/Product?code=026180 (accessed 25/03/2021).
193. Yeung, K.; Connolly, T.; Frennson, D.; Kathrine, A. G.-Y.; P.Hewawasam; Langley, D.; Meng, Z.; Mull, E.; Parcella, K.; Saulnier, M.; Sun, L.; Wang, X.; Xu, N.; Zhu, J.; Scola, M. Compounds Useful as Immunomodulators. US2017/107202, 2017.
194. 2-(2-Bromoethyl)pyridine (CAS 39232-04-7). https://www.scbt.com/p/2-2-bromoethyl-pyridine-39232-04-7 (accessed 15/03/2021).
195. Fujimoto, K.; Tanka, N.; Shimada, I.; Asai, F. Enzamdine Derivative. EP1375482, 2004.
196. Wróbel, J. T.; Hejchman, E., Spiro Derivatives of Tetrahydrothiophene. Synthesis of the Quinolizidine-spiro-2-t; tetrahydrothiophene System Using Solid/Liquid or Liquid/Liquid Phase-Transfer Catalysis. *Synthesis* **1987,** *1987* (05), 452-455.
197. Appel, R., Tertiary Phosphane/Tetrachloromethane, a Versatile Reagent for Chlorination, Dehydration, and P-N Linkage. *Angew. Chem. Int. Ed.* **1975,** *14* (12), 801-811.
198. Tachdjian, C.; Lebl-Rinnova, M.; Wallace, D.; Compounds comprising linked heteroaryl moieties and their use as novel umami flavor modifiers, tastants and taste enhancers for comestible compositions US2006/263411, 2006

199. Finkelstein, H., Darstellung organischer Jodide aus den entsprechenden Bromiden und Chloriden. *Ber. Dtsch. Chem. Ges.* **1910,** *43* (2), 1528-1532.
200. Wang, Z., Finkelstein Reaction. In *Comprehensive Organic Name Reactions and Reagents*, Wang, Z., Ed. 2010; pp 1060-1063.

201. Hancock, R. D.; Ngwenya, M. P., The effect of increase in chelate ring size beyond six-membered on the metal ion size selectivity patterns of tetra-aza macrocycles. *J. Chem. Soc., Dalton Trans.* **1987,** (12), 2911-2915.
202. Lavanant, H.; Virelizier, H.; Hoppilliard, Y., Reduction of copper(ii) complexes by electron capture in an electrospray ionization source. *J. Am. Soc. Mass. Spectrom.* **1998,** *9* (11), 1217-1221.
203. Renny, J. S.; Tomasevich, L. L.; Tallmadge, E. H.; Collum, D. B., Method of continuous variations: applications of job plots to the study of molecular associations in organometallic chemistry. *Angew. Chem. Int. Ed.* **2013,** *52* (46), 11998-12013.
204. Bruneau, E.; Lavabre, D.; Levy, G.; Micheau, J. C., Quantitative analysis of continuous-variation plots with a comparison of several methods: Spectrophotometric study of organic and inorganic 1:1 stoichiometry complexes. *J. Chem. Educ.* **1992,** *69* (10), 833.
205. Carlson, G. A.; McReynolds, J. P.; Verhoek, F. H., Equilibrium Constants for the Formation of Ammine Complexes with Certain Metallic Ions1. *J. Am. Chem. Soc.* **1945,** *67* (8), 1334-1339.
206. Stoll, S.; Schweiger, A., EasySpin, a comprehensive software package for spectral simulation and analysis in EPR. *J. Magn. Reson.* **2006,** *178* (1), 42-55.
207. *MATLAB and Statistics Toolbox Release R2019b*, The MathWorks, Inc.,: Natick, Massachusetts, United States.
208. Misra, P. D. S. K., Multifrequency Aspects of EPR. In *Multifrequency Electron Paramagnetic Resonance*, 2011; pp 23-55.
209. Iwaizumi, M.; Kudo, T.; Kita, S., Correlation between the hyperfine coupling constants of donor nitrogens and the structures of the first coordination sphere in copper complexes as studied by nitrogen-14 ENDOR spectroscopy. *Inorg. Chem.* **1986,** *25* (10), 1546-1550.
210. Garribba, E.; Micera, G., The Determination of the Geometry of Cu(II) Complexes: An EPR Spectroscopy Experiment. *J. Chem. Educ.* **2006,** *83* (8), 1229.
211. Roessler, M. M.; Salvadori, E., Principles and applications of EPR spectroscopy in the chemical sciences. *Chem. Soc. Rev.* **2018,** *47* (8), 2534-2553.
212. Gewirth, A. A.; Cohen, S. L.; Schugar, H. J.; Solomon, E. I., Spectroscopic and theoretical studies of the unusual EPR parameters of distorted tetrahedral cupric sites: correlations to x-ray spectral features of core levels. *Inorg.* **1987,** *26* (7), 1133-1146.
213. Henderson, L. J., Concening the Relationship Between the Strength of Acids and their Capacity to Preserve Neutrality. *Am. J. Physiol.* **1908,** *21* (2), 173-179.
214. Mesmer, C. F. B. a. R. S., *The Hydrolysis of Cations. John Wiley & Sons, New York, London, Sydney, Toronto 1976. 489 Seiten*. John Wiley & Sons, Ltd: 1977; Vol. 81, p 245-246.
215. Courtade, G.; Ciano, L.; Paradisi, A.; Lindley, P. J.; Forsberg, Z.; Sørlie, M.; Wimmer, R.; Davies, G. J.; Eijsink, V. G. H.; Walton, P. H.; Aachmann, F. L., Mechanistic basis of substrate–O₂ coupling within a chitin-active lytic polysaccharide monooxygenase: An integrated NMR/EPR study. *Proc. Natl. Acad. Sci. U.S.A* **2020,** *117* (32), 19178-19189.
216. Jeffrey, G. A., *An Introduction to Hydrogen Bonding*. Oxford University Press: 1997.
217. Zhang, C.-G.; Duan, C.-Y.; Hu, Q.; Yan, D.-Y., Self-assembly in transition metal complexes: structural characterization of a copper histamine nitrate [Cu(II)(him)2(NO3)2]. *J. Chem. Crystallogr.* **1999,** *29* (11), 1153-1155.
218. Hill, E. A.; Weitz, A. C.; Onderko, E.; Romero-Rivera, A.; Guo, Y.; Swart, M.; Bominaar, E. L.; Green, M. T.; Hendrich, M. P.; Lacy, D. C.; Borovik, A. S., Reactivity of an FeIV-Oxo Complex with Protons and Oxidants. *J. Am. Chem. Soc.* **2016,** *138* (40), 13143-13146.

219. Oh, H.; Ching, W.-M.; Kim, J.; Lee, W.-Z.; Hong, S., Hydrogen Bond-Enabled Heterolytic and Homolytic Peroxide Activation within Nonheme Copper(II)-Alkylperoxo Complexes. *Inorg. Chem.* **2019,** *58* (19), 12964-12974.
220. Hirota, S.; Lin, Y.-W., Design of artificial metalloproteins/metalloenzymes by tuning noncovalent interactions. *J. Biol. Inorg. Chem.* **2018,** *23* (1), 7-25.
221. Davis, H. J.; Ward, T. R., Artificial Metalloenzymes: Challenges and Opportunities. *ACS Cent. Sci.* **2019,** *5* (7), 1120-1136.
222. Mann, S. I.; Heinisch, T.; Ward, T. R.; Borovik, A. S., Peroxide Activation Regulated by Hydrogen Bonds within Artificial Cu Proteins. *J. Am. Chem. Soc.* **2017,** *139* (48), 17289-17292.
223. Mann, S. I.; Heinisch, T.; Weitz, A. C.; Hendrich, M. P.; Ward, T. R.; Borovik, A. S., Modular Artificial Cupredoxins. *J. Am. Chem. Soc.* **2016,** *138* (29), 9073-9076.
224. DeGrado, W. F.; Wasserman, Z. R.; Lear, J. D., Protein design, a minimalist approach. *Science* **1989,** *243* (4891), 622.
225. Yu, F.; Cangelosi, V. M.; Zastrow, M. L.; Tegoni, M.; Plegaria, J. S.; Tebo, A. G.; Mocny, C. S.; Ruckthong, L.; Qayyum, H.; Pecoraro, V. L., Protein Design: Toward Functional Metalloenzymes. *Chem. Rev.* **2014,** *114* (7), 3495-3578.
226. Mills, J. H.; Khare, S. D.; Bolduc, J. M.; Forouhar, F.; Mulligan, V. K.; Lew, S.; Seetharaman, J.; Tong, L.; Stoddard, B. L.; Baker, D., Computational Design of an Unnatural Amino Acid Dependent Metalloprotein with Atomic Level Accuracy. *J. Am. Chem. Soc.* **2013,** *135* (36), 13393-13399.
227. Wilson, M. E.; Whitesides, G. M., Conversion of a protein to a homogeneous asymmetric hydrogenation catalyst by site-specific modification with a diphosphinerhodium(I) moiety. *J. Am. Chem. Soc.* **1978,** *100* (1), 306-307.
228. Letondor, C.; Humbert, N.; Ward, T. R., Artificial metalloenzymes based on biotin-avidin technology for the enantioselective reduction of ketones by transfer hydrogenation. *Proc Natl Acad Sci U S A* **2005,** *102* (13), 4683.
229. Miller, K. R.; Paretsky, J. D.; Follmer, A. H.; Heinisch, T.; Mittra, K.; Gul, S.; Kim, I.-S.; Fuller, F. D.; Batyuk, A.; Sutherlin, K. D.; Brewster, A. S.; Bhowmick, A.; Sauter, N. K.; Kern, J.; Yano, J.; Green, M. T.; Ward, T. R.; Borovik, A. S., Artificial Iron Proteins: Modeling the Active Sites in Non-Heme Dioxygenases. *Inorganic Chemistry* **2020,** *59* (9), 6000-6009.
230. Key, H. M.; Dydio, P.; Clark, D. S.; Hartwig, J. F., Abiological catalysis by artificial haem proteins containing noble metals in place of iron. *Nature* **2016,** *534* (7608), 534-537.
231. Jing, Q.; Okrasa, K.; Kazlauskas, R. J., Manganese-Substituted α-Carbonic Anhydrase as an Enantioselective Peroxidase. In *Bio-inspired Catalysts*, Ward, T. R., Ed. Springer Berlin Heidelberg: Berlin, Heidelberg, 2009; pp 45-61.
232. Onoda, A.; Kihara, Y.; Fukumoto, K.; Sano, Y.; Hayashi, T., Photoinduced Hydrogen Evolution Catalyzed by a Synthetic Diiron Dithiolate Complex Embedded within a Protein Matrix. *ACS Catalysis* **2014,** *4* (8), 2645-2648.
233. Davies, R. R.; Distefano, M. D., A Semisynthetic Metalloenzyme Based on a Protein Cavity That Catalyzes the Enantioselective Hydrolysis of Ester and Amide Substrates. *J. Am. Chem. Soc.* **1997,** *119* (48), 11643-11652.
234. Platis, I. E.; Ermacora, M. R.; Fox, R. O., Oxidative polypeptide cleavage mediated by EDTA-iron covalently linked to cysteine residues. *Biochemistry* **1993,** *32* (47), 12761-12767.
235. Yang, H.; Srivastava, P.; Zhang, C.; Lewis, J. C., A General Method for Artificial Metalloenzyme Formation through Strain-Promoted Azide–Alkyne Cycloaddition. *ChemBioChem* **2014,** *15* (2), 223-227.
236. Weber, P. C.; Ohlendorf, D. H.; Wendoloski, J. J.; Salemme, F. R., Structural origins of high-affinity biotin binding to streptavidin. *Science* **1989,** *243* (4887), 85.

237. Hestericová, M.; Heinisch, T.; Alonso-Cotchico, L.; Maréchal, J.-D.; Vidossich, P.; Ward, T. R., Directed Evolution of an Artificial Imine Reductase. *Angew. Chem. Int. Ed.* **2018,** *57* (7), 1863-1868.
238. Jeschek, M.; Reuter, R.; Heinisch, T.; Trindler, C.; Klehr, J.; Panke, S.; Ward, T. R., Directed evolution of artificial metalloenzymes for in vivo metathesis. *Nature* **2016,** *537* (7622), 661-665.
239. Collot, J.; Gradinaru, J.; Humbert, N.; Skander, M.; Zocchi, A.; Ward, T. R., Artificial Metalloenzymes for Enantioselective Catalysis Based on Biotin−Avidin. *J. Am. Chem. Soc.* **2003,** *125* (30), 9030-9031.
240. Liang, A. D.; Serrano-Plana, J.; Peterson, R. L.; Ward, T. R., Artificial Metalloenzymes Based on the Biotin–Streptavidin Technology: Enzymatic Cascades and Directed Evolution. *Acc. Chem. Res.* **2019,** *52* (3), 585-595.
241. Serrano-Plana, J.; Rumo, C.; Rebelein, J. G.; Peterson, R. L.; Barnet, M.; Ward, T. R., Enantioselective Hydroxylation of Benzylic C(sp3)–H Bonds by an Artificial Iron Hydroxylase Based on the Biotin–Streptavidin Technology. *J. Am. Chem. Soc.* **2020,** *142* (24), 10617–10623.
242. Olshansky, L.; Huerta-Lavorie, R.; Nguyen, A. I.; Vallapurackal, J.; Furst, A.; Tilley, T. D.; Borovik, A. S., Artificial Metalloproteins Containing Co4O4 Cubane Active Sites. *J. Am. Chem. Soc.* **2018,** *140* (8), 2739-2742.
243. Laszlo Kurti, B. C., *Strategic Applications of Named Reactions in Organic Synthesis*. Elsevier Academic Press: Burlington, 2005.
244. Kisanga, P. B.; Verkade, J. G., P(RNCH2CH2)3N: An Efficient Promoter for the Nitroaldol (Henry) Reaction. *J. Org. Chem.* **1999,** *64* (12), 4298-4303.
245. Baughman, T. W.; Sworen, J. C.; Wagener, K. B., The facile preparation of alkenyl metathesis synthons. *Tetrahedron* **2004,** *60* (48), 10943-10948.
246. Biffis, A.; Centomo, P.; Del Zotto, A.; Zecca, M., Pd Metal Catalysts for Cross-Couplings and Related Reactions in the 21st Century: A Critical Review. *Chem. Rev.* **2018,** *118* (4), 2249-2295.
247. Miyaura, N.; Yamada, K.; Suzuki, A., A new stereospecific cross-coupling by the palladium-catalyzed reaction of 1-alkenylboranes with 1-alkenyl or 1-alkynyl halides. *Tetrahedron Lett.* **1979,** *20* (36), 3437-3440.
248. Milstein, D.; Stille, J. K., A general, selective, and facile method for ketone synthesis from acid chlorides and organotin compounds catalyzed by palladium. *J. Am. Chem. Soc.* **1978,** *100* (11), 3636-3638.
249. King, A. O.; Okukado, N.; Negishi, E.-i., Highly general stereo-, regio-, and chemo-selective synthesis of terminal and internal conjugated enynes by the Pd-catalysed reaction of alkynylzinc reagents with alkenyl halides. *J. Chem. Soc., Chem. Commun.* **1977,** (19), 683-684.
250. Tamao, K.; Sumitani, K.; Kumada, M., Selective carbon-carbon bond formation by cross-coupling of Grignard reagents with organic halides. Catalysis by nickel-phosphine complexes. *J. Am. Chem. Soc.* **1972,** *94* (12), 4374-4376.
251. Heck, R. F.; Nolley, J. P., Palladium-catalyzed vinylic hydrogen substitution reactions with aryl, benzyl, and styryl halides. *J. Org. Chem.* **1972,** *37* (14), 2320-2322.
252. Sonogashira, K. T., Y.; Hagihara, N, A Covenient Synthesis of Acetylenes: Catlaytic Substitutions of Acetylenetic Hydrogen with Brokoalkenens, Iodoarenes and Bromopyridines. *Tetrahedron Lett.* **1975,** *16*, 4467.
253. Fihri, A.; Bouhrara, M.; Nekoueishahraki, B.; Basset, J.-M.; Polshettiwar, V., Nanocatalysts for Suzuki cross-coupling reactions. *Chem. Soc. Rev.* **2011,** *40* (10), 5181-5203.

254. Hooshmand, S. E.; Heidari, B.; Sedghi, R.; Varma, R. S., Recent advances in the Suzuki–Miyaura cross-coupling reaction using efficient catalysts in eco-friendly media. *Green Chem.* **2019,** *21* (3), 381-405.
255. Whitaker, L.; Harb, H. Y.; Pulis, A. P., One-pot borylation/Suzuki–Miyaura sp2–sp3 cross-coupling. *Chem. Commun.* **2017,** *53* (67), 9364-9367.
256. Königsberger, K.; Chen, G.-P.; Wu, R. R.; Girgis, M. J.; Prasad, K.; Repič, O.; Blacklock, T. J., A Practical Synthesis of 6-[2-(2,5-Dimethoxyphenyl)ethyl]-4-ethylquinazoline and the Art of Removing Palladium from the Products of Pd-Catalyzed Reactions. *Org. Process Res. Dev.* **2003,** *7* (5), 733-742.
257. Cordovilla, C.; Bartolomé, C.; Martínez-Ilarduya, J. M.; Espinet, P., The Stille Reaction, 38 Years Later. *ACS Catal.* **2015,** *5* (5), 3040-3053.
258. Heravi, M. M.; Hajiabbasi, P., Recent advances in Kumada-Tamao-Corriu cross-coupling reaction catalyzed by different ligands. *Monatsh. Chem.* **2012,** *143* (12), 1575-1592.
259. Chinchilla, R.; Nájera, C., The Sonogashira Reaction: A Booming Methodology in Synthetic Organic Chemistry. *Chem. Rev.* **2007,** *107* (3), 874-922.
260. Knowles, J. P.; Whiting, A., The Heck–Mizoroki cross-coupling reaction: a mechanistic perspective. *Org. Biomol. Chem.* **2007,** *5* (1), 31-44.
261. T. W. Green, P. G. M. W., *Protective Groups in Organic Synthesis*. 3rd ed.; Wiley-Interscience: 1999; Vol. 1.
262. Elangovan, A.; Wang, Y.-H.; Ho, T.-I., Sonogashira Coupling Reaction with Diminished Homocoupling. *Org. Lett.* **2003,** *5* (11), 1841-1844.
263. TCI Biotin Pentafluorophenyl Ester CAS RN: 120550-35-8. https://www.tcichemicals.com/IN/en/p/B3173 (accessed 17/03/2021).
264. Chambers, J. M.; Lindqvist, L. M.; Webb, A.; Huang, D. C. S.; Savage, G. P.; Rizzacasa, M. A., Synthesis of Biotinylated Episilvestrol: Highly Selective Targeting of the Translation Factors eIF4AI/II. *Org. Lett.* **2013,** *15* (6), 1406-1409.
265. Green, N. M., A Spectrophotometric Assay for Avidin and Biotin Based on Binding of Dyes by Avidin. *Biochem. J* **1965,** *94* (3), 23C-24C.
266. Bennett, B.; Kowalski, J. M., EPR Methods for Biological Cu(II): L-Band CW and NARS. *Methods Enzymol.* **2015,** *563*, 341-361.
267. Saito, K.; Nakagawa, M.; Ishikita, H., pKa of the ligand water molecules in the oxygen-evolving Mn4CaO5 cluster in photosystem II. *Commun. Chem* **2020,** *3* (1), 89.
268. Lide, D. R., *Handbook of Chemistry and Physics*. 72nd Edition ed.; CRC Press: 1991.
269. Crawford, T. H.; Dalton, J. O., ESR studies of copper(II) complex ions. *Arch. Biochem. Biophys.* **1969,** *131* (1), 123-138.
270. Falk, K. E.; Freeman, H. C.; Jansson, T.; Malmstrom, B. G.; Vanngard, T., Magnetic resonance studies of copper (II)-triglycylglycine complexes. *J. Am. Chem. Soc.* **1967,** *89* (24), 6071-6077.
271. Bordwell, F. G., Equilibrium acidities in dimethyl sulfoxide solution. *Acc. Chem. Res.* **1988,** *21* (12), 456-463.
272. Falk, K. E.; Ivanova, E.; Roos, B.; Vanngard, T., Electron paramagnetic resonance study of copper(II) dimethylglyoxime. I. Theoretical and experimental study of the effect of axial ligands. *Inorg.* **1970,** *9* (3), 556-562.
273. Malmström, B. G.; Vänngård, T., Electron spin resonance of copper proteins and some model complexes. *J. Mol. Biol.* **1960,** *2* (2), 118-124.
274. Walker, F. A.; Sigel, H.; McCormick, D. B., Spectral properties of mixed-ligand copper(II) complexes and their corresponding binary parent complexes. *Inorg. Chem.* **1972,** *11* (11), 2756-2763.

275. Carter, E.; Hazeland, E. L.; Murphy, D. M.; Ward, B. D., Structure, EPR/ENDOR and DFT characterisation of a [CuII(en)2](OTf)2 complex. *Dalton Trans.* **2013,** *42* (42), 15088-15096.
276. Vagin, A.; Teplyakov, A., Molecular replacement with MOLREP. *Acta Crystallogr D Biol Crystallogr* **2010,** *66* (Pt 1), 22-5.
277. Emsley, P.; Cowtan, K., Coot: model-building tools for molecular graphics. *Acta Crystallogr D Biol Crystallogr* **2004,** *60* (Pt 12 Pt 1), 2126-32.
278. Pähler, A.; Hendrickson, W. A.; Kolks, M. A.; Argaraña, C. E.; Cantor, C. R., Characterization and crystallization of core streptavidin. *J. Biol. Chem.* **1987,** *262* (29), 13933-13937.
279. Chance, B., The kinetics of the enzyme-substrate compound of peroxidase. 1943. *Adv. Enzymol. Relat. Areas Mol. Biol.* **1999,** *73*, 3-23.
280. Bagshaw, C. R., Stopped-Flow Techniques. In *Encyclopedia of Biophysics*, Roberts, G. C. K., Ed. Springer Berlin Heidelberg: Berlin, Heidelberg, 2013; pp 2460-2466.
281. Roder, H.; Maki, K.; Cheng, H., Early events in protein folding explored by rapid mixing methods. *Chem. Rev.* **2006,** *106* (5), 1836-1861.
282. Rittle, J.; Green, M. T., Cytochrome P450 Compound I: Capture, Characterization, and C-H Bond Activation Kinetics. *Science* **2010,** *330* (6006), 933.
283. Shoji, O.; Watanabe, Y., Peroxygenase reactions catalyzed by cytochromes P450. *J. Biol. Inorg. Chem.* **2014,** *19* (4), 529-539.
284. Prasad, B.; Mah, D. J.; Lewis, A. R.; Plettner, E., Water Oxidation by a Cytochrome P450: Mechanism and Function of the Reaction. *PLOS ONE* **2013,** *8* (4), e61897.
285. Hessenauer-Ilicheva, N.; Franke, A.; Meyer, D.; Woggon, W.-D.; van Eldik, R., Mechanistic Insight into Formation of Oxo-Iron(IV) Porphyrin π-Cation Radicals from Enzyme Mimics of Cytochrome P450 in Organic Solvents. *Chem. Eur. J* **2009,** *15* (12), 2941-2959.
286. Munro, A. W.; Girvan, H. M.; Mason, A. E.; Dunford, A. J.; McLean, K. J., What makes a P450 tick? *Trends Biochem. Sci* **2013,** *38* (3), 140-150.
287. Jones, S. M.; Transue, W. J.; Meier, K. K.; Kelemen, B.; Solomon, E. I., Kinetic analysis of amino acid radicals formed in H2O2-driven CuI LPMO reoxidation implicates dominant homolytic reactivity. *Proc. Natl. Acad. Sci. U. S. A.* **2020,** *117* (22), 11916.
288. Moeslinger, T.; Brunner, M.; Spieckermann, P. G., Spectrophotometric Determination of Dehydroascorbic Acid in Biological Samples. *Anal. Biochem.* **1994,** *221* (2), 290-296.
289. Nami, F.; Gast, P.; Groenen, E. J. J., Rapid Freeze-Quench EPR Spectroscopy: Improved Collection of Frozen Particles. *Appl. Magn. Reson.* **2016,** *47*, 643-653.
290. Breslmayr, E.; Daly, S.; Požgajčić, A.; Chang, H.; Rezić, T.; Oostenbrink, C.; Ludwig, R., Improved spectrophotometric assay for lytic polysaccharide monooxygenase. *Biotechnol. Biofuels* **2019,** *12* (1), 283.
291. Zhou, M.; Diwu, Z.; Panchuk-Voloshina, N.; Haugland, R. P., A Stable Nonfluorescent Derivative of Resorufin for the Fluorometric Determination of Trace Hydrogen Peroxide: Applications in Detecting the Activity of Phagocyte NADPH Oxidase and Other Oxidases. *Anal. Biochem.* **1997,** *253* (2), 162-168.
292. Mohanty, J. G.; Jaffe, J. S.; Schulman, E. S.; Raible, D. G., A highly sensitive fluorescent micro-assay of H2O2 release from activated human leukocytes using a dihydroxyphenoxazine derivative. *J Immunol Methods* **1997,** *202* (2), 133-41.
293. Westereng, B.; Agger, J. W.; Horn, S. J.; Vaaje-Kolstad, G.; Aachmann, F. L.; Stenstrøm, Y. H.; Eijsink, V. G. H., Efficient separation of oxidized cello-oligosaccharides generated by cellulose degrading lytic polysaccharide monooxygenases. *J. Chromatogr. A* **2013,** *1271* (1), 144-152.

294. Rohrer, J. S.; Basumallick, L.; Hurum, D., High-performance anion-exchange chromatography with pulsed amperometric detection for carbohydrate analysis of glycoproteins. *Biochem. (Mosc.)* **2013,** *78* (7), 697-709.
295. Cataldi, T. R. I.; Campa, C.; De Benedetto, G. E., Carbohydrate analysis by high-performance anion-exchange chromatography with pulsed amperometric detection: The potential is still growing. *Fresenius J. Anal. Chem.* **2000,** *368* (8), 739-758.
296. Westereng, B.; Arntzen, M.; Aachmann, F.; Várnai, A.; Eijsink, V.; Agger, J., Simultaneous analysis of C1 and C4 oxidized oligosaccharides, the products of lytic polysaccharide monooxygenases acting on cellulose. *J. Chromatogr. A* **2016,** *1445*.
297. Goodwin, D. C.; Grover, T. A.; Aust, S. D., Roles of Efficient Substrates in Enhancement of Peroxidase-Catalyzed Oxidations. *Biochemistry* **1997,** *36* (1), 139-147.
298. Gilli, P.; Pretto, L.; Bertolasi, V.; Gilli, G., Predicting Hydrogen-Bond Strengths from Acid−Base Molecular Properties. The pKa Slide Rule: Toward the Solution of a Long-Lasting Problem. *Acc. Chem. Res.* **2009,** *42* (1), 33-44.
299. Palatinus, L.; Chapuis, G., SUPERFLIP - a computer program for the solution of crystal structures by charge flipping in arbitrary dimensions. *J. Appl. Crystallogr.* **2007,** *40* (4), 786-790.
300. Sheldrick, G., A short history of SHELX. *Acta Cryst.* **2008,** *64* (1), 112-122.
301. Deng, L.; Diao, J.; Chen, P.; Pujari, V.; Yao, Y.; Cheng, G.; Crick, D. C.; Prasad, B. V. V.; Song, Y., Inhibition of 1-Deoxy-d-Xylulose-5-Phosphate Reductoisomerase by Lipophilic Phosphonates: SAR, QSAR, and Crystallographic Studies. *J. Med. Chem.* **2011,** *54* (13), 4721-4734.
302. Kittl, R.; Kracher, D.; Burgstaller, D.; Haltrich, D.; Ludwig, R., Production of four Neurospora crassa lytic polysaccharide monooxygenases in Pichia pastoris monitored by a fluorimetric assay. *Biotechnol. Biofuels* **2012,** *5* (1), 79.